

AFFDL-TR-78-175
Volume I

Wright-Patterson
Technical Library
WPAFB, Ohio 45433

Stan
✓

AD-A072122

**EFFECT OF MULTIAXIAL LOADING
ON CRACK GROWTH
Volume I - Technical Summary**

*A. F. LIU
D. F. DITTMER*

*NORTHROP CORPORATION
AIRCRAFT GROUP
HAWTHORNE, CALIFORNIA 90250*

December 1978

FINAL REPORT

SEPTEMBER 1976 - SEPTEMBER 1978

Approved for public release; distribution unlimited.

Best Available Copy

*Air Force Flight Dynamics Laboratory
Air Force Wright Aeronautical Laboratories
Air Force Systems Command
Wright-Patterson Air Force Base, Ohio 45433*

20060921151

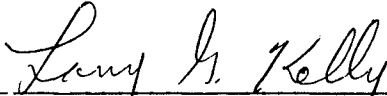
NOTICE

When Government drawings, specifications or other data are used for any purpose other than in connection with a definitely related Government procurement operation, the United States Government thereby incurs no responsibility nor any obligation whatsoever; and the fact that the government may have formulated, furnished, or in any way supplied the said drawings, specifications, or other data, is not to be regarded by implication or otherwise as in any manner licensing the holder or any other person or corporation, or conveying any rights or permission to manufacture, use, or sell any patented invention that may in any way be related thereto.

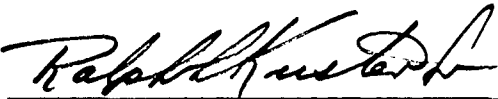
This report has been reviewed by the Information Office (OI) and is releasable to the National Technical Information Service (NTIS). At NTIS, it will be available to the general public, including foreign nations.

This technical report has been reviewed and is approved for publication.


DONALD R. HOLLOWAY, Capt, USAF
Project Engineer


LARRY G. KELLY, Actg Chief
Structural Integrity Branch

FOR THE COMMANDER


RALPH L. KUSTER, JR., Col, USAF
Chief, Structures & Dynamics Division

"If your address has changed, if you wish to be removed from our mailing list, or if the addressee is no longer employed by your organization please notify AFFDL/FBE, W-PAFB, OH 45433 to help us maintain a current mailing list."

Copies of this report should not be returned unless return is required by security considerations, contractual obligations, or notice on a specific document.

UNCLASSIFIED

SECURITY CLASSIFICATION OF THIS PAGE (When Data Entered)

REPORT DOCUMENTATION PAGE		READ INSTRUCTIONS BEFORE COMPLETING FORM
1. REPORT NUMBER AFFDL-TR-78-175, Volume I	2. GOVT. ACCESSION NO.	3. RECIPIENT'S CATALOG NUMBER
4. TITLE (and Subtitle) EFFECT OF MULTIAXIAL LOADING ON CRACK GROWTH VOLUME I. TECHNICAL SUMMARY		5. TYPE OF REPORT & PERIOD COVERED Final Report 15 Sept. 1976-15 Sept 1978
		6. PERFORMING ORG. REPORT NUMBER NOR 78-161, Volume I
7. AUTHOR(s) A.F. Liu and D.F. Ditmer		8. CONTRACT OR GRANT NUMBER(s) F33615-76-C-3121
9. PERFORMING ORGANIZATION NAME AND ADDRESS Northrop Corporation Aircraft Group 3901 West Broadway, Hawthorne, CA 90250		10. PROGRAM ELEMENT, PROJECT, TASK AREA & WORK UNIT NUMBERS 486U-02-24
11. CONTROLLING OFFICE NAME AND ADDRESS Air Force Flight Dynamics Laboratory (FBE) Wright-Patterson AFB, OH 45433		12. REPORT DATE December 1978
		13. NUMBER OF PAGES 219
14. MONITORING AGENCY NAME & ADDRESS (if different from Controlling Office)		15. SECURITY CLASS. (of this report) Unclassified
		15a. DECLASSIFICATION/DOWNGRADING SCHEDULE
16. DISTRIBUTION STATEMENT (of this Report) Approved for public release; distribution unlimited.		
17. DISTRIBUTION STATEMENT (of the abstract entered in Block 20, if different from Report)		
18. SUPPLEMENTARY NOTES		
19. KEY WORDS (Continue on reverse side if necessary and identify by block number) Fracture Mechanics, Stress Intensity Factors, Fatigue Crack Growth, Testing, Biaxial Loading, Crack Tip Plasticity, Metals.		
20. ABSTRACT (Continue on reverse side if necessary and identify by block number) An exploratory research program has been conducted to systematically evaluate the effects of biaxial stress ratio on constant amplitude and variable ampli- tude fatigue crack growth rates. A series of experiments and analyses have been carried out on the cyclic crack growth behavior of center-cracked cruciform specimens under various biaxial loading conditions. The results may be summarized as follows. (continued)		

DD FORM 1 JAN 73 1473

UNCLASSIFIED
SECURITY CLASSIFICATION OF THIS PAGE (When Data Entered)

UNCLASSIFIED

SECURITY CLASSIFICATION OF THIS PAGE(When Data Entered)

Block No. 20 (continued)

1. Crack will grow straight in a biaxial stress field when the stress component parallel to the crack is equal to or smaller than the stress component normal to the crack.
2. Elastic K factors are obtainable for both straight and curved cracks and are adequate for correlating the biaxial growth rate data.
3. At a given stress intensity level, the constant amplitude crack growth rates are the same in all the biaxial loading conditions.
4. In out-of-phase loading conditions, the crack growth rate and crack growth directions are the same as those in the in-phase loading conditions.
5. Crack tip plastic zone size variations with biaxial ratio appeared to have no effect on constant-amplitude crack growth rate.
6. As for the variable amplitude tests, it is very evident that cracks grow faster at positive biaxial stress states, but slower at negative biaxial loading conditions.

UNCLASSIFIED

SECURITY CLASSIFICATION OF THIS PAGE(When Data Entered)

FOREWORD

This report describes results of work performed by the Northrop Corporation, Aircraft Group, Hawthorne, California, under Air Force Contract F33615-76-C-3121, "Effect of Multiaxial Loading on Crack Growth," Project 486U, "Advanced Metallic Structures - Advanced Development Program," Task 486U02, work unit 486U0224. The effort was sponsored by the Air Force Flight Dynamics Laboratory, Air Force Wright Aeronautical Laboratories, Air Force Systems Command, Wright-Patterson Air Force Base, Ohio. Captains John E. Allison and Donald R. Holloway of the AFFDL/FBE were the Air Force Project Engineers.

The program was performed by the Structures Research Department of Northrop Corporation, Aircraft Group, under the overall supervision of L. L. Jeans, Manager, Structural Life Assurance Research. Mr. A. F. Liu was the Northrop Program Manager and Principal Investigator. He was assisted by D. F. Dittmer on experimental tasks; J. R. Yamane, Dr. J. P. Buban, and Dr. H. P. Kan on analytical tasks. Dr. M. M. Ratwani provided guidance on cracked finite element analysis.

This report covers work accomplished during the period September 1976 through September 1978. This report consists of three volumes.

Volume I	Technical Summary
Volume II	Compilation of Experimental Data
Volume III	Compilation of Interferometry Photographs

Volumes II and III are available upon request. Send requests to:

AFFDL/FBE
ATTN: Capt. D.R. Holloway
Wright-Patterson AFB, OH 45433

TABLE OF CONTENTS

SECTION	PAGE
I INTRODUCTION	1
II STATEMENT OF WORK	2
III BIAXIAL TESTING MACHINE	4
IV SPECIMEN CONFIGURATION	10
V STRESS SURVEY	17
VI STRESS INTENSITY FACTORS	20
6.1 Straight Crack	20
6.2 Angle Crack	21
6.3 Cracks at a Hole	26
6.4 Curved Crack	30
VII CRACK TIP PLASTIC ZONE SIZES	34
7.1 Finite Element Analysis	34
7.2 Interferometry Measurements	53
7.3 Backtracked Residual Plastic Zones	60
VIII CRACK GROWTH ANALYSIS METHODOLOGY	91
8.1 Fatigue Crack Growth Under Constant Amplitude Cyclic Loading	91
8.2 The Modified Willenborg Model	95
8.3 The New Crack Growth Retardation Model	99

TABLE OF CONTENTS (con't)

SECTION	PAGE
IX EXPERIMENTS	106
9.1 Material Characterization Tests	107
9.2 Constant Amplitude Biaxial Crack Growth Rate Tests	107
9.2.1 Test Results	114
9.2.2 Correlation of High Biaxial Ratio Test Data	128
9.3 The Effect of Cyclic Stress Ratio	144
9.4 Crack Coming Out From a Hole Tests	144
9.5 Variable Amplitude Tests	156
9.5.1 Single Overload Tests	156
9.5.2 Spectrum Load Tests	189
9.6 Out-Of-Phase Loading Tests	199
9.7 Miscellaneous Tests	203
9.7.1 Sustained Load Tests	203
9.7.2 Angle Crack Tests	205
9.7.3 Fracture Tests	210
X GUIDELINES FOR FATIGUE CRACK GROWTH ANALYSIS	215
XI RECOMMENDATIONS FOR FUTURE RESEARCH	216
REFERENCES	217

LIST OF ILLUSTRATIONS

FIGURE		PAGE
1	Biaxial Loading Machine	5
2	Close up of the Biaxial Loading Machine	6
3	Control Unit	7
4	Cruciform Specimen	11
5	The Center Section of the Cruciform Specimen (containing a curved crack)	12
6	Finite Element Model for One-Quarter of a Cruciform Specimen	13
7	Load-Stress Relationship at the Center Point of a Cruciform Specimen	15
8	Stress Gradient Along the X-Axis of a Cruciform Specimen	16
9	Rosette Gauge Location	18
10	Stress Intensities for Center Through Cracks in a Cruciform Specimen	22
11	Finite Element Model for Angle Crack	24
12	Comparison of Stress Intensities for a 45° Crack and 0° Crack in a Cruciform Specimen	25
13	Evaluation of Bowie's Factor for Biaxial Loading	27
14	Stress Intensity Factors for Two Cracks Coming Out from a Circular Hole in a Finite Width Shett	29
15	Notations for a Curved Crack	31
16	Notations for a Curved Crack	33
17	Finite Element Model for Elastic-Plastic Analysis	35
18	Crack Tip Plastic Zone for 7075-T7351 at 30 ksi (NASTRAN analysis)	37
19	Crack Tip Plastic Zone for 7075-T7351 at 30 ksi (NASTRAN analysis)	38

LIST OF ILLUSTRATIONS (con't)

FIGURE		PAGE
20	Crack Tip Plastic Zone for 7075-T7351 at 30 ksi (NASTRAN analysis)	39
21	Crack Tip Plastic Zone for 7075-T7351 at 30 ksi (NASTRAN analysis)	40
22	Crack Tip Plastic Zone for 2024-T351 at 30 ksi (NASTRAN analysis)	41
23	Crack Tip Plastic Zone for 2024-T351 at 30 ksi (NASTRAN analysis)	42
24	Crack Tip Plastic Zone for 2024-T351 at 30 ksi (NASTRAN analysis)	43
25	Crack Tip Plastic Zone	47
26	Crack Tip Plastic Zone for 7075-T7351 (NASTRAN analysis)	49
27	Crack Tip Plastic Zone for 7075-T7351 (NASTRAN analysis)	50
28	Crack Tip Plastic Zone for 2024-T351 (NASTRAN analysis)	51
29	Crack Tip Plastic Zone for 2024-T351 (NASTRAN analysis)	52
30	Interferometry Photograph of Cruciform Specimen No. 7-114, Test Case No. 99	56
31	Interferometry Photograph of Cruciform Specimen No. 7-114, Test Case No. 99	57
32	Interferometry Photograph of Cruciform Specimen No. 2-24, Test Case No. 101	58
33	Schematic Illustration of Three Typical Interferometry Patterns	59
34	Interferometry Measurement of Crack Tip Plastic Zone Sizes	61
35	Interferometry Measurement of Crack Tip Plastic Zone Sizes	62
36	Interferometry Measurement of Crack Tip Plastic Zone Sizes	63

LIST OF ILLUSTRATIONS (con't)

FIGURE		PAGE
37	Interferometry Measurement of Crack Tip Plastic Zone Sizes	64
38	Interferometry Measurement of Crack Tip Plastic Zone Sizes	65
39	Interferometry Measurement of Crack Tip Plastic Zone Sizes	66
40	Interferometry Measurement of Crack Tip Plastic Zone Sizes	67
41	Interferometry Measurement of Crack Tip Plastic Zone Sizes	68
42	Interferometry Measurement of Crack Tip Plastic Zone Sizes	69
43	Interferometry Measurement of Crack Tip Plastic Zone Sizes	70
44	Interferometry Measurement of Crack Tip Plastic Zone Sizes	71
45	Interferometry Measurement of Crack Tip Plastic Zone Sizes	72
46	Interferometry Measurement of Crack Tip Plastic Zone Sizes	73
47	Interferometry Measurement of Crack Tip Plastic Zone Sizes	74
48	Interferometry Measurement of Crack Tip Plastic Zone Sizes	75
49	Comparison of Interferometry and NASTRAN Crack Tip Plastic Zone Sizes	76
50	Comparison of Interferometry and NASTRAN Crack Tip Plastic Zone Sizes	77
51	Comparison of Interferometry and NASTRAN Crack Tip Plastic Zone Sizes	78
52	Comparison of Interferometry and NASTRAN Crack Tip Plastic Zone Sizes	79
53	Comparison of Interferometry and NASTRAN Crack Tip Plastic Zone Sizes	80
54	Comparison of Interferometry and NASTRAN Crack Tip Plastic Zone Sizes	81
55	Comparison of Interferometry and NASTRAN Crack Tip Plastic Zone Sizes	82

LIST OF ILLUSTRATIONS (con't)

FIGURE		PAGE
56	Experimentally Determined Residual Crack Tip Plastic Zones	85
57	Experimentally Determined Residual Crack Tip Plastic Zones	86
58	Experimentally Determined Residual Crack Tip Plastic Zones	87
59	Experimentally Determined Residual Crack Tip Plastic Zones	88
60	Experimentally Determined Residual Crack Tip Plastic Zones	89
61	Experimentally Determined Residual Crack Tip Plastic Zones	90
62	Definition of Effective Crack Angle (α) and Crack Takeoff Angle (θ) in Propagation of a Curved Crack	94
63	Load Interaction Zone at Crack Tip	96
64	Effective Stress in the Willenborg Model	98
65	Crack Growth Rate Inside an Overload Zone	100
66	Growth Rate Curve Resulting from the Application of a Single Overload	103
67	Effective K-Ranges Inside an Overload Zone	104
68	Typical Tensile Stress-Strain Curve, 7075-T7351, LT, t=.18 inch	108
69	Typical Tensile Stress-Strain Curve, 2024-T351, LT, t=.18 inch	109
70	Cyclic Crack Growth Rate Behavior of 7075-T7351 Aluminum	116
71	Cyclic Crack Growth Rate Behavior of 7075-T7351 Aluminum	117
72	Cyclic Crack Growth Rate Behavior of 7075-T7351 Aluminum	118
73	Cyclic Crack Growth Rate Behavior of 7075-T7351 Aluminum	119
74	Cyclic Crack Growth Rate Behavior of 7075-T7351 Aluminum	120
75	Cyclic Crack Growth Rate Behavior of 2024-T351 Aluminum	121
76	Cyclic Crack Growth Rate Behavior of 2024-T351 Aluminum	122

LIST OF ILLUSTRATIONS (con't)

FIGURE		PAGE
77	Cyclic Crack Growth Rate Behavior of 2024-T351 Aluminum	123
78	Cyclic Crack Growth Rate Behavior of 2024-T351 Aluminum	124
79	Cyclic Crack Growth Rate Behavior of 2024-T351 Aluminum	125
80	Crack Growth Histories of the 7075-T7351 Cruciform Specimens	126
81	Crack Growth Histories of the 2024-T351 Cruciform Specimens	127
82	Crack Growth Profile of 7075-T7351 Cruciform Specimen No. 7-38 Test Case No. 141	129
83	Crack Growth Profile of 7075-T7351 Cruciform Specimen No. 7-38 Test Case No. 68	130
84	Crack Growth Profile of 7075-T7351 Cruciform Specimen No. 7-4 Test Case No. 142	131
85	Crack Growth Rate Behavior of 7075-T7351 Cruciform Specimen No. 7-38 Test Case No. 141	132
86	Crack Growth Rate Behavior of 7075-T7351 Cruciform Specimen No. 7-38 Test Case No. 141	133
87	Crack Growth Rate Behavior of 7075-T7351 Cruciform Specimen No. 7-38 Test Case No. 141	134
88	Crack Growth Rate Behavior of 7075-T7351 Cruciform Specimen No. 7-28 Test Case No. 68	135
89	Crack Growth Rate Behavior of 7075-T7351 Cruciform Specimen No. 7-28 Test Case No. 68	136
90	Crack Growth Rate Behavior of 7075-T7351 Cruciform Specimen No. 7-28 Test Case No. 68	137
91	Crack Growth Rate Behavior of 7075-T7351 Cruciform Specimen No. 7-4 Test Case No. 142	138
92	Crack Growth Rate Behavior of 7075-T7351 Cruciform Specimen No. 7-4 Test Case No. 142	139
93	Crack Growth Rate Behavior of 7075-T7351 Cruciform Specimen No. 7-4 Test Case No. 142	140

LIST OF ILLUSTRATION (con't)

FIGURE		PAGE
94	Baseline Crack Growth Rate Behavior for 7075-T7351, LT Direction (CCT Specimen, R = 0.1, f = 5 Hz)	141
95	Baseline Crack Growth Rate Behavior from 7075-T7351, LT Direction (CCT Specimen, R = 0.1, f = 5 Hz)	145
96	Baseline Crack Growth Rate Behavior for 2024-T351, LT Direction (CCT Specimen, R = 0.1, f = 5 Hz)	146
97	Cyclic Crack Growth Behavior of 7075-T7351 Cruciform Specimen	151
98	Cyclic Crack Growth Behavior of 7075-T7351 Cruciform Specimen	152
99	Cyclic Crack Growth Behavior of 2024-T351 Cruciform Specimen	153
100	Cyclic Crack Growth Behavior of 2024-T351 Cruciform Specimen	154
101	Crack Growth History of 7075-T7351 Cruciform Specimen No. 7-114 Test Case No. 99	158
102	Crack Growth History of 7075-T7351 Cruciform Specimen No. 7-25 Test Case No. 103	159
103	Crack Growth History of 7075-T7351 Cruciform Specimen No. 7-113 Test Case No. 104	160
104	Crack Growth History of 7075-T7351 Cruciform Specimen No. 7-53 Test Case No. 105	161
105	Crack Growth History of 2024-T351 Cruciform Specimen No. 2-24, Test Case No. 101	162
106	Crack Growth History of 2024-T351 Center Cracked Panel, Specimen No. LT-2-5 Test Case No. 102	163
107	Crack Growth History of 2024-T351 Cruciform Specimen No. 2-38 Test Case No. 108	164
108	Crack Growth History of 2024-T351 Cruciform Specimen No. 2-34 Test Case No. 109	165
109	Crack Growth History of 2024-T351 Cruciform Specimen No. 2-41, Test Case No. 110	166

LIST OF ILLUSTRATIONS (con't)

FIGURE		PAGE
110	Crack Growth Rate Behavior of 7075-T7351, Cruciform Specimen No. 7-114 Test Case No. 99	167
111	Crack Growth Rate Behavior of 7075-T7351, Cruciform Specimen No. 7-25 Test Case No. 103	168
112	Crack Growth Rate Behavior of 7075-T7351, Cruciform Specimen No. 7-113 Test Case No. 104	169
113	Crack Growth Behavior of 7075-T7351, Cruciform Specimen No. 7-53 Test Case No. 105	170
114	Crack Growth Behavior of 2024-T351, Cruciform Specimen No. 2-24 Test Case No. 101	171
115	Crack Growth Rate Behavior of 2024-T351, CCT Specimen No. LT-2-5 Test Case No. 102	172
116	Crack Growth Rate Behavior of 2024-T351, Cruciform Specimen No. 2-38 Test Case No. 108	173
117	Crack Growth Rate Behavior of 2024-T351, Cruciform Specimen No. 2-34 Test Case No. 109	174
118	Crack Growth Rate Behavior of 2024-T351, Cruciform Specimen No. 2-41 Test Case 110	175
119	Crack Tip Plastic Zone Sizes in 7075-T7351 Cruciform Specimen	180
120	Crack Tip Plastic Zone Sizes in 2024-T351 Cruciform Specimen	181
121	Crack Tip Plastic Zone Sizes in 2024-T351 Cruciform Specimen	183
122	Crack Growth History of 2024-T351 Cruciform Specimen No. 2-24, Test Case No. 101	184
123	Crack Growth History of 2024-T351 Center Cracked Panel, Specimen No. LT-2-5 Test Case No. 102	185
124	Crack Growth History of 2024-T351 Cruciform Specimen No. 2-38, Test Case No. 108	186
125	Crack Growth History of 2024-T351 Cruciform Specimen No. 2-34, Test Case No. 109	187

LIST OF ILLUSTRATIONS (con't)

FIGURE		PAGE
126	Crack Growth History of 2024-T351, Cruciform Specimen No. 2-41, Test Case No. 110	188
127	Crack Growth History of Cruciform Specimens under Biaxial Spectrum Load Conditions	192
128	Spectrum Crack Growth Test of 7075-T7351, Cruciform Specimen No. 7-8, Test Case No. 116	193
129	Spectrum Crack Growth Test of 7075-T7351, Cruciform Specimen No. 7-102, Test Case No. 114	194
130	Spectrum Crack Growth Test of 7075-T7351, Cruciform Specimen No. 7-63, Test Case No. 200	195
131	Spectrum Crack Growth Test of 7075-T7351, Cruciform Specimen No. 7-90, Test Cast No. 115	196
132	Sketch of a Crack Growth Profile of 7075-T7351 Cruciform Specimen No. 7-5, Test Case No. 83	206
133	Crack Growth Profile of 7075-T7351 Cruciform Specimen No. 7-91, Test Case No. 81	207
134	Cyclic Crack Growth Behavior of a 45° Angle Crack	208
135	Crack Growth Profile of 7075-T7351 Cruciform Specimen No. 7-92, Test Case No. 79	209
136	Cyclic Crack Growth Behavior of a 45° Angle Crack	211
137	Crack Growth Resistance Curve for 7075-T7351 CCT Specimen	213
138	Crack Growth Resistance Curve for 2024-T351 CCT Specimen	214

LIST OF TABLES

TABLE		PAGE
1	Stress Intensity Factors for a 45° Crack in a Cruciform Specimen	23
2	NASTRAN Crack Tip Plastic Zone for 7075-T7351 Alloy	45
3	NASTRAN Crack Tip Plastic Zone for 2024-T351 Alloy	46
4	Basic Biaxial Ratio Effect Tests	110
5	Comparison Between Analysis Methods for a Curved Crack	142
6	Predicted Crack Growth History of a 7075-T7351 Specimen	147
7	Predicted Crack Growth History of a 7075-T7351 Specimen	148
8	Actual Crack Growth History of a 7075-T7351 Cruciform Specimen	149
9	Low Amplitude Tests	150
10	Cracks at a Circular Hole Test	155
11	Variable Amplitude Tests	157
12	Periodic Single Overload Test Results	177
13	Block Spectrum	190
14	Truncated Spectrum	191
15	Spectrum Load Test Results	198
16	Loading Conditions for 180° Out-Of-Phase Cyclic Stress Tests	202
17	Miscellaneous Tests	204

LIST OF SYMBOLS

a	One half of the total crack length, or the distance between a point on the X-axis to the center of the cruciform specimen, mm (inches)
a_x	Projected length of "a", perpendicular to σ_x , mm (inches)
a_y	Projected length of "a", perpendicular to σ_y , mm (inches)
B	Biaxial ratio, σ_x/σ_y , or block of a loads spectrum
f	Cyclic frequency (Hz)
F_{ty}	Material uniaxial tensile yield strength, kPa (ksi)
K_{max}	Stress intensity corresponding to σ_{max} , $MN(M)^{3/2}$ (ksi \sqrt{inch})
K_{min}	Stress intensity corresponding to σ_{min} , $MN(M)^{3/2}$ (ksi \sqrt{inch})
K_{OL}	K_{max} at over load $MN(M)^{3/2}$ (ksi \sqrt{inch})
P_x	Load applied to X-axis of a cruciform specimen, always parallel to the crack, N (kip)
P_y	Load applied to Y-axis of a cruciform specimen, always perpendicular to the crack, N (kip)
R	Cyclic stress ratio, $\sigma_{y, min}/\sigma_{y, max}$
r_p	Crack tip plastic zone width, mm (inches)
W_c	Width of a center cracked specimen, mm (inches)
ΔK	$K_{max} - K_{min}$, $MN(M)^{3/2}$ (ksi \sqrt{inch})
σ_x	Stress parallel to the crack, tension or compression, kPa (ksi)
σ_y	Stress perpendicular to the crack, always in tension, kPa (ksi)

Original measurements are in English units.

SUMMARY

A series of experiments and analyses were carried out on the cyclic crack growth behavior of center-cracked cruciform specimens under various biaxial loading conditions ($-1.5 \leq \sigma_x/\sigma_y \leq 1.75$ for constant amplitude tests, $-0.5 \leq \sigma_x/\sigma_y \leq 0.5$ for periodic single overload and spectrum load tests). The results may be summarized as follows:

1. For cracks perpendicular to σ_y the crack grew straight except for $\sigma_x \leq \sigma_y$.
2. Elastic K factors were obtained for both straight and curved cracks and were adequate for correlating the biaxial crack growth rate data.
3. The direction of crack growth, the crack tip stress intensity and the crack growth rate were controlled by the most dominant stress component in a multiaxial stress field. For a straight crack, the effect of σ_x on constant amplitude crack growth rate was negligible provided the crack tip stress intensity factors, in a given biaxial stress field, were properly computed. Crack growth rates for the curved and the straight cracks were the same at a given stress intensity level.
4. In out-of-phase loading conditions, the crack growth rate and crack growth directions (for $\sigma_x \leq \sigma_y$) were the same as those in the in-phase loading condition.
5. Crack tip plastic zone size variations with biaxial ratio appeared to have no effect on constant amplitude crack growth rate.
6. At lower stress intensity levels, the analytically determined crack tip plastic zone sizes qualitatively correlated with those directly measured from the test coupons (by using an interferometry microscope). At higher K levels, the validity of the interferometry measured plastic zone sizes was questionable.

7. As for the variable amplitude tests, it was very evident that cracks grew faster at positive biaxial stress states but slower at negative biaxial loading conditions compared to uniaxial loading conditions. The crack growth retardation behavior were similar in both uniaxial and biaxial states of stresses; i.e., the delay cycles were controlled by the load interactions. Therefore, existing retardation models could be used to predict delay cycles in both uniaxial and biaxial stress fields provided that the crack tip plastic zone sizes in a given stress state, were accurately determined.

SECTION I

INTRODUCTION

Fracture mechanics techniques are currently being used to perform damage tolerant analysis on many types of aircraft structural components. Because the problems of multiaxial loading are very common in aircraft airframe and engine components, it is important to evaluate and quantify multiaxial effects in order to improve the crack propagation prediction capability for design purposes.

Consider that a plate, containing a through-the-thickness crack, is subjected to a biaxial stress field. One of the stress components is acting perpendicular to the crack and another component parallel to the crack. For problems that are solved using purely elastic formulation [1, 2], the crack tip stress intensity, K_1 , in the opening mode, is theoretically not affected by the lateral stress component. On the other hand, it can be shown by elastic-plastic analysis [2-8] that the size of a crack tip plastic zone varies with biaxial loading conditions. Therefore, one may speculate that the crack tip stress intensity (K) as well as the crack growth rate (da/dN) will also be influenced by the presence of the lateral stress component. Experimental data concerning the biaxial loading effect on cyclic crack growth rate, residual strength, and the direction of crack growth, are available [9-19]. However, the results of these few investigations have been inconsistent, and none of them contained enough data to offer conclusive evidence to support, or to correlate with, the existing theories.

The objective of this investigation was to systematically evaluate the effect of the biaxial stress field on cyclic crack growth rate behavior. An analytical/experimental study program was designed to answer the following questions:

1. Do biaxial stresses affect crack tip stresses intensity, cyclic crack growth rate, crack growth direction, or crack tip plastic zone size?
2. Is an elastic - K adequate for correlating the biaxial da/dN data?
3. Is the crack tip plastic zone important in the mechanics of crack growth?

SECTION II

STATEMENT OF WORK

An exploratory research program was conducted to systematically evaluate the effects of biaxial stress ratio on constant amplitude and variable amplitude fatigue crack growth rates. The scope of the program included the following:

1. The specimen design was optimized by finite element analysis. The analytic results also determined the load and stress relationship on the optimized specimen geometry.
2. A strain survey was conducted to verify the analytic load-stress relationship.
3. A crack-finite-element technique, and other appropriate means, were used to determine elastic crack tip stress intensity factors for a crack in the selected specimen geometry. Crack geometries included the straight crack, inclined crack, crack(s) at a hole, and curved crack.
4. A total of 118 specimens made of 7075-T7351 and 2024-T351 aluminum alloys were tested under various biaxial loading conditions. A vast amount of cyclic crack growth rate and fracture data was developed. The scope of the test program is outlined in the following:
 - A. Evaluation of the basic biaxial effects by conducting constant amplitude fatigue crack growth tests at various biaxial stress ratios ($-1.5 \leq B \leq 1.75$), at $R = 0.1$.

- B. Evaluation of the basic biaxial effects by conducting constant amplitude fatigue crack growth tests at $R = 0.7$ (i.e., evaluation of the R effect).
 - C. Evaluation of the biaxial ratio effects on fatigue crack(s) coming out from a hole configuration.
 - D. Evaluation of crack growth retardation behavior under biaxial, variable loading conditions (with $-0.5 \leq B \leq +0.5$).
 - E. Evaluation of the biaxial stress effect on constant amplitude fatigue crack growth rate under out-of-phase loading conditions.
 - F. Miscellaneous tests including sustained load tests, angle crack in a biaxial stress field, and fracture tests.
5. The "loaded" crack tip plastic zone sizes, at various biaxial stress ratios, were determined by using the elastic-plastic finite element modeling technique. The "loaded" and the "unloaded" crack tip plastic zone sizes were also measured from the surface of a specimen (during a cyclic loading test) by using an interferometry microscope.
6. The experimental data were analyzed to determine whether or not biaxial stress would affect the fatigue crack growth behavior. A computer program was prepared to compute the crack growth rate, as well as the crack growth direction, under constant amplitude biaxial loading. Variable amplitude fatigue crack growth rate data were correlated with the modified Willenborg model and a new crack growth retardation model was developed.
7. Based on the results of this research program, guidelines and procedures for predicting safe-crack-growth-life in a biaxial stress field were derived.

SECTION III

BIAXIAL TESTING MACHINE

A biaxial test machine, shown in Figures 1 to 3, was made specifically for testing of the specimens described in Section 4. The unit consists of three hydraulic actuators mounted on a horizontal frame made of aluminum channel (provisions for a fourth hydraulic actuator were integrated into the test machine design). Two of the actuators are plus and minus 55 kip capacity mounted opposing each other (this direction is designated the "X" direction). The third actuator is plus and minus 77 kip capacity and is mounted perpendicular to the other two actuators in the "Y" direction. No actuator (presently) opposes the plus and minus 77 kip actuator; instead, this end is fixed (similar to a typical crosslead). Each actuator mount is attached to the test frame through pin-bearing arrangements (upper and lower) which allow the actuators to swivel (in a horizontal plane). This was required to prevent possible actuator damage from side loading (which could occur during specimen failure, for example). The bearing-pin fit is approximately a 0.001 inch clearance, which minimizes load train stop. Each actuator is terminated into a large device (spiral locking rings are used for proper prestressing of threaded adapters). The device holds a second pin-bearing arrangement (similar to the actuator pin-bearing arrangement); this pin serves as the loading pin, which the grips contact. The specimen loading arms are "sandwiched" between these grips in a seven-bolt hole pattern. The top cover plate is removable for specimen set-up and is locked down after such. The fixed end of the test frame is constrained so that the device cannot swivel. This is required for tests involving compression loading.

Three load cells are used in the test frame. These are mounted to the device on both 55 kip ends and on the fixed end, (i.e., each load cell is mounted on the device opposing the corresponding actuators). All load cells are plus and minus 100 kip fatigue rated GSE load cells. Each actuator is also equipped with an LVDT, and is controlled by a 15 gpm Moog servo-valve.



Figure 1. Biaxial Loading Machine

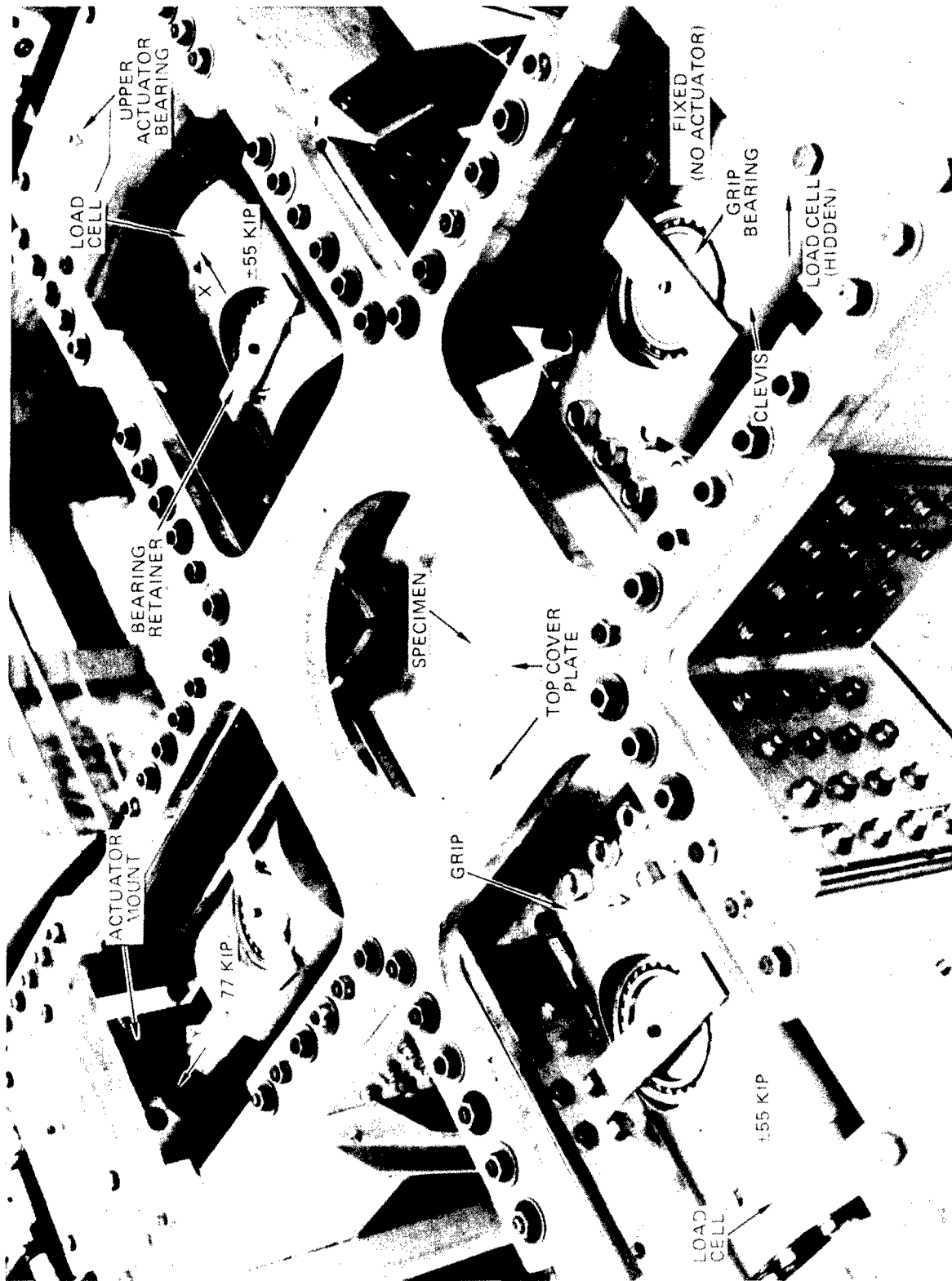


Figure 2. Close Up Of The Biaxial Loading Machine

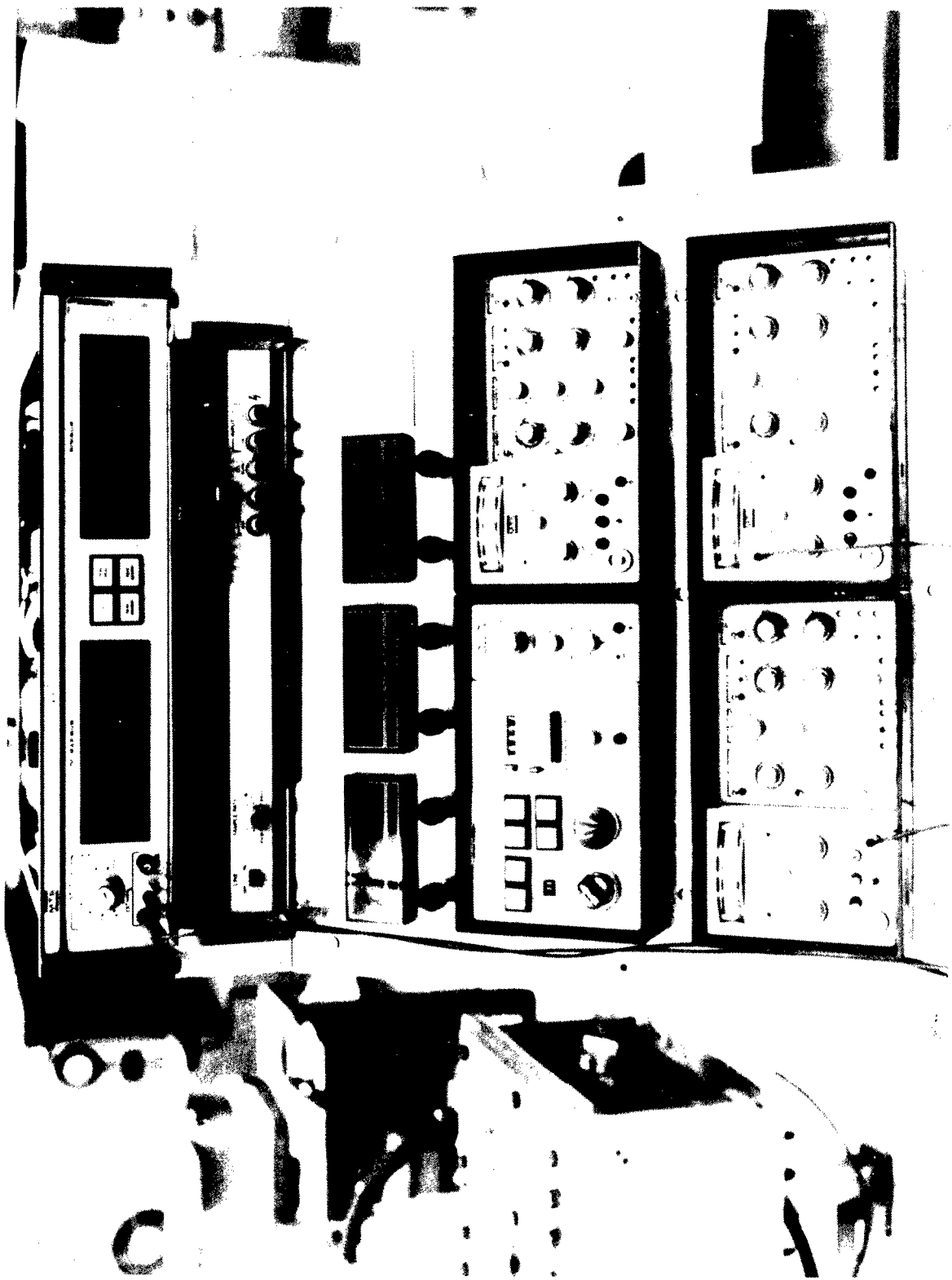


Figure 3. Control Unit

The three actuators are controlled from a console consisting of three MTS Model 406 servo controllers and one MTS Model 436 control unit. Dual MTS Model 430 digital indicators were used for monitoring of load and stroke signals. An MTS Model 410 digital function generator was used for commanding of constant amplitude and static (strain survey) tests. An automated control unit was used for commanding of spectrum tests.

For all tests, the mode of control of the system is described as follows. The 77 kip and one of the 55 kip actuators were run in load control commanded by the servo-controller (Model 406) load control. The second 55 kip actuator was run in stroke control. The command signal to this actuator was the stroke feedback from the opposing 55 kip actuator. This method of control was employed so that the two 55 kip actuators displaced in continuous phase; therefore, the specimen centerpoint (X-direction) was held fixed and thus maintained proper specimen positioning for loading in the Y-direction. Note, however, that the specimen centerpoint in the Y-direction is not so constrained (since there is no fourth actuator). Therefore, some off-center line loading was imposed in the X-direction. From check outs, it was determined that the lateral displacement of the 55 kip actuator was approximately 0.001 inch per kip (77 kip load) at the specimen centerpoint. Considering the distance from specimen center to actuator swivel point (about 27 inches), the angular misalignment is quite small and is considered insignificant.

A typical example of test set-up is described below. The precracked test specimen was mounted in the biaxial test frame using low pressure load control. Small tensile loads (approximately 500 pounds) were applied in both directions. To set the specimen position in the X-direction, the 55 kip actuator in stroke control was positioned so that the 77 kip actuator had minimum stroke displacement. This minimum occurred when the 77 kip actuator was in line with the opposing fixture device. Final bolt tightening was performed and the loads were returned to zero level.

The load cycling was initiated and the spans (amplitude control potentiometers) were opened in small increments (alternating between X and Y actuators). The two digital peak indicators monitoring load were used to indicate actual load response. Five adjustments on the spans were made until the desired load peaks were accurate to one percent.

Phase angle is optimized by adjusting servo-controller gains and comparing X and Y load/time traces on a storage oscilloscope. Such gains are "tweaked" in until no discernible phase lag/lead is noticed (this applies to 0° phase testing; for 180° phase the feedback signals for one of the load cells is inverted to permit a comparison). Finally, the spans usually require a slight readjustment after gain adjustment to maintain load peaks accurate to better than plus and minus one percent.

This complete procedure is accomplished in a matter of a few minutes at most (as more experience was gained this time interval was reduced considerably).

SECTION IV

SPECIMEN CONFIGURATION

There are many types of specimens that we can use to accomplish a biaxial loading condition. For example, Pook and Holmes [11] used a flat cruciform specimen containing longitudinal slots in the loading arms; Beck [16] used a very large square sheet and loaded the sheet through many little straps attached around the sheet edges. The criteria for designing a specimen configuration to fulfill all the objectives in the present study were:

1. The specimen should be capable of taking compression load.
2. The specimen should be designed to avoid fatigue damage at the grip or in any area other than that containing the crack.
3. The size of the specimen should be large enough to minimize boundary effects on crack tip stress intensity; but it should not be too large, so that the required load levels can be kept within the capacity of the testing machine.
4. The stress distribution across the specimen width should be fairly uniform.
5. The specimen configuration should be simple in order to minimize machining costs.

A cruciform specimen configuration was selected for generating biaxially loaded crack growth rate data. Generally, the specimen had an overall length of 597 mm (23.5 inches) including grip areas at each end of the loading arms. It also had a thinner region, 152.4 mm (6 inches) in diameter, in the center of the specimen. An overall view of the specimen is shown in Figure 4. Figure 5 is a close up photograph of the center section. Loading conditions and dimensions of the specimen are shown in Figure 6.

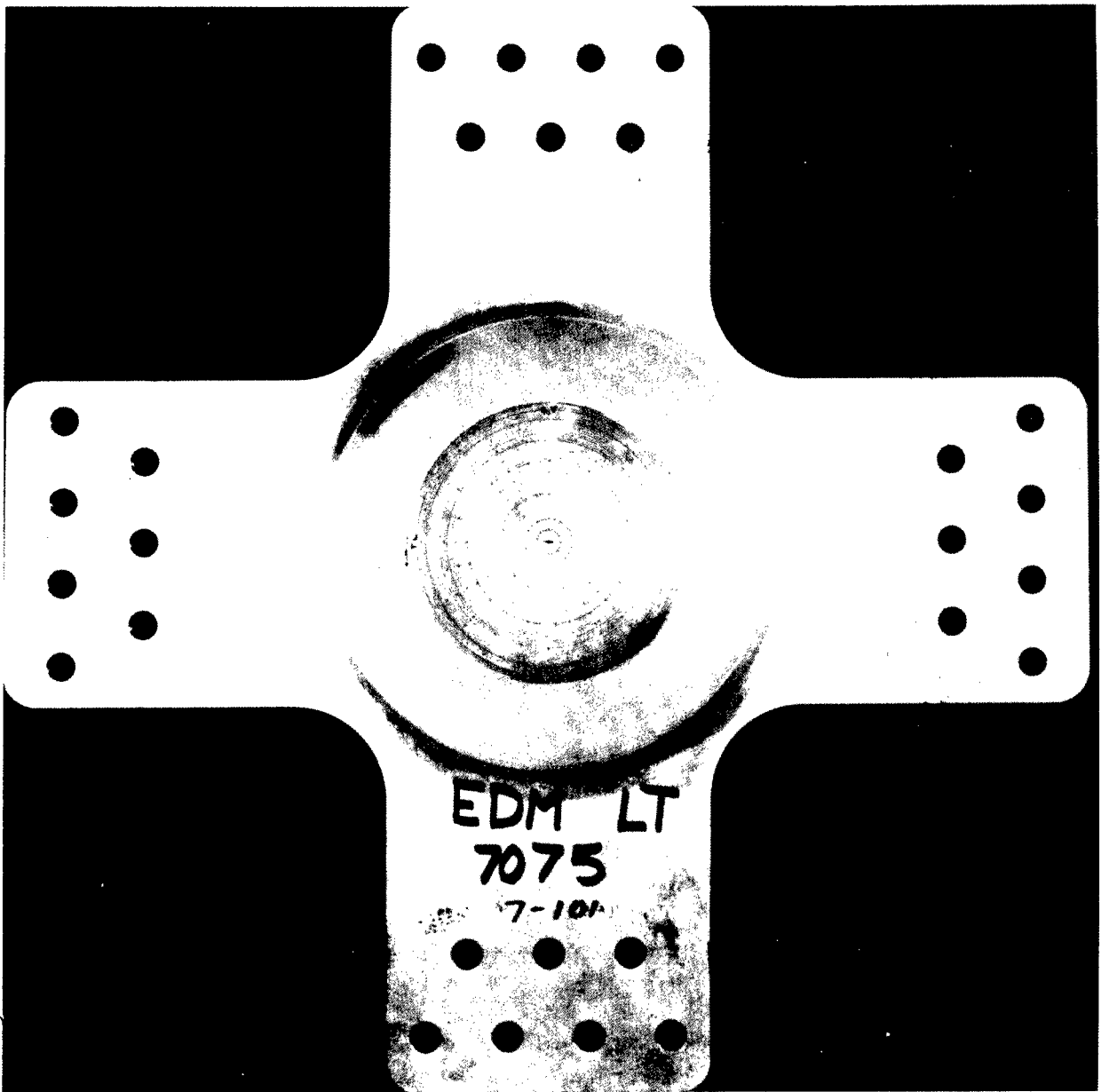
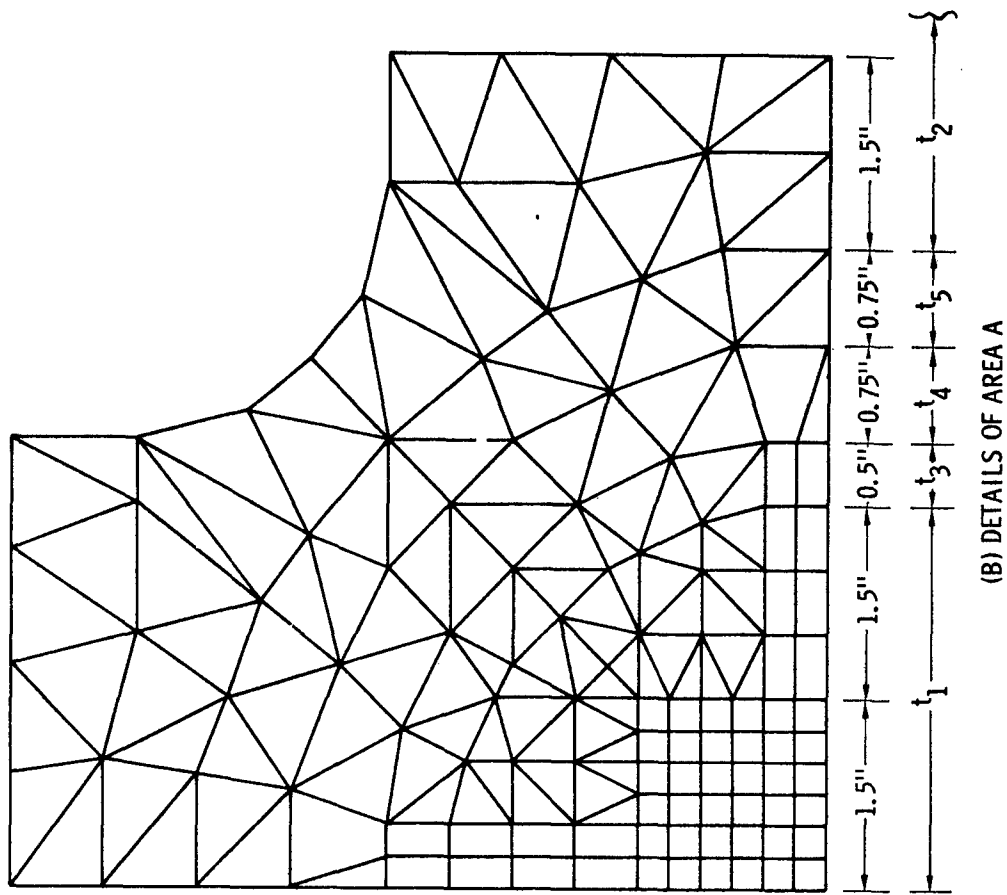


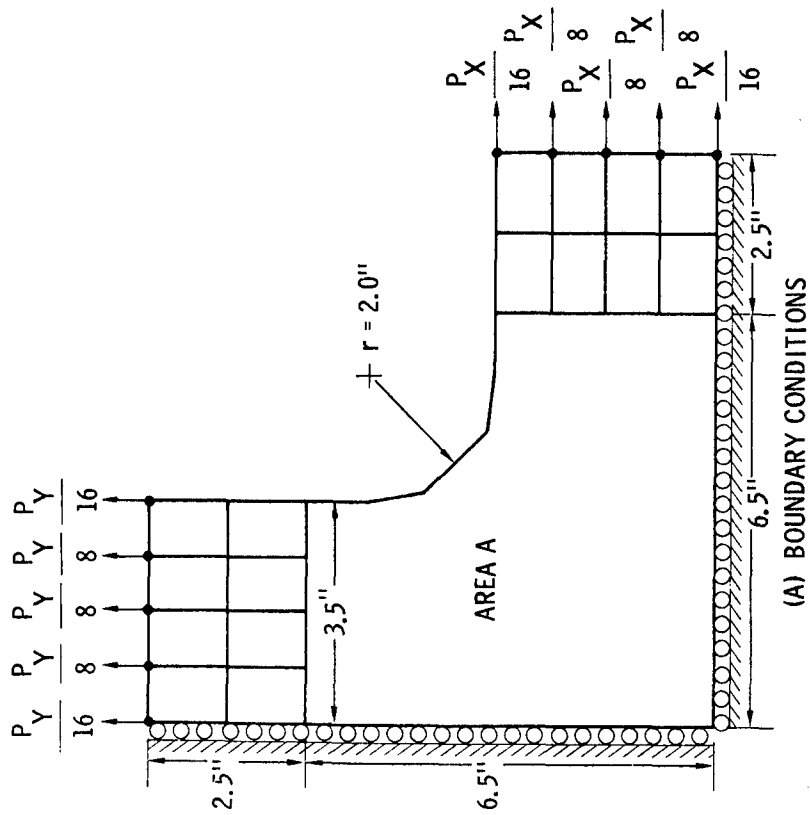
Figure 4. Cruciform Specimen



Figure 5. The Center Section of a Cruciform Specimen (containing a curved crack)



(B) DETAILS OF AREA A



(A) BOUNDARY CONDITIONS

Figure 6. Finite Element Model For One-Quarter of a Cruciform Specimen

It was determined that the thickness of the center region (t_1) and the thickness and width of the loading arms (t_2 and W) were the three primary variables affecting the stress distribution. A 17.7 mm (0.5 inch) thick loading arm was selected for t_2 to eliminate one of the three variables and also to minimize material and machining costs. The t_1 and W dimensions were optimized by conducting stress analysis on a dummy panel configuration (without crack). Stress distributions across the thin section were determined by using the NASTRAN computer program. Figure 6 shows the finite element model representing one quarter of the cruciform specimen. Here $t_1 = 4.57$ mm (0.18 inch), $W = 17.78$ cm (7 inches) and $t_2 = 17.7$ mm (0.5 inch). Also shown in Figure 6, are three rings of triangular elements of different intermediate thicknesses (t_3 , t_4 and t_5) to simulate the curvature connecting t_1 and t_2 .

The analytical results are presented by the curves of Figures 7 and 8. In Figure 7, the load and stress relationship at the center of the specimen is presented; the magnitude of σ_y and σ_x (per one thousand pounds of P_y) are plotted as functions of P_x to P_y ratio. The load and stress relationship (the NASTRAN lines in Figure 7) can be represented by the following equations.

$$\sigma_y = \frac{P_y}{12} [6.55 - 1.73 (P_x/P_y)] \quad (1)$$

$$\sigma_x = \frac{P_y}{12} [6.57 (P_x/P_y) - 1.75] \quad (2)$$

For an actual test, the required P_x and P_y values corresponding to any desirable σ_x and σ_y combinations can be determined by solving Equations 1 and 2.

In Figure 8, stress distributions along the X-axis of the cruciform specimen are presented. Since the specimen was symmetrical about its center lines, the magnitudes of σ_x and σ_y are plotted as functions of a . The stress distributions corresponding to many P_x/P_y ratios were determined; however, only four typical examples are shown here. A complete set of stress distribution curves is presented in Volume II of this report.

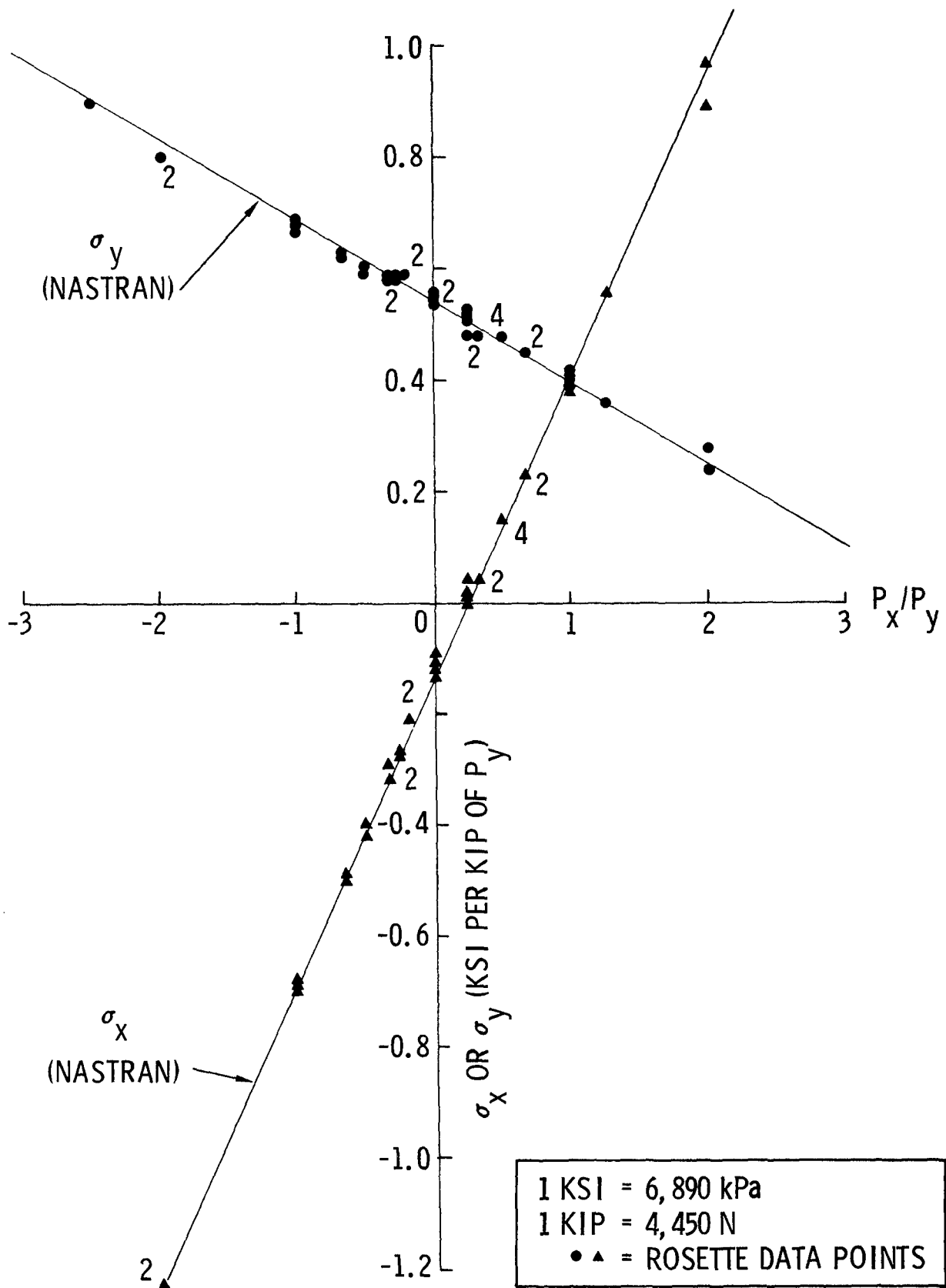


Figure 7. Load-Stress Relationship at the Center Point of a Cruciform Specimen

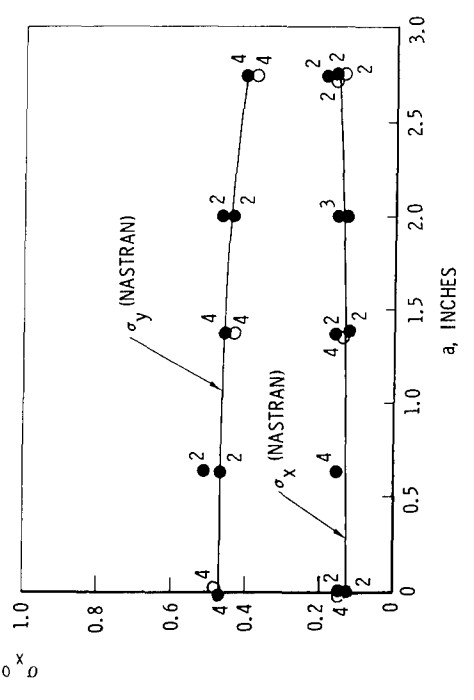
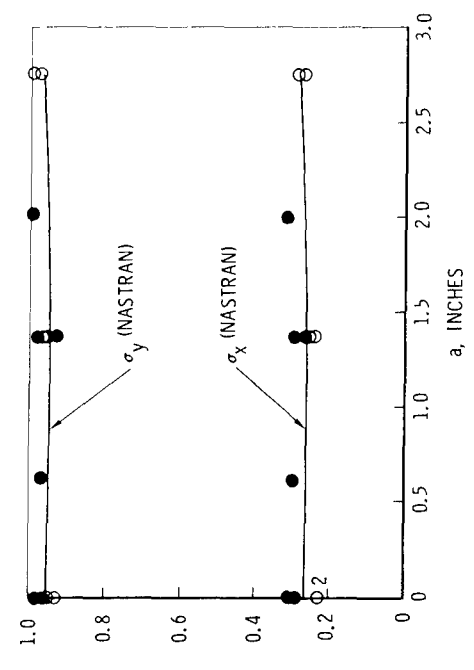
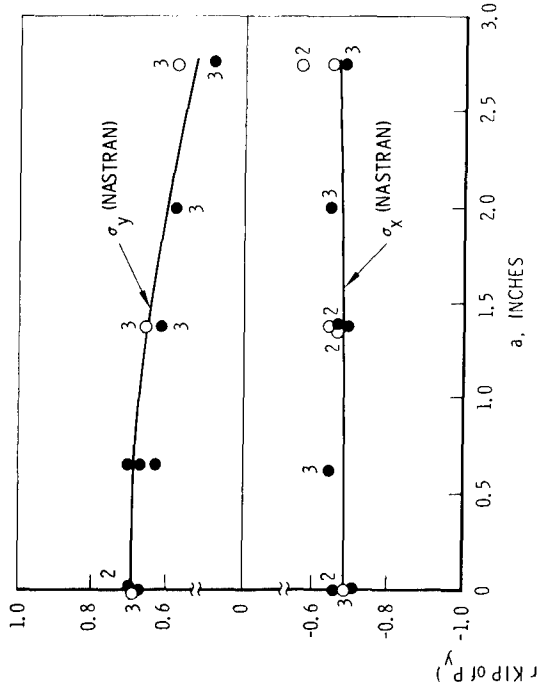
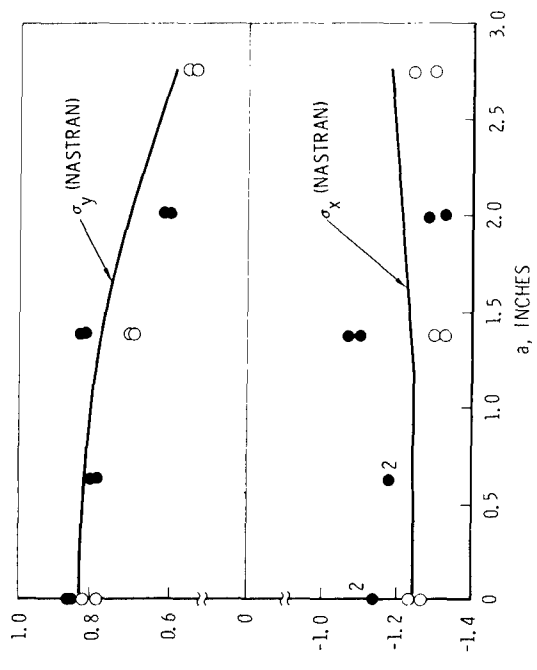


Figure 8. Stress Gradient along the X-Axis of a Cruciform Specimen

SECTION V
STRESS SURVEY

One cruciform specimen of each material was instrumented with rectangular rosettes along the X-axis of the specimen. The specimens (without crack or cut, or elox) were loaded in the horizontal biaxial loading machine under various biaxial load ratios (e.g., 0, ± 0.5 , ± 1.0 , ± 2.0 , etc.). Stress distributions along the X-axis of the specimen were determined by strain measurements at five locations, one pair of back-to-back rosettes at the center of the specimen and two rosettes on each side of the center covering a 69.85 mm (2.75 inch) radius. Two of the side locations also had back-to-back rosettes (see Figure 9). A guide was used to prevent out-of-phase plane buckling under compression loads.

At each loading condition, up to four load levels were applied and two readings were taken at each load level. The specimen was placed in the machine at two orientations. One set of the strain gauge data was taken while the Y-axis of the specimen was lined up with the 244,750 N (55 kip) load cells and another set of strain gauge data was taken while the Y-axis of the specimen was lined up with the 342,650 N (77 kip) load cells (i.e., the specimen was rotated 90°). Typical experimental data are plotted on Figures 7 and 8. It is observed in these figures that the correlations between strain gauge results and the NASTRAN finite element analysis results are very good. Note that, in these figures, each data point represents an average of two readings. Occasionally, there is a number adjacent to a data point indicating that more than one data point was superimposed on another; e.g., the number four implies that the data point represents an average of eight measurements (four load levels and two reading per each load level).

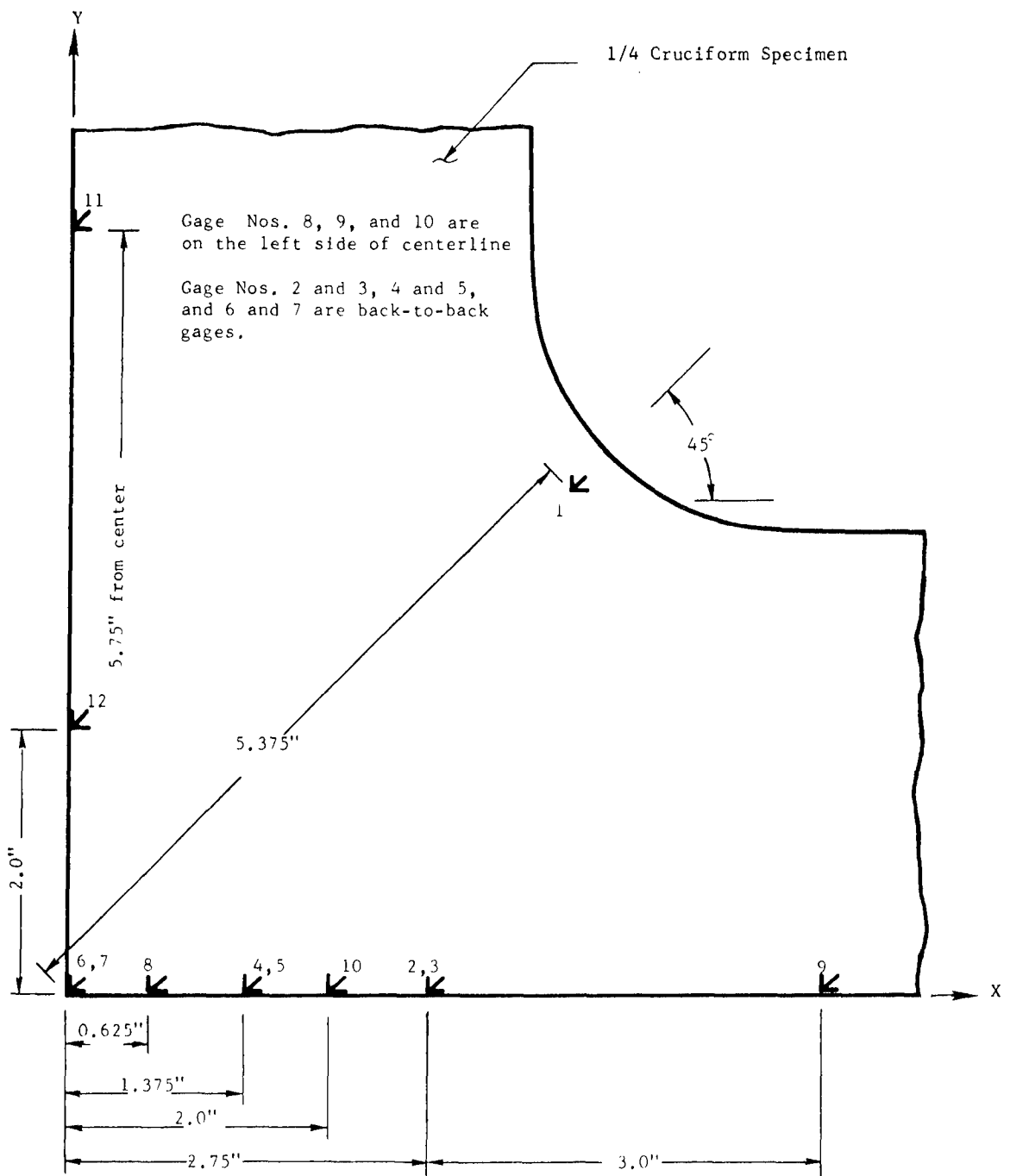


Figure 9. Rosette Gauge Locations

The solid and the open symbols in Figure 8 indicate the results from back-to-back gauges. Since the results for the back-to-back gauges were almost identical, only one side of the results is presented in Figure 7. It is significant to note that experimental data (a complete set of the data is presented in Volume II of this report) showed that the load response characteristics of the cruciform specimen were not affected by the position of the specimen; i.e., whether the Y-axis of the specimen was placed in line with the 342,650 N(77 kip) or the 244,750 N(55 kip) load cells, the strain gauge results were identical.

SECTION VI
STRESS INTENSITY FACTORS

6.1 Straight Crack

In the theory of linear elastic fracture mechanics, crack tip stress intensity can be expressed as

$$K = \sigma_y \sqrt{\pi a} \cdot F(a) \quad (3)$$

where σ_y is the gross area stress normal to the crack. In case of a center cracked specimen (CCT), σ_y will be the far field uniform stress and $F(a)$ accounts for the boundary conditions. According to [20],

$$F(a) = \left[1 - .025 \left(\frac{2a}{W_c} \right)^2 + .06 \left(\frac{2a}{W_c} \right)^4 \right] \cdot \sqrt{\text{Sec} \left(\frac{\pi a}{W_c} \right)} \quad (4)$$

In case of a cruciform specimen, for a given ratio of biaxial loads, there is a pair of stress components, σ_x and σ_y , at every point along a predetermined crack plane. In this case, the crack plane will be the X-axis in Figure 6. As postulated in [1], the elastic K value for a given crack length in a biaxial state of stress should be the same as in the uniaxial loading condition. In other words, the K-expression of Equation 3 is applicable to the cruciform specimen except that σ_y would be the (reference) stress in the center of the uncracked specimen and $F(a)$ would be a function of the boundary conditions and the stress gradient of σ_y along the X-axis.

A finite element analysis of the cruciform specimen with cracks was conducted using the finite element model of Figure 6 to determine elastic K values. A special "crack tip" element, originally developed by Tong, et al, [21] was incorporated into the NASTRAN. In each case analyzed, e.g., each crack length, a special element was placed in the general finite element model occupying a region representative of the predetermined crack tip location, and the elements representing the crack

were freed from the boundary restrictions. Eight specimens with crack lengths ($a = 6.35$ to 69.85 mm) were loaded to various biaxial loading ratios with $\sigma_y = 12$ ksi. The results are plotted in Figure 10. Several K values calculated from Equation 3 with $F(a) = 1.0$ are also plotted in Figure 10 for comparison. It is seen that the effects of loading conditions on elastic K values are negligible and that the cracked cruciform specimen behaves actually like an infinite sheet especially at positive biaxial loading conditions. It is even more important to note that the apparent deviations in K, for a crack length greater than 38.1 mm (1.5 inches), were mainly due to the effect of specimen geometry rather than the effect of biaxial loading ratios. The hypothesis is substantiated by the fact that the K values for long cracks under negative σ_x loads were actually lower than those under positive σ_x loads. Comparing Figures 8A and 8B to Figures 8C and 8D, it is evident that the tension-compression loading cases exhibited more reductions in the σ_y stresses in the area near the rim.

6.2 Angle Crack

Table 1 shows the cracked finite element analysis results for a 45° crack in a cruciform specimen. Three loading cases were analyzed; i.e., $\sigma_x = 0$, $\sigma_x = \sigma_y$ and $\sigma_x = -\sigma_y$. In all three cases, the input stress for σ_y was 12 ksi. Due to the unsymmetric nature of the problem, a full specimen model was used (see Figure 11). Stress intensities at both ends of the crack were computed. As shown in Table 1, the calculated K-values were almost the same at each crack tip. Theoretically, in an infinite sheet, the $\sigma_x = \sigma_y$ loading condition will be pure Mode 1 and the $\sigma_x = -\sigma_y$ loading condition will be pure Mode 2. As can be seen in Table 1, the K_2 values for $\sigma_x = \sigma_y$ and the K_1 values for $\sigma_x = -\sigma_y$ were negligibly small. The K-values for a 45° crack and the K-values for a 0° crack are plotted in Figure 12. It is seen that under a one-to-one biaxial ratio, the K_1 values for the 45° crack agree with those for the 0° crack. On the other hand, the absolute K_2 values for the 45° crack agree with the K_1 values for the 0° crack when the specimen is subjected to a one-to-minus one biaxial loading condition. As for the uniaxial condition ($\sigma_x = 0$), K_1 and K_2 values for the 45° crack were approximately equal to one-half of the correspondingly pure Mode 1 and pure Mode 2 stress intensity values. The expected values, according to the angle

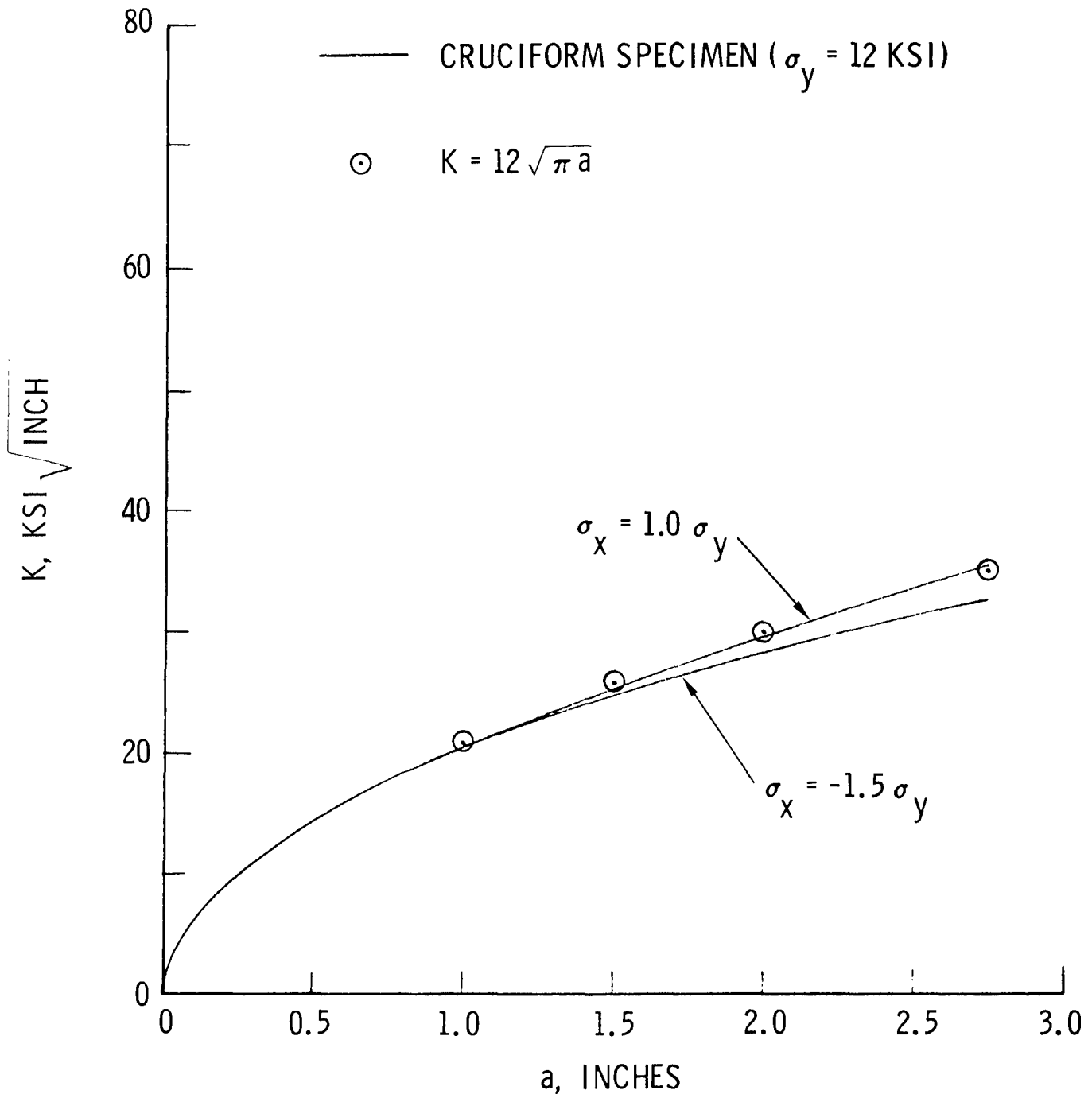


Figure 10. Stress Intensities for Center Through-Cracks in a Cruciform Specimen

TABLE 1. STRESS INTENSITY FACTORS FOR A 45° CRACK IN A CRUCIFORM SPECIMEN

(a), Mode I

σ_x/σ_y	a, inches	2	1.5	1.0	0.75	0.30
0		1.52 E4	1.22 E4	1.03 E4	0.914 E4	0.491 E4
1		3.03 E4	2.39 E4	2.03 E4	1.79 E4	0.966 E4
-1		0.007 E4	0.042 E4	0.038 E4	0.032 E4	0.0125 E4
0		1.58 E4	1.19 E4	1.02 E4	0.901 E4	0.483 E4
1		3.10 E4	2.35 E4	2.00 E4	1.78 E4	0.981 E4
-1		0.052 E4	0.018 E4	0.026 E4	0.024 E4	-0.0178 E4

$\left. \begin{matrix} K_I \text{ (psi/inch)} \\ \text{at one crack tip} \end{matrix} \right\}$
 $\left. \begin{matrix} K_I \text{ at} \\ \text{another crack tip} \end{matrix} \right\}$

(b), Mode II

σ_x/σ_y	a, inches	2	1.5	1.0	0.75	0.3
0		-1.31 E4	-1.18 E4	-0.936 E4	-0.818 E4	-0.315 E4
1		0.149 E4	0.079 E4	0.069 E4	0.064 E4	0.342 E3
-1		-2.77 E4	-2.45 E4	-1.94 E4	-1.70 E4	-0.664 E4
0		-1.37 E4	-1.14 E4	-0.912 E4	-0.802 E4	-0.315 E4
1		0.082 E4	0.127 E4	0.097 E4	0.081 E4	0.295 E3
-1		-2.82 E4	-2.41 E4	-1.92 E4	-1.69 E4	-0.661 E4

$\left. \begin{matrix} K_{II} \text{ (psi/inch)} \\ \text{at one crack tip} \end{matrix} \right\}$
 $\left. \begin{matrix} K_{II} \text{ at} \\ \text{another crack tip} \end{matrix} \right\}$

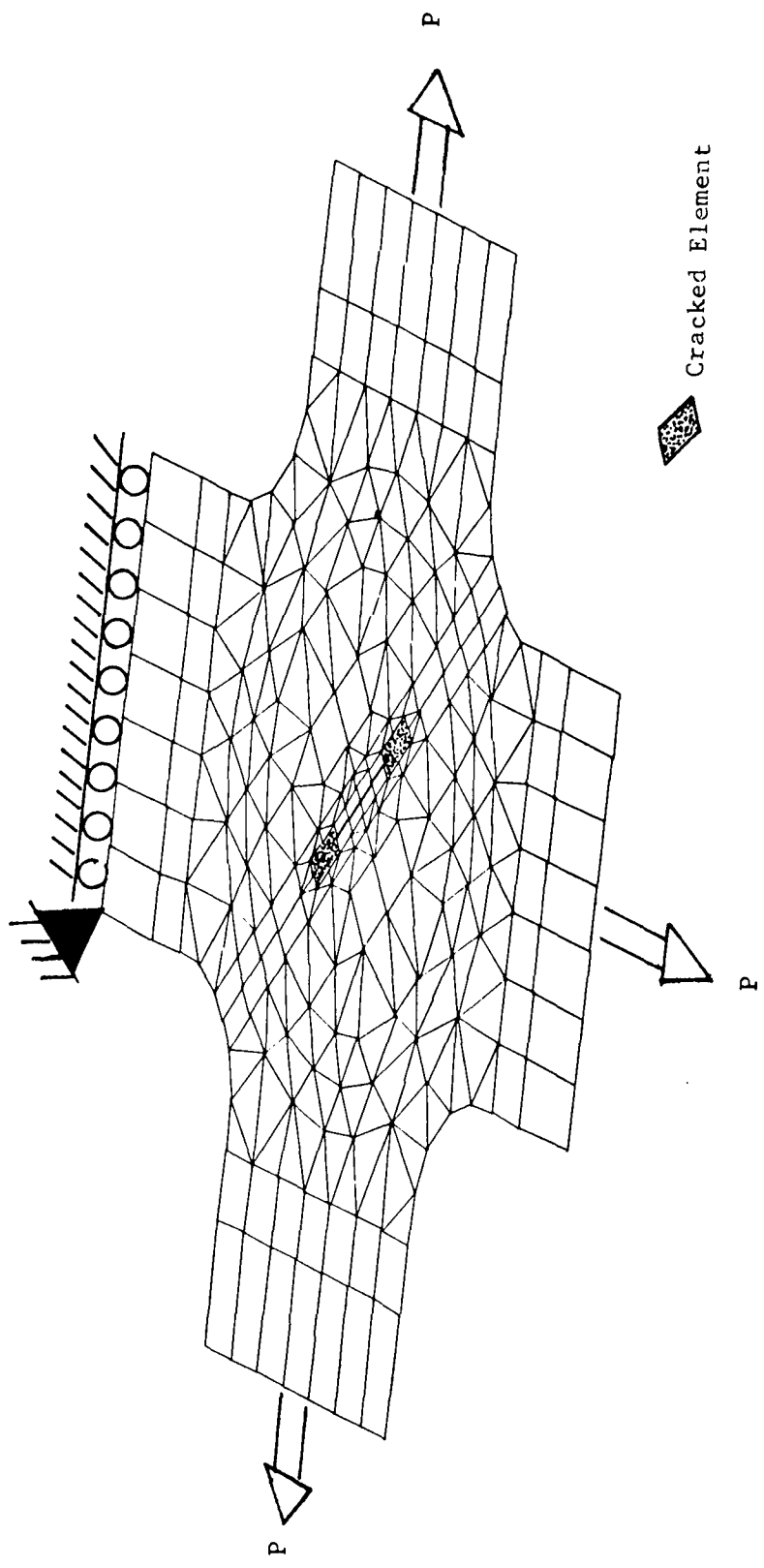


Figure 11. Finite Element Model for Angle Crack

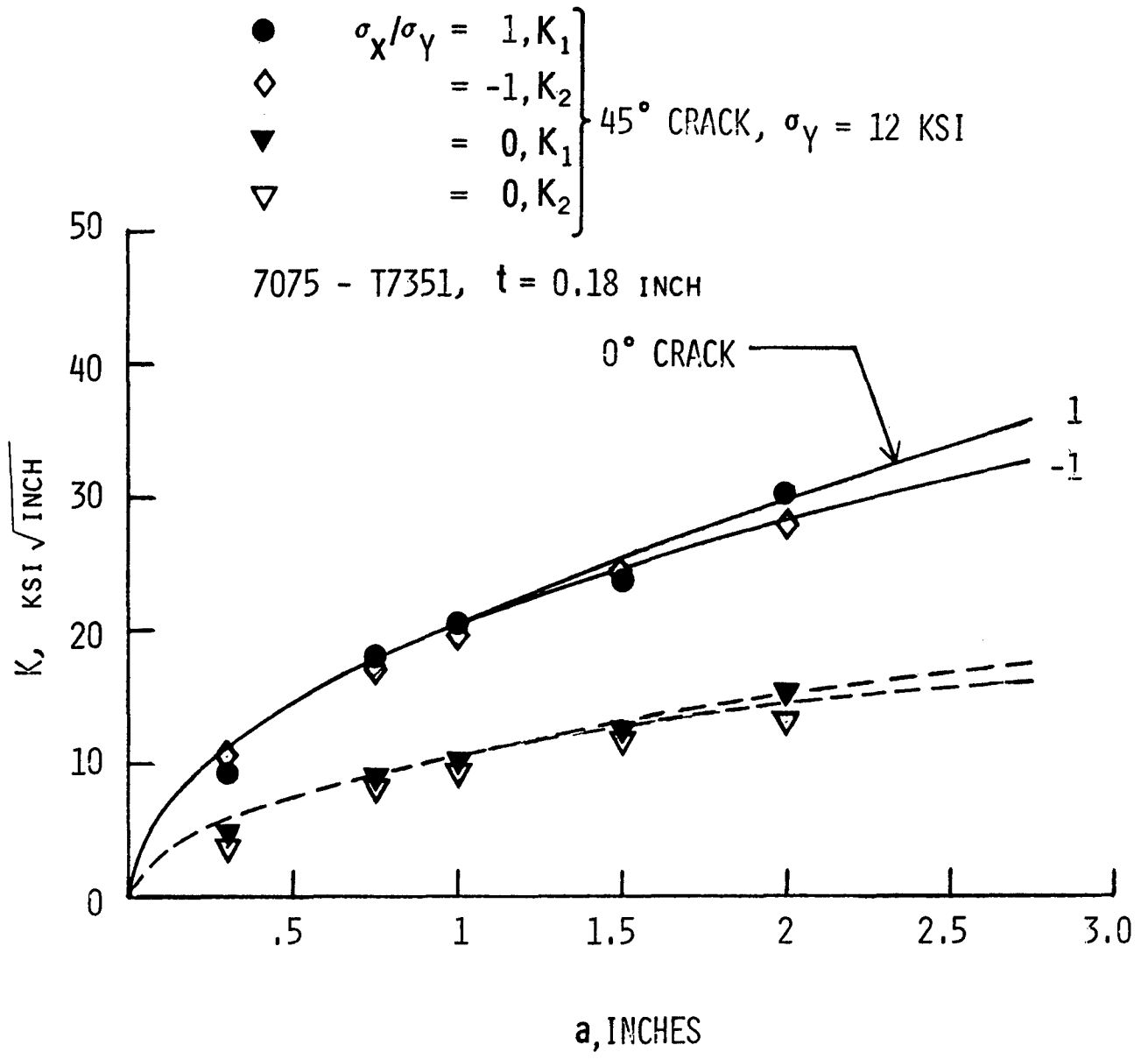


Figure 12. Comparison of Stress Intensities for a 45° Crack and a 0° Crack in a Cruciform Specimen

crack equations given in [1], are indicated by the dotted lines in Figure 12. It should be noted that the minus sign for K_2 in Table 1 was only a sign convention used to indicate the slip direction of a Mode 2 crack (the relative motion between the two surfaces of a crack); therefore, only the absolute values of K_2 are plotted in Figure 12. On the other hand, the minus sign for K_1 in Table 1 indicates that the crack was not open, i.e., K_1 was actually equal to zero.

6.3 Crack At A Hole

In Section 6.1, it was discussed that lateral tension or compression stresses would not affect the elastic stress intensity factors for a central crack in a plate. However, if a crack (or cracks) is coming out of a circular hole in a plate, compressive loading parallel to the crack can cause tensile Mode 1 stress intensity factors. On the other hand, tensile stresses parallel to the crack reduce the stress concentrations at the hole and thus reduce the crack tip stress intensity factor. The Bowie solutions, [22] have provided stress intensity factors for a single crack (or cracks) emanating from the edge of a circular hole, in an infinitely wide plate, under uniaxial and the one-to-one biaxial loading conditions. For any other biaxial load ratios (either tension combined with tension or tension combined with compression), stress intensity factor can be developed by using superpositions of the uniaxial and biaxial solutions of Bowie as illustrated in Figure 13. Following this superposition logic, stress intensity for any biaxial loading combinations can be expressed as

$$K = \left\{ (\sigma_y - \sigma_x) B_0 + \sigma_x B_1 \right\} \sqrt{\pi a} \quad (5)$$

where B_0 is the Bowie factor for uniaxial loading, and B_1 is the Bowie factor for one-to-one biaxial loading, and a is the crack length on either side of the hole. Letting $B = \sigma_x / \sigma_y$, Equation 5 can be written as

$$K = \sigma_y \sqrt{\pi a} \left\{ (1 - B) B_0 + B \cdot B_1 \right\} \quad (6)$$

and the sign for B may be either (+) or (-).

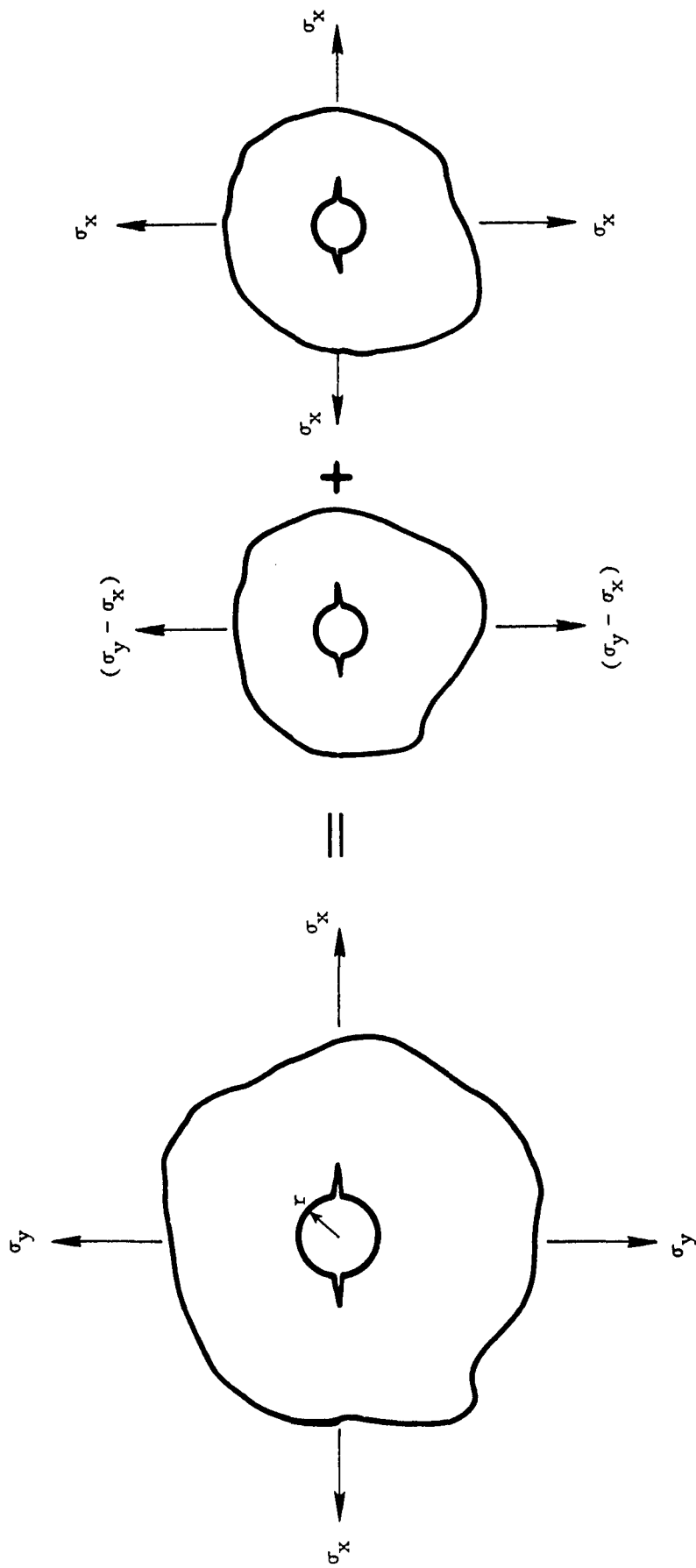


Figure 13. Evaluation of Bowie's Factor for Biaxial Loading

If the hole is inside a finite width plate, the plate dimensions influence the stress concentration at the edge of the hole and thereby varies the stress intensity factor. Referring back to Section 6.1, finite width dimension also increases the crack tip stress intensity as if the hole was never there. Modifications to Equation 6 have been reported in the literature (see [20] and [23] for $B=0$). For engineering purposes, Equation 6 can be written as

$$K = \sigma_y \sqrt{\pi a} \left\{ (1 - B) B_0 + B \cdot B_1 \right\} \cdot F \quad (7)$$

For a circular hole inside a rectangular sheet, F can be a compounded factor which is a product of the Bowie solution, the Howland solution [24], and the stress intensity factor of Equation 4. The validity of these assumptions has been checked out by experiment and by cracked finite element analysis. An example, taken from [25], for $B=0$, is presented in Figure 14. There, the solid line is the computed compound factor. The test data points were developed by using the backtracking of da/dN data technique as described in [26]. Notice that the experimental data points at $a/r \geq 4.5$ (at the end of that test) were significantly higher than the compounded factor as well as the cracked finite element analysis results. Realizing that the total crack length, at that time, was larger than one half of the specimen width, anti-plane crack tip buckling and/or excessive shear lip might have developed causing the alternation of the crack growth behavior.

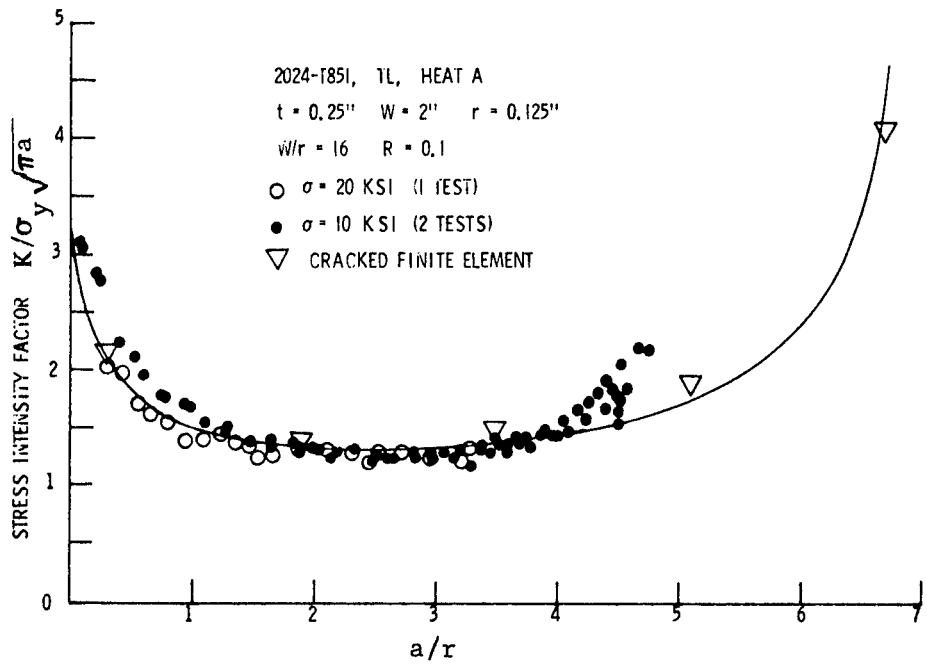


Figure 14. Stress Intensity Factors For Two Cracks Coming Out From A Circular Hole In A Finite Width Sheet

6.4 Curved Crack

It has been demonstrated by elastic analysis [27] [28] that a crack will grow straight (stay on its initial path) under tension-compression biaxial stresses, but the crack will turn away from its initial path if the biaxial stress ratio is larger than unity, i.e., if $\sigma_x > \sigma_y$ in tension. For a curved crack in a biaxial stress field, an approximate method used by Leever, et al [12] can be used to compute K. Since their method of analysis primarily deals with an inclined crack (with respect to either σ_y or σ_x), it would be necessary to compute both the opening mode stress intensity K_1 , and the sliding mode crack tip stress intensity, K_2 . Therefore, their equation has been written as

$$K_1 = F_{1y} \sigma_y \sqrt{\pi a_y} + F_{1x} \sigma_x \sqrt{\pi a_x} \quad (8)$$

$$K_2 = F_{2y} \sigma_y \sqrt{\pi a_y} + F_{2x} \sigma_x \sqrt{\pi a_x} \quad (9)$$

where

$$F_{1x} = \frac{1}{\left(3 - \cos \frac{\alpha}{2}\right) \sin^{\frac{1}{2}} \frac{\alpha}{2}} \left\{ \cos \frac{\alpha}{4} - \cos \frac{7\alpha}{4} - \cos \frac{5\alpha}{4} \sin^4 \frac{\alpha}{4} + 2 \sin \frac{5\alpha}{4} \sin \frac{\alpha}{2} \sin^2 \frac{\alpha}{4} \right\} \quad (10)$$

$$F_{1y} = \frac{1}{\left(3 - \cos \frac{\alpha}{2}\right) \cos^{\frac{1}{2}} \frac{\alpha}{2}} \left\{ \cos \frac{\alpha}{4} + \cos \frac{7\alpha}{4} + \cos \frac{5\alpha}{4} \sin^4 \frac{\alpha}{4} - 2 \sin \frac{5\alpha}{4} \sin \frac{\alpha}{2} \sin^2 \frac{\alpha}{4} \right\} \quad (11)$$

$$F_{2x} = \frac{1}{\left(3 - \cos \frac{\alpha}{2}\right) \sin^{\frac{1}{2}} \frac{\alpha}{2}} \left\{ \sin \frac{\alpha}{4} - \sin \frac{7\alpha}{4} - \sin \frac{5\alpha}{4} \sin^4 \frac{\alpha}{4} - 2 \sin \frac{5\alpha}{4} \cos \frac{\alpha}{2} \sin^2 \frac{\alpha}{4} \right\} \quad (12)$$

$$F_{2y} = \frac{1}{\left(3 - \cos \frac{\alpha}{2}\right) \cos^{\frac{1}{2}} \frac{\alpha}{2}} \left\{ \sin \frac{\alpha}{4} + \sin \frac{7\alpha}{4} + \sin \frac{5\alpha}{4} \sin^4 \frac{\alpha}{4} + 2 \sin \frac{5\alpha}{4} \cos \frac{\alpha}{2} \sin^2 \frac{\alpha}{4} \right\} \quad (13)$$

and the definitions for a_x , a_y , and α are given in Figure 15 where α is an angle tangent to the crack at an instantaneous point on the crack path; i.e., the angle between X-axis and the line connecting two consecutive crack length data points.

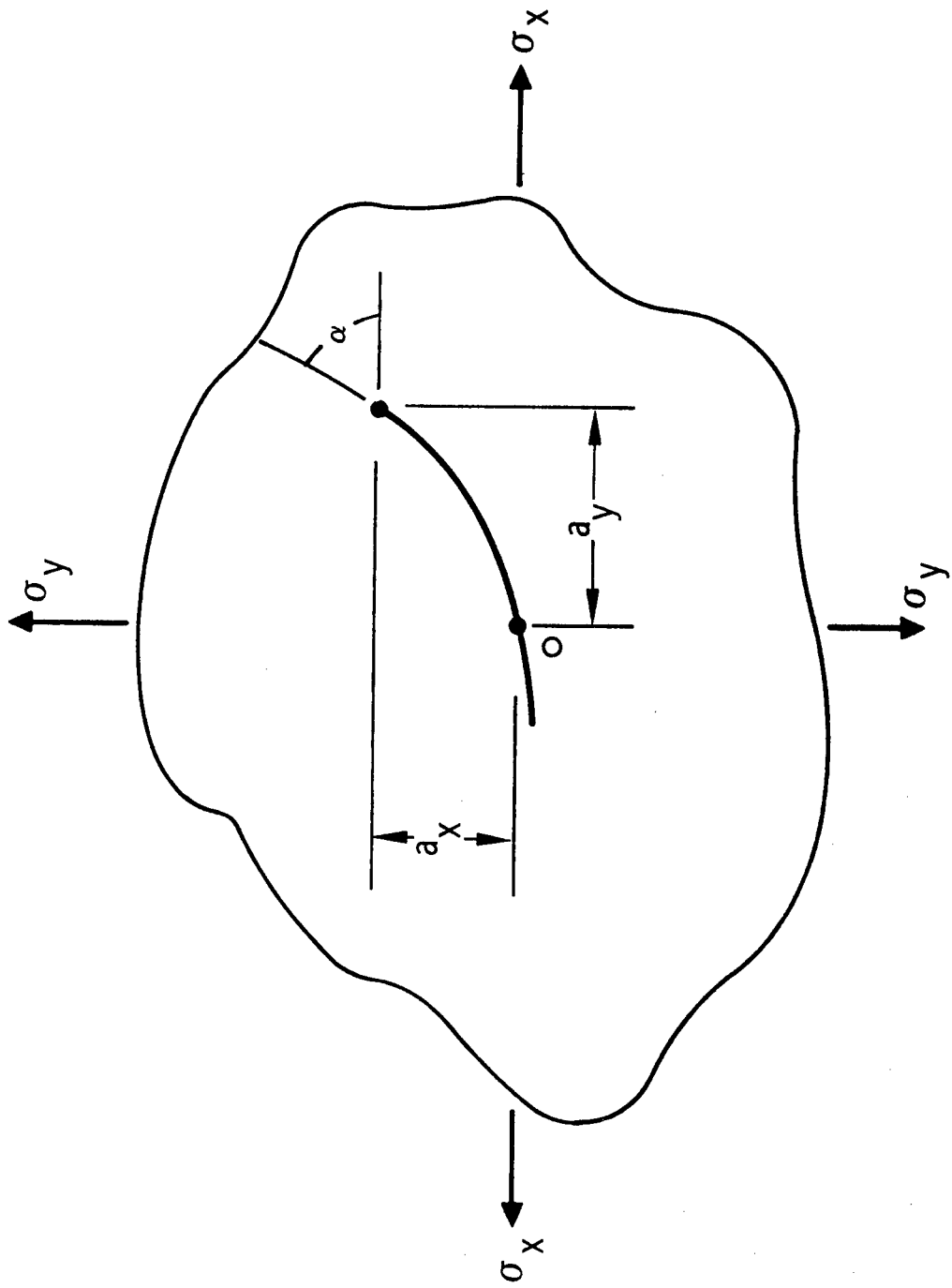


Figure 15. Notations for a Curved Crack

When Equations 8 and 9 are used to correlate crack growth rate and/or residual strength test data, it is necessary to adopt a failure criterion (to an equivalent K value) accounting for the combined effects of K_1 and K_2 at the crack tip. There are numerous failure criteria available in the literature, e.g., [29] to [31]. In this study, the following possibilities were considered:

$$K = (K_1^2 + K_2^2)^{\frac{1}{2}} \quad (14)$$

based on Irwin's theory of fracture [29], and

$$K = K_1 + K_2 \quad (15)$$

derived from experimental data on fracture testing of aluminum alloys and 4340 steel [16 and 32].

A simplified method for calculating K was also considered. This method simply calculates K values in the following manner. It has been determined by cracked finite element analysis that the K values at all crack lengths in the flat circle of the cruciform specimen (for $\sigma_x \leq \sigma_y$) are essentially the same as for an infinite sheet under uniaxial tension. Therefore, $K = \sigma \sqrt{\pi a}$. Here, σ is taken to be the maximum stress perpendicular to the crack at each small segment on the crack growth path, as schematically illustrated in Figure 16. It is seen that σ changes as the crack propagates. It equals σ_y at the beginning of the test and gradually changes to σ_x when the crack has completely turned 90°. The crack length "a" used in this method of calculation is rather arbitrary. As indicated in Figure 16, the distance connecting the center of the specimen and middle point of a da segment is used as an equivalent "a". In this approach, since an effective stress which opens the crack is used for computing an effective K, it may be considered that the K_2 term has been lumped into the calculation.

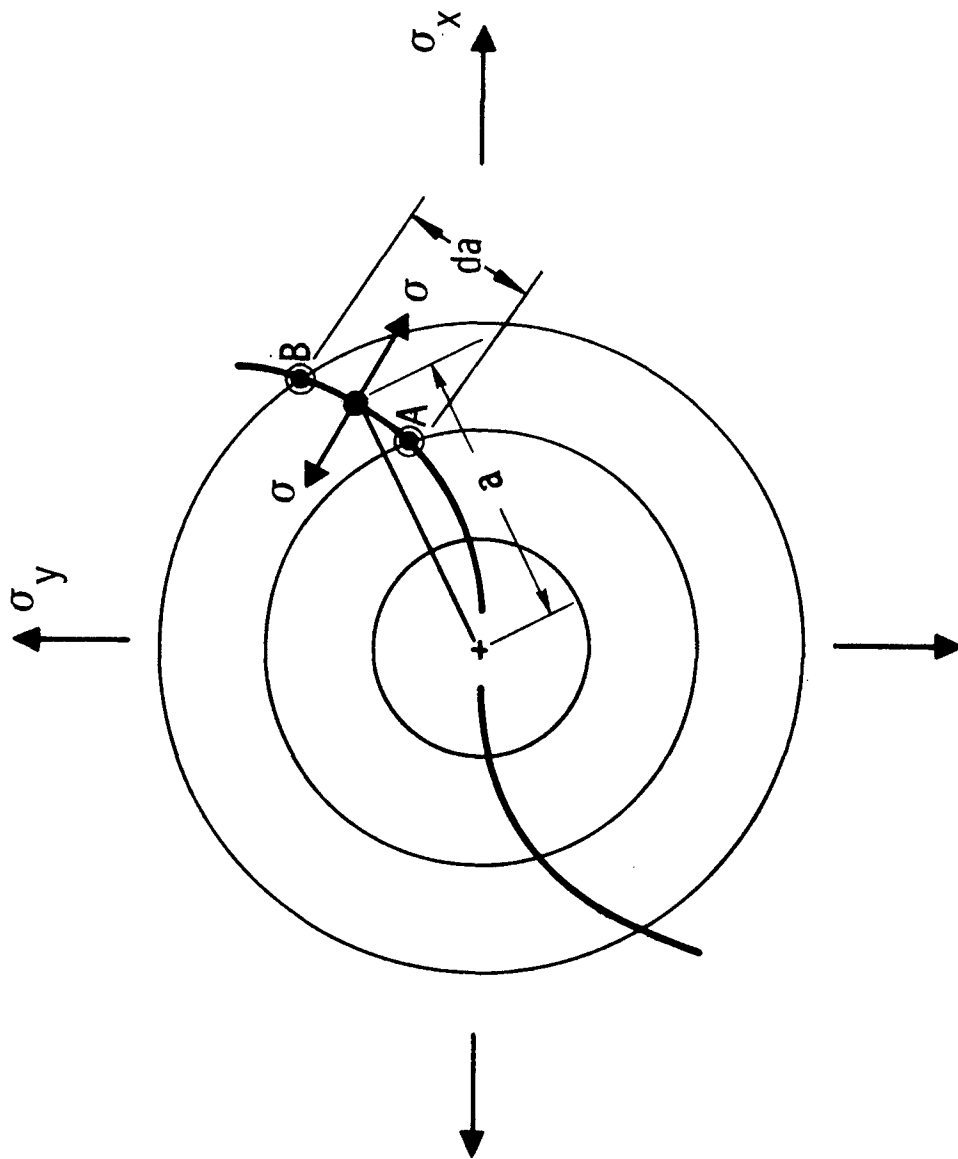


Figure 16. Notations for a Curved Crack

SECTION VII

CRACK TIP PLASTIC ZONE SIZES

A crack tip plastic zone is formed during the upward excursion of each loading cycle. After removal of the applied load, or in the valley of a loading cycle, there is a residual plastic zone remaining at the crack tip. The sizes of these crack tip plastic zones are functions of crack length, stress level, biaxial stress ratio and the state of stress triaxiality at the crack tip (e.g., plane stress or plane strain). In a constant amplitude loading case, the crack growth rate behavior may be related to the crack tip plastic zone size at the peak of a load cycle. However, in a variable amplitude loading situation, taking a high-low block loading sequence, for example, it is commonly believed that the residual plastic zone produced by the high load is the source affecting the crack growth retardation behavior. In this study, the "loaded" crack tip plastic zones were determined by elastic-plastic finite element (NASTRAN) analyses, and also by taking interferometry photographs at the crack tip during a cyclic crack growth test. The "residual" crack tip plastic zones were determined by interferometry measurements and also by backtracking of crack growth data obtained from periodically overloaded specimens. The details about these techniques and the results obtained from each of these techniques are discussed below.

7.1 Finite Element Analysis

Elastic-plastic NASTRAN analyses were conducted to determine crack tip plastic zone sizes in a biaxially loaded cruciform specimen. The finite element model shown in Figure 17 represents a quarter of a circular section of 3.5 inches in radius. The location of the nodal points on the outer circumference of this model matches those shown in Figure 6. The arrangement and size of the elements (not cracked) along the crack line, especially in the vicinity of the crack tip, were modified for each crack size.

E = Elastic Element

P = Plastic Element

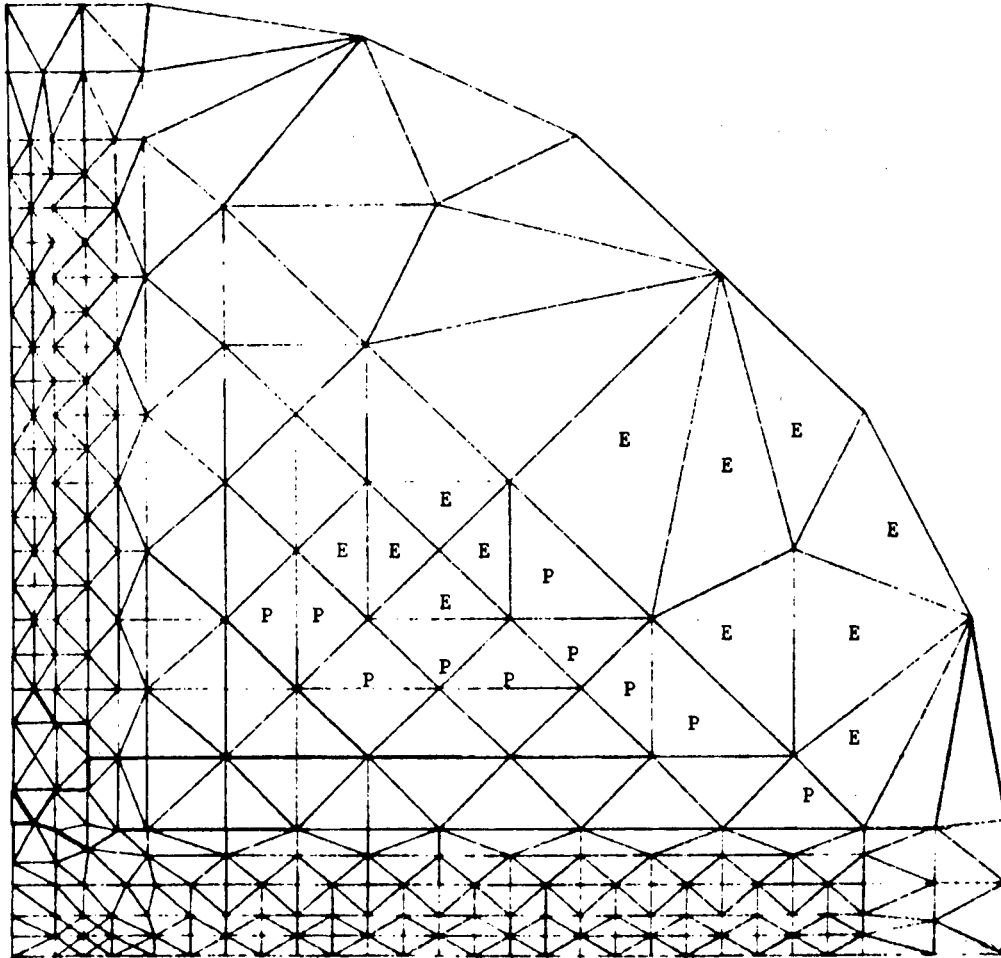


Figure 17. Finite Element Model for Elastic-Plastic Analysis

For example, fewer plastic elements and finer elements were used around the crack tip for shorter crack lengths because smaller crack tip plastic zones had been expected, and vice versa. The elastic-plastic boundary arrangement such as those shown in Figure 17 was used for the cases of a 1.5 inch crack in a 7075-T7351 specimen and a 1.0 inch crack in a 2024-T351 specimen.

The general procedure for these analyses was to apply the required loads (for a desired stress level and biaxial ratio) onto the old model (coarse grid, all elastic, see Figures 6A and 6B) without a crack. The loads at the nodal points around the 3.5 inches radius were determined and these loads were then applied onto the new model (Figure 17) with cracks. The same loads could be used for different crack lengths as long as their biaxial stress ratio and magnitude were the same thereby saving considerable computer time.

Taking the stresses from the NASTRAN print out, the Von Mises stress in each plastic element was computed. An element was considered yielded when its Von Mises stress exceeded the elastic proportional limit of the material (58 ksi for 7075-T7351 and 52 ksi for 2024-T351). A plastic zone was defined by gathering a group of the yielded elements. Plastic zone contour maps for five loading cases ($\sigma_x/\sigma_y = 0, \pm 0.5, \pm 1.0$) at 30 ksi for both 7075-T7351 and 2024-T351 materials, at seven crack lengths ($a = 0.25, 0.5, 1.0$ and 1.5 for 7075-T7351 and $a = 0.25, 0.5$ and 1.0 for 2024-T351 specimens) are presented in Figures 18 through 24. Note the dotted circle in Figure 18 which maps a very small plastic zone is only an estimated value. In these cases the elements directly surrounding the crack tip were not yielded (based on the calculated Von Mises stress), and the plastic zone was assumed to be one-half of the element sizes since the Von Mises stresses computed were based on the stresses at the centroid of each element. As for the huge plastic zones in Figures 21 and 24, the incompleted zones for $\sigma_x = -\sigma_y$ were due to the fact that these plastic zones were so big and their actual sizes were beyond the boundary of the elastic and plastic elements (see Figure 17).

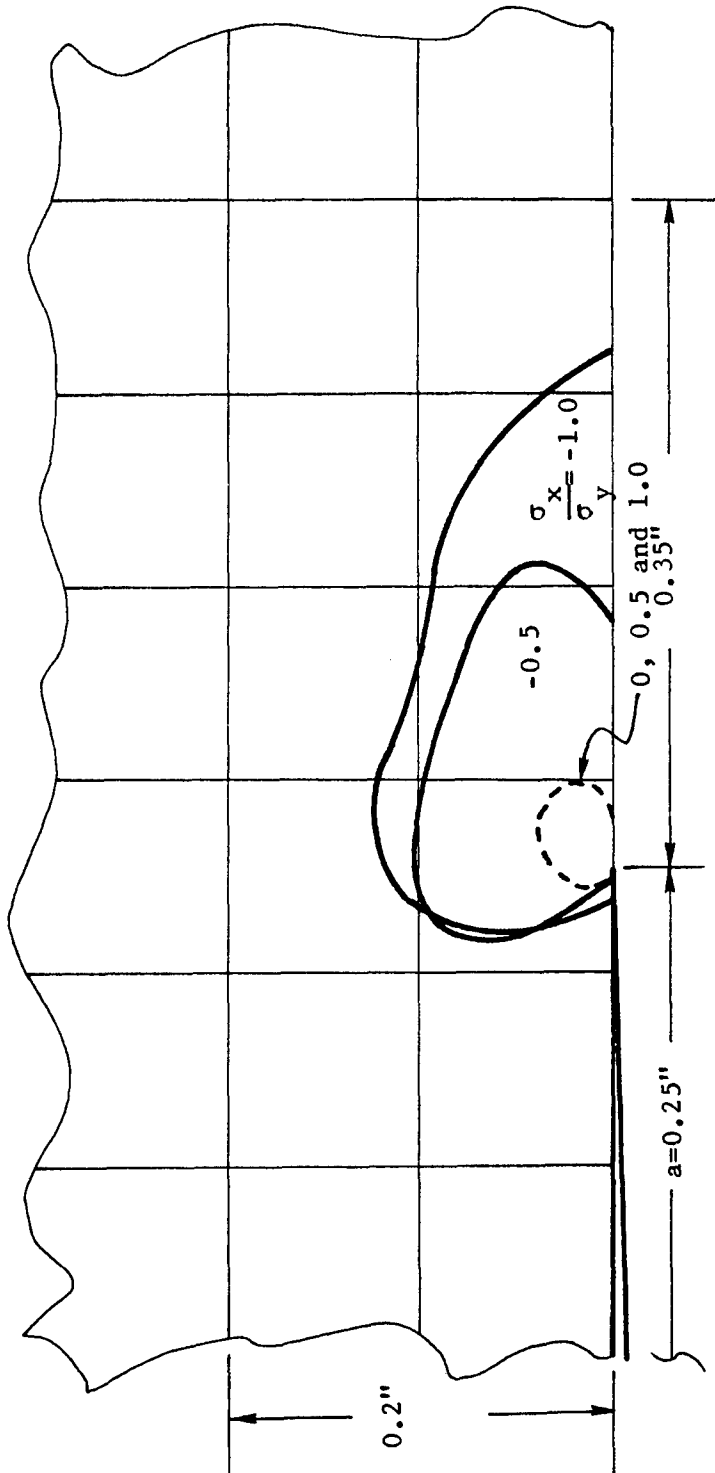


Figure 18. Crack Tip Plastic Zone for 7075-T7351 at 30 ksi (NASTRAN analysis)

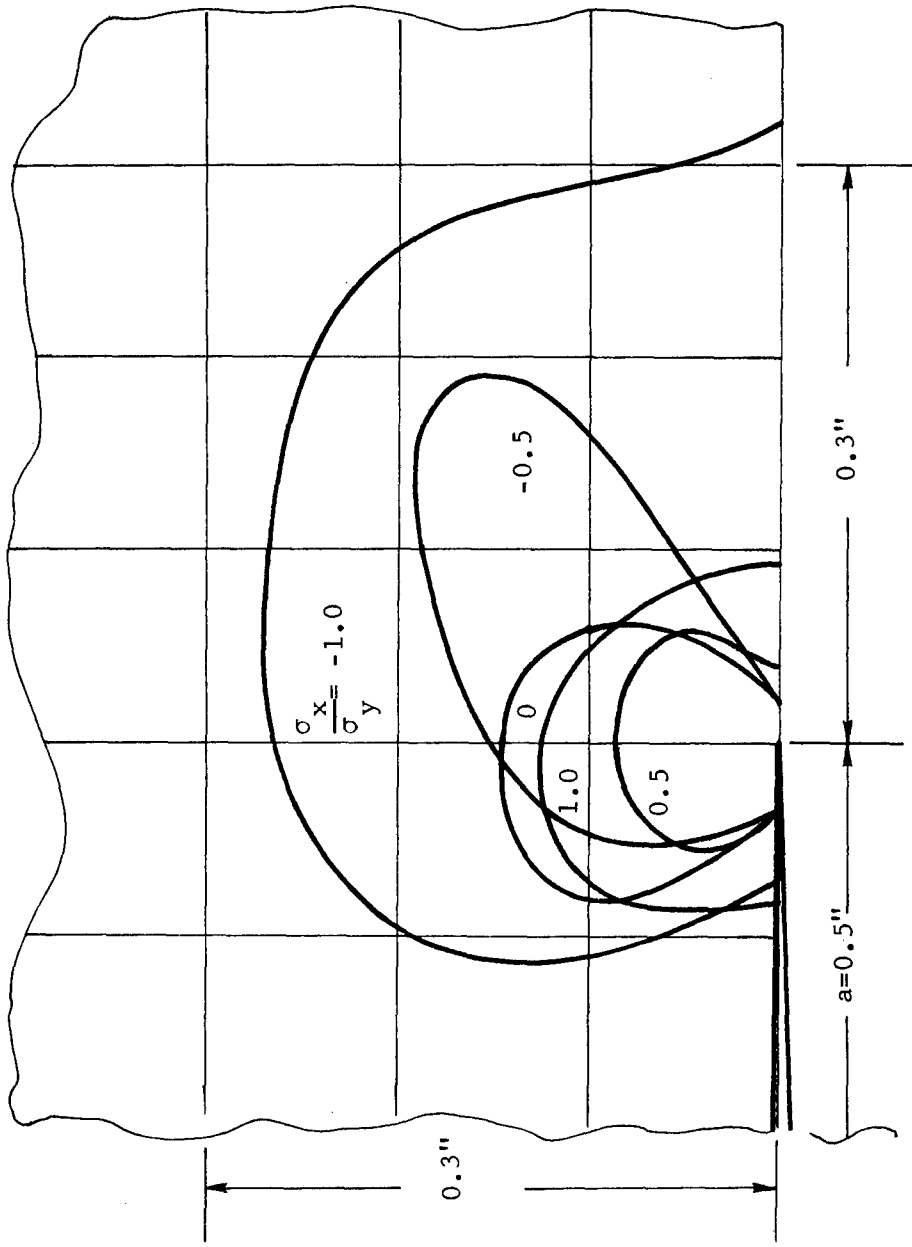


Figure 19. Crack Tip Plastic Zone for 7075-T7351 at 30 ksi (NASTRAN analysis)

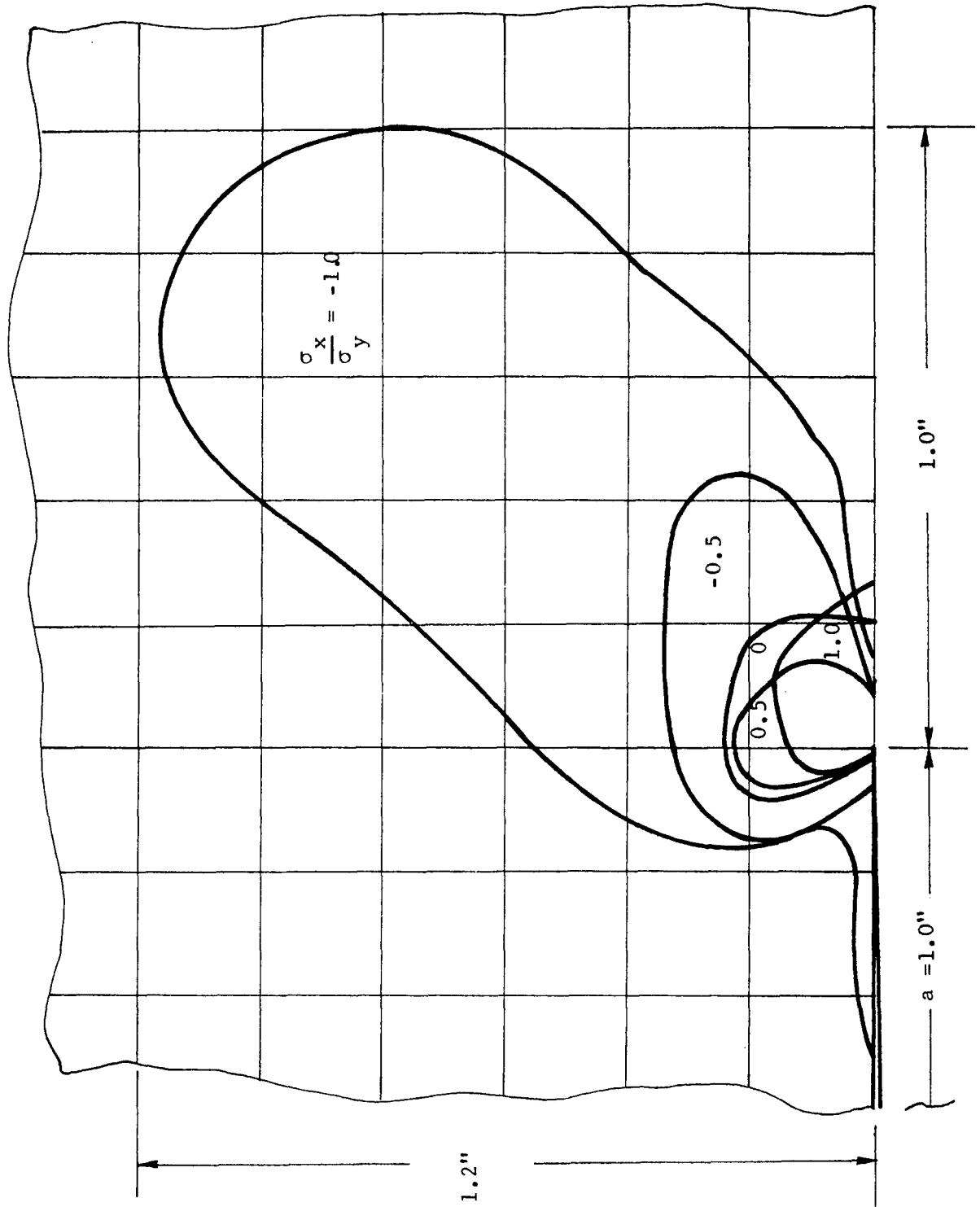


Figure 20. Crack Tip Plastic Zone for 7075-T7351 at 30 ksi (NASTRAN analysis)

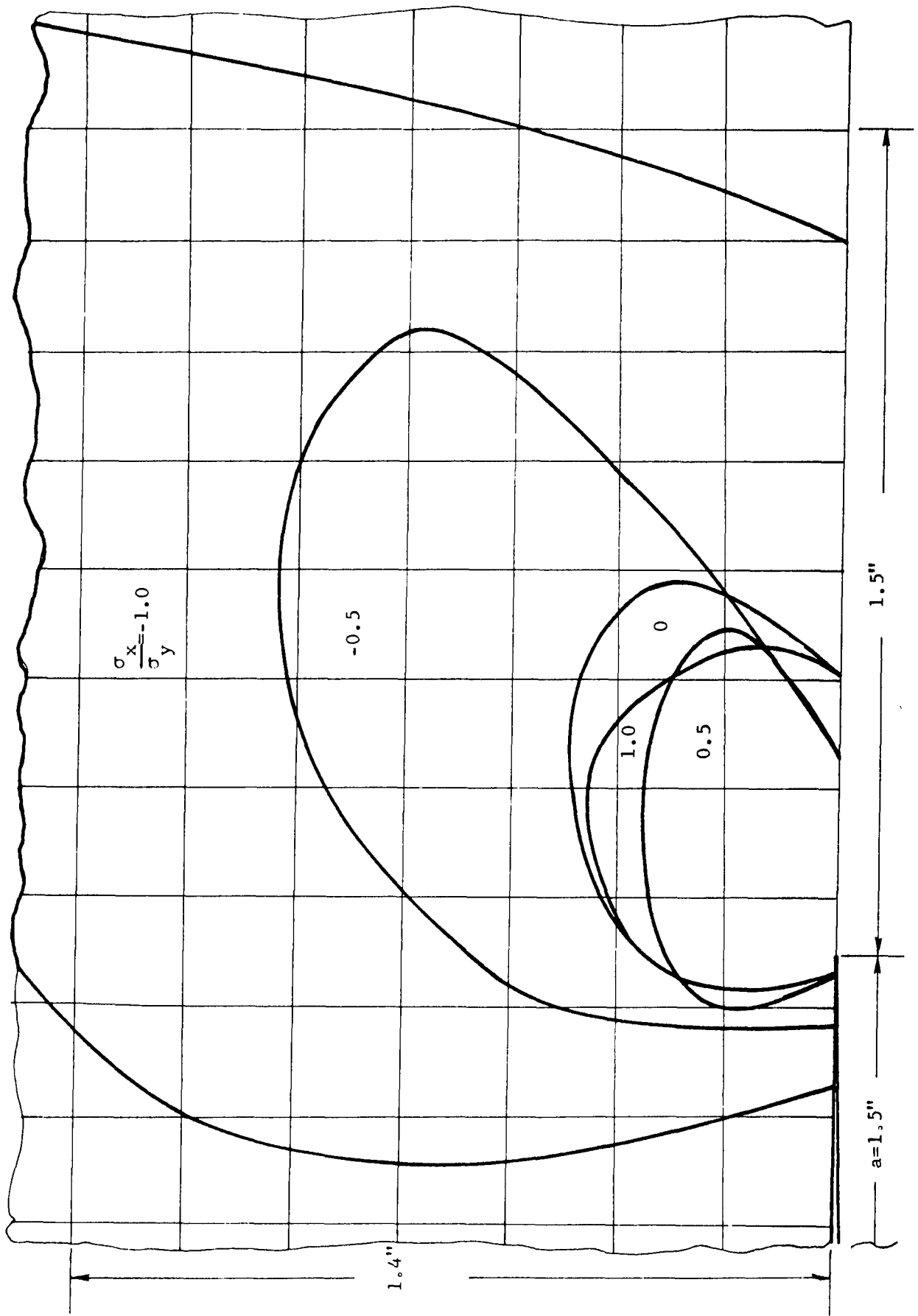


Figure 21. Crack Tip Plastic Zone for 7075-T7351 at 30 ksi (NASTRAN analysis)

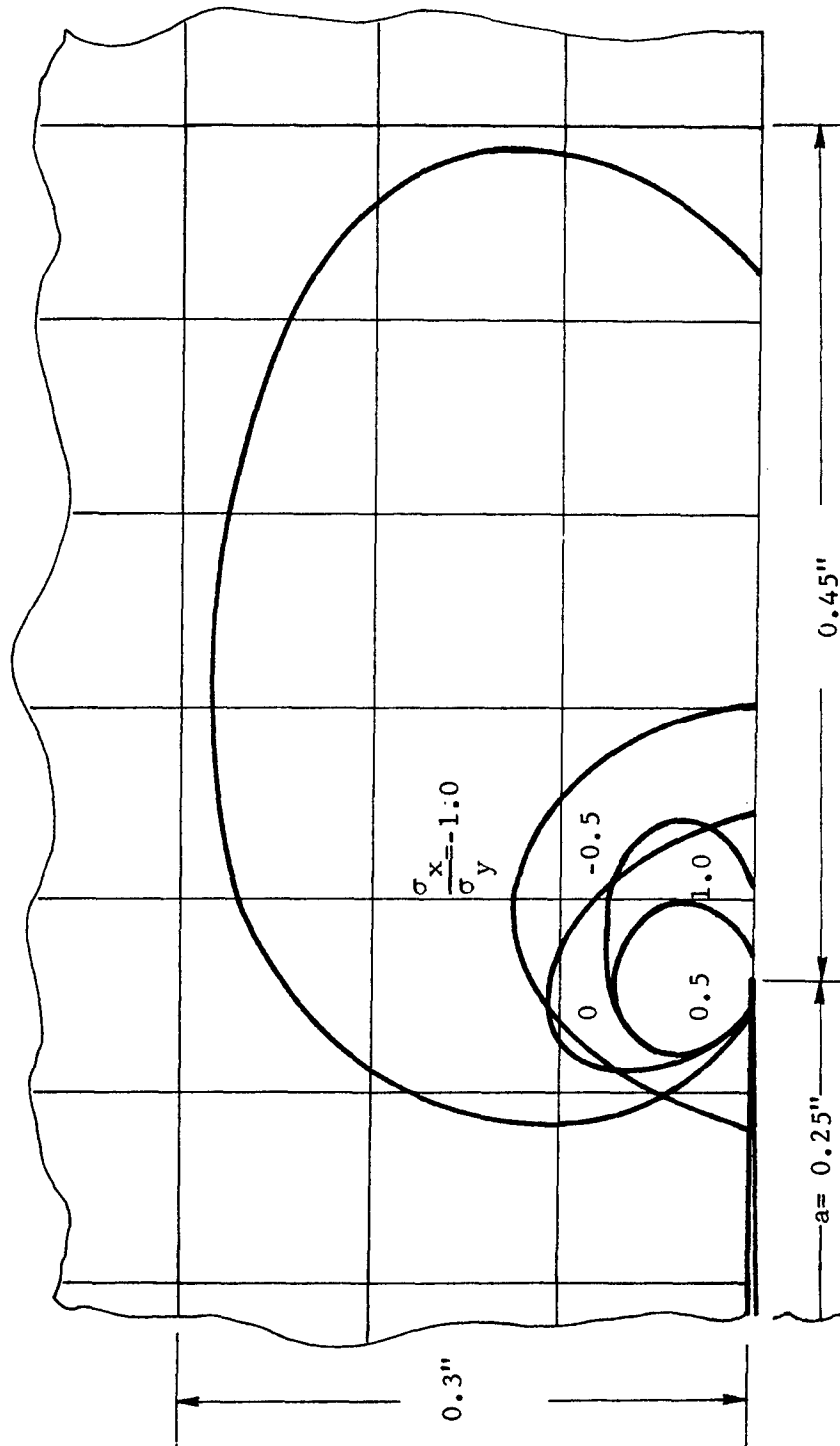


Figure 22. Crack Tip Plastic Zone for 2024-T351 at 30 ksi (NASTRAN analysis)

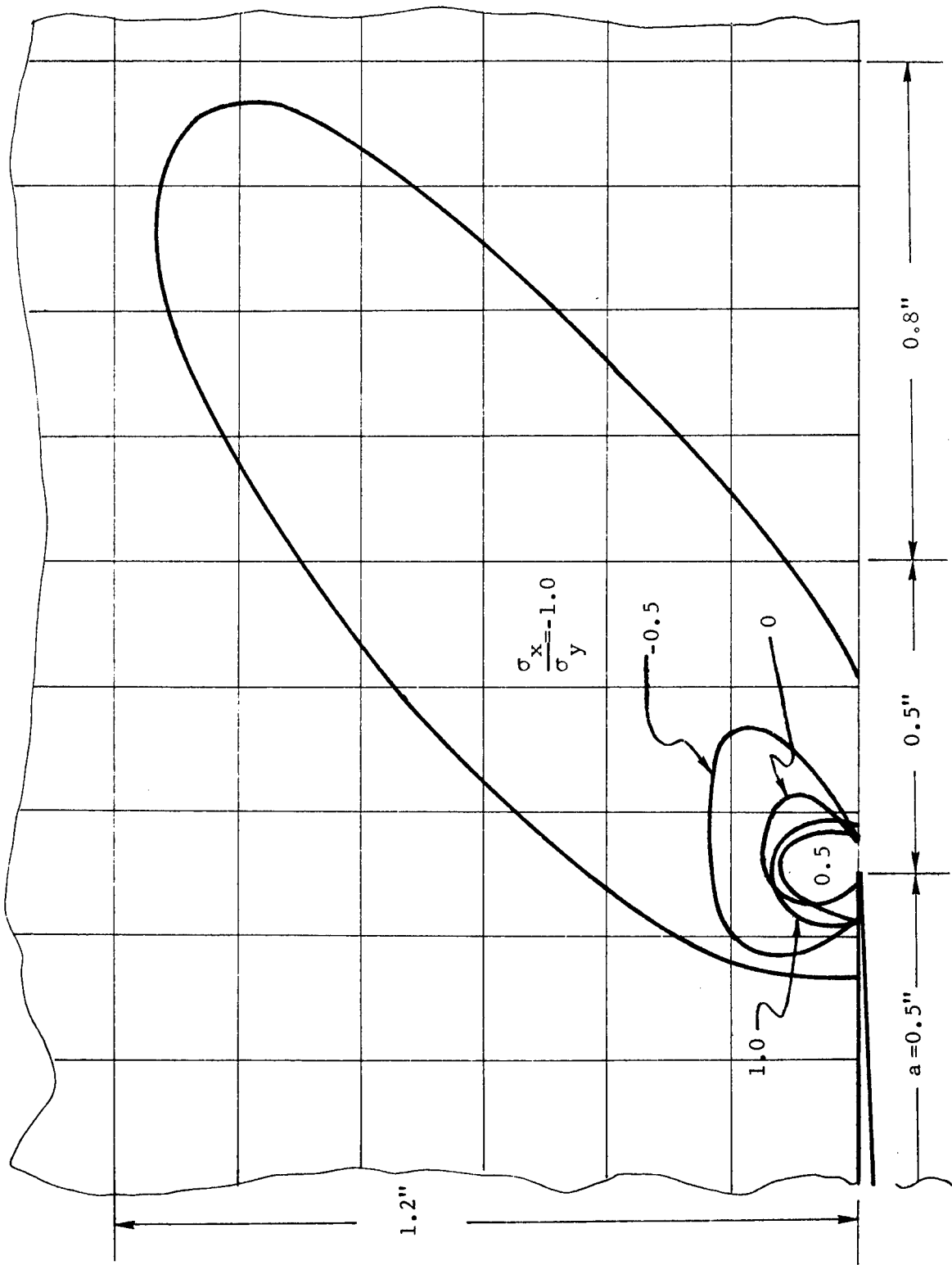


Figure 23. Crack Tip Plastic Zone for 2024-T351 at 30 ksi (NASTRAN analysis)

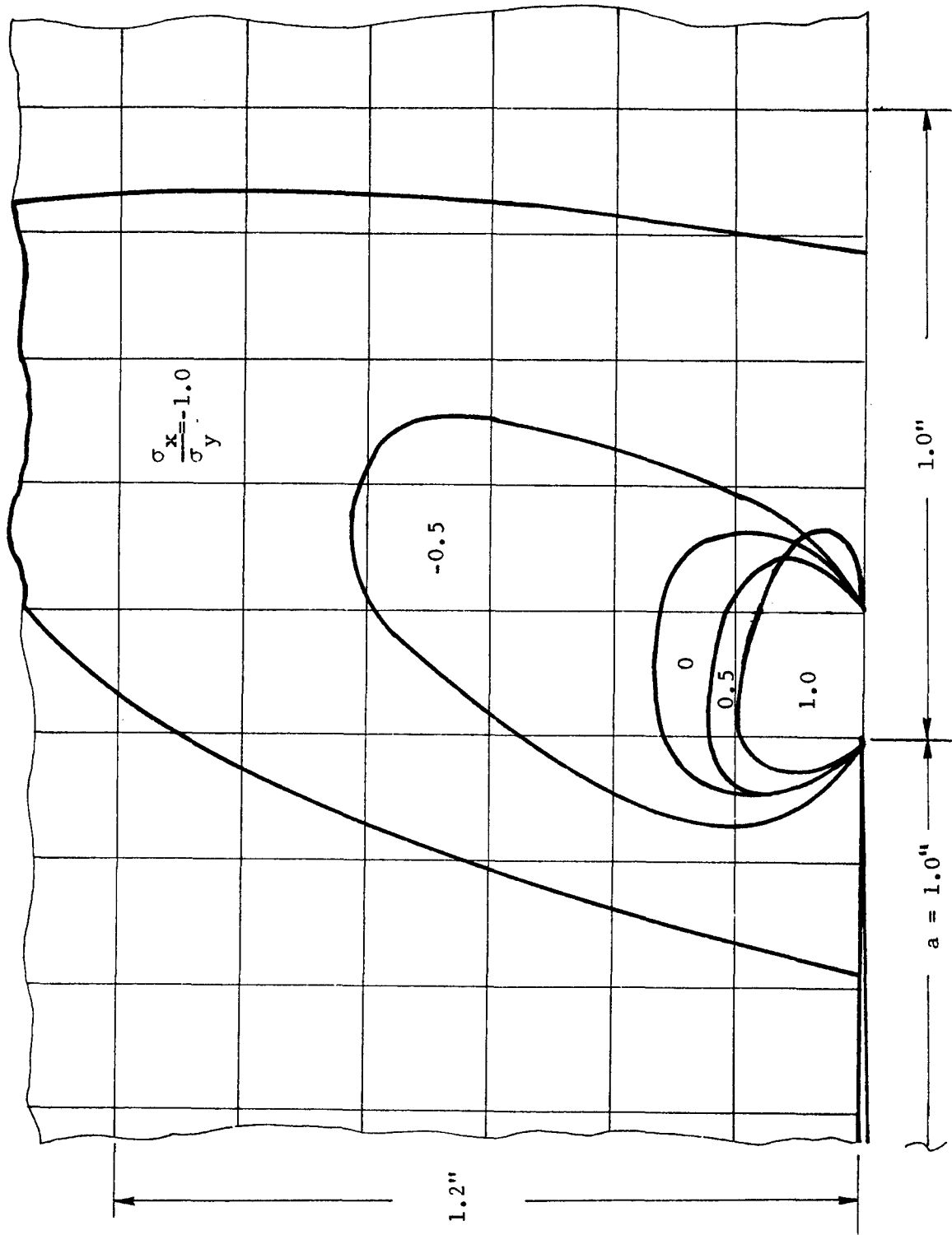


Figure 24. Crack Tip Plastic Zone for 2024-T351 at 30 ksi (NASTRAN analysis)

Crack tip plastic zone sizes at lower stress levels were also determined by elastic-plastic NASTRAN analyses. The plastic zone dimensions for all the cases were measured from each contour map (reduced from the NASTRAN data) and are listed in Tables 2 and 3. The methods used for the measurements are described in the following.

The shape and the dimension of a crack tip plastic zone are functions of crack length, stress level, and the mechanical properties of a given material. For a crack under uniaxial tension, in a plane stress state, the classical equations of Irwin, and Rice [33], are respectively

$$r_p = \frac{1}{\pi} (K_{\max}/F_{ty})^2 \quad (16)$$

and

$$r_p = \frac{\pi}{8} (K_{\max}/F_{ty})^2 \quad (17)$$

However, the characteristic dimension r_p has never been clearly defined. As seen in Figures 18 to 24, the plastic zone shapes varied among all the cases.

The commonly familiar plastic zone shape (the butterfly shape) is schematically shown in Figure 25. Here we define the dimension \bar{r}_p to be the largest distance between the crack tip and the border of the plastic zone. Then we compute an equivalent dimension r_p representing the diameter of a circle. The area of such an imaginary circle is set equal to the total area of the butterfly.

TABLE 2. NASTRAN CRACK TIP PLASTIC ZONE FOR 7075-T7351 ALLOY

a (Inch)	σ_y (Ksi)	\bar{r}_p (Inch)	r_p (Inch)	$\left(\frac{K_{\max}}{F_{ty}}\right)^2$ (Inch)	σ_x/σ_y
.25	30.0	.05	.068	.196	0
.5	30.0	.152	.186	.393	↓
1.0	30.0	.27	.384	.785	
1.0	25.2	.181	.234	.554	
1.5	30.0	.75	.922	1.178	
.25	30.0	.05	.068	.196	
.5	30.0	.086	.134	.393	↓
1.0	30.0	.275	.248	.785	
1.0	24.0	.0875	.192	.503	
1.5	30.0	.636	.766	1.178	
.25	30.0	.05	.068	.196	
.5	30.0	.125	.206	.393	↓
.5	25.2	.1375	.172	.277	
1.0	25.2	.162	.248	.554	
1.0	30.0	.27	.234	.785	
1.5	30.0	.655	.81	1.178	
.25	30.0	.17	.206	.196	
.5	30.0	.242	.288	.393	↓
.5	24.0	.171	.225	.251	
.5	20.0	.156	.136	.174	
1.0	24.0	.225	.383	.503	
1.0	30.0	.549	.654	.785	
1.5	30.0	1.419	1.666	1.178	
.25	30.0	.27	.292	.196	-1.0
.5	30.0	.32	.54	.393	↓
.5	25.2	.262	.374	.277	
1.0	25.2	.8	.868	.554	
1.0	30.0	1.4	1.89	0.785	

TABLE 3. NASTRAN CRACK TIP PLASTIC ZONE FOR 2024-T351 ALLOY

a (Inch)	σ_y (Ksi)	\bar{r}_P (Inch)	r_P (Inch)	$\left(\frac{K_{max}}{F_{ty}}\right)^2$ (Inch)	σ_x/σ_y
.25	30.0	.11	.172	.283	0
.5	30.0	.19	.244	.565	↓
.5	24.0	.1625	.19	.362	
1.0	30.0	.413	.562	1.131	
.25	30.0	.0742	.108	.283	
.5	20.0	.1	.108	.251	↓
.5	30.0	.141	.194	.565	
1.0	30.0	.306	.45	1.131	
1.0	20.0	.169	.202	.503	
.25	30.0	.109	.144	.283	1.0
.5	30.0	.13	.216	.565	↓
1.0	24.0	.269	.316	.724	
1.0	30.0	.36	.45	1.131	
.25	30.0	.141	.24	.283	
.5	30.0	.277	.428	.565	↓
.5	20.0	.171	.18	.251	
1.0	20.0	.313	.36	.503	
1.0	30.0	.918	1.012	1.131	
.25	30.0	.453	.594	.283	-1.0
.5	30.0	1.6	1.756	.565	↓
.5	20.0	.33	.561	.251	

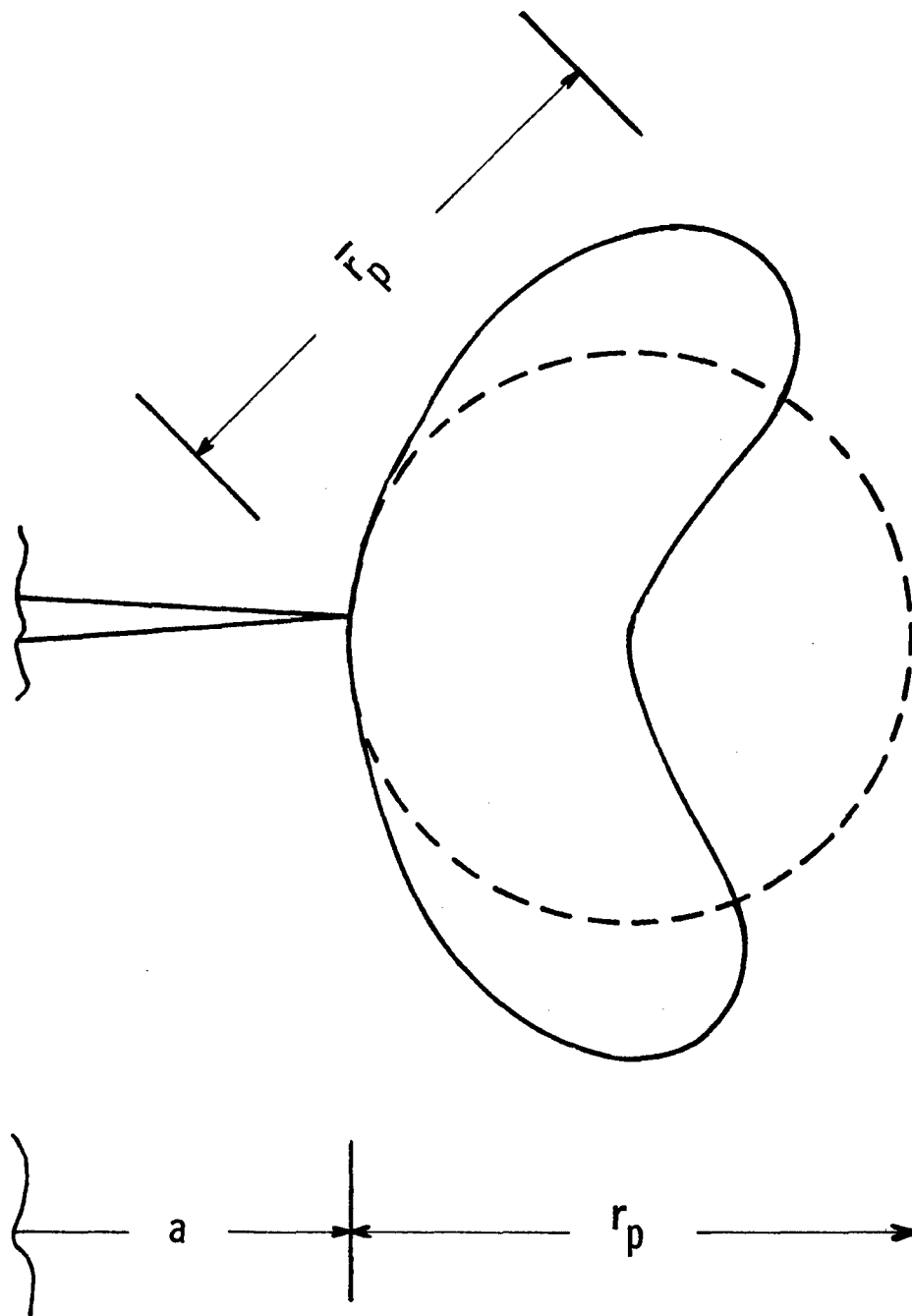


Figure 25. Crack Tip Plastic Zone

Both dimensions, \bar{r}_p and r_p , are listed in Tables 2 and 3, and are plotted in Figures 26 to 29 as functions of a normalized plasticity density parameter, $(K_{\max}/F_{ty})^2$. Also in these figures are the plastic zone sizes computed by using Equations 16 and 17. These theoretical values are included here to compare with the NASTRAN results for the uniaxial condition ($\sigma_x = 0$). It also provides some indication of the relative sizes of the crack tip plastic zones for cracks subjected to other biaxial loading conditions. Facts that can be observed from Figures 26 to 29 are listed in the following:

1. For the same data point the r_p dimension is usually, although not always, slightly larger than the \bar{r}_p dimension.
2. The plastic zone sizes for biaxial ratios of 0.5 and 1.0 are approximately the same and are insignificantly smaller than those for the uniaxial tension.
3. The plastic zone sizes for tension-compression biaxial ratios are significantly larger than those for the uniaxial tension and tension-tension biaxial conditions; the higher the tension-compression ratio, the larger plastic zone size.
4. The \bar{r}_p dimensions for the uniaxial tension cases fit in between the theoretical values of Rice and Irwin whereas the r_p dimensions are slightly larger than the Rice plastic zones.
5. For the 2024-T351 specimen, the relationship between r_p (or \bar{r}_p) and the plasticity density parameter, $(K_{\max}/F_{ty})^2$, is linear for at least four out of the five biaxial loading conditions (excepting $B = -1.0$ which is questionable). However, for the 7075-T7351 specimen at a given biaxial ratio, this relationship is linear up to a certain $(K_{\max}/F_{ty})^2$ value. For the -1.0 biaxial ratio cases, the crack tip plastic zone for the 2024-T351 specimen is always larger than those for the 7075-T7351 specimen. As for the other four biaxial ratios, the plastic zone sizes for both 2024-T351 and 7075-T7351 are the same as long as the r_p (or \bar{r}_p) and $(K_{\max}/F_{ty})^2$ relationships for both specimens are linear.

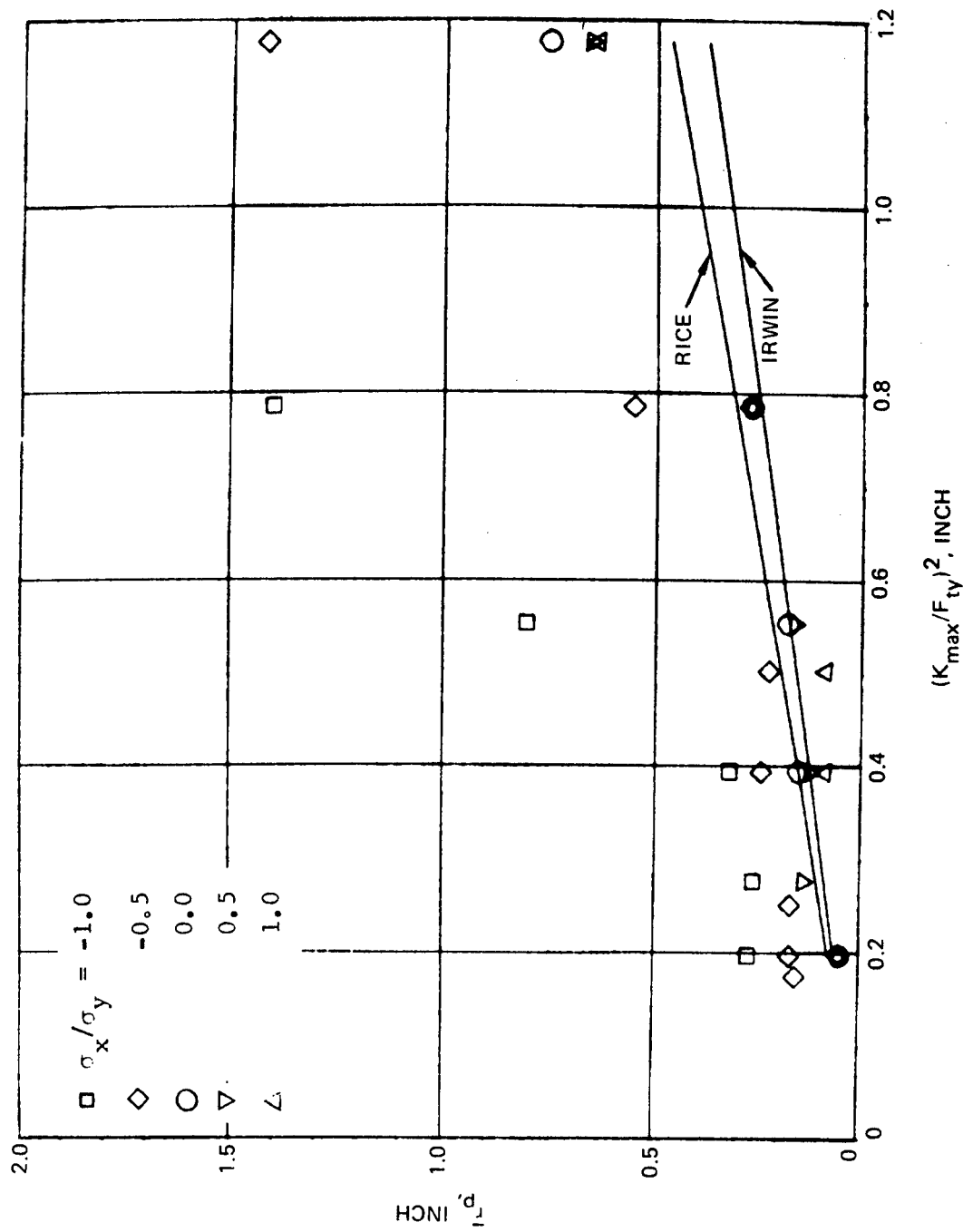


Figure 26. Crack Tip Plastic Zone for 7075-T7351 (NASTRAN analysis)

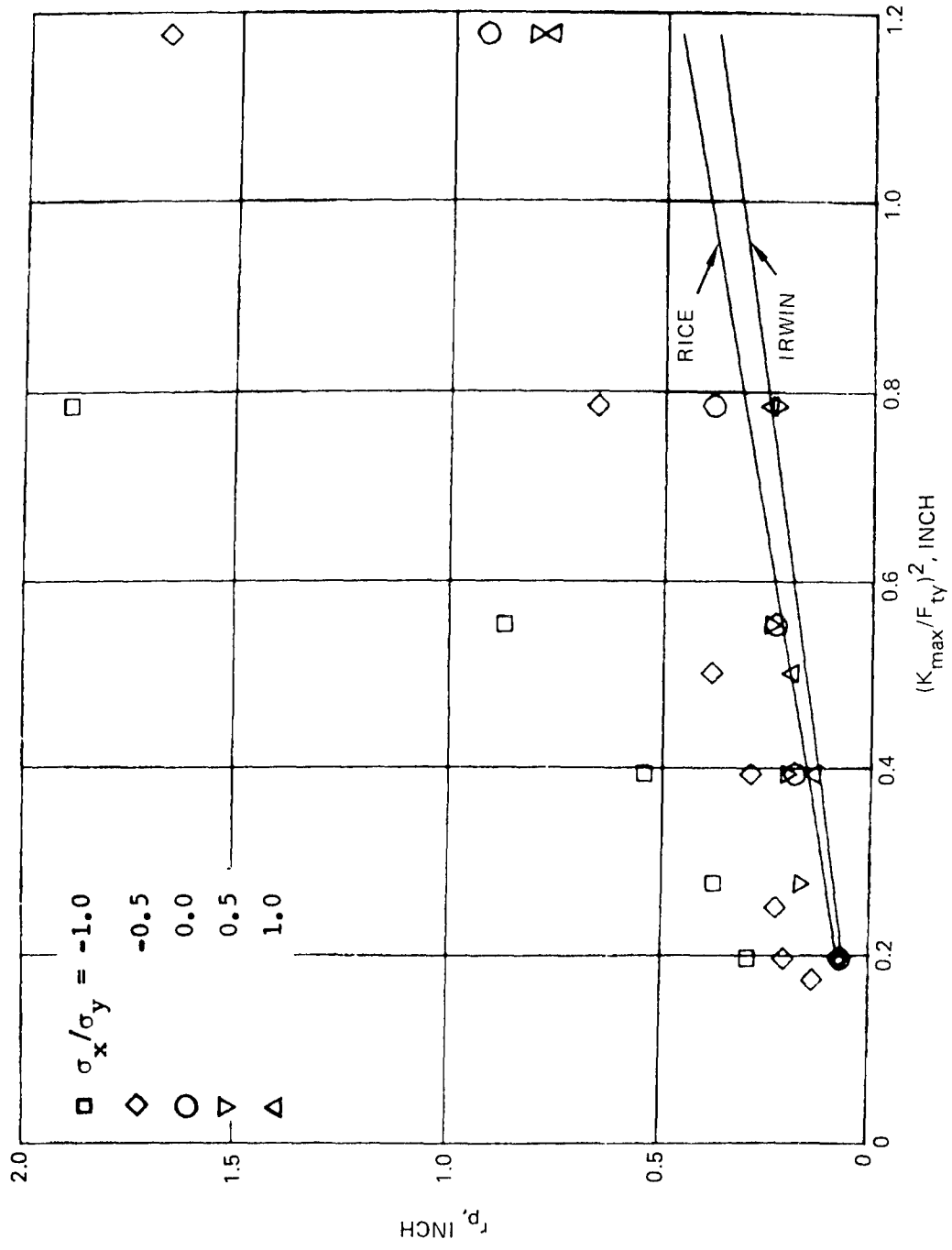


Figure 27. Crack Tip Plastic Zone for 7075-T7351 (NASTRAN analysis)

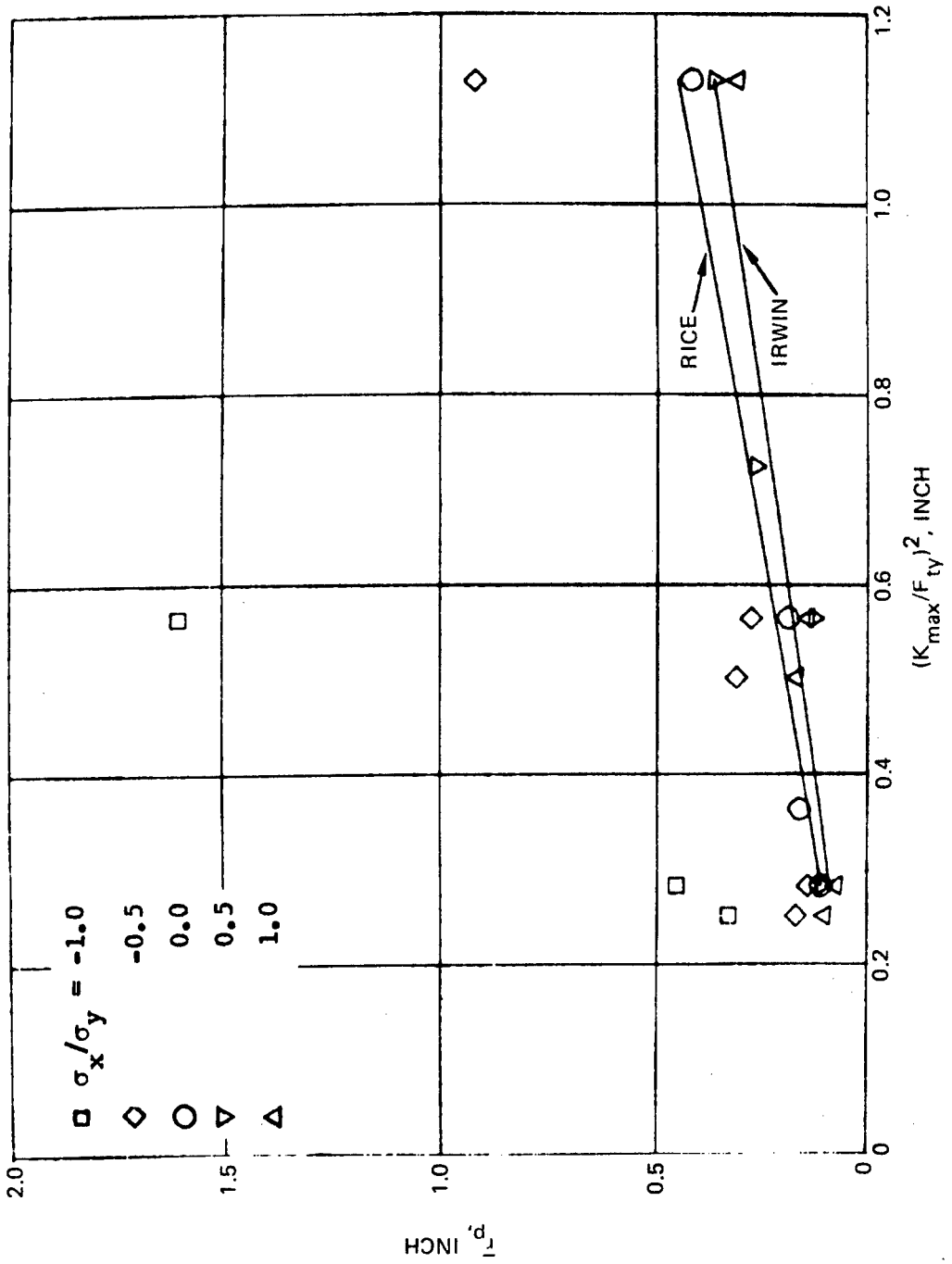


Figure 28. Crack Tip Plastic Zone for 2024-T351 (NASTRAN analysis)

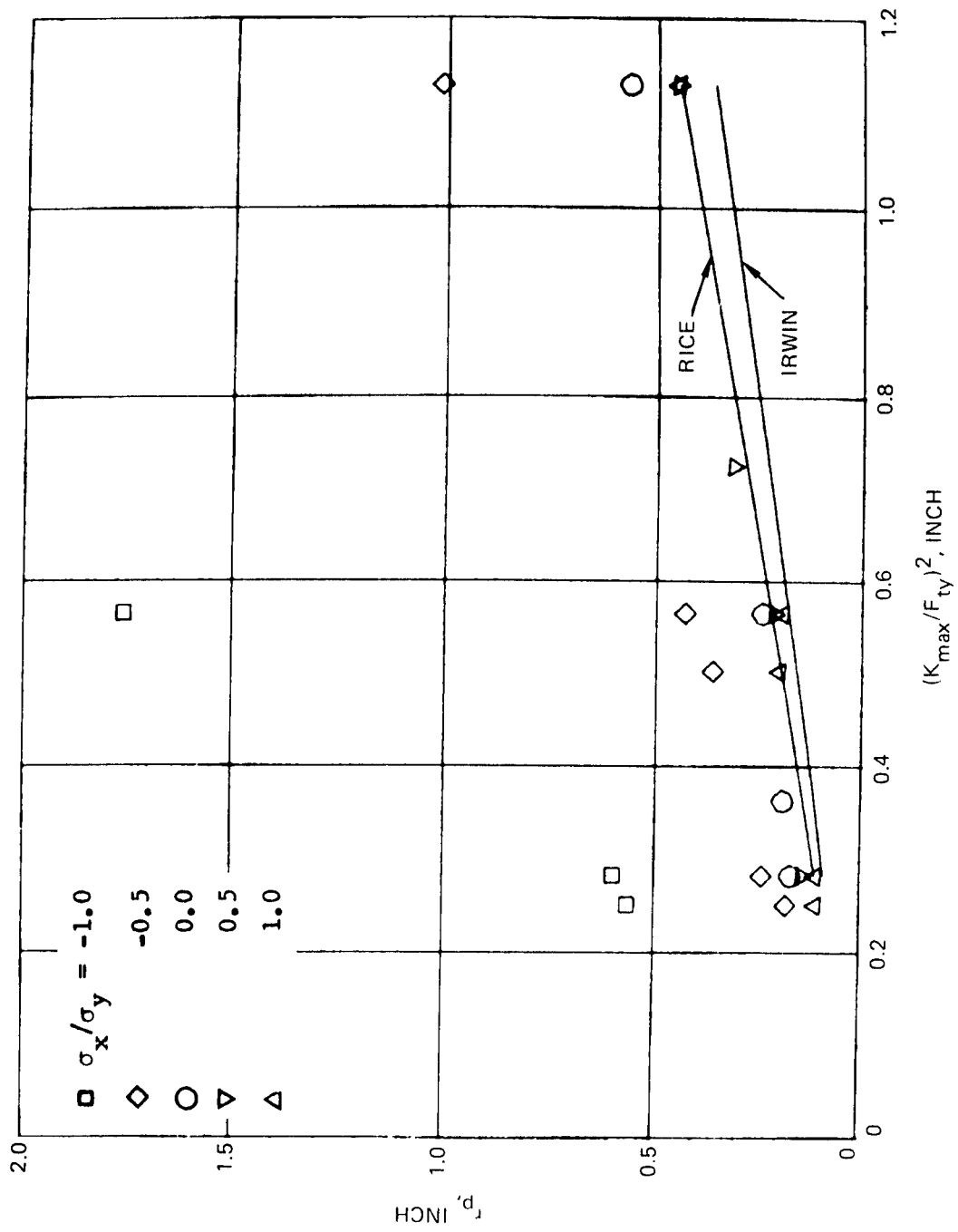


Figure 29. Crack Tip Plastic Zone for 2024-T351 (NASTRAN analysis)

Actually, plastic zone size nonlinearity exists in both 7075-T7351 and 2024-T351 specimens. The reason for its not being observed in the 2024-T351 specimen was due to the fact that the largest crack size in the 2024-T351 specimen was one-inch ($2a = 2$ inches), whereas the largest crack size in the 7075-T7351 specimen was 1.5 inches ($2a = 3$ inches). For a given stress level, the K_{\max}/F_{ty} ratios for these two cases (a 2-inch crack in a 2024-T351 specimen and a 3-inch crack in a 7075-T7351 specimen) are approximately the same. Taking a 30 ksi applied stress level for example, the $(K_{\max}/F_{ty})^2$ value is approximately equal to 1.15 and the corresponding plastic zone size for the 7075-T7351 specimen is significantly larger than those for the 2024-T351 specimen. The significantly larger crack dimension in the 7075-T7351 specimen (3 inches long as opposed to a 2 inch crack in the 2024-T351 specimen) might have induced some geometric effect on the development of a crack tip plastic zone.

7.2 Interferometry Measurement

For the interferometry tests, photoimprinted grids were not used as in other tests. Instead a transparent grid (of identical design to that used for photoimprinting) was mounted in a fixture attached to the specimen. This fixture was so designed to ensure repeatable positioning (for each interferometer scan, this was necessarily removed).

A Wild M20 interferometer was adapted for use in the biaxial frame. The interferometer base was positioned on the top cover plate of the test frame with the objective lens protruding down through the access hole of the cover plate. For each plastic zone mapped, the interferometer was positioned parallel to the crack direction and subsequent interference photographs taken. The Wild M20 was limited to a minimum magnification of 45x. This required that the plastic zone be mapped by taking several photographs which were later assembled into a composite.

Some clear limitations on the use of this interference microscope become apparent.

1. A high degree of subjectivity was involved in setting up the equipment, i.e., there was no absolute criterion for the adjustment required to generate the interference patterns. This was particularly true for large plastic zone where no "flat" surface can be discerned at 45x. The actual adjustments made were often done on a trail/error basis, i.e., the entire zone was mapped and remapped until a coherent composite was attained.
2. For the plastic zone measured at load, the vibrations from the test frame made it extremely tedious to produce decent consistent photographs.

Interferometry photographs were taken from 30 specimens. In each specimen, photographs were taken at the crack tip at two to four crack dimensions ranging from 0.2 to 2.0 inches of total crack length. Whenever possible, photographs were taken at zero load (after unloaded from maximum load) and then at peak load (after reloaded to maximum load from zero load). The first picture taken represented the residual plastic zone. For those periodically overloaded specimens, the interferometry photographs were actually taken at zero load prior to, and after, the overload. The first picture taken represented the residual plastic zone produced by the constant amplitude stress and the second picture represented the residual plastic zone of the overload.

Three patterns of interferometry fringes are shown in Figures 30 to 32. These fringe patterns are typical of all the photographs taken from all the specimens. Figure 33 is a schematic representation of these fringe patterns. The pattern of Figure 30, or Figure 33(a), is usually associated with constant amplitude at a lower stress intensity level (either "loaded" or "unloaded") whereas the other two patterns usually appeared after an overload. For the constant amplitude at higher K level cases, the interferometry fringe pattern was somewhat in between Figures 30 and 31.

Each of the interferometry contours actually measures the depth of the surface depression of the metal sheet around the crack, i.e., each fringe represents a certain amount of vertical displacement. When the contour line(s) becomes out of focus, or diverges, the material outside of that contour is probably not deformed. Therefore, it can logically be said that the last visible contour (e.g., line A in Figures 30 and 32) divides the plastically deformed and undeformed materials and thereby maps out the crack tip plastic zone. As for those fringe patterns shown in Figure 31 or Figure 33(b), the division for a plastic zone is not clear. Comparing Figures 33(b) and 33(c) the main difference between these two patterns is that all the contour lines in Figure 32 or Figure 33(c), immerse into the crack tip whereas many of the outer contour lines in Figure 31 or Figure 33(b), do not close all the way to the crack tip. Therefore, some contour lines which start to turn around and become parallel to the crack line were selected to represent the crack tip plastic zone. When uncertainty arose, two contour lines were selected, one representing a minimum r_p value and another representing a possible r_p value (see Figure 31).

The interferometry photographs taken from all 30 specimens are compiled in Volume III of this report. The crack tip plastic zone sizes (the r_p values) reduced from each of these photographs are presented in Figures 34 to 48 comparing the "loaded" and the "unloaded" plastic zone sizes at each biaxial stress ratio. Comparison of the analytically (elastic-plastic NASTRAN) and the experimentally (interferometry) determined plastic zone sizes (at load) are presented in Figures 49 to 55. It can be observed from these figures that:

1. Excepting the one-to-minus one biaxial ratio case, the experimentally determined crack tip plastic zone (at peak load) correlates with those determined by using elastic-plastic finite element analysis technique.



Figure 30. Interferometry Photograph of Cruciform Specimen No. 7-114, TC No. 99

7075-T7351, a = 0.5 inch
 $\sigma_x = 0, \sigma_y = 24$ ksi, over-
loaded. Magnification: 22.6 X

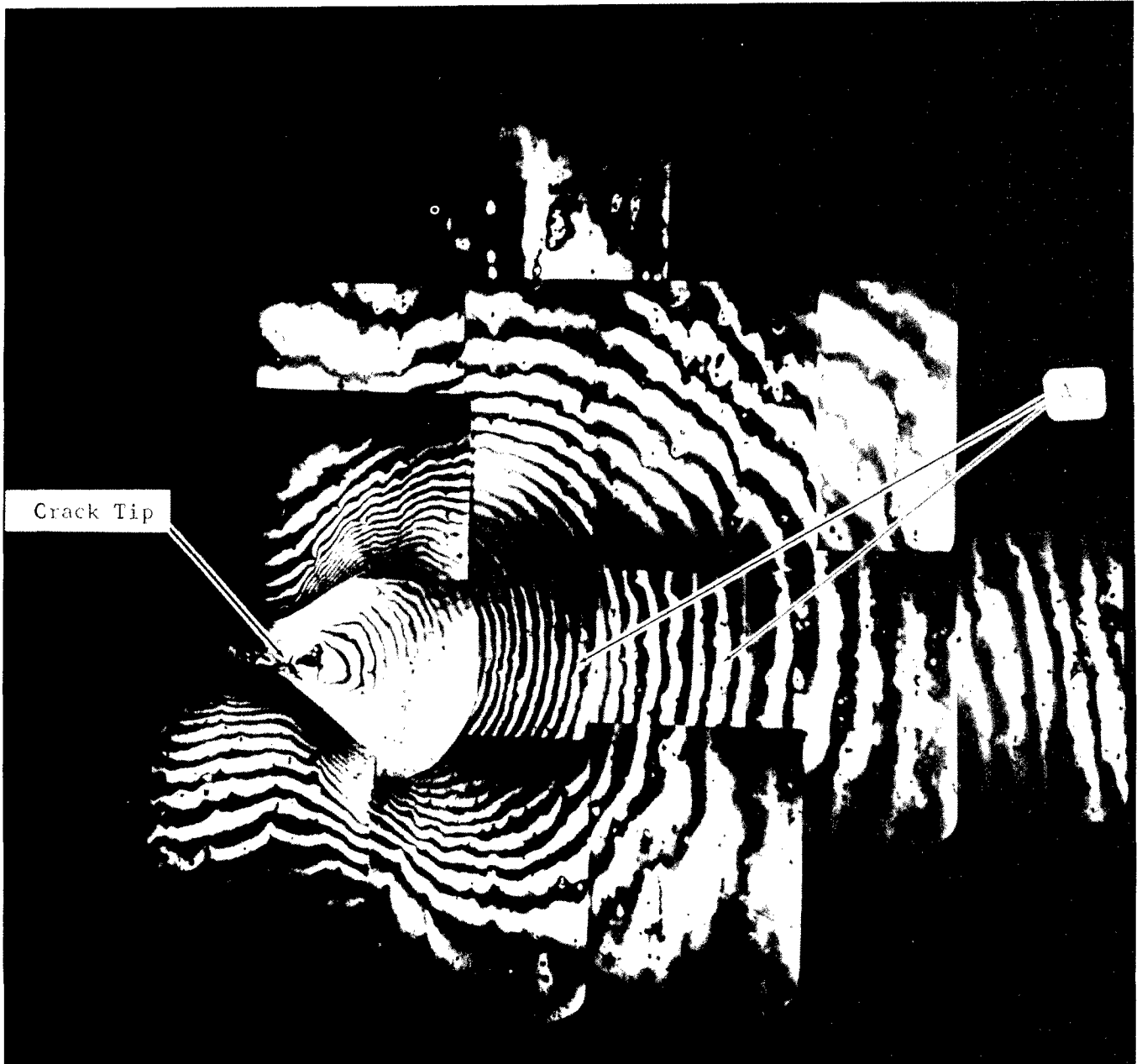


Figure 31. Interferometry Photograph of Cruciform Specimen No. 7-114, TC No. 99

2024-T7351, $a = 0.26$ inch
 $\sigma_x = 0, \sigma_y = 20$ ksi over-
loaded. Magnification: 70.3 X

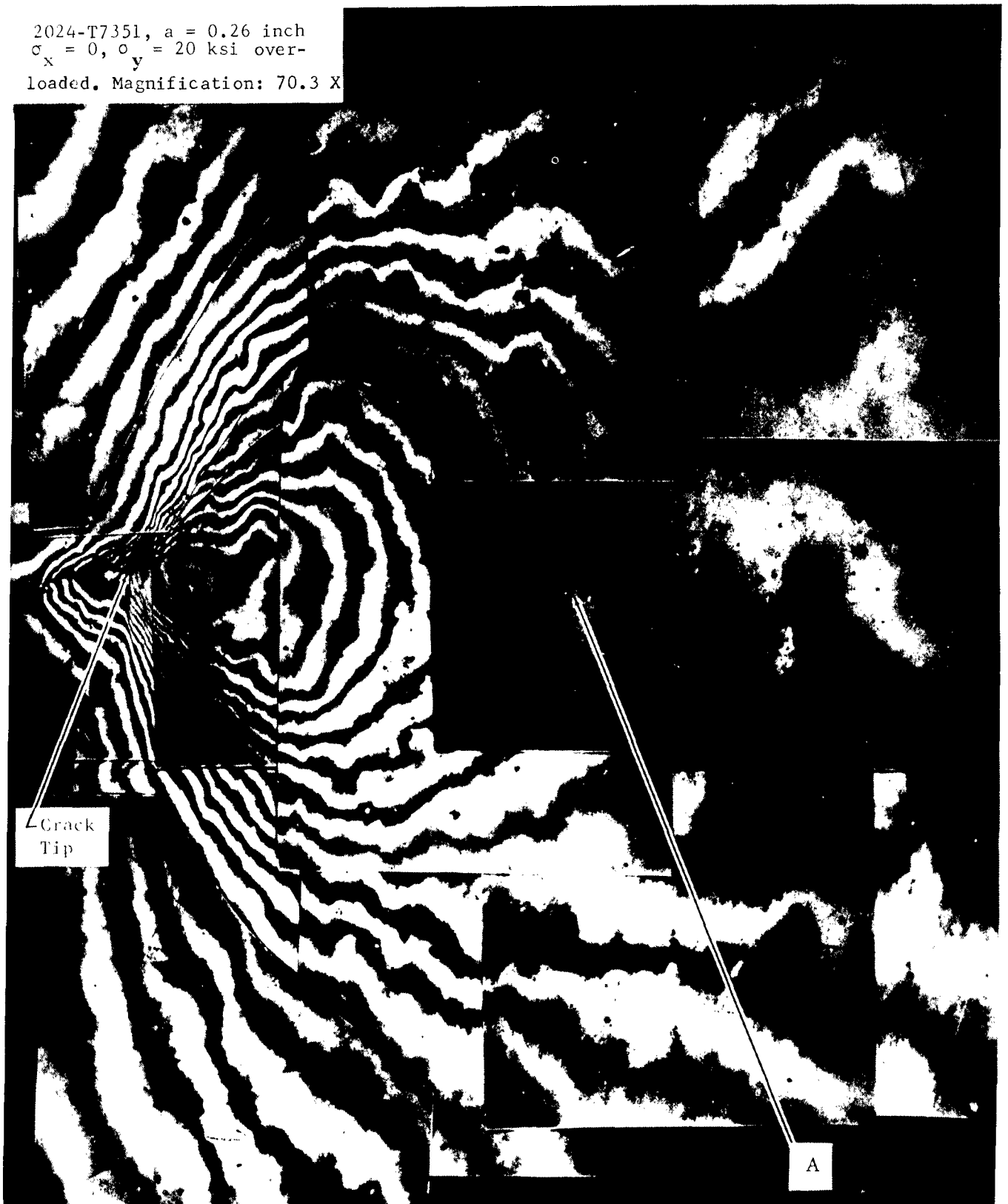


Figure 32. Interferometry Photograph of Cruciform Specimen No. 2-24, TC No. 101

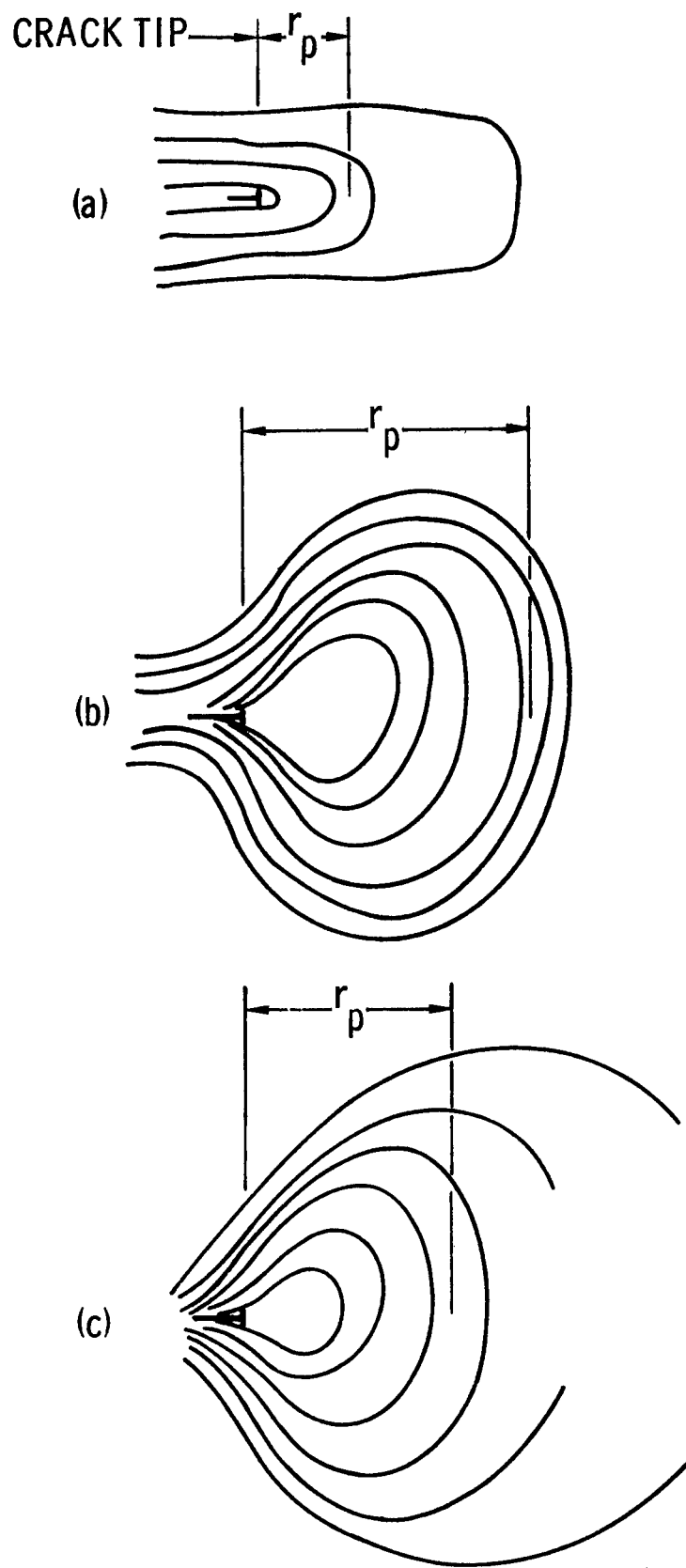


Figure 33. Schematic Illustration of Three Typical Interferometry Patterns

2. Excepting the one-to-one biaxial case, the unloaded plastic zone sizes for all other biaxial ratios are generally scattered around the Irwin/Rice plastic zone equations. However, when $(K_{\max}/F_{ty})^2 > 0.4$ the interferometry plastic zones are significantly and consistently, in all the cases, smaller than the Irwin/Rice plastic zones. This might be an indication of the limitation of the interferometry technique.
3. For the one-to-one biaxial ratio, both the loaded and unloaded plastic zones, at any $(K_{\max}/F_{ty})^2$ value, are smaller than the Irwin/Rice plastic zones.
4. The plastic zones at load are generally bigger than the unloaded plastic zones. However, the exact ratios between these two types of plastic zones cannot be determined at this time.

7.3 Backtracked Residual Plastic Zones

The existing crack growth retardation models generally assure that all the crack growth interaction activities will take place inside a load interaction zone (equivalent to a crack tip plastic zone) created by the high load. Once the crack has propagated through this interaction zone, a normal crack growth rate will be resumed. Therefore, it will be possible to trace the extent (the size) of such an interaction zone from actual crack growth rate data. Taking the crack growth rate data for the periodically loaded specimens (see Figures 110 to 118 in Section 9.5.1) for example, in part (a) of each figure, all da/dN data points including those affected by load interactions are plotted as a function of an apparent (uncorrected) K_{\max} level. Since each retarded da/dN data point associates with a crack length, according to the hypothesis stated earlier, it would be logical to assume that the size of the load interaction zone is equal to the difference between the crack length at overload and the effective crack length associated with the last traceable retarded da/dN data point.

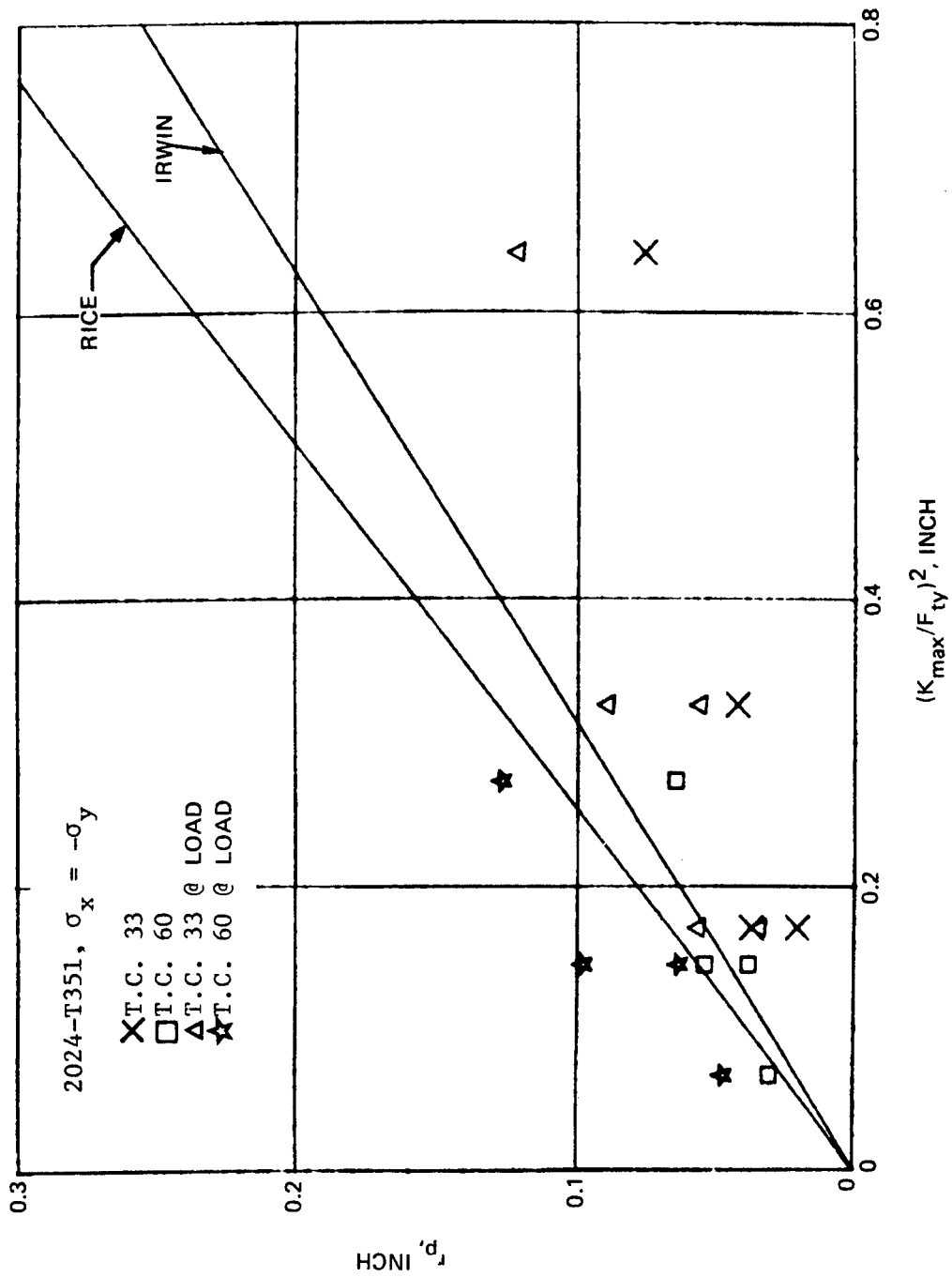


Figure 34. Interferometry Measurement of Crack Tip Plastic Zone Sizes

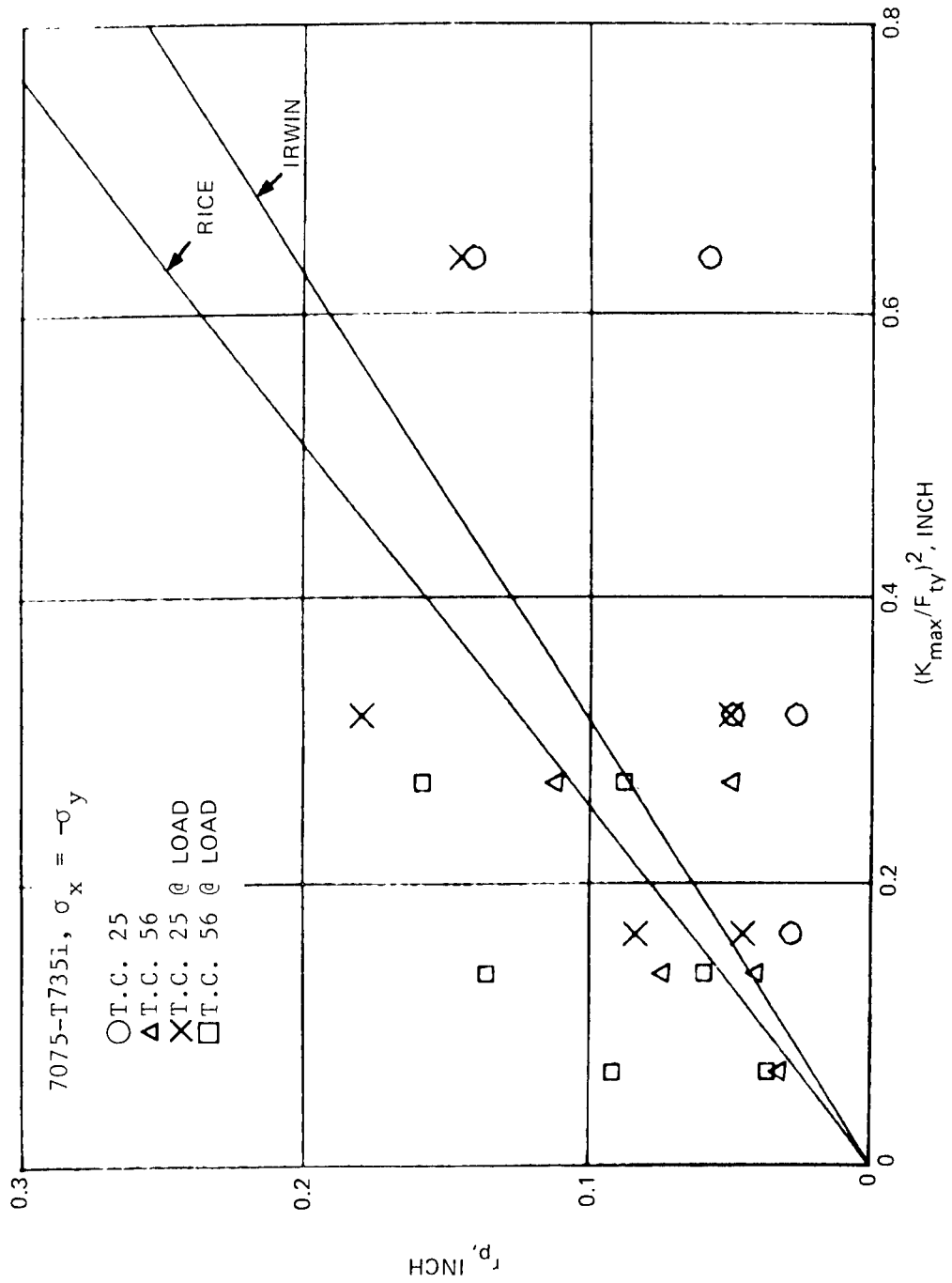


Figure 35. Interferometry Measurement of Crack Tip Plastic Zone Sizes

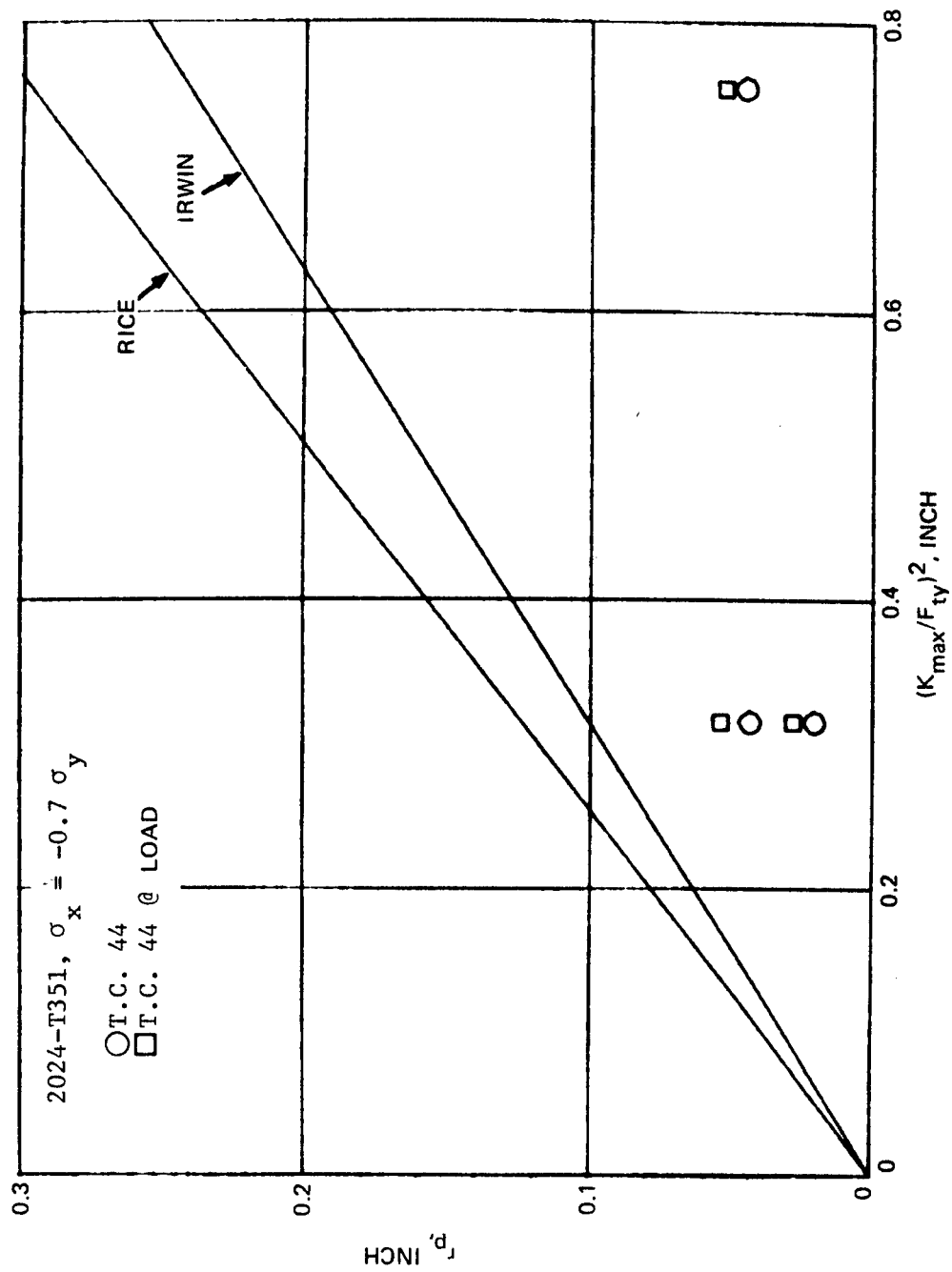


Figure 36. Interferometry Measurement of Crack Tip Plastic Zone Sizes

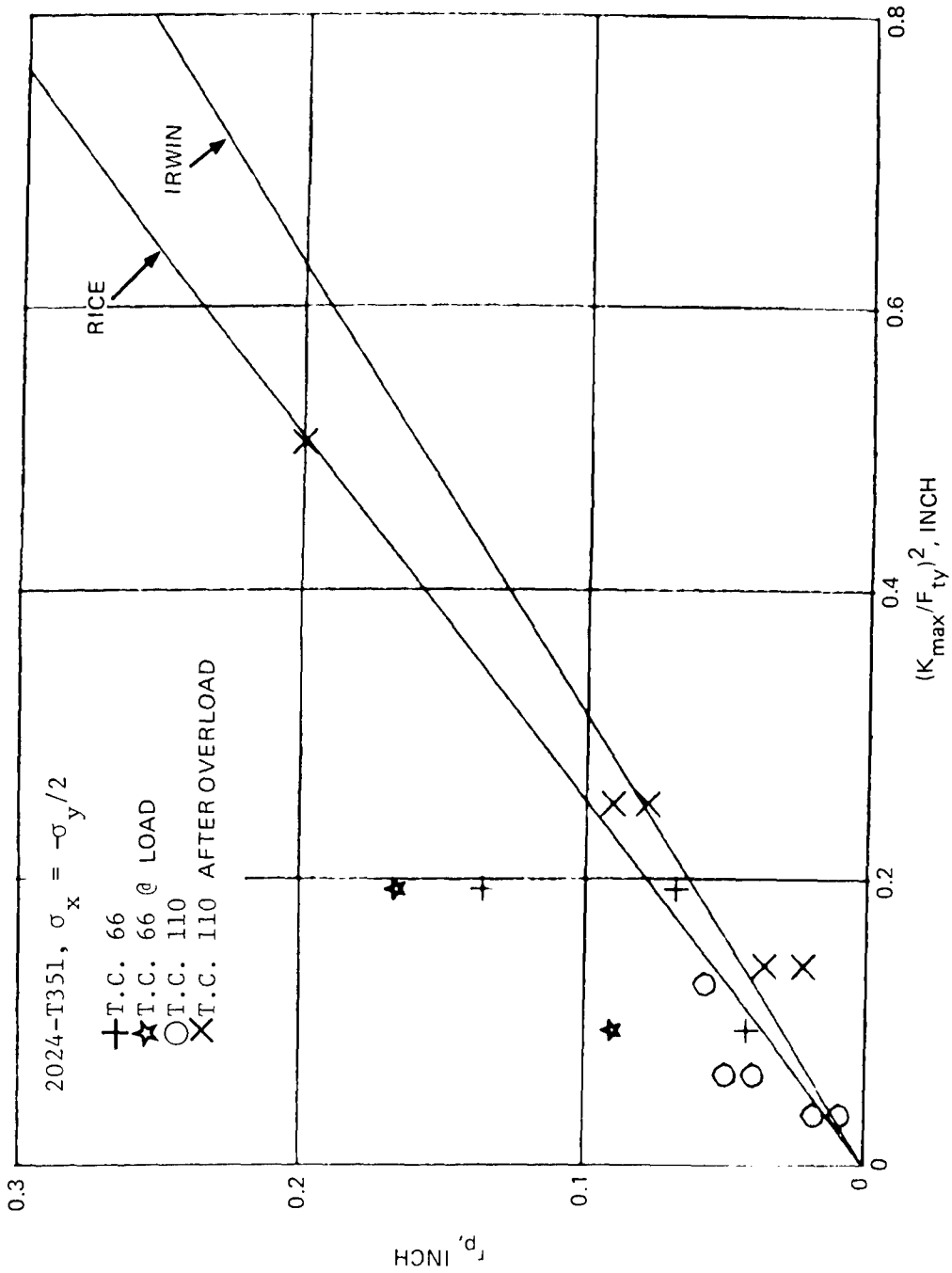


Figure 37. Interferometry Measurement of Crack Tip Plastic Zone Sizes

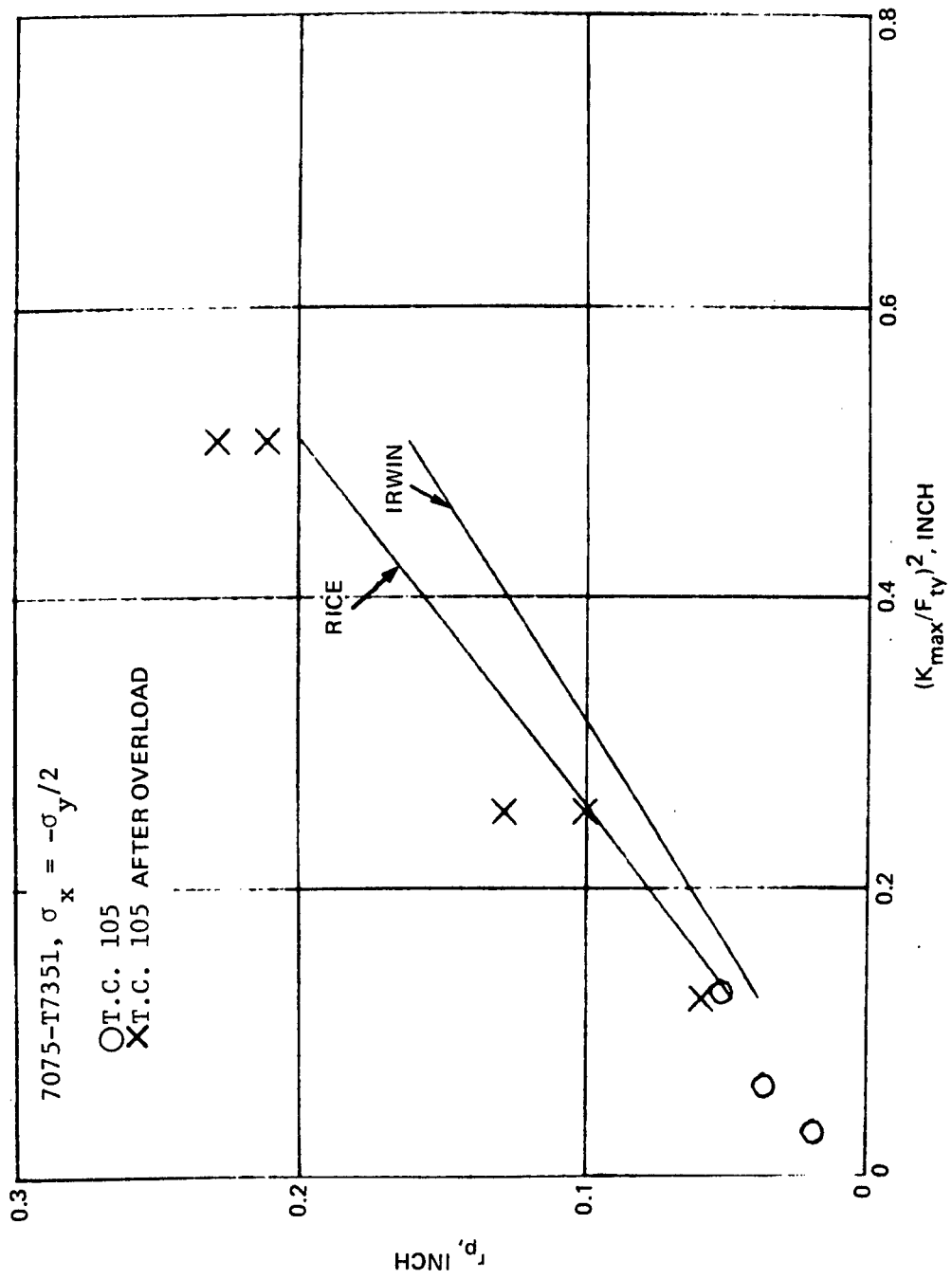


Figure 38. Interferometry Measurement of Crack Tip Plastic Zone Sizes

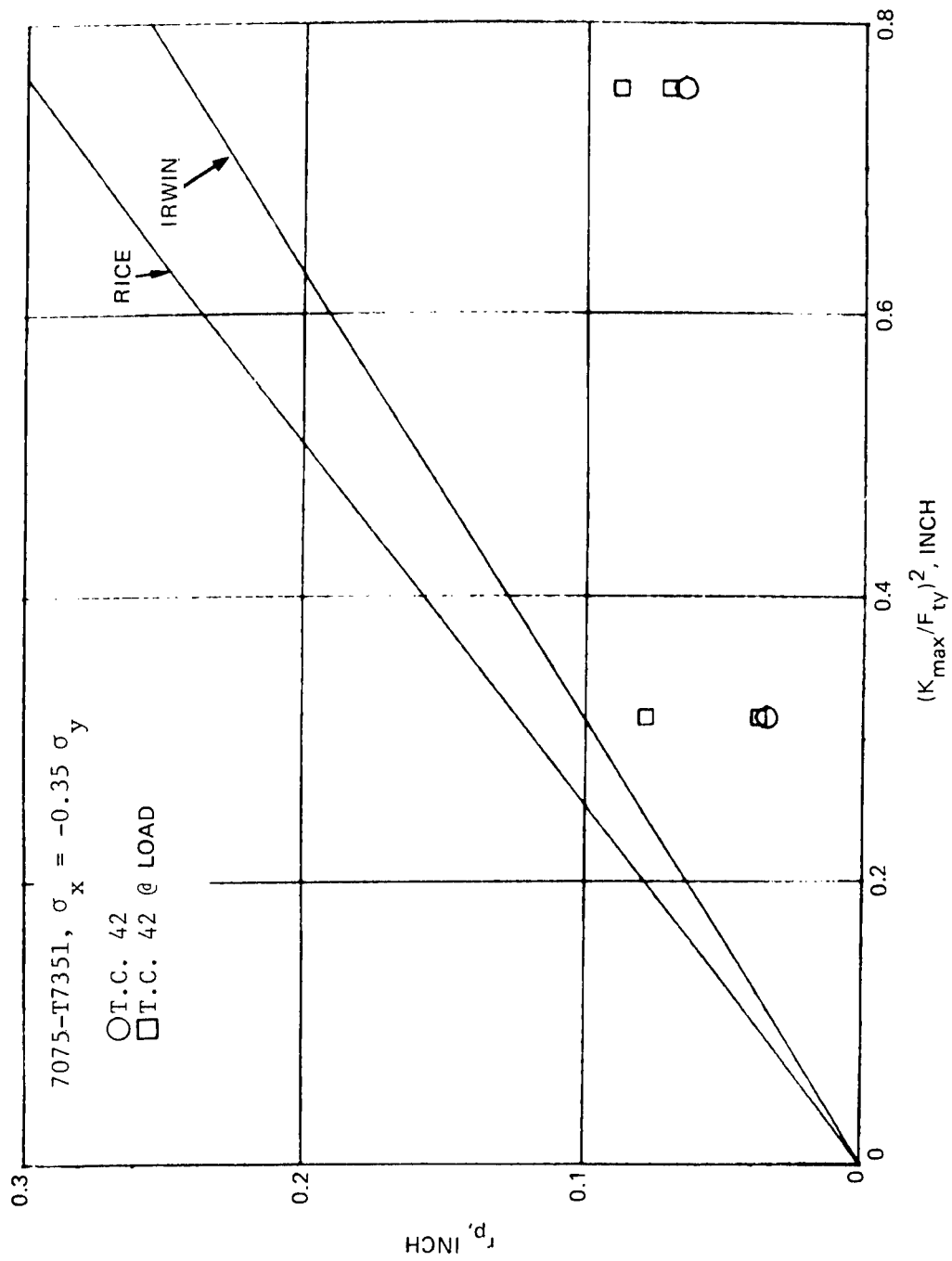


Figure 39. Interferometry Measurement of Crack Tip Plastic Zone Sizes

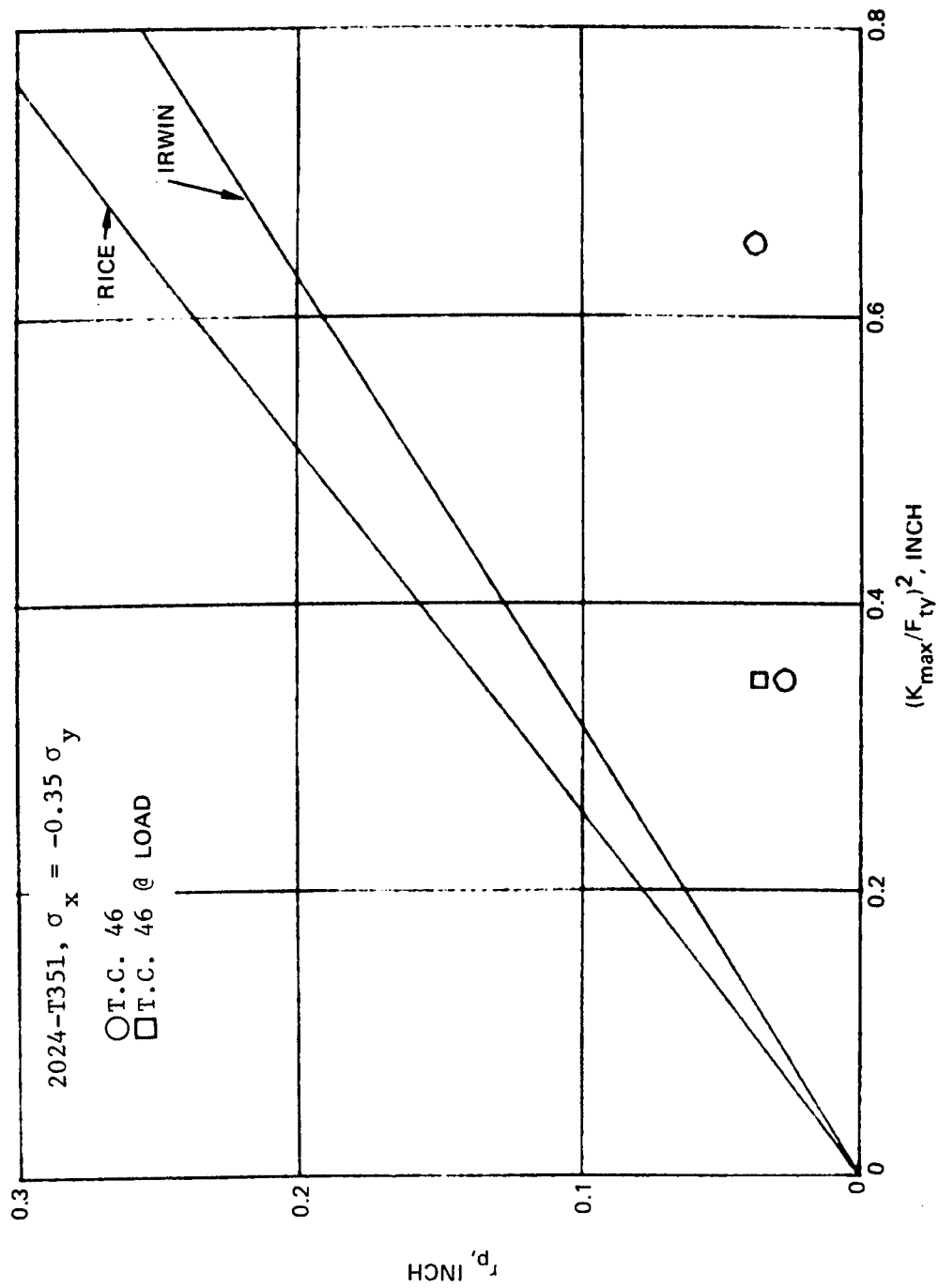


Figure 40. Interferometry Measurement of Crack Tip Plastic Zone Sizes

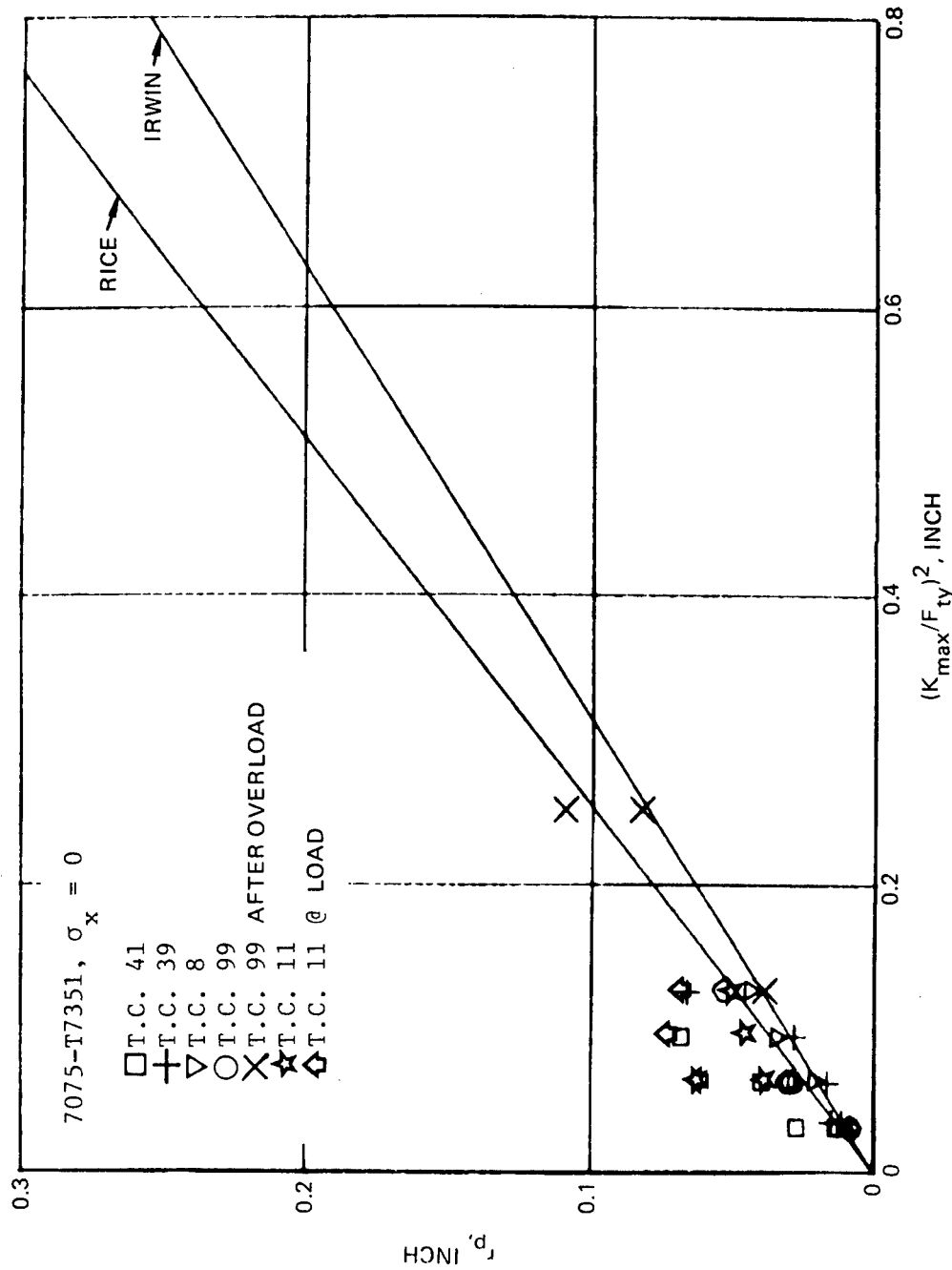


Figure 41. Interferometry Measurement of Crack Tip Plastic Zone Sizes

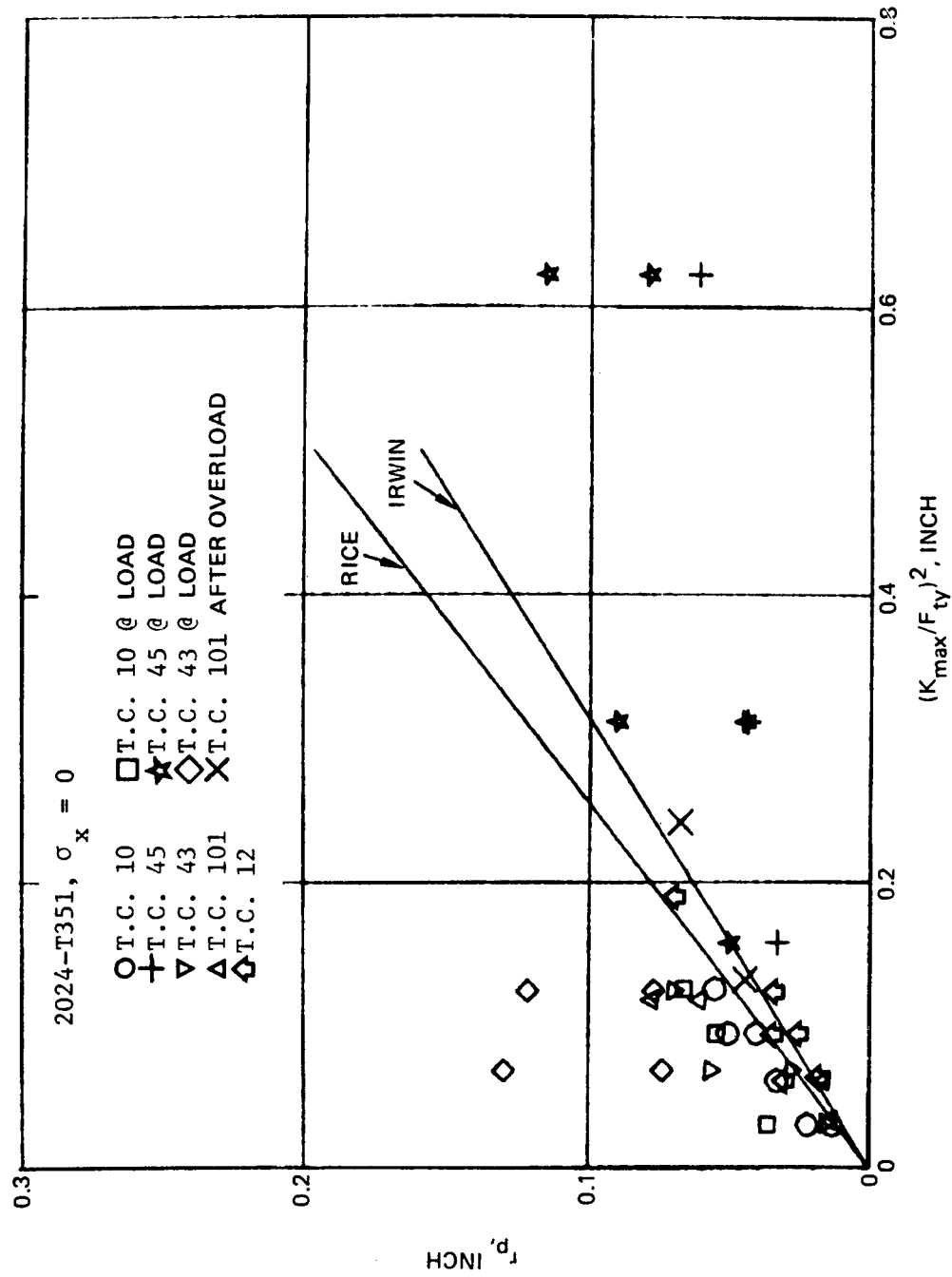


Figure 42. Interferometry Measurement of Crack Tip Plastic Zone Sizes

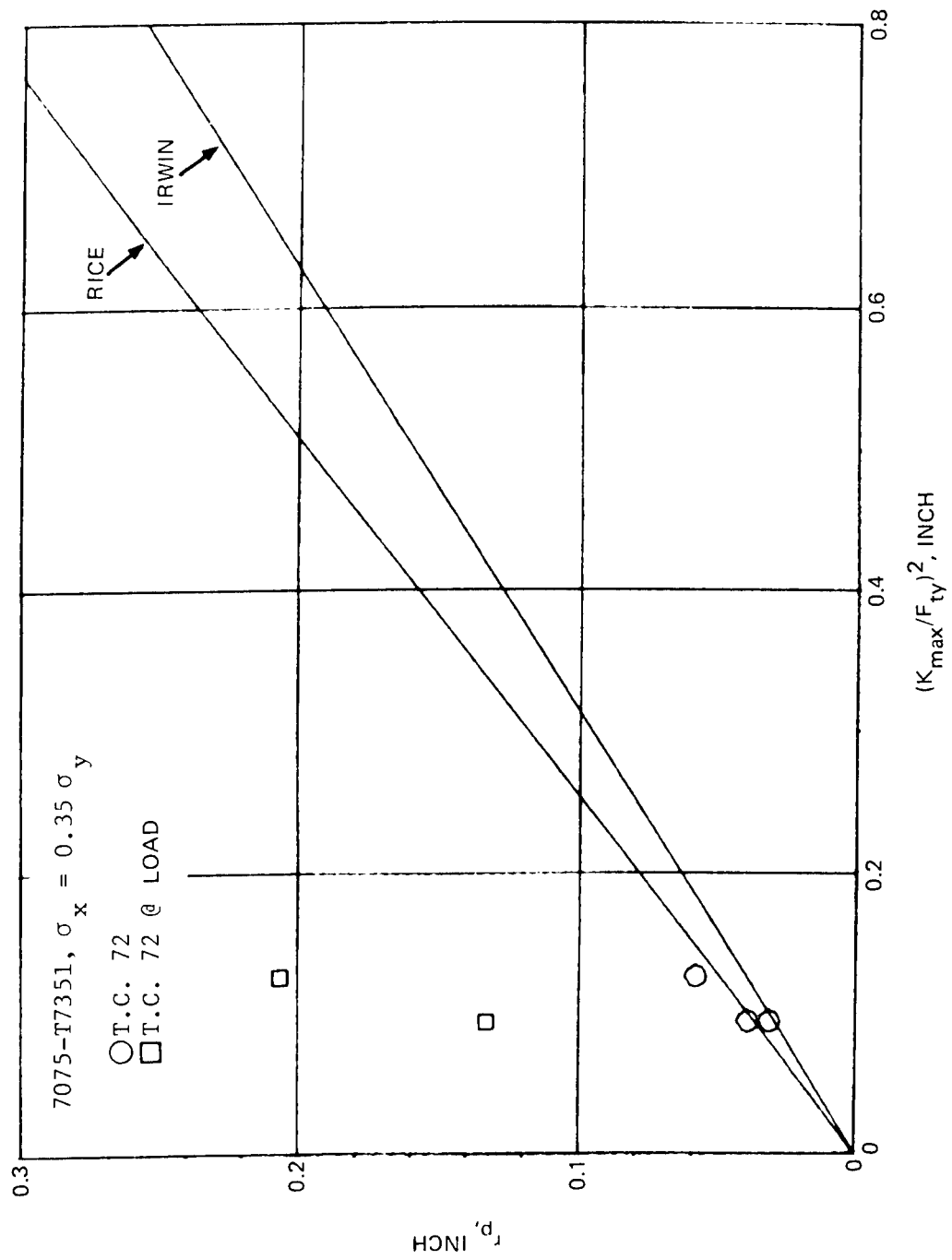


Figure 43. Interferometry Measurement of Crack Tip Plastic Zone Sizes

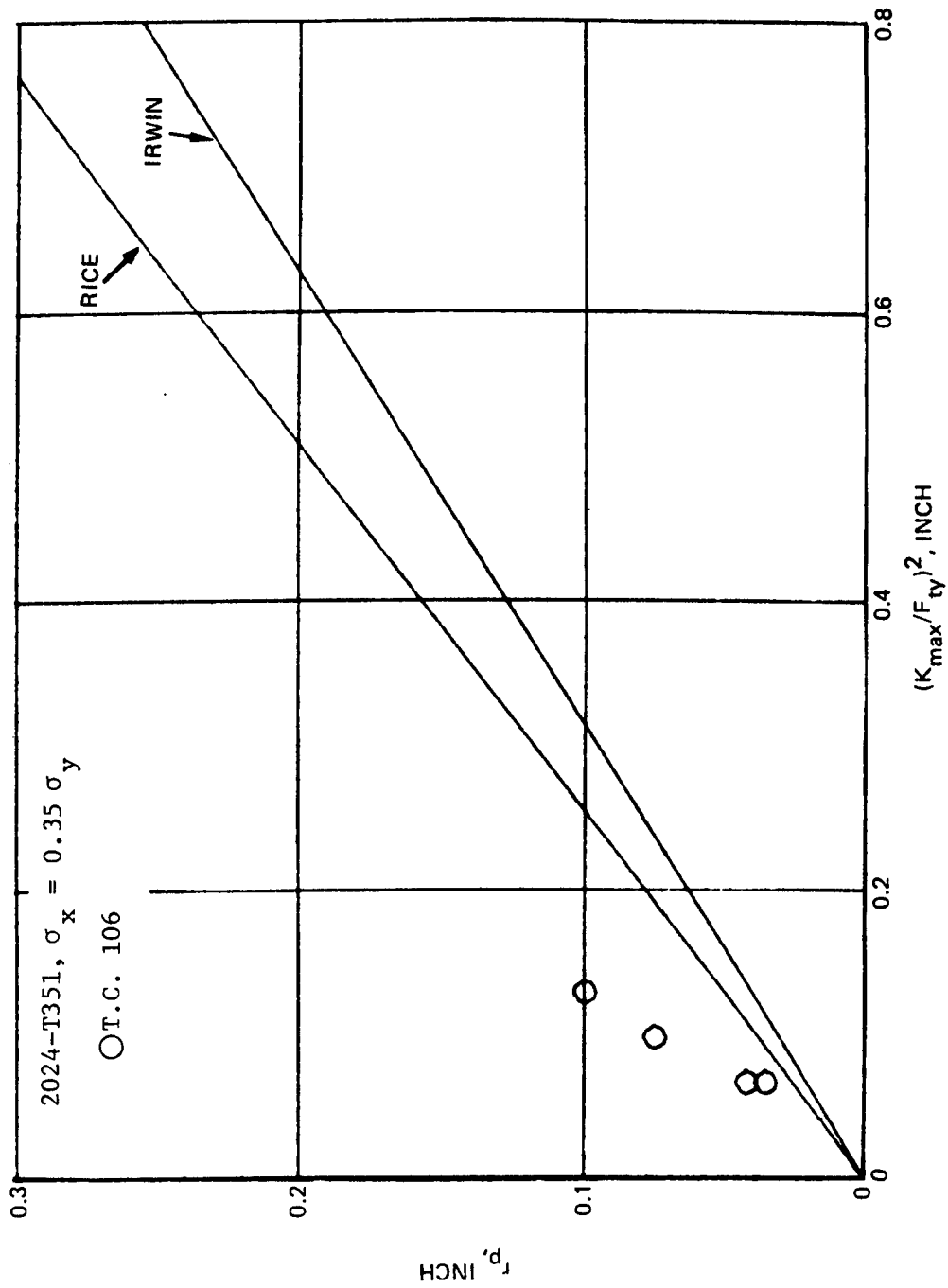


Figure 44. Interferometry Measurement of Crack Tip Plastic Zone Sizes

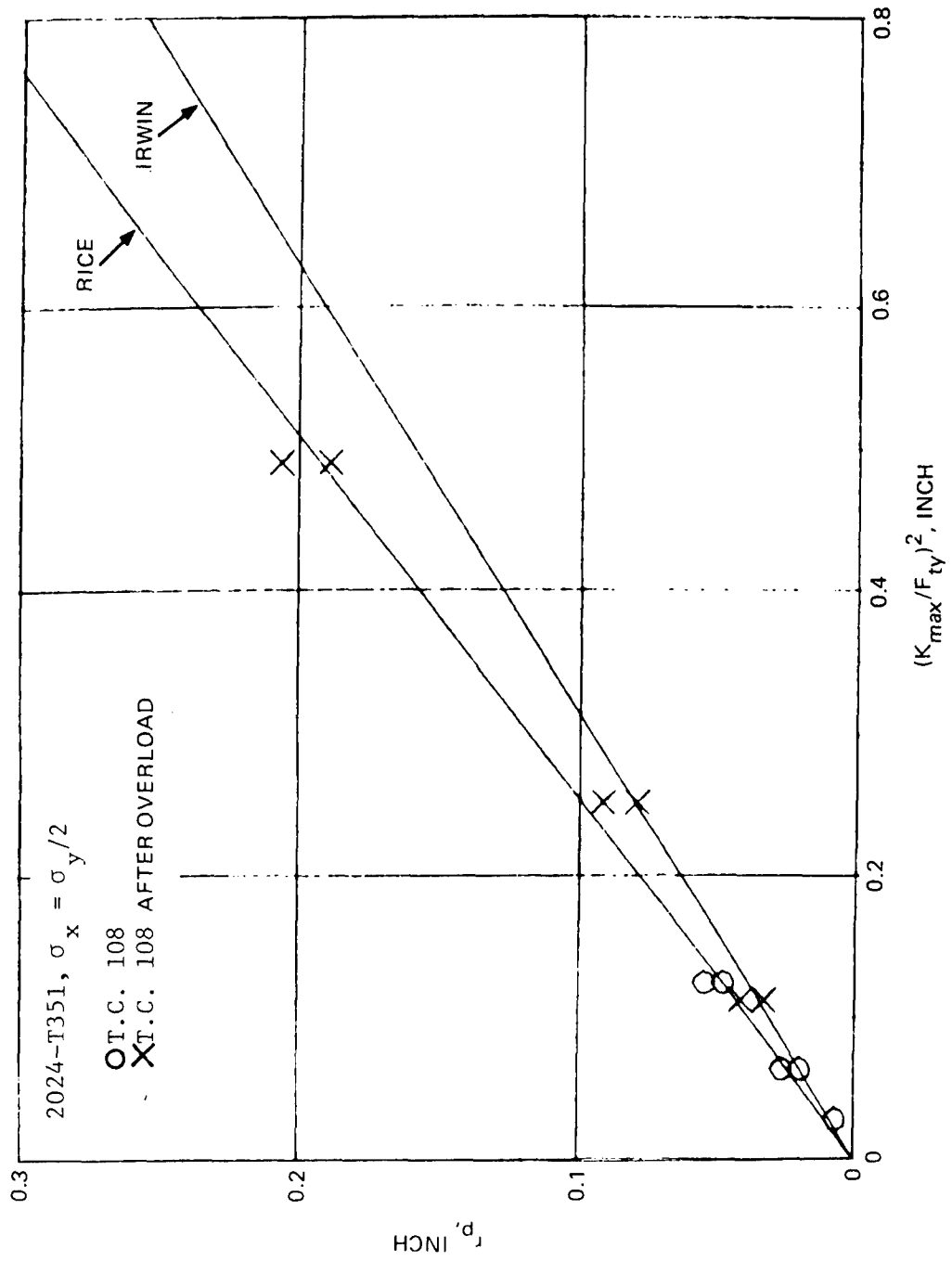


Figure 45. Interferometry Measurement of Crack Tip Plastic Zone Sizes

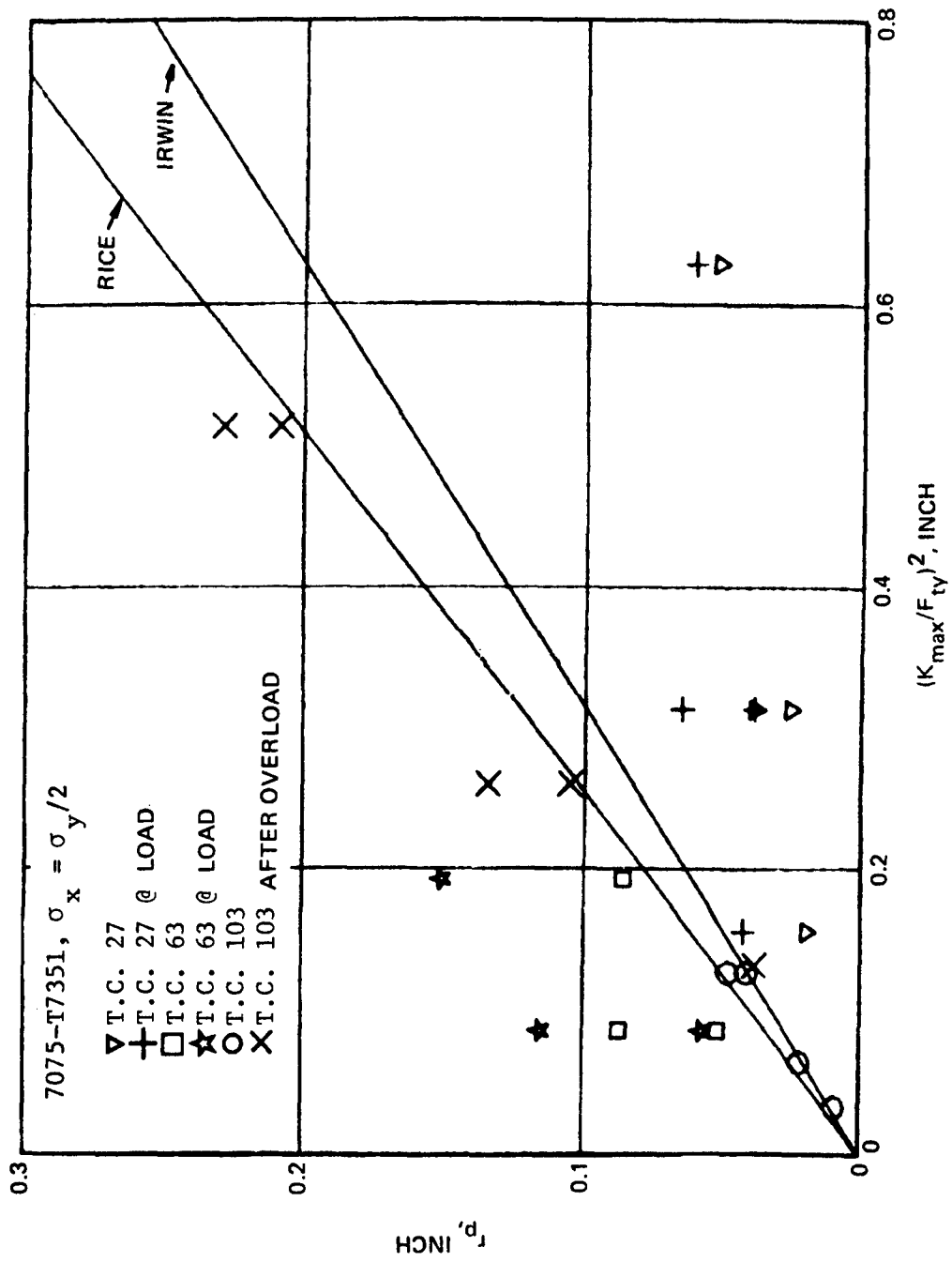


Figure 46. Interferometry Measurement of Crack Tip Plastic Zone Sizes

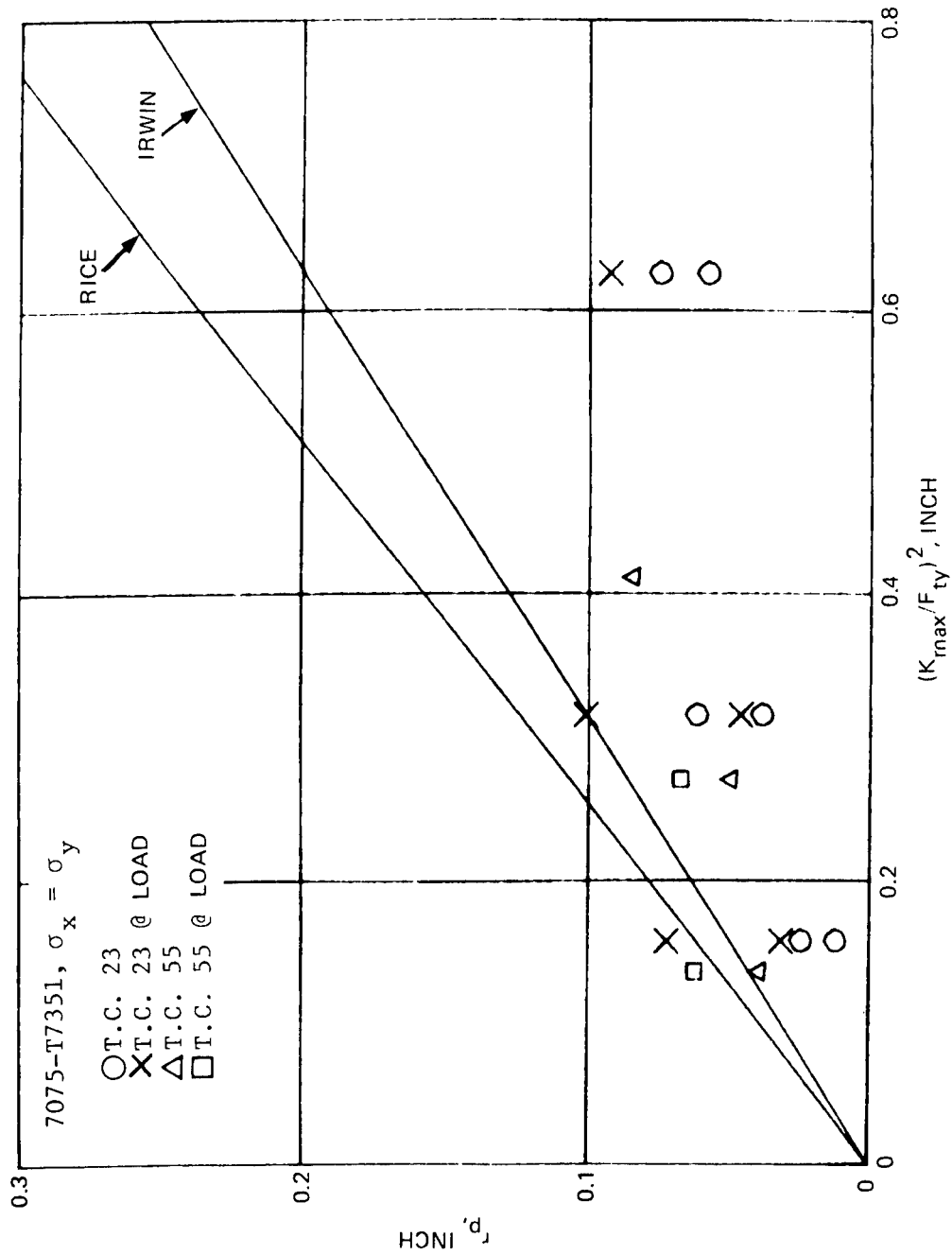


Figure 47. Interferometry Measurement of Crack Tip Plastic Zone Sizes

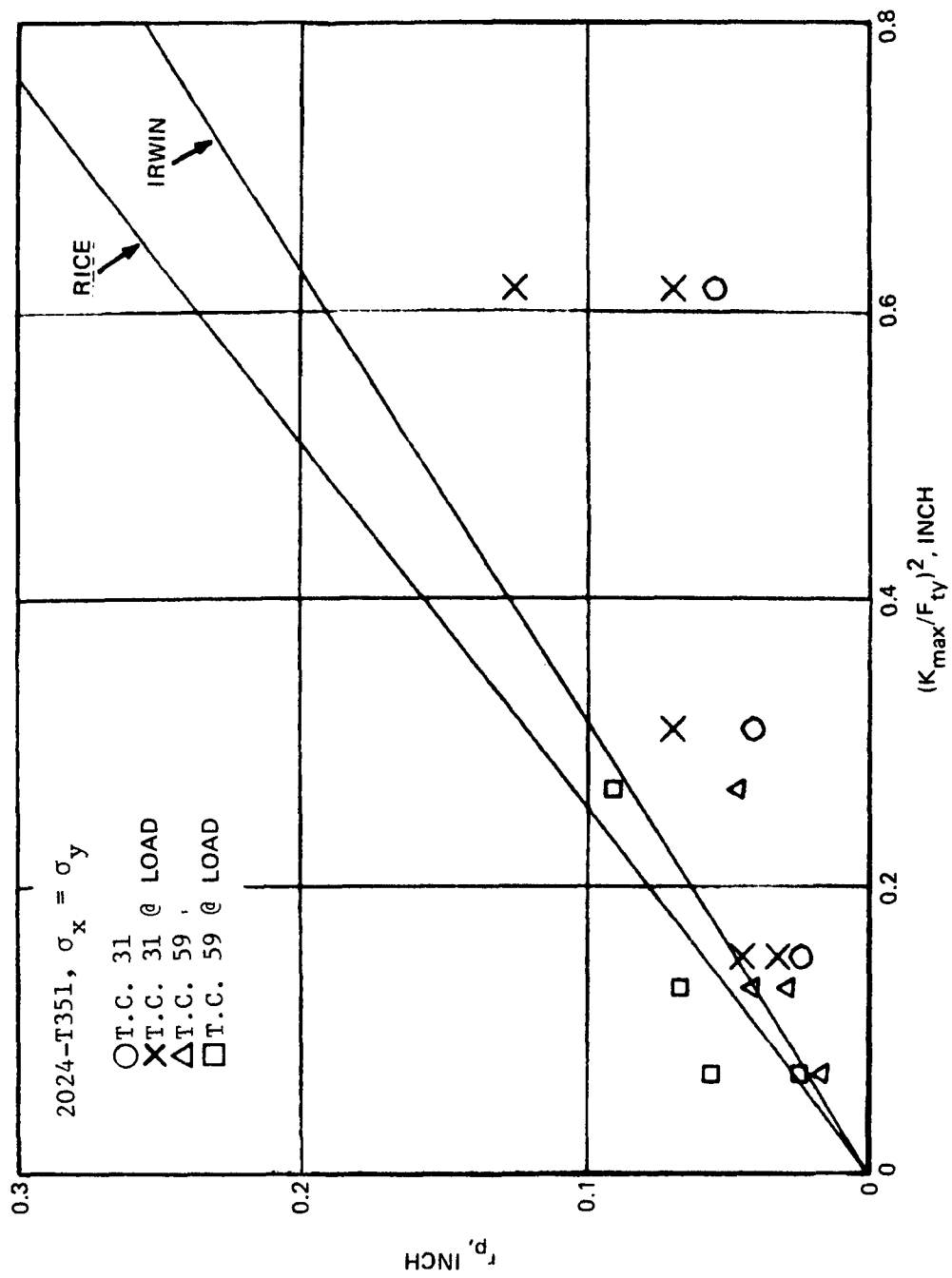


Figure 48. Interferometry Measurement of Crack Tip Plastic Zone Sizes

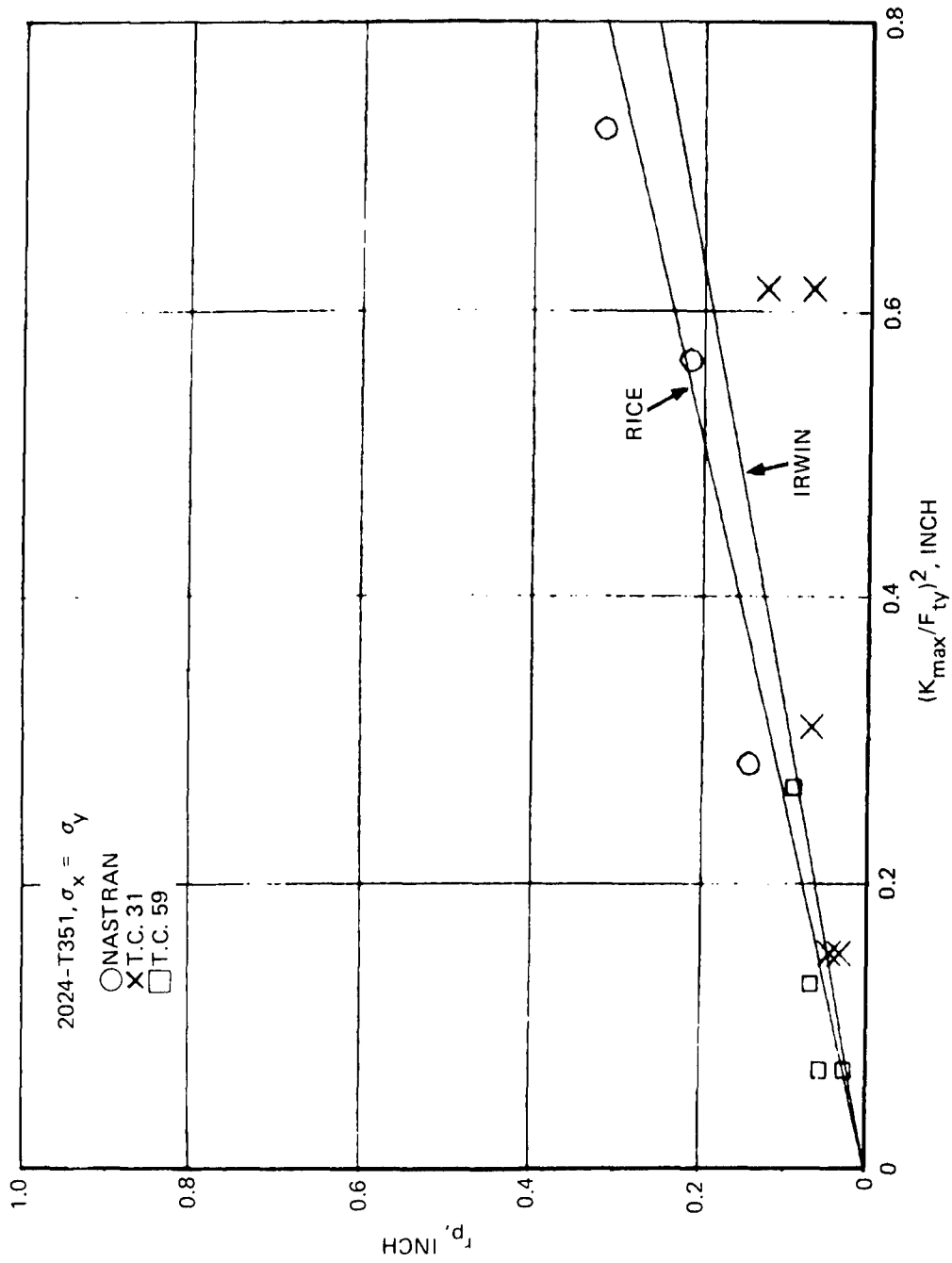


Figure 49. Comparison of Interferometry and NASTRAN Crack Tip Plastic Zone Sizes

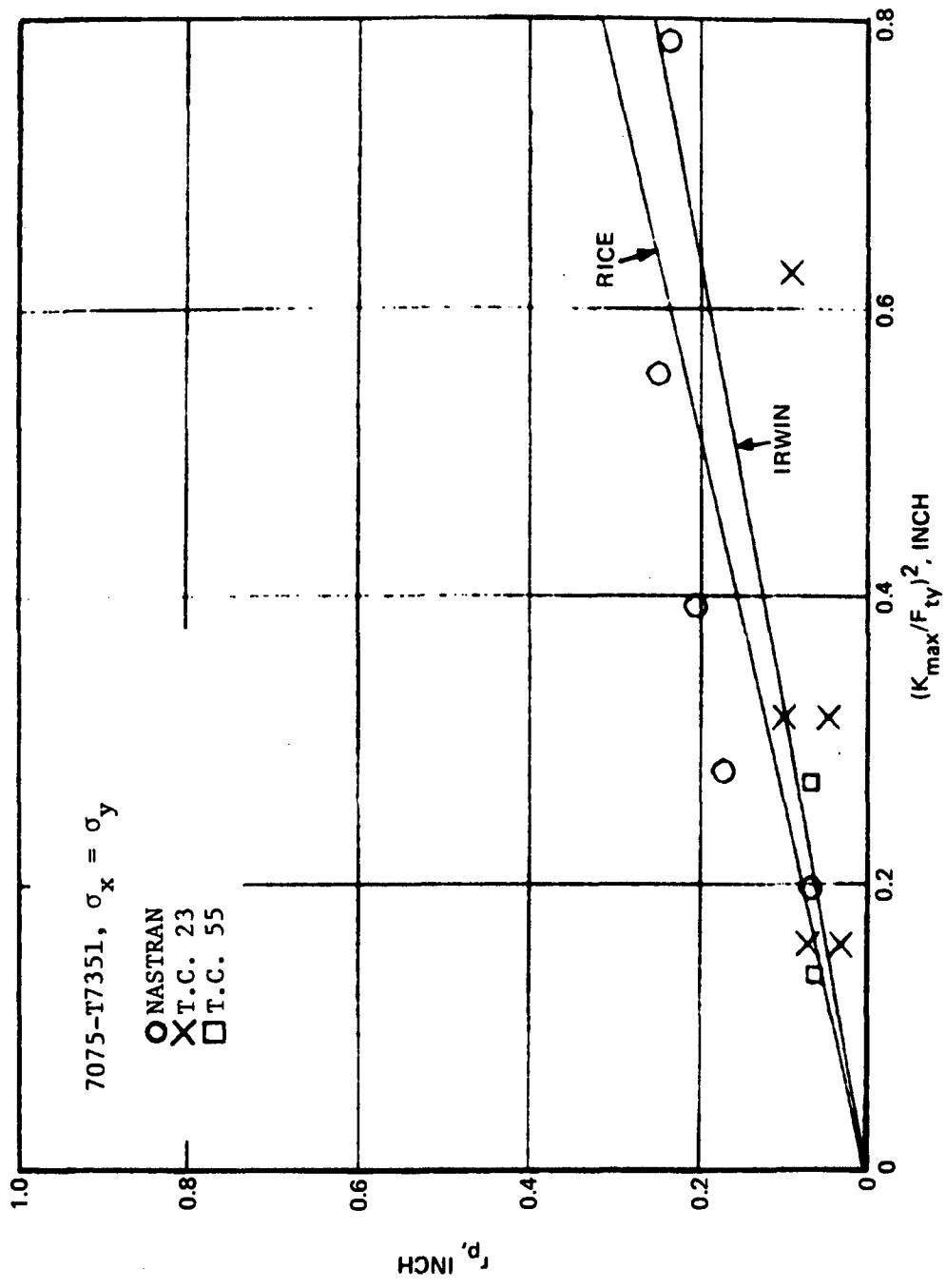


Figure 50. Comparison of Interferometry and NASTRAN Crack Tip Plastic Zone Sizes

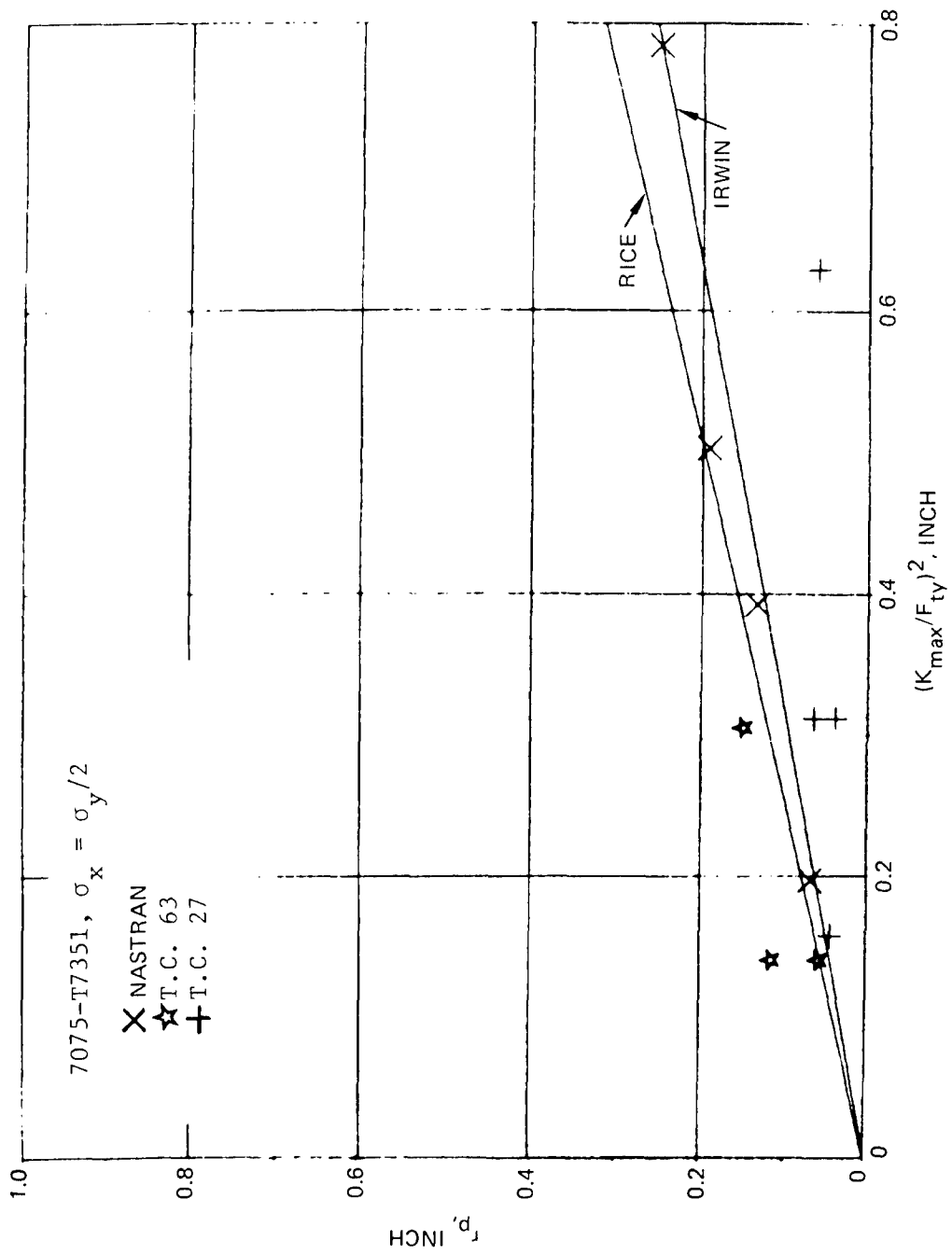


Figure 51. Comparison of Interferometry and NASTRAN Crack Tip Plastic Zone Sizes

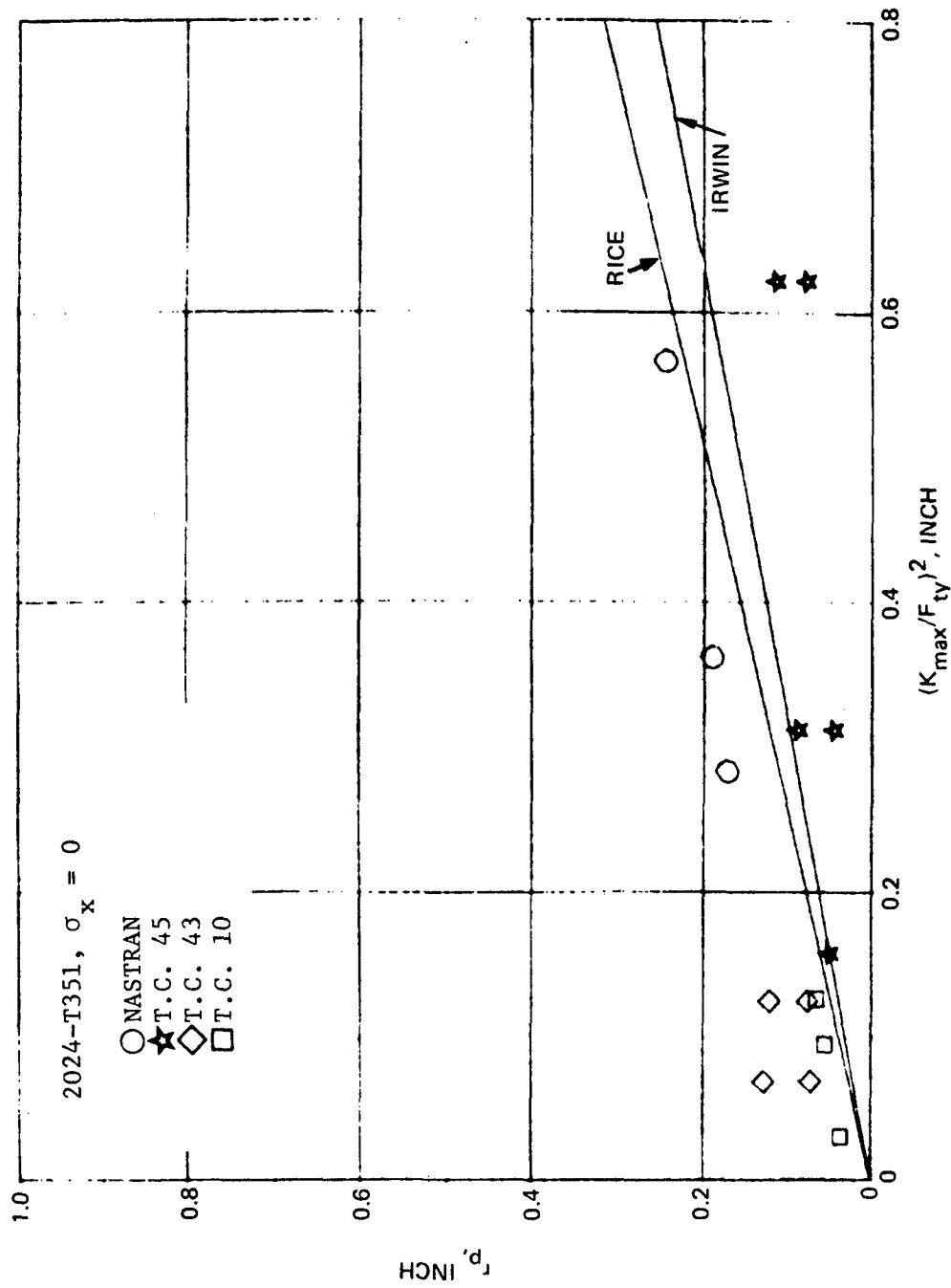


Figure 52. Comparison of Interferometry and NASTRAN Crack Tip Plastic Zone Sizes

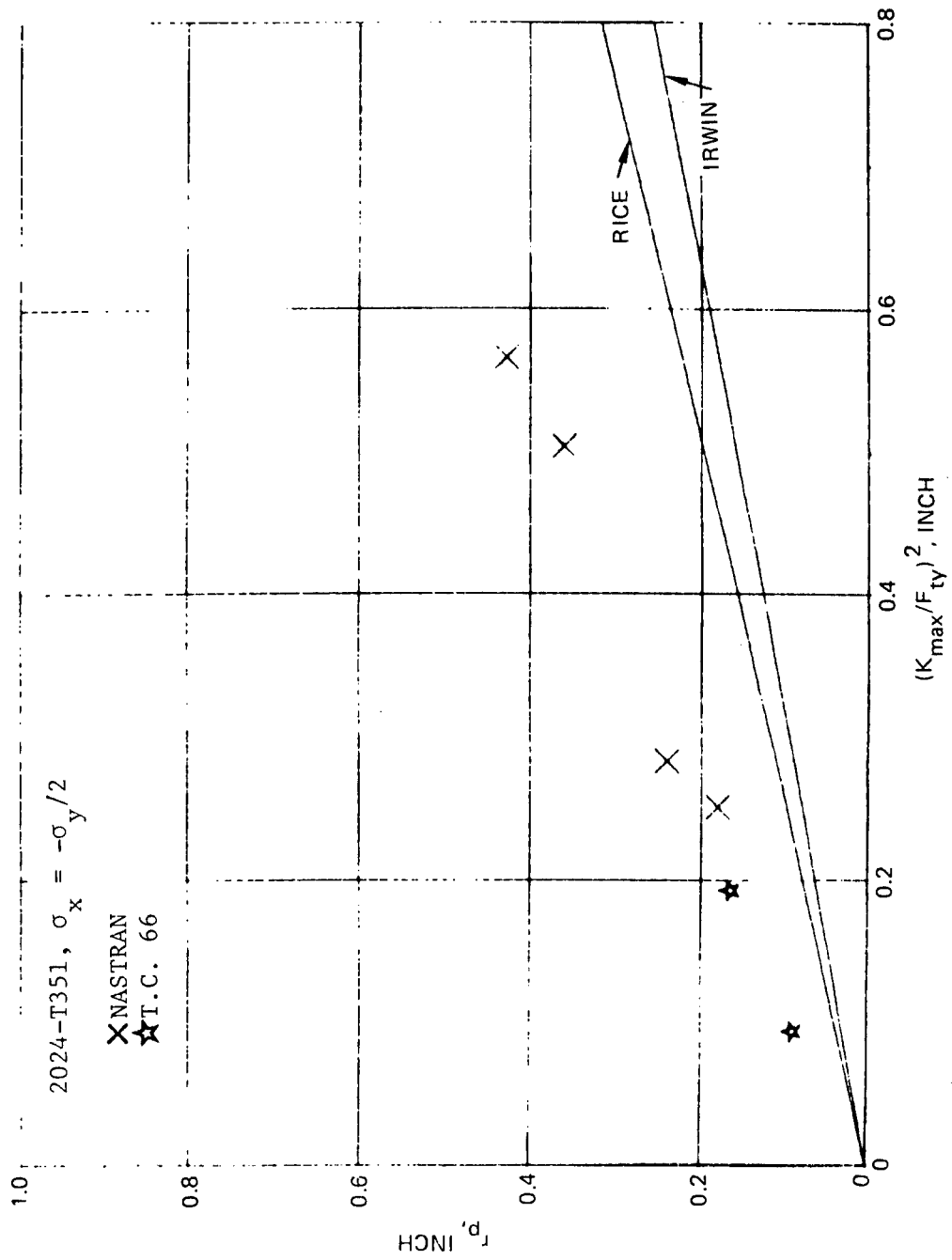


Figure 53. Comparison of Interferometry and NASTRAN Crack Tip Plastic Zone Sizes

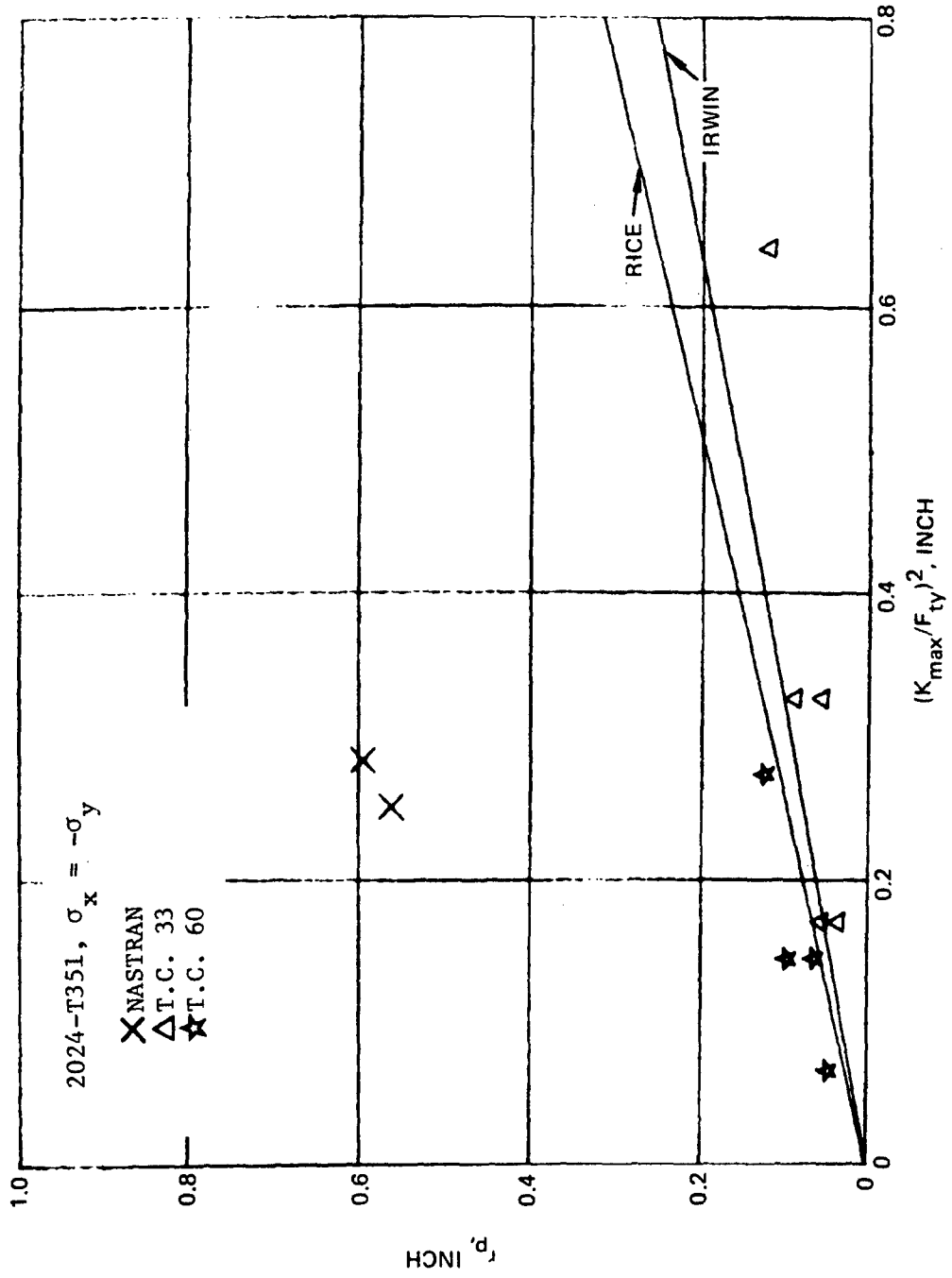


Figure 54. Comparison of Interferometry and NASTRAN Crack Tip Plastic Zone Sizes

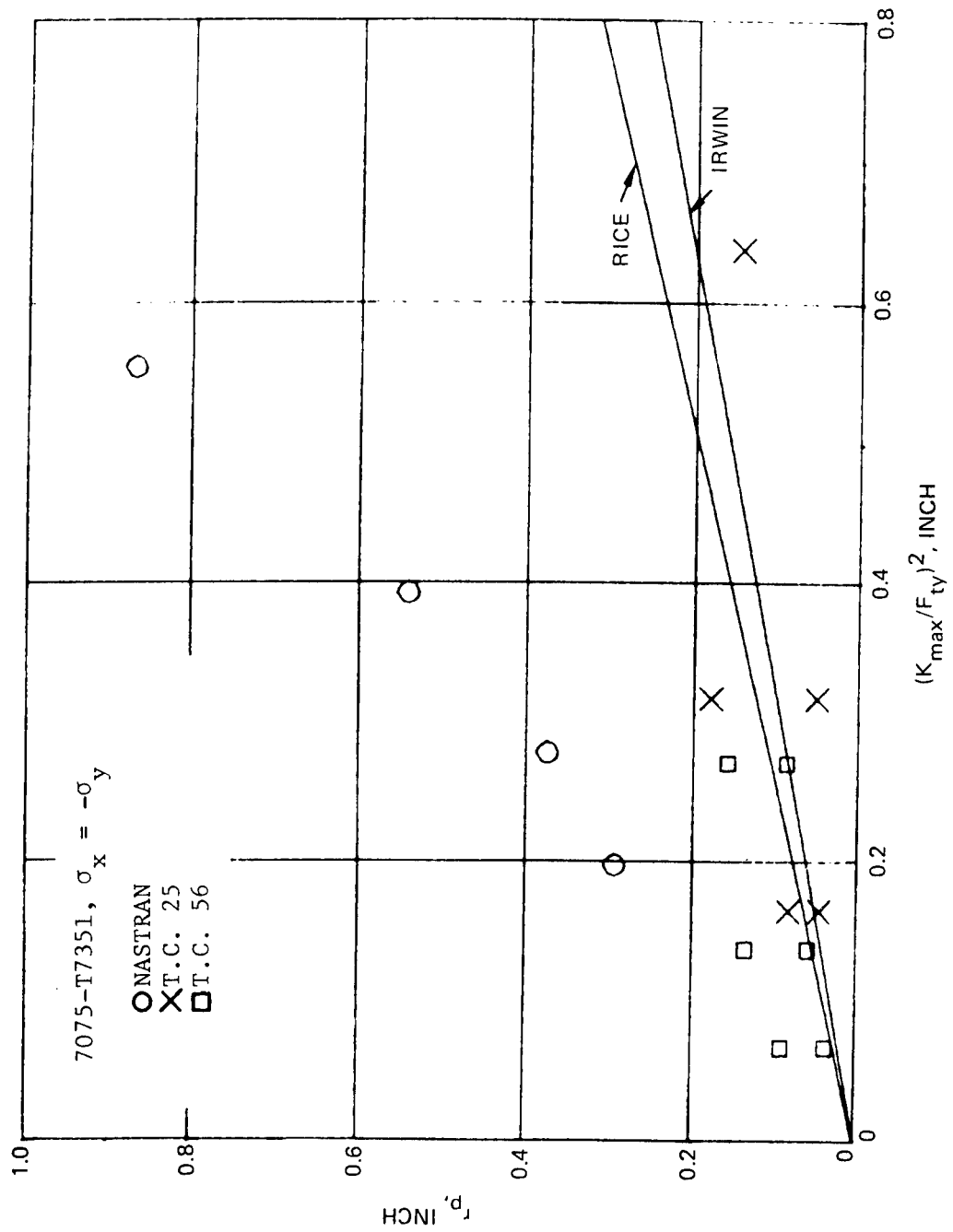


Figure 55. Comparison of Interferometry and NASTRAN Crack Tip Plastic Zone Sizes

The backtracked plastic zone sizes and the residual plastic zones (determined by interferometry measurement after each overload) are plotted in Figures 56 to 61 for comparison. Note in these figures, the K_{\max} is computed using the overload stress and the crack length at overload. Since these r_p values were obtained from the interpretation of interferometry fringe patterns or backtracking of da/dN values, when uncertainty arose (note the uncertainties came from the appearance of the fringe pattern or the scatter of the material da/dN data), a minimum r_p value and a possible r_p value were determined and both values are plotted in the figure. Also due to the fact that in some cases the crack had grown longer on one side and shorter on the other side, the plastic zone sizes for the left crack tip and the right crack tip were treated as two independent data points. The interferometry photographs were always taken from the right side of the crack.

Examination of Figures 56 to 61 reveals the following:

1. At lower K levels, both the interferometry residual plastic zones and the backtracked residual plastic zones are close to the sizes computed by Equations 16 and 17, for monotonic loading condition.
2. At higher K levels, the backtracked residual plastic zones are significantly larger than those calculated using the equations of Irwin and Rice.
3. At higher K levels the backtracked residual plastic zones for the 2024-T351 specimens seem to be larger than those for the 7075-T7351 specimens.
4. The effect of biaxial loading ratios on residual plastic zone sizes cannot be identified (note the biaxial ratios for these specimens were 0, ± 0.5). However, it seems that the r_p values for the -0.5 biaxial ratio cases (in either one of the two aluminum alloys) could possibly be larger than those in the other two biaxial conditions; i.e., it might be an indication of a biaxial loading effect.

5. As indicated by the backtracked plastic zones, the residual plastic zones increased rapidly when the plasticity density parameters, $(IK_{\max}/F_{ty})^2$, exceed 0.4; this is a phenomenon much similar to those previously observed in the "loaded" plastic zones (determined by NASTRAN). At this moment, it is not certain whether these nonlinearities were indications of a real physical phenomenon or just special cases that had been associated with the cruciform specimen configuration.

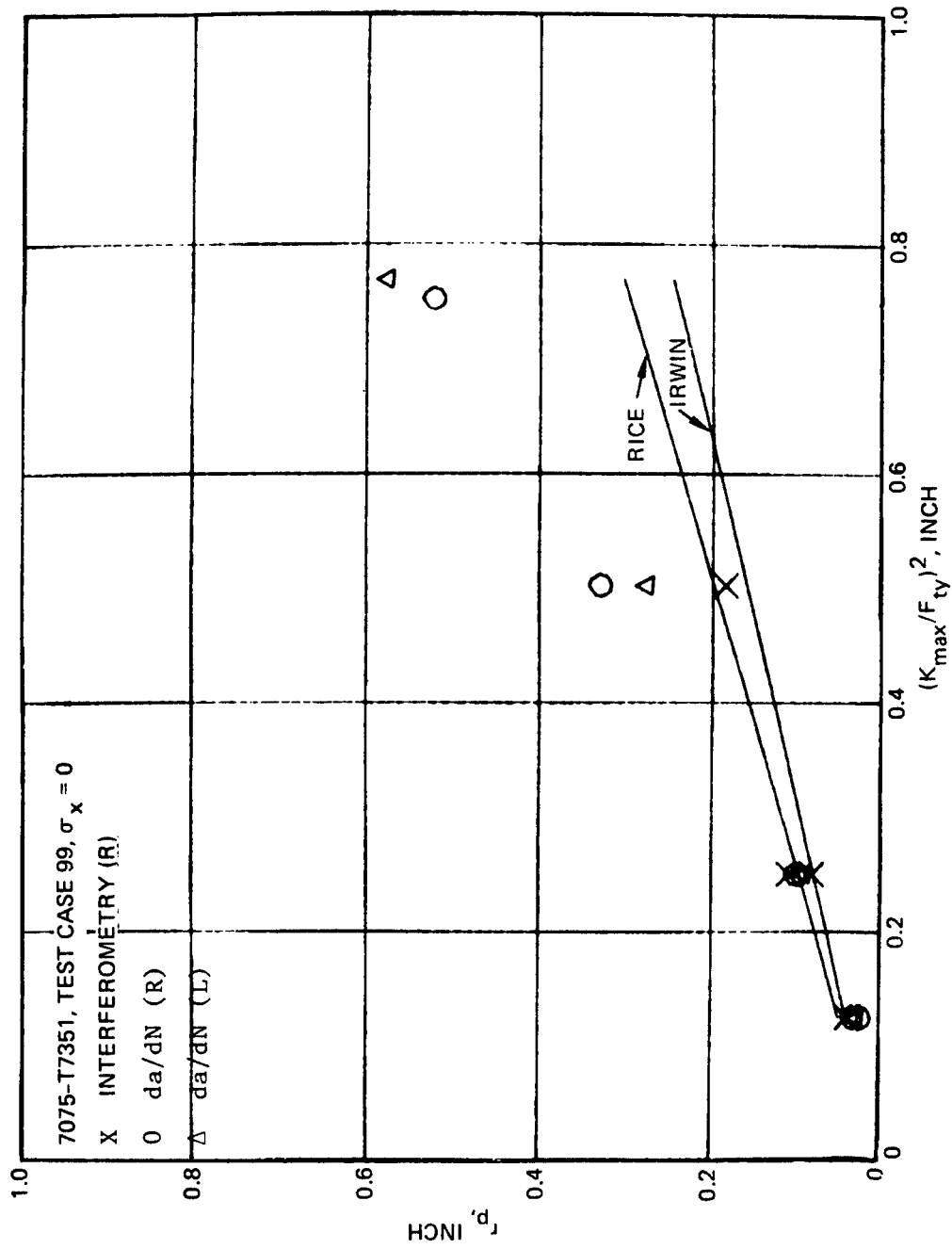


Figure 56. Experimentally Determined Residual Crack Tip Plastic Zone

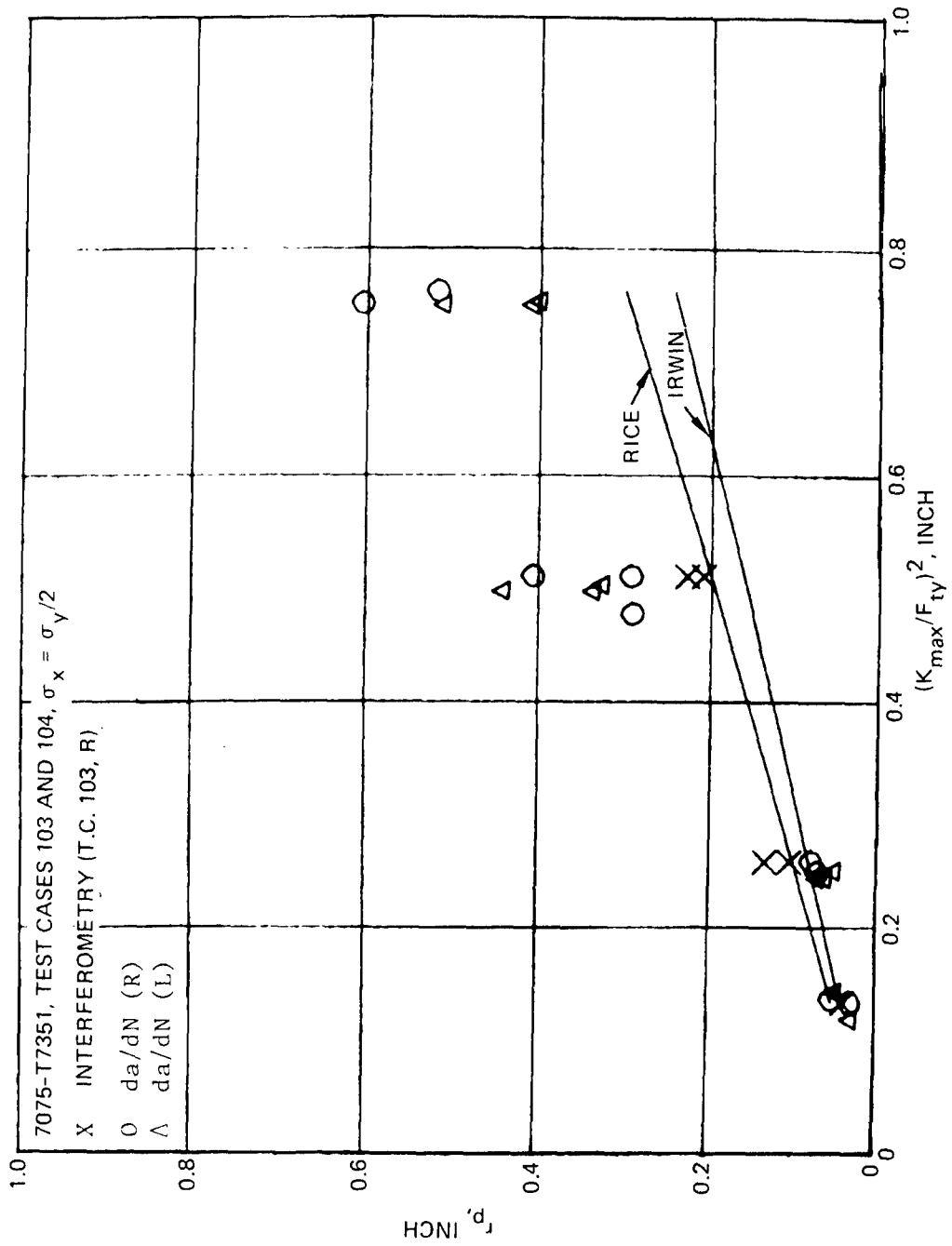


Figure 57. Experimentally Determined Residual Crack Tip Plastic Zone

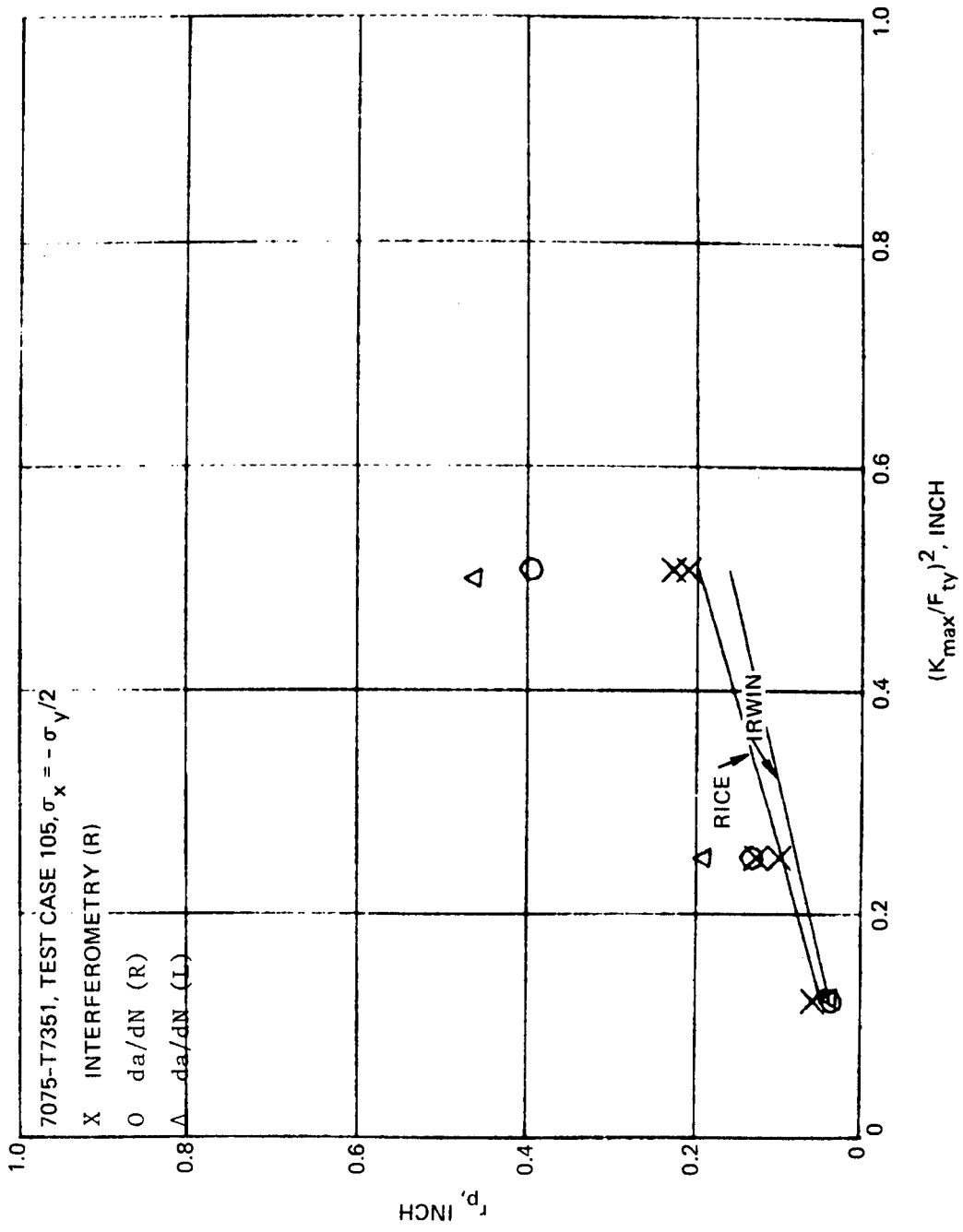


Figure 58. Experimentally Determined Residual Crack Tip Plastic Zone

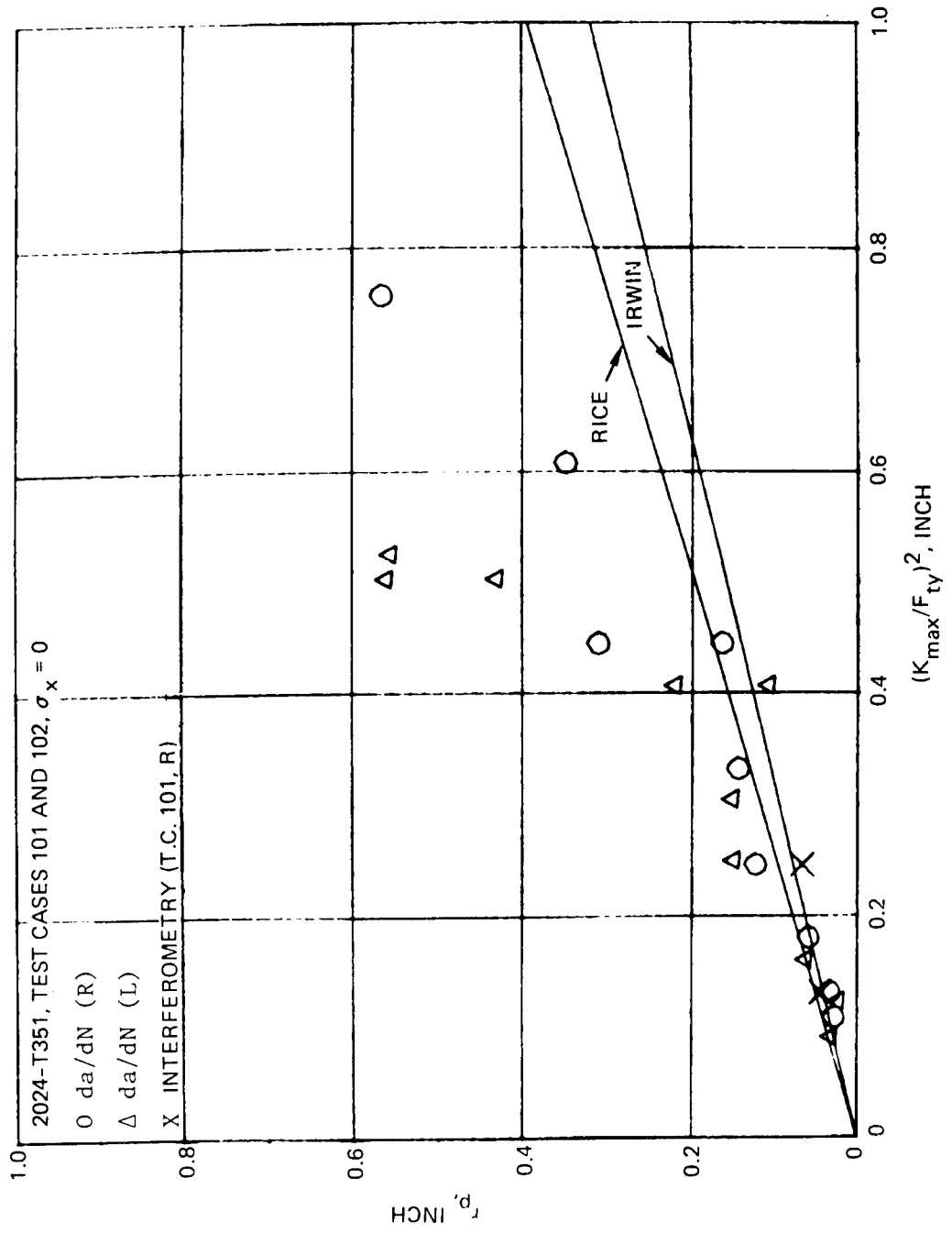


Figure 59. Experimentally Determined Residual Crack Tip Plastic Zone

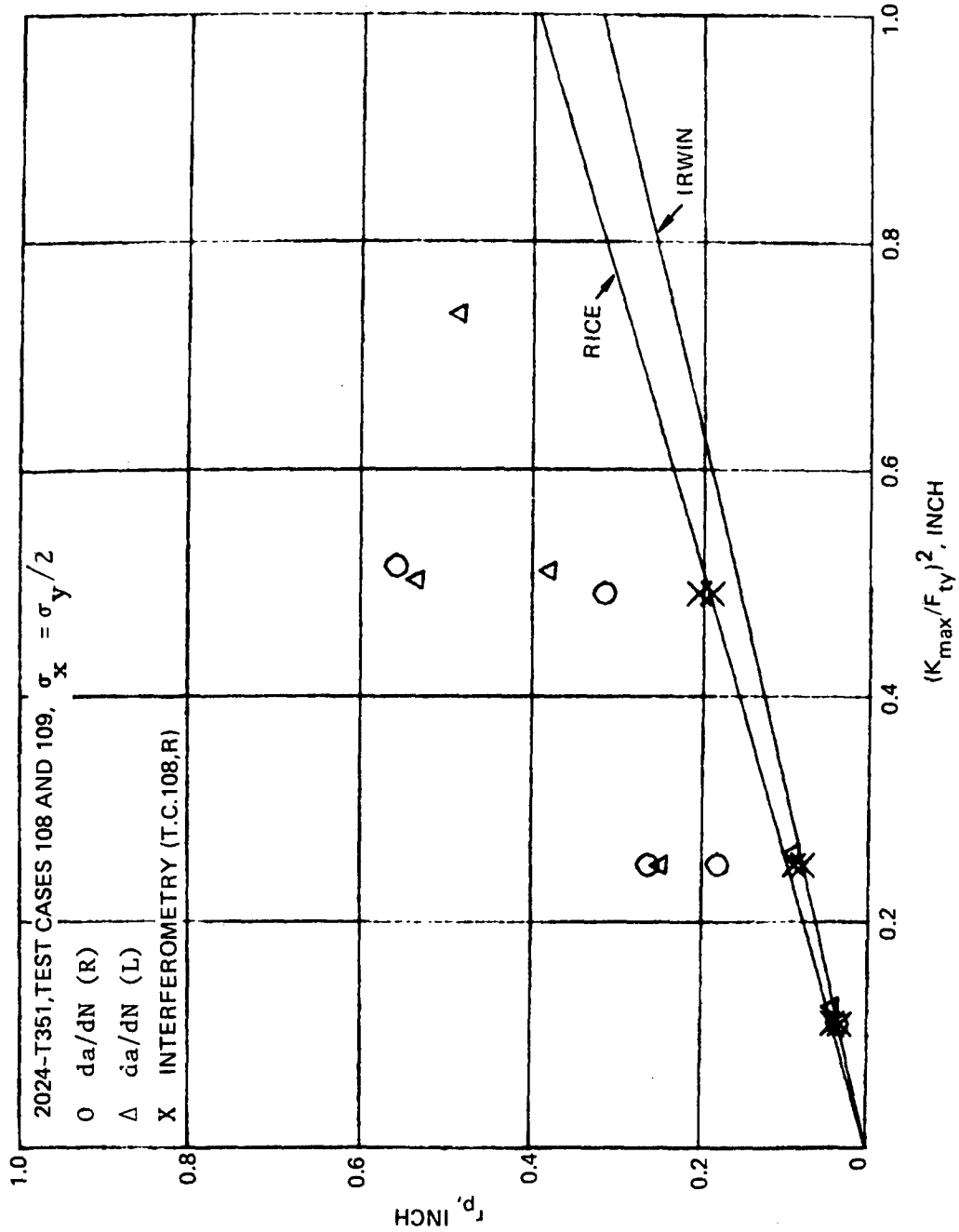


Figure 60. Experimentally Determined Residual Crack Tip Plastic Zone

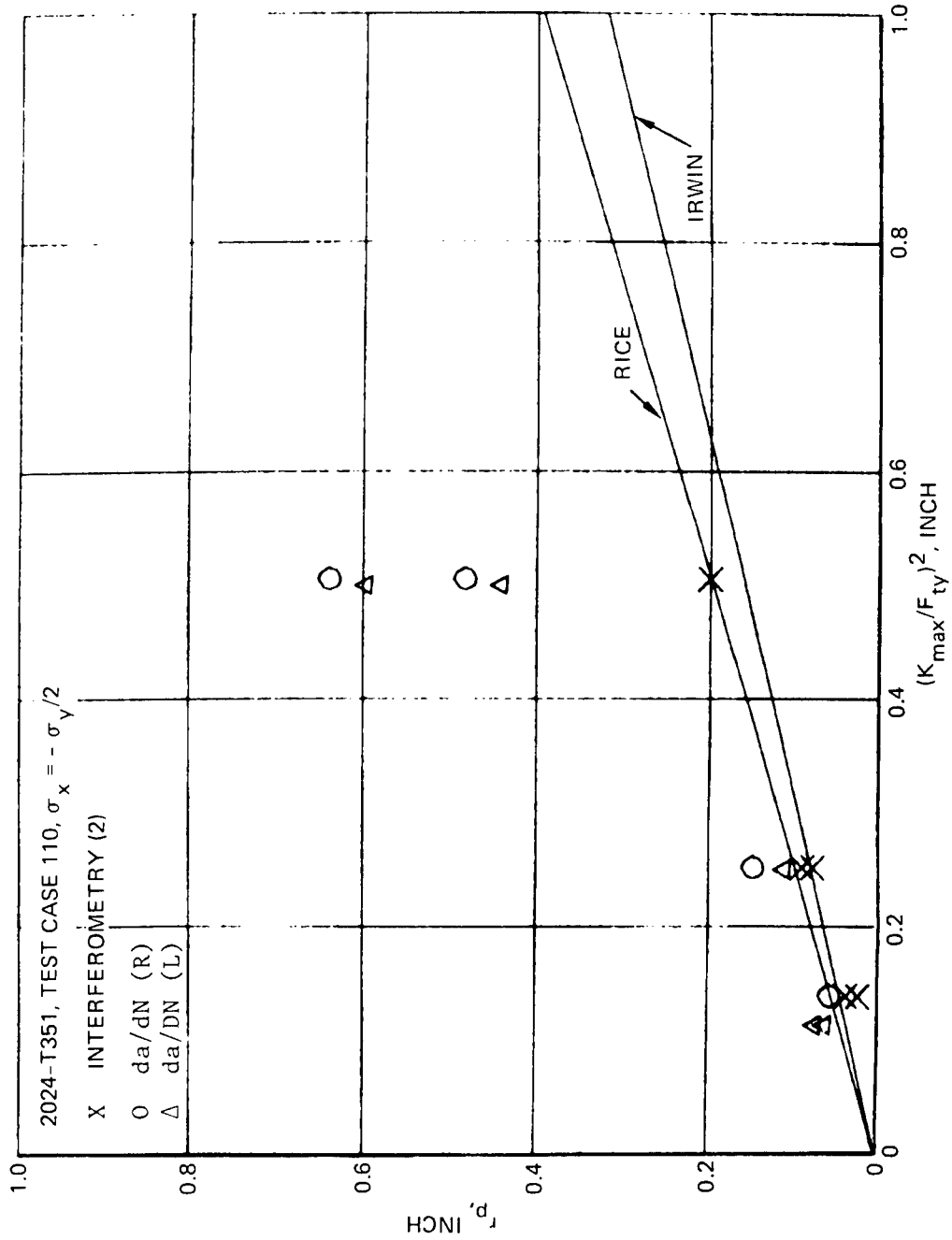


Figure 61. Experimentally Determined Residual Crack Tip Plastic Zone

SECTION VIII

CRACK GROWTH ANALYSIS METHODOLOGY

In this section, the mechanics of crack growth under constant amplitude and variable amplitude loading conditions are discussed. Analytic procedures for calculating the predicted crack growth histories are outlined. Three computer programs were constructed. The first program dealt with the crack growth rate and the crack growth direction for a crack propagating in a biaxial stress field. The second program adopted the Modified Willenborg model to compute crack growth history for a crack under variable amplitude loading conditions.

Taking advantage of the actual crack growth rate variations (for a crack inside an overloaded zone) and the "crack closure" phenomenon reported by Von Euw [34] and Elber [35], proper assumptions were made to tie these two crack propagation mechanisms together into one unified mathematical procedure. This new crack growth retardation model was incorporated into the third computer program.

All the methodologies discussed in the following sections are correlated with the experimental data presented in Section 9.

8.1 Fatigue Crack Growth Under Constant Amplitude Cyclic Loading

As will be shown in the later sections, for negative biaxial ratios, and for positive biaxial ratios up to 1.0, the crack will grow straight (stay on its initial path) and crack growth rates are not affected by the lateral stresses (parallel to the crack). Therefore, crack growth analysis can be done by using conventional methods as long as the K factors (in terms of σ_y) are properly determined.

For biaxial ratios larger than 1.0, available analytical results and the present experimental results show that the crack will turn away from its initial plane. There are two problems in conducting a computerized crack growth path analysis. The first problem is how to determine the K and the da/dN values, and the second problem is how to predict the subsequent crack growth direction (from a current crack tip location). Stress intensity factors for a curved crack have been discussed in Section 6.4. Based on the test results of all the tests conducted on negative biaxial ratios, and positive biaxial ratios up to 1.0, it can be assumed that crack growth rate will be the same for tension-high tension biaxial ratios. Therefore, the criterion for determining the accuracy of a correlation is that there should be no effect on crack growth rate if K is correctly determined. Consequently, whether the K is determined by the vector sum of K_1 and K_2 (Equation 14), or by just adding K_1 and K_2 (Equation 15), or by using the "equivalent a " method (Figure 16); the best correlation of all should show a da/dN versus K curve identical to the material baseline crack growth rate curve (or any crack growth rate curve for $B \leq 1.0$). As will be discussed in Section 9.2.2, Equation 15 is the best candidate and the "equivalent a " method is the second best candidate for determining K values along a curved crack. At this point, one might ask if K_2 should vanish after the crack starts to propagate. The following discussions may clear up the pros and the cons in the mechanics of crack growth under mixed-mode conditions.

For a stationary inclined crack in uniaxial, as well as biaxial, stress field, both K_1 and K_2 exist at the crack tip. The classical theory of fracture mechanics [30] has predicted that the crack will rotate immediately on propagation and propagates in the direction where K_1 is maximum. The angle of initial crack extension is negative (clockwise) as referenced to the original crack line. Numerous investigations, e.g., [36] on uniaxial tension and [37] on biaxial tension-compression, have shown that the magnitude of K_2 decreases rapidly after a very small amount of crack extension. Crack tip stress intensity at various points in the remaining portion of the crack path will be predominantly K_1 . However, the classical theory is only applicable to loading conditions such that the magnitude of σ_x is always lower than σ_y , i.e., σ_x is in compression, $\sigma_x = 0$, or $\sigma_x < \sigma_y$.

When a crack is subjected to a one-to-one biaxial ratio, the stresses in all directions are the same; therefore, the crack will grow straight regardless of its original orientation. If σ_x is larger than σ_y in tension, recent analytical results [28] have shown that the crack will turn toward the Y-axis. Regardless of whether the original crack plane is either parallel or inclined to σ_x , the angles of initial crack extension will be positive (counterclockwise) and the crack will end up normal to σ_x , the most dominating stresses where maximum K_1 is enhanced. Analytic solutions relating the angle of initial crack extension and the original orientation of the crack is available [28]. However, there has been no analysis concerning the status of stress intensity variations after the crack has extended. Referring back to Equations 8 and 9, since Leever treated the S-shaped crack geometry as being a simulation of Sih's arch crack problem [38], the general implication is that as long as the crack maintains an equivalently arched shape, both K_1 and K_2 exist at the crack tip. Furthermore, since the crack propagation angle is positive in all the $\sigma_x > \sigma_y$ loading cases, the curved crack will remain as S-shaped after each increment of crack growth. Therefore, it is anticipated that both K_1 and K_2 will appear at the beginning of each loading cycle.

A schematic illustration elucidating the major steps in the computerized routine for growing a curved crack is given in Figure 62. Suppose the crack is originally set at α_0 degrees in respect to the X-axis. Making use of the crack angle and biaxial ratio relationships given by Eftis and Subramonian [28], i.e.,

$$1.75 \left\{ D_1 \cdot (3\cos \theta - 1) - 3D_2 \sin \theta \right\} + 4D_3 \sin^{\frac{\theta}{2}} \cos \theta = 0 \quad (18)$$

with

$$D_1 = -3(1-B)\sin \alpha \cdot \cos(90^\circ - \alpha)$$

$$D_2 = B + (1-B)\sin^2(90^\circ - \alpha)$$

$$D_3 = (1-B)\cos^2(90^\circ - \alpha)$$

one may obtain a crack propagating angle, θ_0 , which defines the direction that the crack will takeoff. At the same time, a parallel calculation has to be made determining the K value at the crack tip (Equation 15 was used).

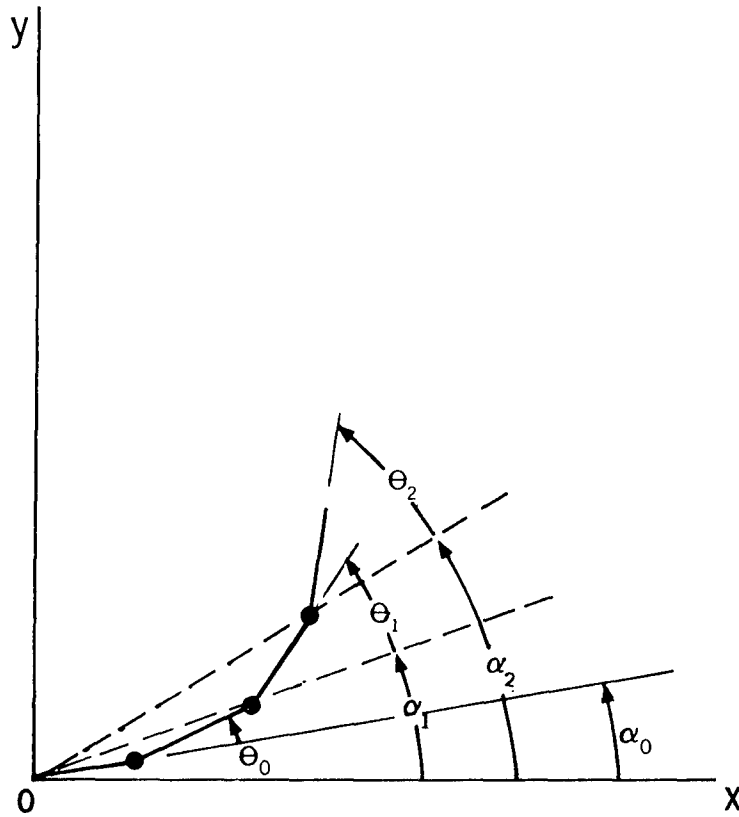


Figure 62. Definitions for Effective Crack Angle (α) and Crack Takeoff Angle (θ) in Propagation of a Curved Crack.

Subsequently, the "da" value for that load cycle can be determined through a crack growth rate equation which presents the baseline crack growth rate behavior. Since θ_0 is known, the da_x and da_y components can be computed and added to the previous a_x and a_y values, thereby determining the new crack tip location. The next step of crack extension can be predicted by repeating the whole routine of calculations (i.e., determining the θ_1 and the new da_x and da_y values). It should be noted that the Eftis criterion, Equation 18, was originally solved for a straight crack, not a kinked (or curved) crack. The effectiveness of Equation 18, for predicting the new θ 's, depends on how to choose a new α after each step of crack extension. In the present computer program, all the new α 's are determined by using a fixed origin system; i.e., an effective new α is defined to be the angle between the X-axis and the line connecting the origin and the new crack tip (as shown in Figure 62).

8.2 The Modified Willenborg Model

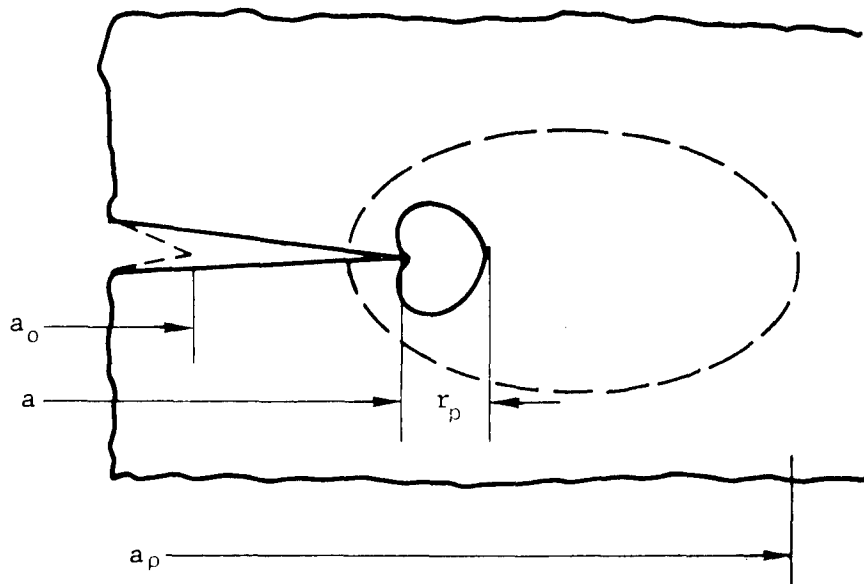
When the current plastic zone at the crack tip is surrounded by the greatest prior plastic zone, as shown in Figure 63, Willenborg, et al, [39] assumed that the effective stress for crack growth is reduced to a lower level (as compared to the actually applied stress level) and thus retardation in crack growth rate occurs. The load interaction zones r_p and r_0 are defined as follows:

$$r_p = \frac{F(a)^2 \gamma \eta a}{2} \left(\frac{\sigma_{\max}}{F_{ty}} \right)^2 \quad (19)$$

and

$$r_0 = \frac{F(a)^2 \gamma \eta a_{OL}}{2} \left(\frac{\sigma_{OL}}{F_{ty}} \right)^2 \quad (20)$$

where F_{ty} is the material tensile yield strength and $F(a)$ is the stress intensity geometry factor, e.g., Equation 4 for a center cracked panel. The parameter γ reflects the state of stresses, i.e., $\gamma = 1.0$ for plane stresses and $\gamma = 1/3$ for plane strain; η is either equal to 2.0 (indicates a full zone) or 1.0 (indicates a half zone, the so called plastic zone radius, r_y). Note Equations 19 and 20 are the so-called Irwin plastic zone



WHERE a_0 INITIAL CRACK LENGTH
 a CURRENT CRACK LENGTH
 r_p CURRENT LOAD INTERACTION ZONE
 a_p GREATEST PRIOR LOAD INTERACTION FRONT

Figure 63. Load Interaction Zone at Crack Tip

equations (i.e., same as Equation 16). A Rice equation can be obtained just by multiplying a factor of 1.23374 to the Irwin equation. As previously discussed in Section 7, the plastic zone sizes are most likely a nonlinear function of $(K_{\max}/F_{ty})^2$ and may also be somewhat affected by biaxial stress ratios.

The stresses used in this model are illustrated in Figure 64. In Figure 64, the stresses σ_{\max} and σ_{\min} are the spectrum stresses in a stress event, σ_{ap} is the applied stress which is defined as an imaginary stress that creates a plastic zone whose boundary coincides with the greatest prior interface, i.e.

$$\sigma_{ap} = \frac{F_{ty}}{F(a)} \sqrt{\frac{2(a_p - a)}{a \cdot \gamma \cdot \eta}} \quad (21)$$

The stress σ_{red} , the reduction in applied stress, is defined as the difference between σ_{ap} and the maximum stress in the spectrum, σ_{\max} , i.e.,

$$\sigma_{red} = \sigma_{ap} - \sigma_{\max} \quad (22)$$

The effective stresses are then obtained as

$$(\sigma_{\max})_{eff} = \sigma_{\max} - \sigma_{red} \quad (23)$$

$$(\sigma_{\min})_{eff} = \sigma_{\min} - \sigma_{red} \quad (24)$$

where both $(\sigma_{\max})_{eff}$ and $(\sigma_{\min})_{eff}$ are restricted to be non-negative. After obtaining the effective stresses, the crack growth rate is determined from the effective stress intensity range, effective stress intensity ratio, and the material baseline (constant amplitude growth rate) data.

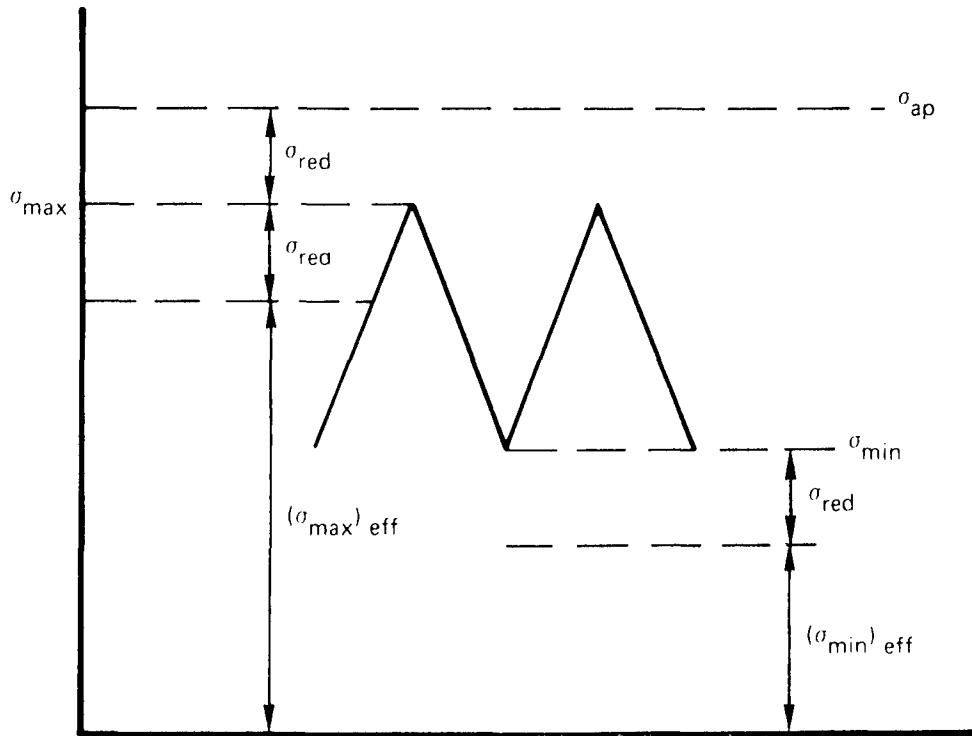


Figure 64. Effective Stresses in the Willenborg Model

From the above outline of the model, the following observation can be made about this model; (1) Negative stress ratio is excluded, (2) No additional parameter is introduced, and (3)

$$\Delta K_{\text{eff}} = \begin{cases} (K_{\text{max}})_{\text{eff}} - (K_{\text{min}})_{\text{eff}} = \Delta K, & \text{if } \sigma_{\text{min}} \geq \sigma_{\text{red}} \\ (K_{\text{max}})_{\text{eff}}, & \begin{cases} \text{if } \sigma_{\text{min}} < \sigma_{\text{red}} \\ \text{and } \sigma_{\text{max}} > \sigma_{\text{red}} \end{cases} \\ 0, & \text{if } \sigma_{\text{max}} \leq \sigma_{\text{red}} \end{cases} \quad (25)$$

and

$$R_{\text{eff}} = \begin{cases} (K_{\text{min}})_{\text{eff}} / (K_{\text{max}})_{\text{eff}} \leq \sigma_{\text{min}} / \sigma_{\text{max}}, & \text{if } \sigma_{\text{min}} \geq \sigma_{\text{red}} \\ 0, & \text{if } \sigma_{\text{min}} < \sigma_{\text{red}} \end{cases} \quad (26)$$

If $\sigma_{\min} \geq \sigma_{\text{red}}$ only the reduction in stress ratio causes crack growth retardation. Thus in selecting a crack growth rate equation for analysis it must include a term to account for the R effect. For $\sigma_{\min} < \sigma_{\text{red}}$ and $\sigma_{\max} \geq \sigma_{\text{red}}$, both ΔK and R are reduced. Finally, when $\sigma_{\max} \leq \sigma_{\text{red}}$ complete crack arrest occurred; this situation arises if the overload ratio is 2.0 or higher. However, experimental data have shown that an overload shutoff ratio of 2.0 is nonconservative in many cases. Therefore, modification of the model is necessary. Using a stress intensity approach, Gallagher & Hughes [40] applied a correction factor to Willenborg's reduction in applied stress. That is,

$$\sigma_{\text{red}}^{\text{mod}} = \Phi \sigma_{\text{red}} \quad (27)$$

with

$$\Phi = \frac{1 - (K_{\text{TH}}^{\text{max}} / K_{\text{max}})}{S - 1} \quad (28)$$

This modification introduces two additional constants; (1) S is the overload shutoff ratio, and (2) $K_{\text{TH}}^{\text{max}}$ is associated with the fatigue crack growth rate threshold for R = 0.

8.3 The New Crack Growth Retardation Model

In Von Euw's dissertation [34], he reported that the crack growth rates for the lower loads subsequent to a higher load were retarded. However, he also observed that the minimum fatigue crack propagation rate did not occur immediately following the application of the overload. Instead, the lowest growth rate was reached after the crack had extended over a distance within the overload plastic zone. A schematic representation of this behavior is presented in Figure 65. In Figure 65, a_{OL} and r_0 are taken to be the same as those previously defined in the Modified Willenborg Model except that all the plastic zones are defined to be the full plastic zone (i.e., with $\eta = 2.0$); a_1 is the crack length after the application of a high load (overload) and r_1 is the crack tip plastic zone for a_1 at a lower load. It was assumed (also supported by experimental observation) that the crack would resume its normal growth rate when it travelled through the overload plastic zone, i.e., for its crack tip plastic zone to travel a distance of a^* indicated in the

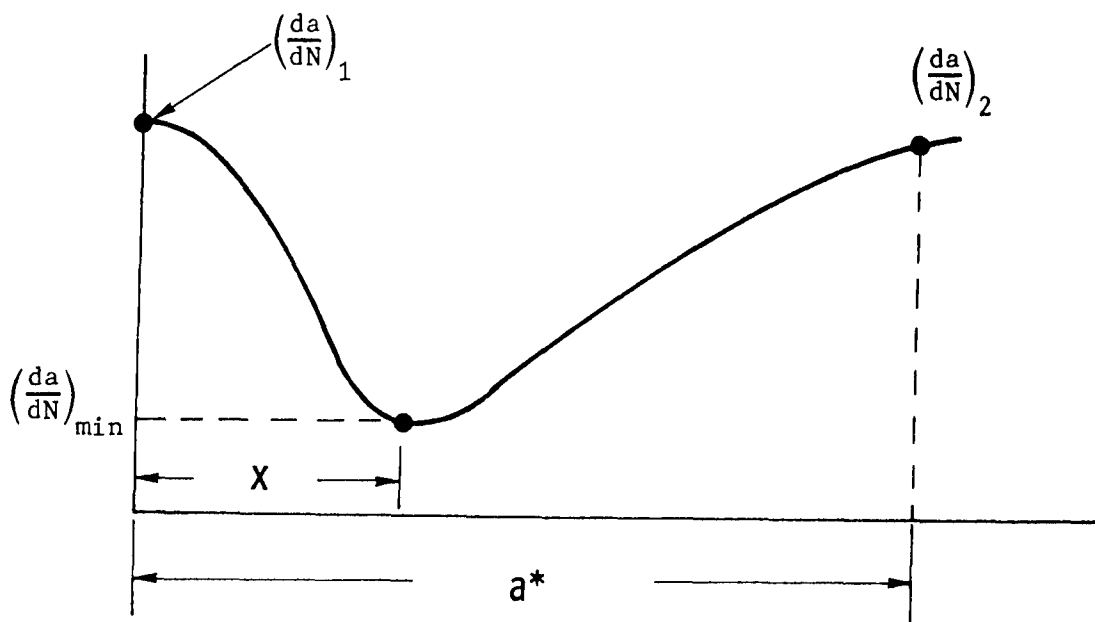
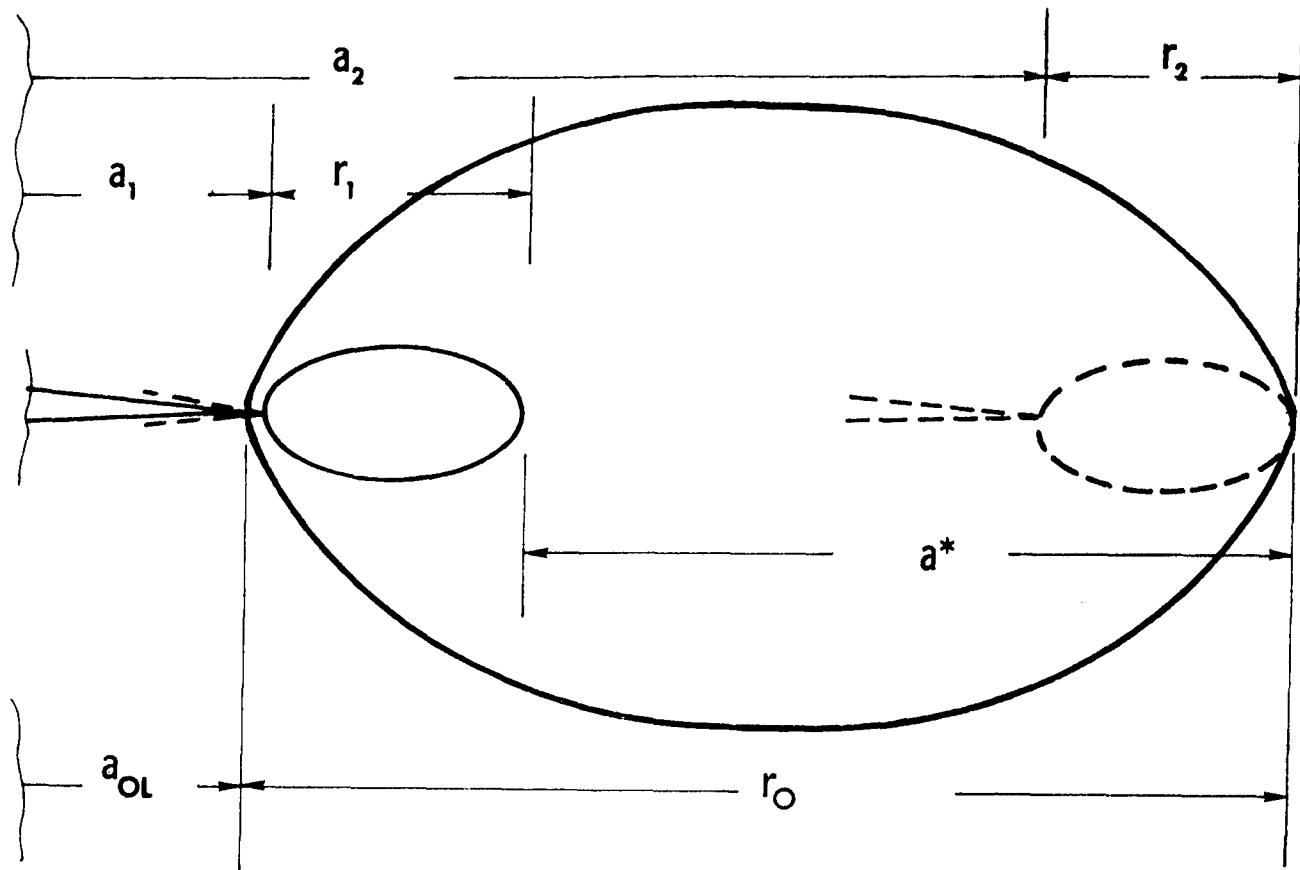


Figure 65. Crack Growth Rate Behavior Inside an Overloaded Zone

top portion of Figure 65. For constant amplitude loading with occasional single overloads, it is convenient to assume that $r_2 = r_1$, i.e., $a^* = r_0 - r_1$. This assumption has enabled us to construct the bottom part of Figure 65. In that figure, $(da/dN)_1$ corresponds to a_1 and $(da/dN)_2$ corresponds to a_2 ($= a_1 + a^*$). The distance at which the crack growth rate reaches minimum is approximately equal to 1/8 to 1/4 of the total overload plastic zone as determined by Von Euw's experiments on 2024-T3 aluminum alloy.

To calculate the number of delay cycles (N^*) for the crack to travel through a^* , the following assumptions have been made.

1. Both $(da/dN)_1$ and $(da/dN)_2$ are regular crack growth rates, i.e., not retarded.
2. The crack growth rate behavior within the r_0 zone follows the Paris Equation [41], and crack growth retardations are benefited from "crack closure."
3. $(da/dN)_{min}$ occurs at $x = a^*/4$
4. da/dN is linear between $(da/dN)_1$ and $(da/dN)_{min}$, and is also linear between $(da/dN)_{min}$ and $(da/dN)_2$.

Following these assumptions, we can write

$$\frac{da}{dN} = \left(\frac{da}{dN}\right)_1 - \frac{\left(\frac{da}{dN}\right)_1 - \left(\frac{da}{dN}\right)_{min}}{\xi a^*} \cdot x \quad (29)$$

for $0 \leq x \leq \xi a^*$, and

$$\frac{da}{dN} = \frac{1}{(1-\xi)} \left[\left(\frac{da}{dN}\right)_{min} - \xi \left(\frac{da}{dN}\right)_2 \right] + \frac{\left(\frac{da}{dN}\right)_2 - \left(\frac{da}{dN}\right)_{min}}{(1-\xi)a^*} \cdot x \quad (30)$$

for $\xi a^* < x \leq a^*$ with $\xi = 1/4$.

After integration, the total number of delay cycles within the overload plastic zone will be

$$N^* = \frac{\xi a^*}{\left(\frac{da}{dN}\right)_1 - \left(\frac{da}{dN}\right)_{\min}} \ln \frac{\left(\frac{da}{dN}\right)_1}{\left(\frac{da}{dN}\right)_{\min}} + \frac{(1-\xi)a^*}{\left(\frac{da}{dN}\right)_2 - \left(\frac{da}{dN}\right)_{\min}} \ln \frac{\left(\frac{da}{dN}\right)_2}{\left(\frac{da}{dN}\right)_{\min}} \quad (31)$$

The resulting crack length versus cycles history is schematically illustrated in Figure 66.

The crack opening concept is adopted to calculate the crack growth rates inside the overload plastic zone. The effective ΔK values in each stress event can be obtained following the assumptions set above and the definitions given in Figure 67. There $(\Delta K_e)_1 = \Delta K_1$ and $(\Delta K_e)_2 = \Delta K_2$. The minimum effective ΔK would be equal to the difference between K_{op} (K -opening at overload) and K_{\max} at $(a_1 + \xi a^*)$. Therefore, this model actually relocates the position of $(\Delta K_e)_{\min}$ from a_1 to $(a_1 + \xi a^*)$ and also redistributed the variations of ΔK_e from a small to normal distribution to a normal-small-normal distribution.

Thus, the crack growth rates at various positions inside the overload plastic zone are

$$\begin{aligned} \left(\frac{da}{dN}\right)_1 &= C \cdot (\Delta K)_1^n \\ &= C \left[(\sigma_{\max} - \sigma_{\min}) \sqrt{\pi a_1} \right]^n \end{aligned} \quad (32)$$

$$\begin{aligned} \left(\frac{da}{dN}\right)_2 &= C \cdot (\Delta K)_2^n \\ &= C \left[(\sigma_{\max} - \sigma_{\min}) \sqrt{\pi a_2} \right]^n \end{aligned} \quad (33)$$

$$\left(\frac{da}{dN}\right)_{\min} = C (\Delta K_e)_{\min}^n \quad (34)$$

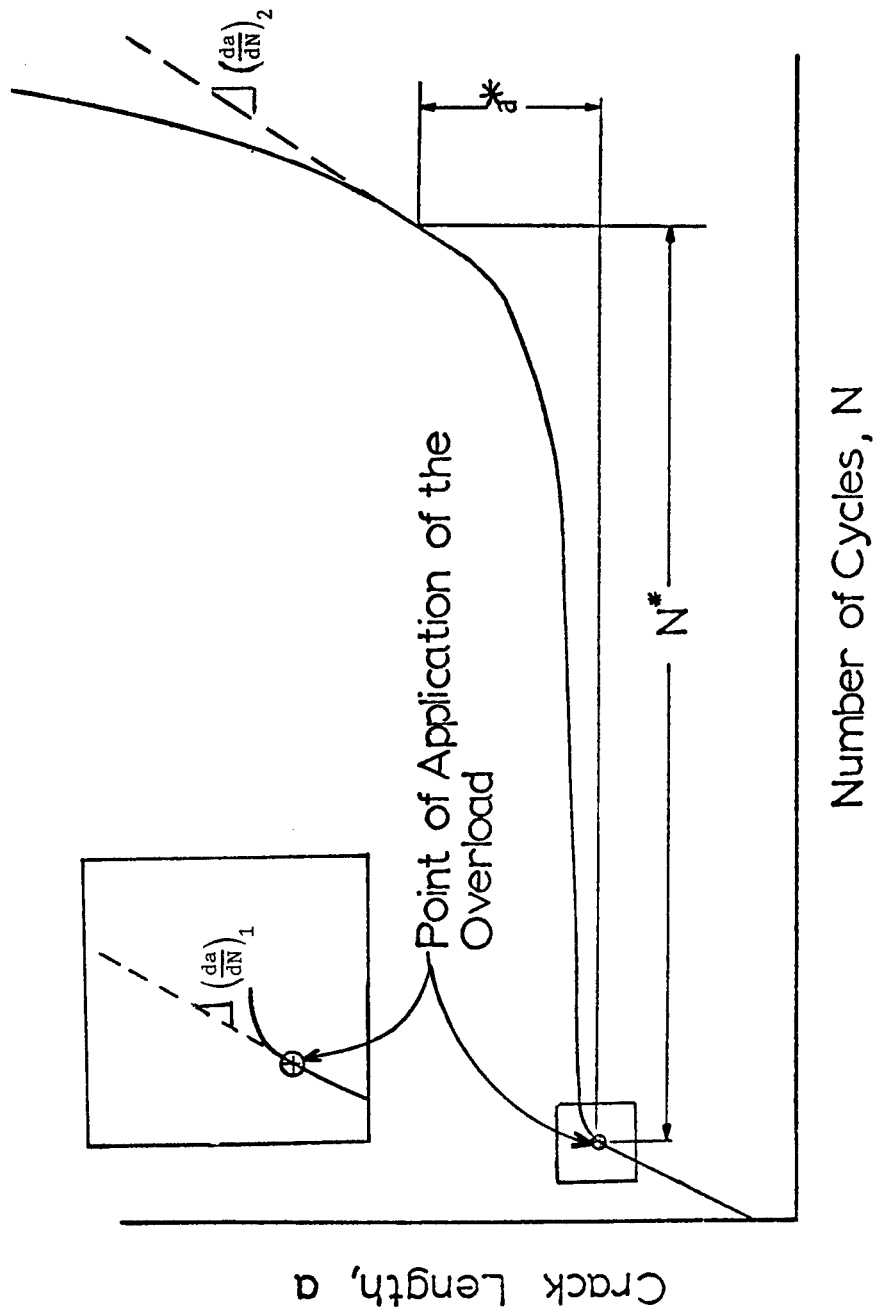


Figure 66. Growth Rate Curve Resulting from the Application of a Single Overload

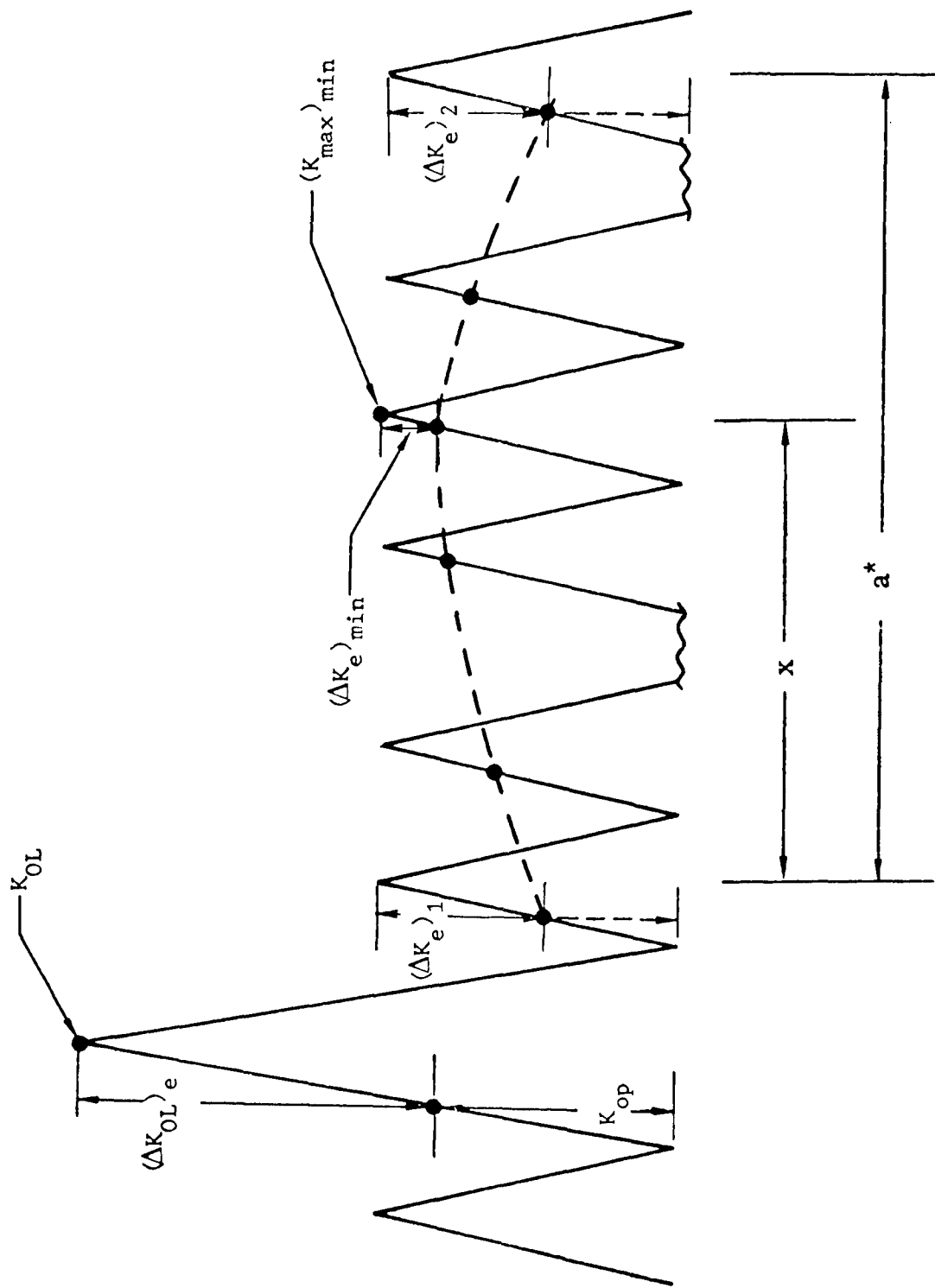


Figure 67. Effective K-Ranges inside an Overloaded Zone

and

$$\begin{aligned}
 (\Delta K_e)_{\min} &= (K_{\max})_{\min} - K_{op} \\
 &= (K_{\max})_{\min} - [K_{OL} - (\Delta K_{OL})_e] \\
 &= (K_{\max})_{\min} - K_{OL} + (\Delta K_{OL}) \cdot (C_1 + C_2 \cdot r_0) \\
 &= \sigma_{\max} \sqrt{\pi(a_1 + \xi a^*)} - \sigma_{OL} \sqrt{\pi a_{OL}} \\
 &\quad + \left\{ C_1 + C_2 \cdot \frac{(\sigma_{\min})_{OL}}{(\sigma_{\max})_{OL}} \right\} \cdot \left\{ (\sigma_{\max})_{OL} - (\sigma_{\min})_{OL} \sqrt{\pi a_{OL}} \right\} \quad (35)
 \end{aligned}$$

The C and n are the constants in the Paris Equation for the baseline material; C_1 and C_2 are Elber's crack closure parameters. The crack growth rates between these points can be obtained by interpolations.

SECTION IX

EXPERIMENTS

A group of 118 specimens were tested to investigate the effects of biaxial stress ratio on fatigue crack growth rate behavior of 7075-T7351 and 2024-T351 aluminum alloys. The specimens were divided into the following groups.

1. To investigate the basic biaxial ratio effects (including the applied stress level) - 57 specimens.
2. To investigate the cyclic stress ratio effects (at $R = 0.7$) - 12 specimens.
3. To investigate the behavior of cracks coming out from a hole - 10 specimens.
4. To investigate the effect of biaxial stress ratios on crack growth retardation behavior - 13 specimens.
5. To investigate the biaxial loading effects under out-of-phase loading conditions - 14 specimens.
6. Miscellaneous tests including fatigue crack growth under sustained load conditions, angle cracks and fracture tests - 12 specimens.

Tensile coupons, center cracked panels (CCT), and cruciform specimens were fabricated from 10 sheets of 7075-T7351 and four sheets of 2024-T351 plate stocks. All the sheets of each material were from the same heat. The size of these commercial aluminum plates was 121.92 cm (4 feet) wide by 365.76 cm (12 feet) long by 17.7 mm (0.5 inch) thick. The specimens were cut from randomly selected areas in these aluminum plates. The testing conditions and descriptions of experimental procedures for each test type are given in the following sections whenever is appropriate. Discussion and correlation of experimental data are also presented in the same section where testing of a particular test type is presented.

9.1 Material Characterization Tests

Thirty-six tensile test coupons were machined from all 14 sheets of aluminum alloys. Specimen configuration was as specified in ASTM Standard E8, with specimen thickness equal to 4.572 mm (0.18 inch). A 178,000 N (40 kip) MTS machine was used for conducting the tensile tests.

The average tensile yield strength (the 0.2 percent offset value) for the 7075-T7351 alloy was 412,022 kPa (59.8 ksi) for both the LT and the TL directions. The average tensile yield strength for the 2024-T351 alloy was 367,237 kPa (53.3 ksi) for the LT direction and 319,007 kPa (46.3 ksi) for the TL direction. Engineering stress-strain curves were also obtained from each tensile test. One typical curve was selected from each alloy and it was used for conducting the elastic-plastic finite element analyses.

These two tensile stress-strain curves are presented in Figures 68 and 69. A complete set of the stress-strain curves, for all 36 specimens, are compiled in Volume II of this report. Tabulated tensile properties for all 36 tests are also reported in Volume II of this report.

9.2 Constant Amplitude Biaxial Crack Growth Rate Tests

Thirty 7075-T7351 specimens and 27 2024-T351 specimens were tested under various biaxial loading conditions ($-1.5 \leq \sigma_x / \sigma_y \leq 1.75$) at $R = 0.1$, and at various applied stress levels ($0.2 \leq \sigma_y / F_{ty} \leq 0.6$). The testing conditions, for each test, are listed in Table 4. Unless otherwise noted, the loading profiles for σ_x and σ_y cyclic stresses were such that $\sigma_{x, \min}$ occurred at $\sigma_{y, \max}$ for the negative biaxial ratios whereas $\sigma_{x, \max}$ occurred at $\sigma_{y, \max}$ for the positive biaxial conditions.

For all tests involving compression loading, an antibuckling guide was used. The apparatus for preventing specimen buckling consisted of two square-shaped aluminum plates and two circular steel plates. The steel plates were inserted into the circular hole in the center of the aluminum plate. The test specimen was sandwiched in between the aluminum plates. The crack could be seen from an open slot 19.05 mm (0.75 inch) wide and 12.7 cm (5 inches) long in the center of the circular plate. The circular

Specimen No. LT-7-2, E=10,340 ksi

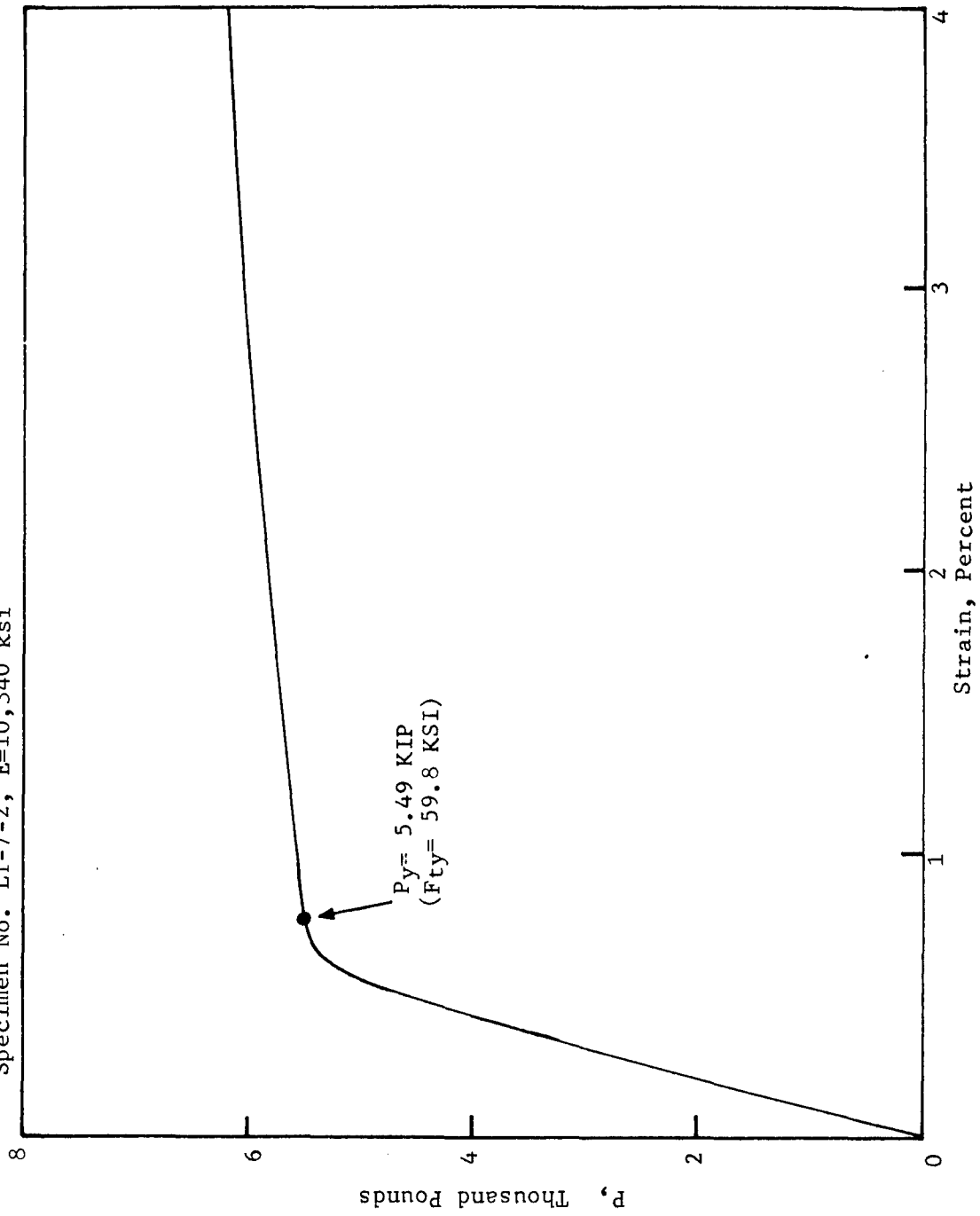


Figure 68. Typical Tensile Stress-Strain Curve, 7075-T7351, LT, t = .18 Inch

Specimen No. LT-2-12, E = 10,390 ksi

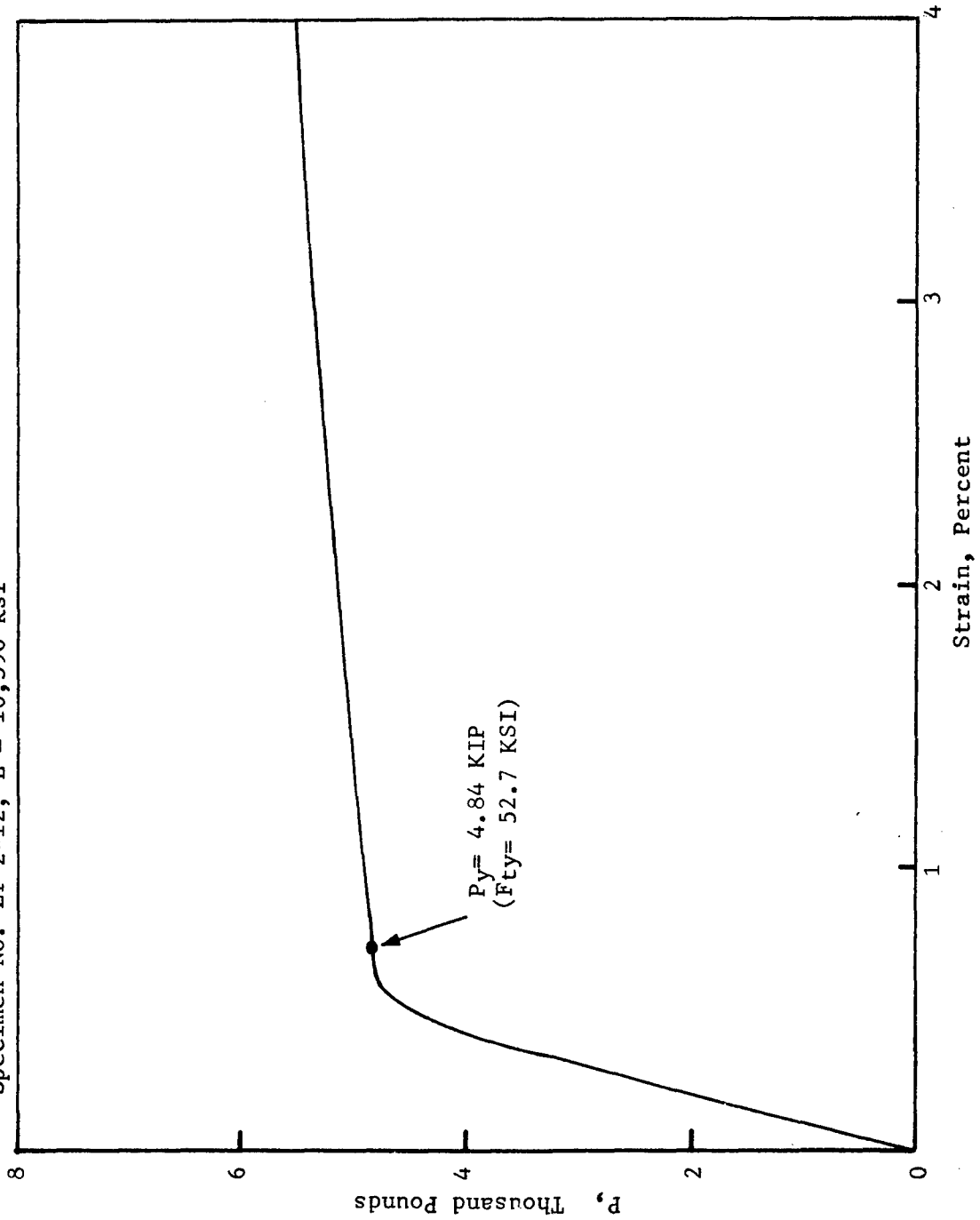


Figure 69. Typical Tensile Stress-Strain Curve, 2024-T351, LT, t = .18 Inch

TABLE 4. BASIC BIAxIAL RATIO EFFECT TESTS

Material	Test Case	$\sigma_{y,max}$	$\sigma_{y,min}$	$\sigma_{x,max}$	$\sigma_{x,min}$	f	Notes
7075-T7351	70	12.0	1.2	-1.8	-18.0	8	
7075-T7351	25	12.0	1.2	-1.2	-12.0	10	1
7075-T7351	26	12.0	1.2	-1.2	-12.0	5	
7075-T7351	56	18.0	1.8	-1.8	-18.0	5	1
7075-T7351	58	18.0	1.8	-0.9	-9.0	5	
7075-T7351	135	18.0	1.8	-0.9	-9.0	2	
7075-T7351	64	30.0	3.0	-1.5	-15.0	2	
7075-T7351	29	12.0	1.2	-0.6	-6.0	5	
7075-T7351	30	12.0	1.2	-0.6	-6.0	10	
7075-T7351	27	12.0	1.2	6.0	0.6	7	1
7075-T7351	28	12.0	1.2	6.0	0.6	8	
7075-T7351	139	30.0	3.0	15.0	1.5	2	
7075-T7351	63	30.0	3.0	15.0	1.5	2	1
7075-T7351	57	18.0	1.8	9.0	0.9	5	
7075-T7351	133	18.0	1.8	18.0	1.8	5	
7075-T7351	55	18.0	1.8	18.0	1.8	3	1
7075-T7351	23	12.0	1.2	12.0	1.2	10	1
7075-T7351	24	12.0	1.2	12.0	1.2	5	
7075-T7351	141	12.0	1.2	15.0	1.5	5	
7075-T7351	68	12.0	1.2	18.0	1.8	5	
7075-T7351	142	12.0	1.2	21.0	2.1	5	
7075-T7351	1	6.0	0.6	0	0	5	2
7075-T7351	2	10.0	1.0	0	0	5	2
7075-T7351	123	4.8	0.48	0	0	10	2 3 4
7075-T7351	7	12.0	1.2	0	0	5	
7075-T7351	8	12.0	1.2	0	0	10	1
7075-T7351	125	4.8	0.48	0	0	10	2 3 4 5
7075-T7351	131	20.0	2.0	0	0	5	2 5 6

TABLE 4. (continued)

Material	Test Case	$\sigma_{y,max}$	$\sigma_{y,min}$	$\sigma_{x,max}$	$\sigma_{x,min}$	f	Notes
7075-T7351	5	7.0	0.7	0	0	5	 
7075-T7351	13	12.0	1.2	0	0	5	
2024-T351	60	15.0	1.5	-1.5	-15.0	5	
2024-T351	33	10.0	1.0	-1.0	-10.0	10	
2024-T351	34	10.0	1.0	-1.0	-10.0	5	
2024-T351	137	30.0	3.0	-1.5	-15.0	2	
2024-T351	66	25.0	2.5	-1.25	-12.5	2	
2024-T351	140	25.0	2.5	-1.25	-12.5	2	
2024-T351	62	15.0	1.5	-0.75	-7.5	5	
2024-T351	37	10.0	1.0	-0.5	-5.0	10	
2024-T351	38	10.0	1.0	-0.5	-5.0	5	
2024-T351	35	10.0	1.0	5.0	0.5	10	
2024-T351	36	10.0	1.0	5.0	0.5	5	
2024-T351	136	15.0	1.5	7.5	0.75	2	
2024-T351	61	15.0	1.5	7.5	0.75	5	
2024-T351	65	25.0	2.5	12.5	1.25	2	
2024-T351	138	30.0	3.0	15.0	1.5	2	
2024-T351	134	10.0	1.0	10.0	1.0	5	
2024-T351	31	10.0	1.0	10.0	1.0	8	
2024-T351	32	12.0	1.2	12.0	1.2	5	
2024-T351	59	15.0	1.5	15.0	1.5	5	
2024-T351	3	10.0	1.0	0	0	5	
2024-T351	4	6.0	0.6	0	0	5	
2024-T351	9	10.0	1.0	0	0	5	
2024-T351	10	10.0	1.0	0	0	10	
2024-T351	6	6.0	0.6	0	0	5	 

TABLE 4. (continued)

Material	Test Case	$\sigma_{y,max}$	$\sigma_{y,min}$	$\sigma_{x,max}$	$\sigma_{x,min}$	f	Notes
2024-T351	132	8.0	0.8	0	0	5	2 5 6
2024-T351	14	10.0	1.0	0	0	5	5
2024-T351	149	6.0	0.6	0	0	10	7 2

- 1 Interferometry photographs
- 2 CCT specimen
- 3 20Hz for $da/dN < 10^{-6}$ inch/cycle
- 4 Precracking data for the fracture specimen
- 5 TL direction
- 6 Tested in the biaxial loading machine
- 7 Tested in distilled water

plate could be rotated to follow the crack growth direction. All the metal plates in this device were coated with teflon (approximately 0.06 inch thick). The outer plates were clamped to the loading arms of the specimen. The outer plates had set-screw adjustments around the inner circle which in turn "clamp" the circular plates to contact the specimen flat surface. Actually these plates were allowed only to contact (i.e., the clamping load was only a few pounds). From the strain-survey results, no noticeable effect of load interaction due to the use of such constraints was noticed.

Both the CCT and the cruciform specimens were used to develop crack growth rate data for uniaxial loading conditions ($\sigma_x = 0$). All but two of the CCT specimens were tested in a 356,000 N (80 kip) MTS machine. The last two CCT specimens and the cruciform specimens were tested in the biaxial loading frame to insure that compatible crack growth rate data would be developed from both the CCT and the cruciform specimens. The loading characteristics of the newly-built biaxial test unit were checked out through testing of the CCT specimens in both testing machines.

The size of the CCT specimens was 17.78 mm (7 inches) wide by 40.64 cm (16 inches) long, having the central portion tapered down from 17.7 mm (0.5 inch) to 4.572 mm (0.18 inch). The cruciform specimen configuration was discussed in the previous section.

Since in some biaxial loading cases the crack might not grow perpendicular to the principal loading direction, it was desirable to measure the crack in both magnitude and direction. A photographic polar grid such as that shown in Figure 5B was printed onto the very finely polished cruciform specimen surface. Tick marks were placed at every 15 degrees around the circumferential grid line, and the spacing between grid lines was 1.27 mm (0.05 inch).

Both the CCT and the cruciform specimens were precracked from an initial EDM slot, at the center of the specimen, to the desired initial flaw size (approximately 3.81 mm in total length). All specimens were precracked at test maximum load level by applying tension-tension load cycles normal to the EDM slot using the MTS machine or the biaxial loading frame whichever was convenient. Crack length measurements were made at very small increments to obtain an adequate understanding of the crack growth behavior. For the cruciform specimens, testing was terminated when the crack growth rate was faster than $2.54 \mu\text{m}/\text{cycle}$ (10^{-4} inch/cycle) or the crack had reached the border of the flat area. In the tension-compression biaxial ratio tests, testing was terminated when the crack reached the end of the opening slot in the buckling prevention device (4 to 5 inches in total crack length).

The effect of cyclic frequencies was not the primary interest of this investigation. However, due to the nature of the biaxial loading tests, and the operation characteristics of the biaxial test unit, lower frequencies had to be used for testing at higher applied loads, whereas higher frequencies could be applied to lower load test cases. Therefore, as shown in Table 4, some test cases consisted of several replications, and each of them was run at a different cyclic frequency to insure that test results would be consistent with the range of frequencies being applied.

9.2.1 Test Results

Stress intensities for cracks in the CCT specimens were computed using Equations 3 and 4. For the cruciform specimens, the test results indicated that the crack grew straight in all the tests with $\sigma_x \leq \sigma_y$. However, when σ_x exceeded σ_y , the crack turned away from its initial plane and finally ended up propagating in a direction perpendicular to σ_x (see the example shown in Figure 5B for $\sigma_x = 1.5 \sigma_y$).

Stress intensity values presented in Figure 10 (adjusted by the actual σ_y in each test) were used to correlate the da/dN data for the straight cracks. A complete set of the tabulated a versus N data and da/dN versus K_{max} curves for each test are compiled in Volume II of this report. Compositated da/dN versus K_{max} curves for each of the six biaxial ratios (0, ± 0.5 , ± 1.0 , and -1.5) are presented in Figures 70 to 79. Examination of all the test results revealed that all the crack growth rate curves are almost identical, i.e., for the same material and cyclic stress amplitude, there was no effect on fatigue crack growth rate due to differing biaxial stress ratios. It is significant to note that each of these compositated da/dN curves, (e.g., Figures 72 and 76) are composed from many sets of test data points and each set of those data had been generated from different combinations of stress levels and cyclic frequencies. Six test technicians were involved at different times in collecting the crack length versus cycles records for all the tests. Even so, it is very evident that the crack growth rate behavior for all the tests remained consistent. As also shown in Figures 70 to 79, some data points at higher K levels exhibited lower crack growth rate values. These data points were reduced from long cracks ($a > 2.75$ inches) in the cruciform specimen. Extrapolated K values were used during data reduction. The actual K values for these crack lengths might have been significantly reduced due to the reduction of stress at the area near the rim of the specimen.

The effect of biaxial loading conditions on crack growth can also be evaluated from the a versus N curves plotted in Figures 80 and 81. There the scatter (on N) for growing a crack from 0.5 inch to 4.0 inches was only $\pm 16\%$ (32% total scatter band) for the 7075-T7351 specimens and $\pm 17\%$ (34% total scatter band) for the 2024-T351 specimens. As identified in these figures, the scatter band for the 7075-T7351 specimens at $B = 1.0$ was already 21% (as compared to the 32% total scatter band). For the 2024-T351 specimens, the 34% total scatter band actually represented the scatter band for the -1.0 biaxial ratio specimens. No definite trend in the biaxialty effects are shown in these figures.

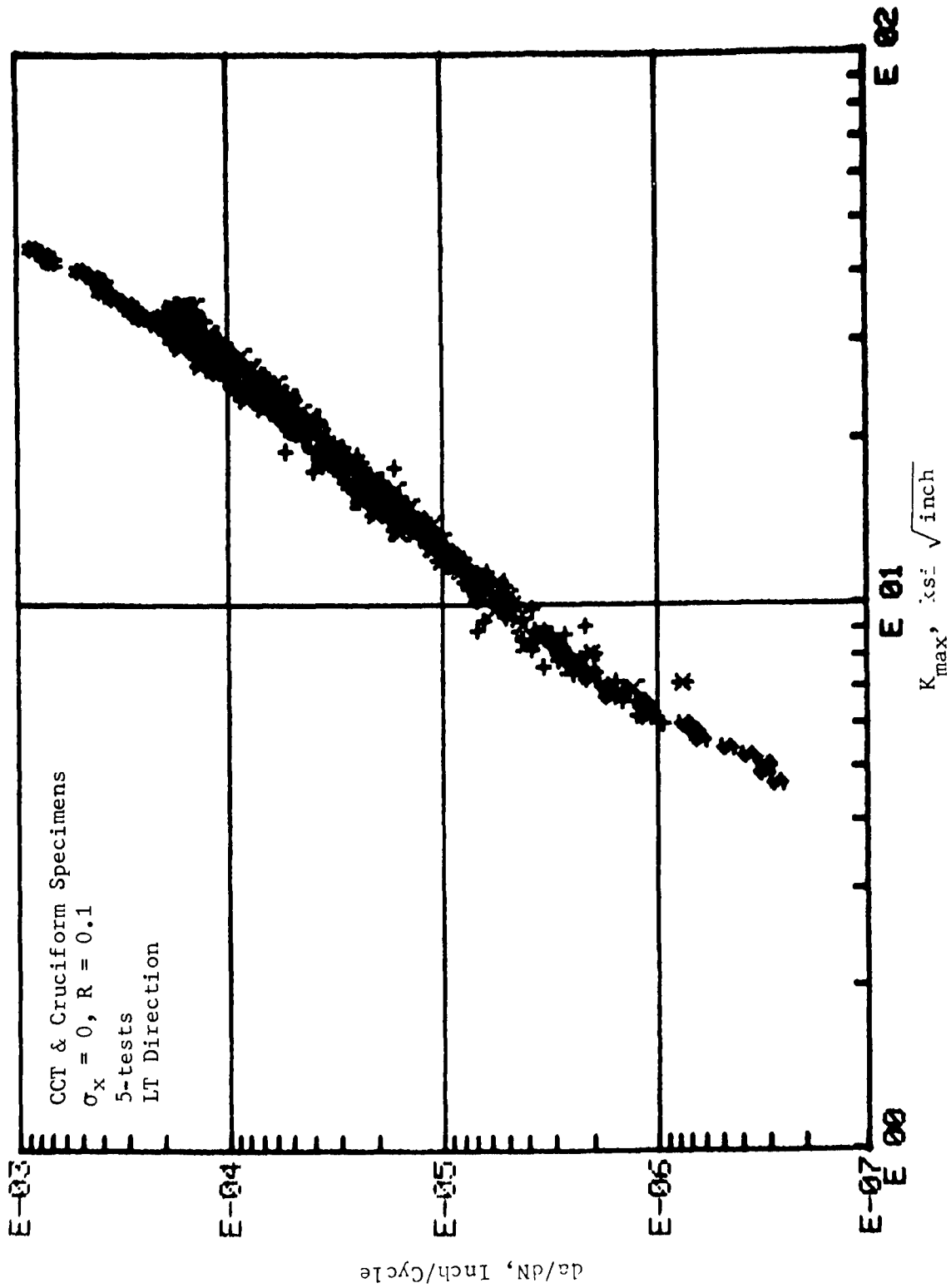


Figure 70. Cyclic Crack Growth Rate Behavior of 7075-T7351 Aluminum

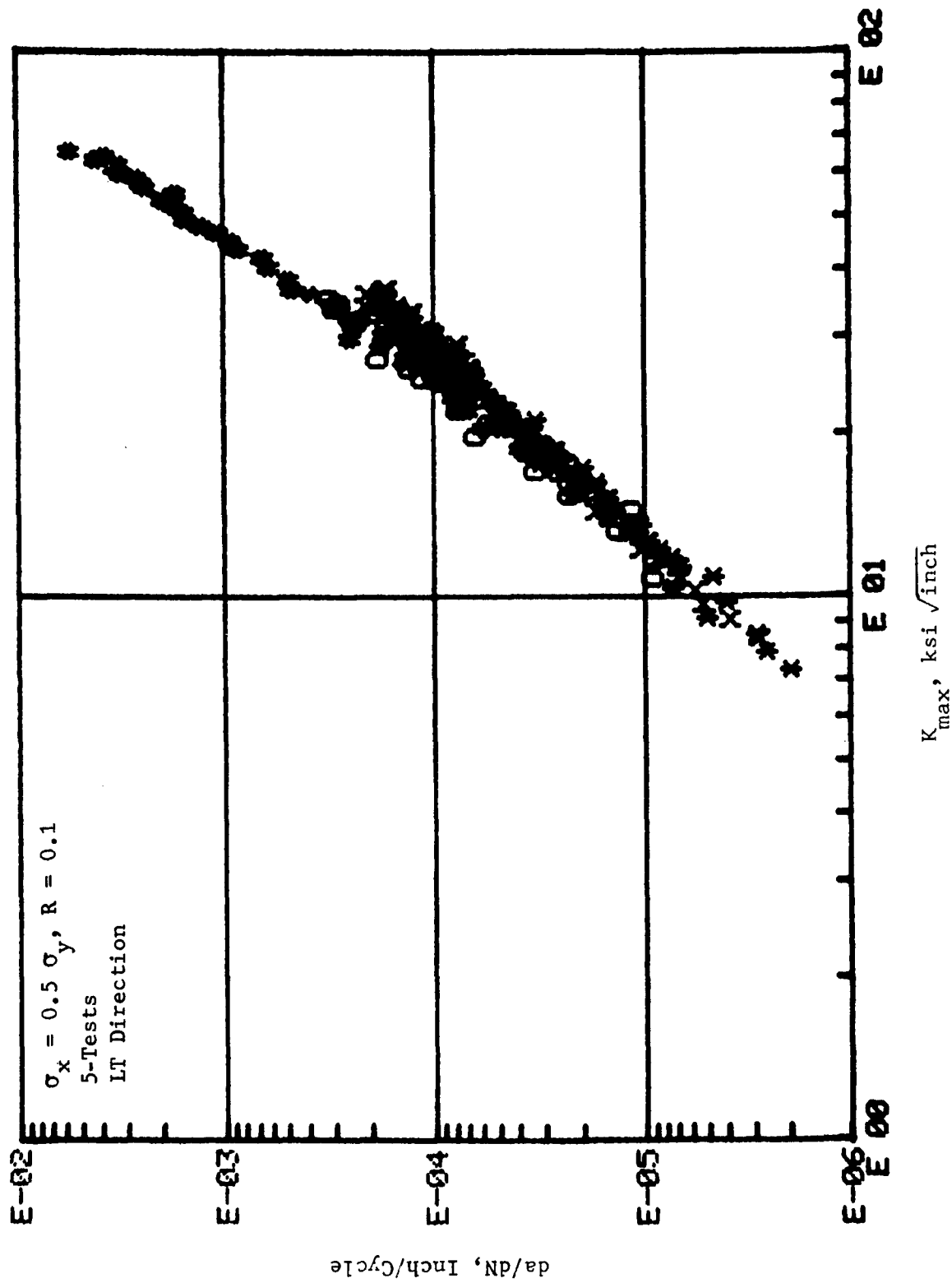


Figure 71. Cyclic Crack Growth Rate Behavior of 7075-T7351 Aluminum

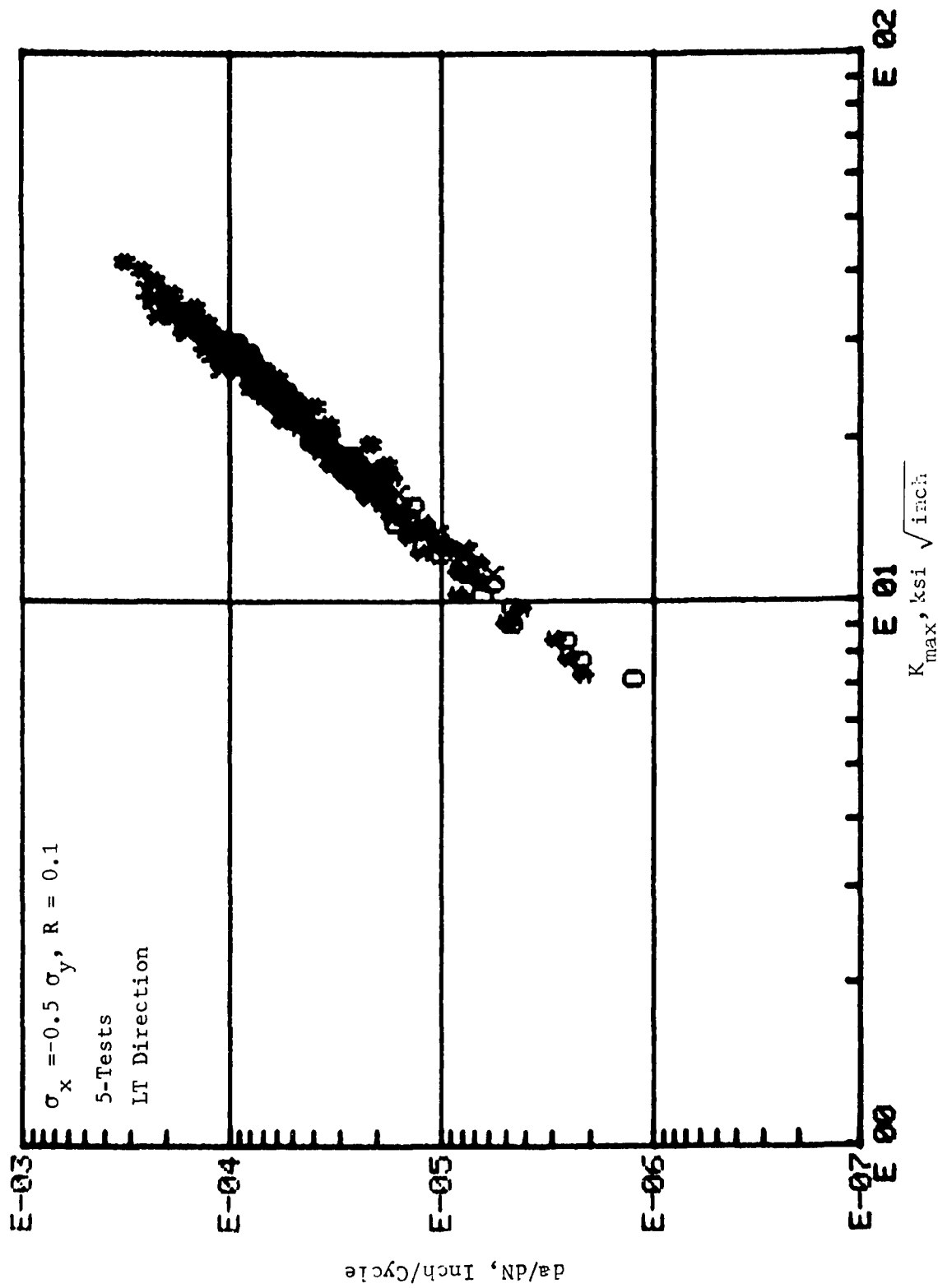


Figure 72. Cyclic Crack Growth Rate Behavior of 7075-T7351 Aluminum

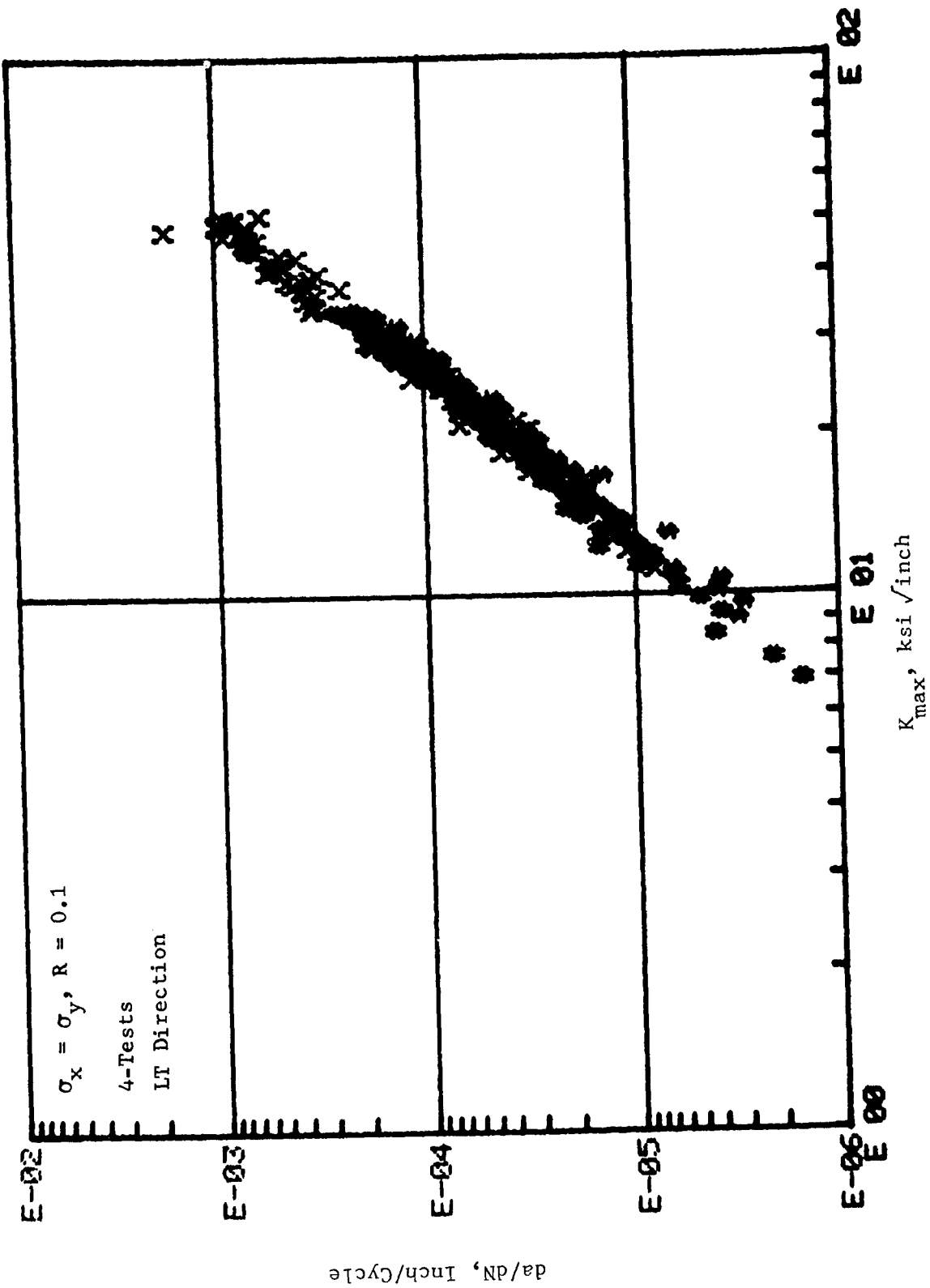


Figure 73. Cyclic Crack Growth Rate Behavior of 7075-T7351 Aluminum

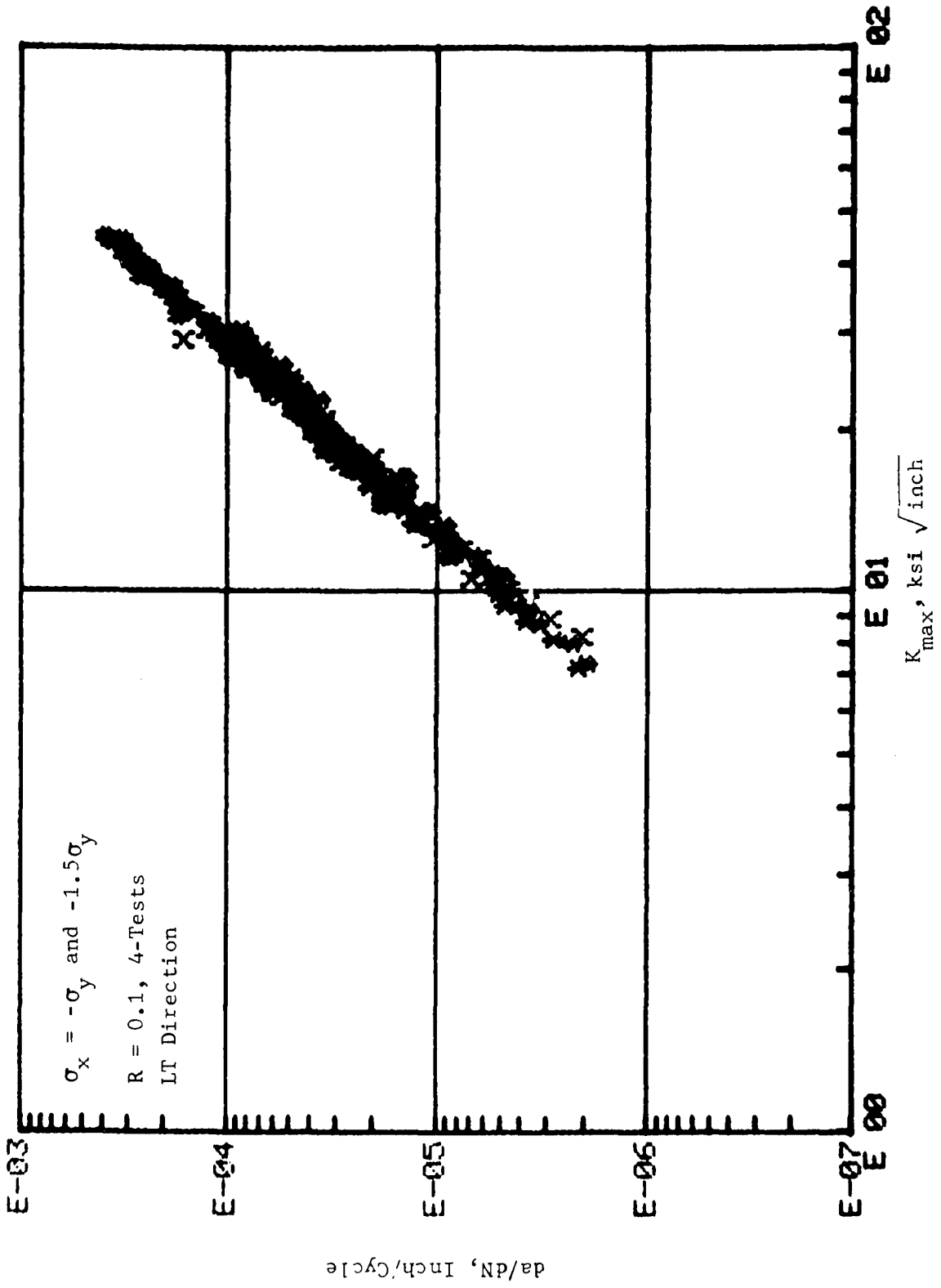


Figure 74. Cyclic Crack Growth Rate Behavior of 7075-T7351 Aluminum

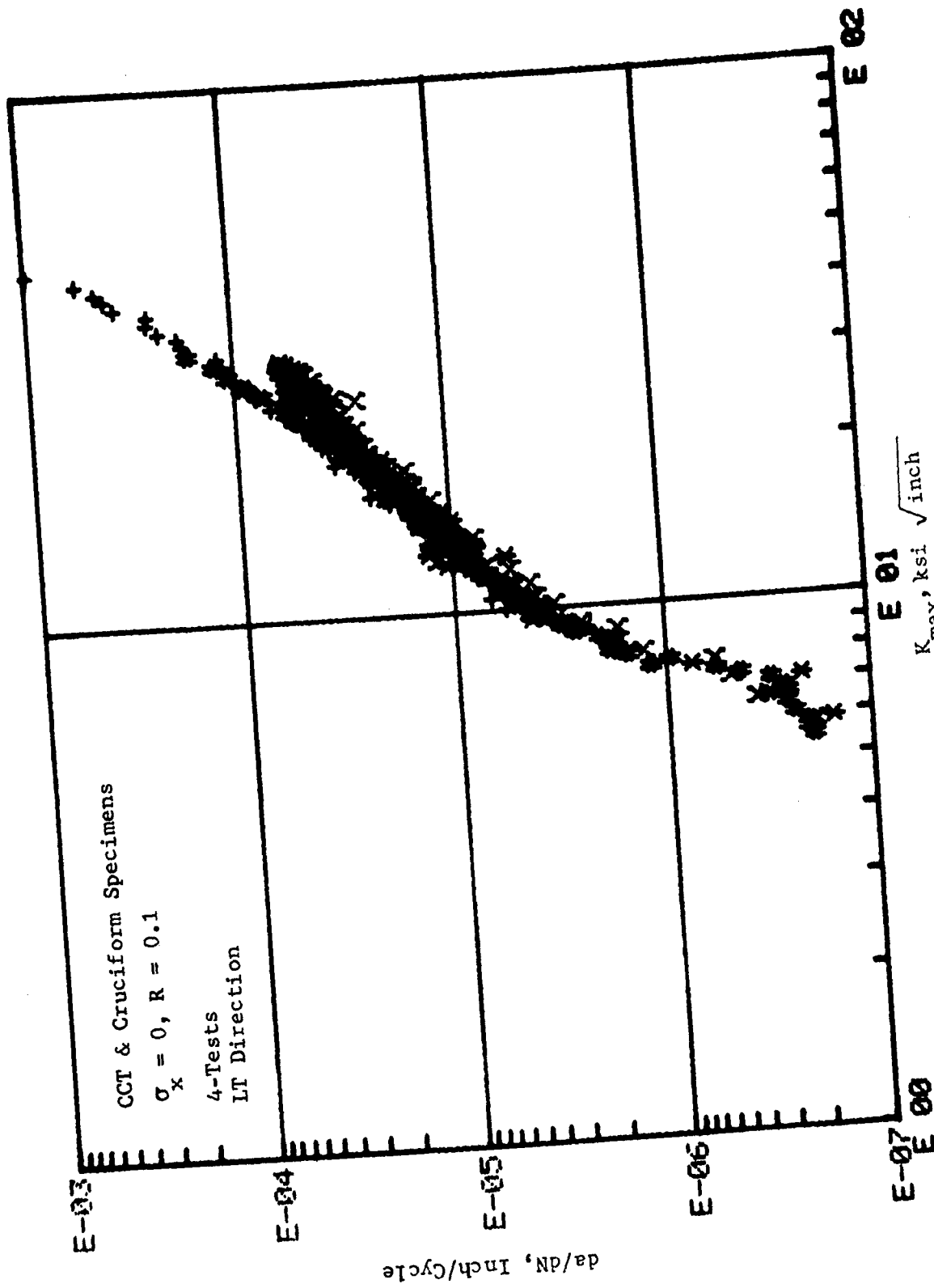


Figure 75. Cyclic Crack Growth Rate Behavior of 2024-T351 Aluminum

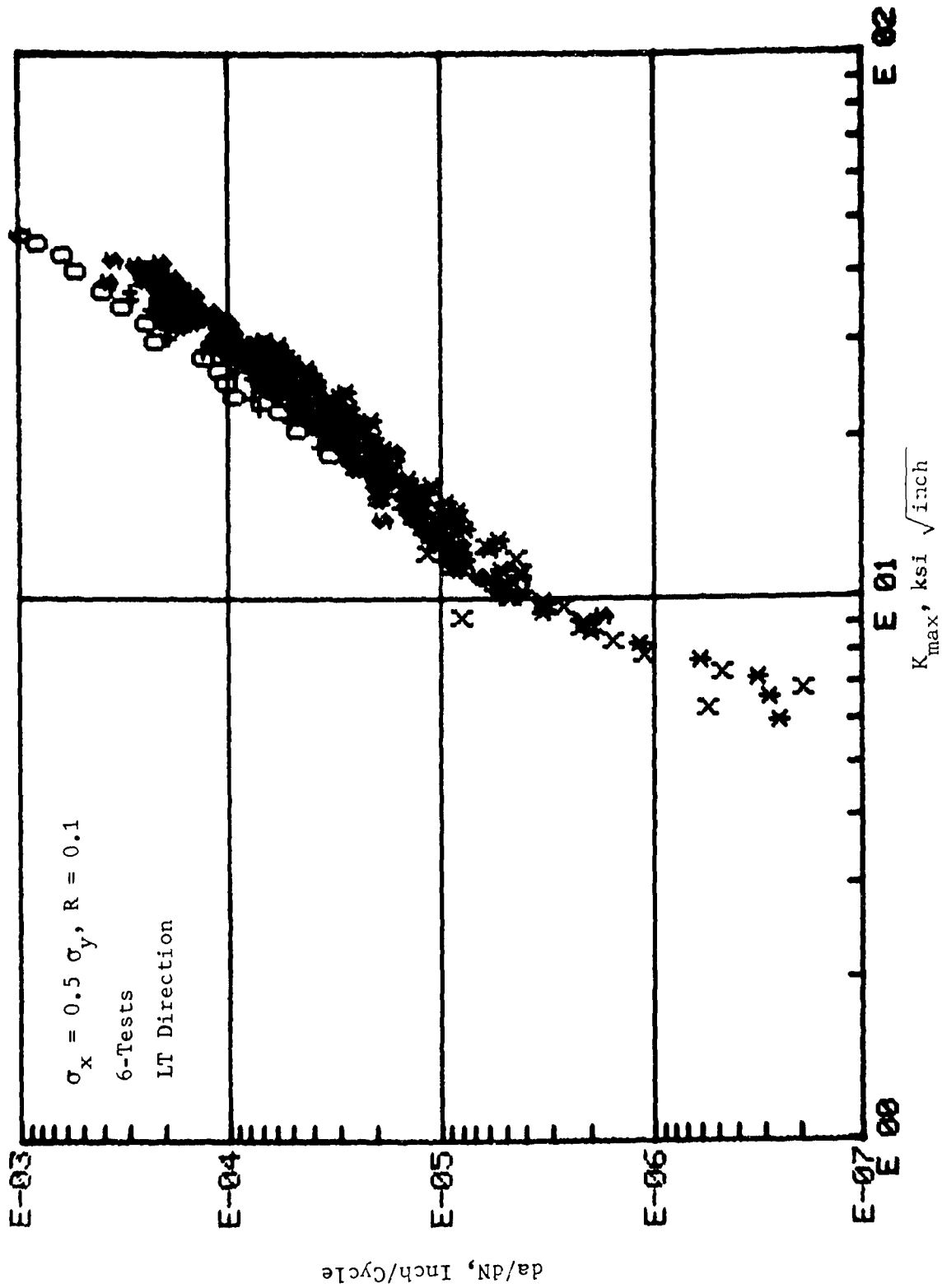


Figure 76. Cyclic Crack Growth Rate Behavior of 2024-T351 Aluminum

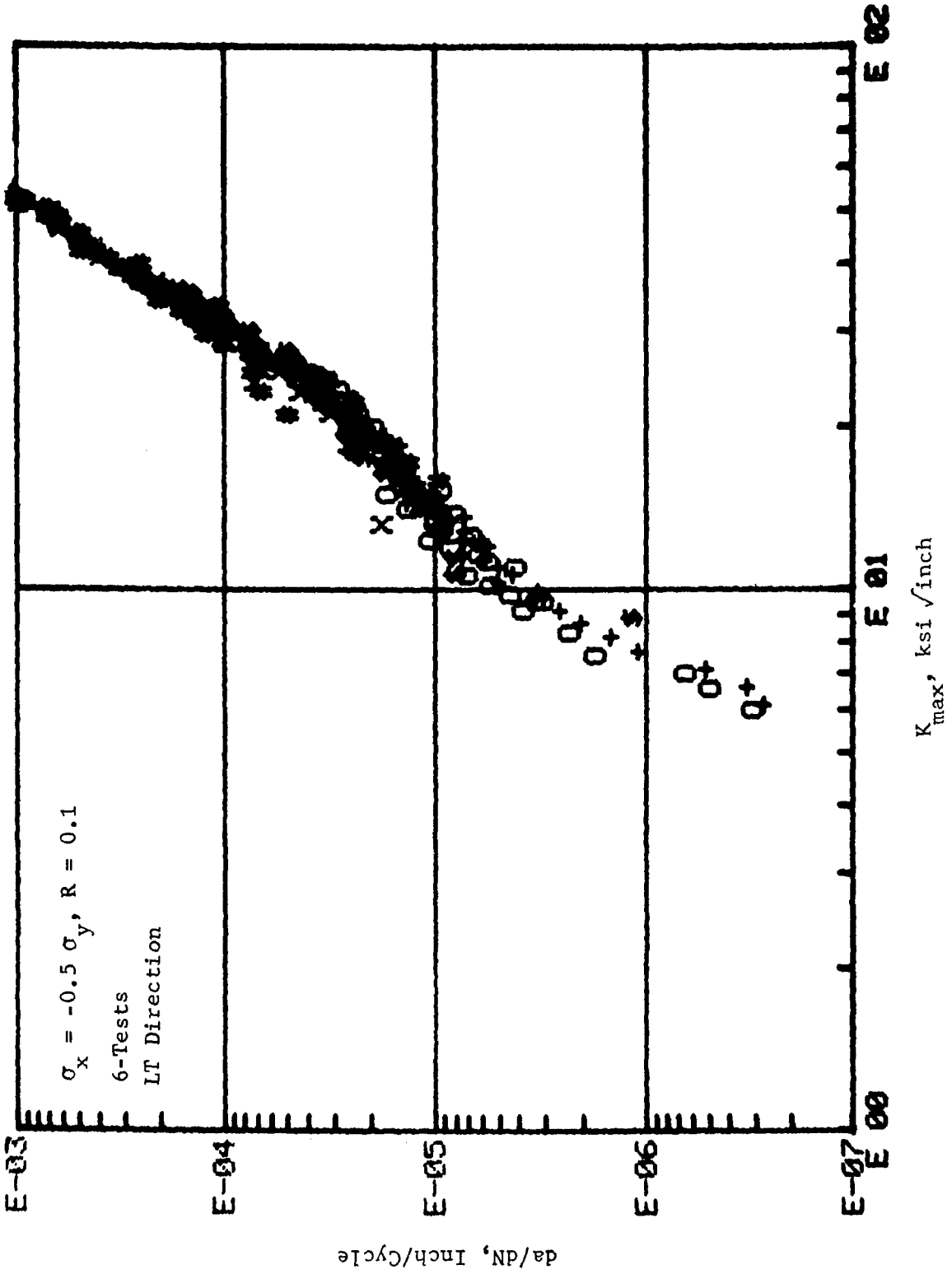


Figure 77. Cyclic Crack Growth Rate Behavior of 2024-T351 Aluminum

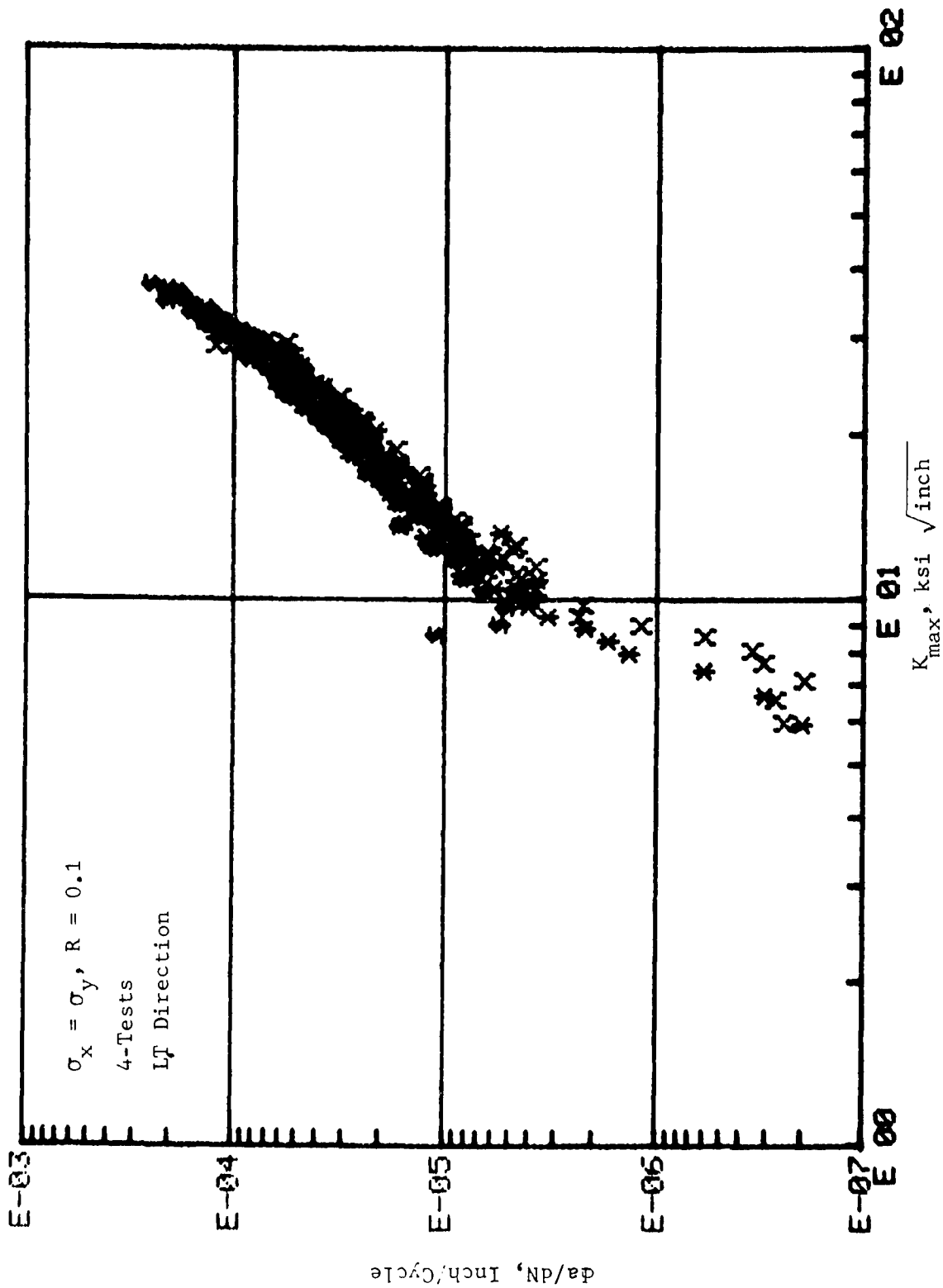


Figure 78. Cyclic Crack Growth Rate Behavior of 2024-T351 Aluminum

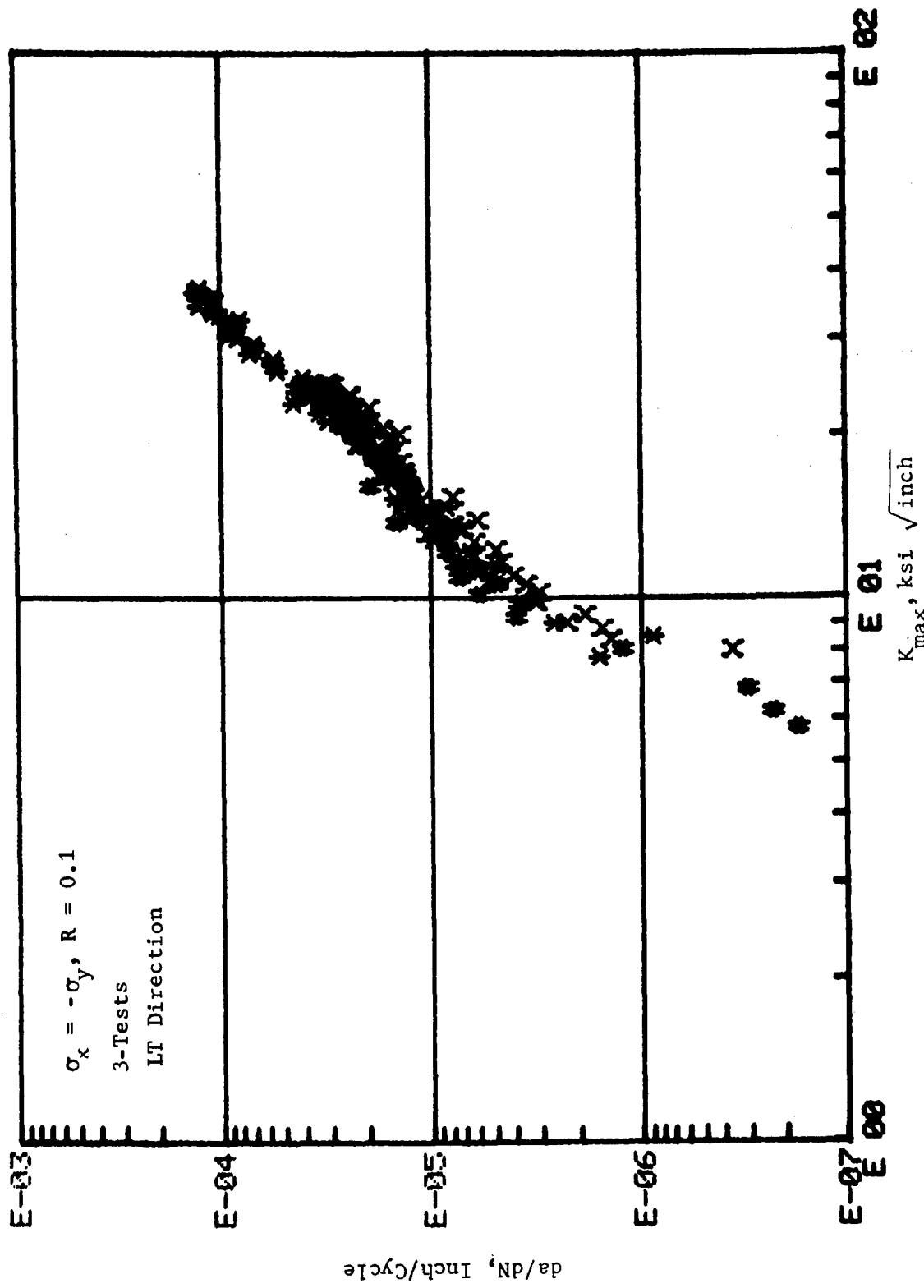


Figure 79. Cyclic Crack Growth Rate Behavior of 2024-T351 Aluminum

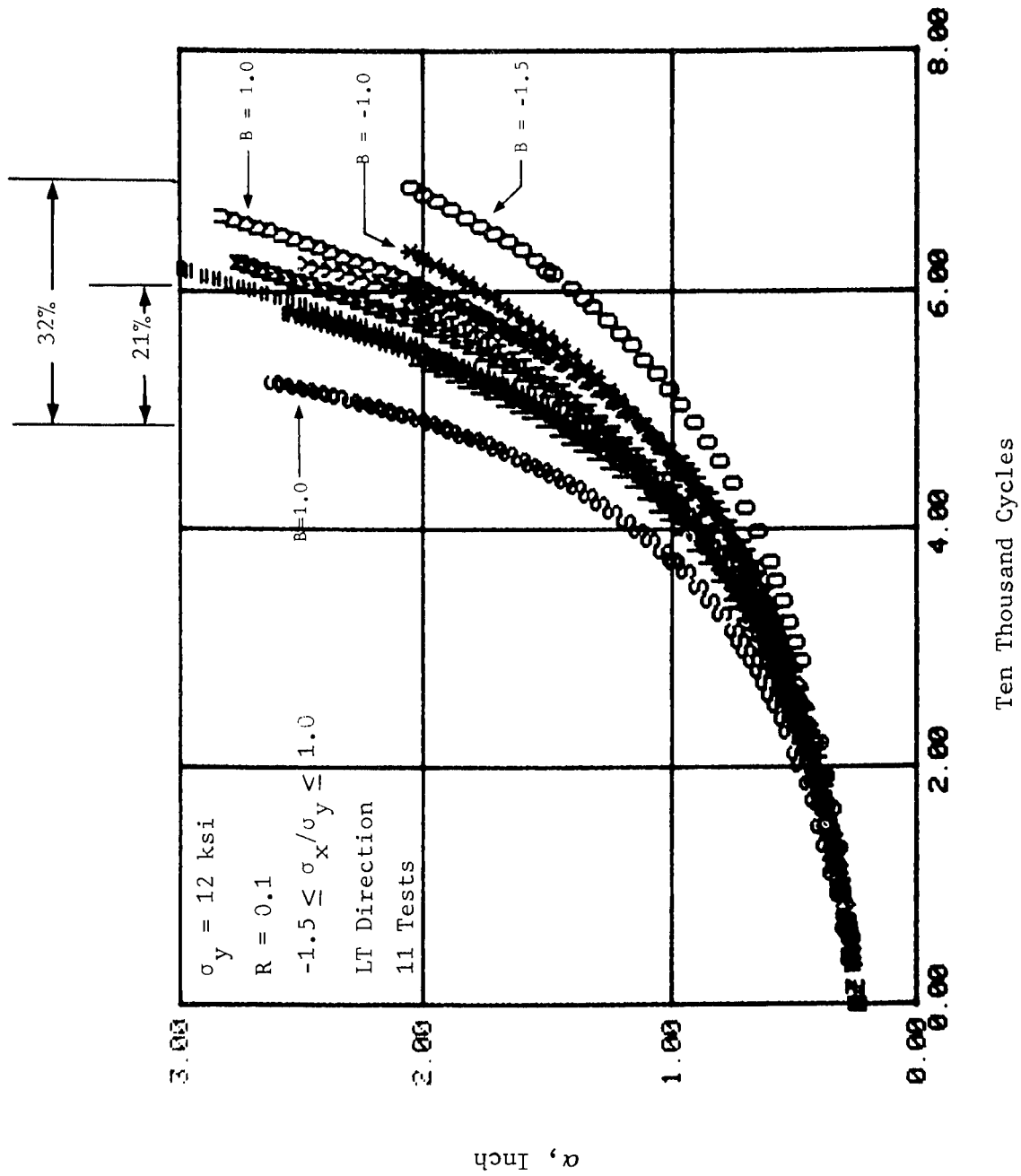


Figure 80. Crack Growth Histories of the 7075-T7351 Cruciform Specimen

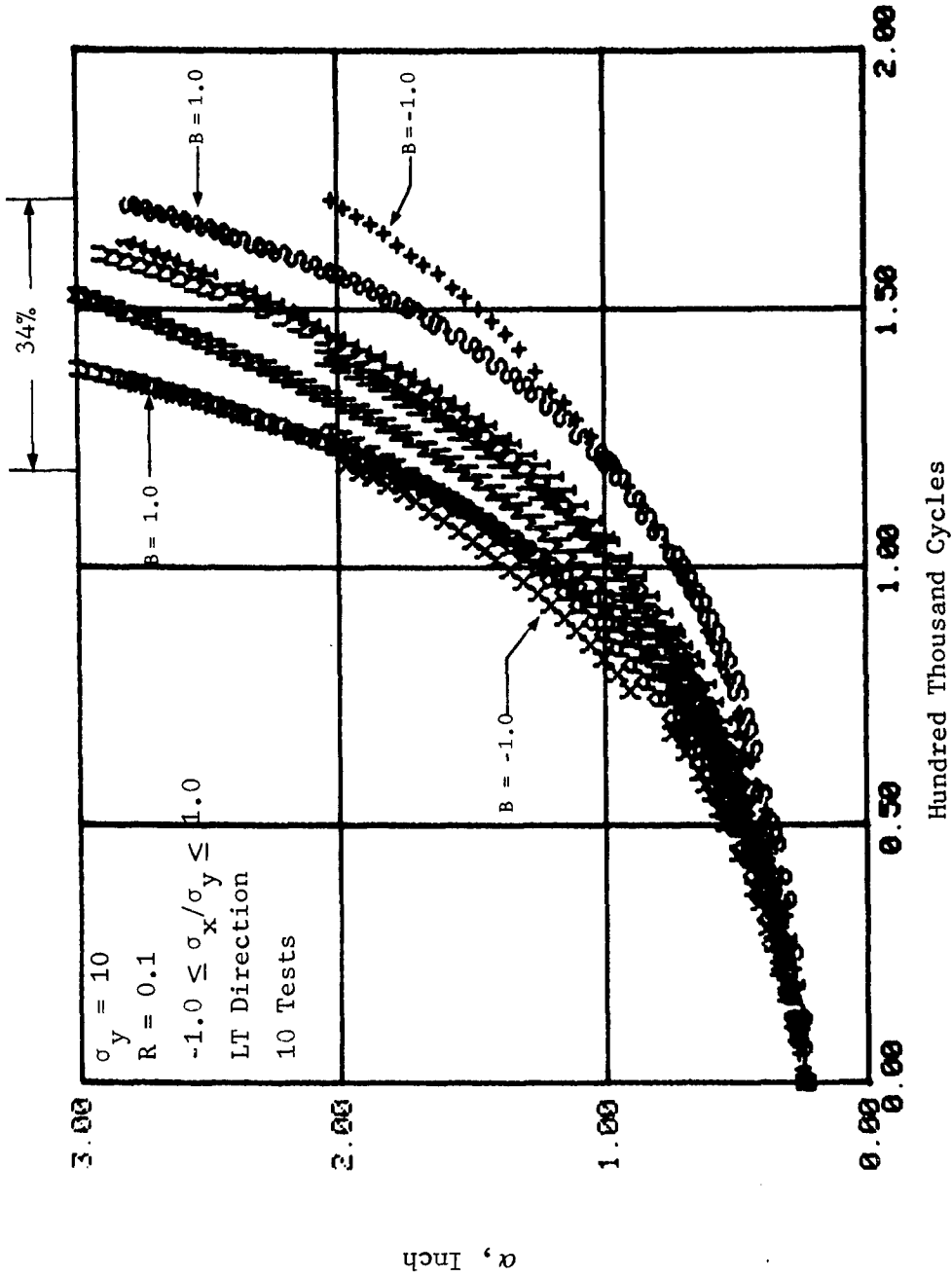


Figure 81. Crack Growth Histories of the 2024-T351 Cruciform Specimens

9.2.2 Correlation of High Biaxial Ratio Test Data

Three specimens (Test Case Nos. 141, 68 and 142) were tested under high biaxial ratio conditions. The biaxial stress ratios were 1.25, 1.50 and 1.75. The crack growth profiles for these tests are shown in Figures 82 to 84. It is seen in these figures that the crack turned away from its initial plane, and adjusted itself to become normal to the most dominating stress component, the higher the biaxial stress ratio, the sooner the crack would complete the crack path transitions.

There were two problems in the high biaxial stress ratio cases. The first problem was how to determine the K and the da/dN values and the second problem was how to predict the shape of the crack growth path. It was apparent that the crack growth rate (under constant amplitude loading conditions) should be the same for all biaxial ratios as long as the K values at the crack tip were appropriately determined. All the three methods discussed in Section 6.4 were evaluated and the results are discussed below.

The value of da for a curved crack is defined to be the distance connecting two consecutive measurements. Referring to Figure 16, the circles represent the polar photo grids printed on the cruciform specimen. Suppose one reading was taken at Point A and another reading was subsequently taken at Point B; da would be the distance between Points A and B as indicated in the figure. Then dN would be the difference between the number of cycles taken at Points A and B.

Stress intensity values for each data point (raw data are compiled in Volume II of this report) were computed and plotted against the associated da/dN values. The crack growth rate curves constructed by each of the three methods (for computing K) for each of the three tests are presented in Figures 85 to 93. Comparing all nine crack growth rate curves to the material baseline crack growth rate curve (Figure 94), it is revealed that all three methods generally correlate well with the uniaxial loading case. Table 5 presents a comparison of the K values calculated from all three methods for all three high biaxial ratio conditions. The comparisons were made by superimposing the baseline material da/dN versus K curve onto

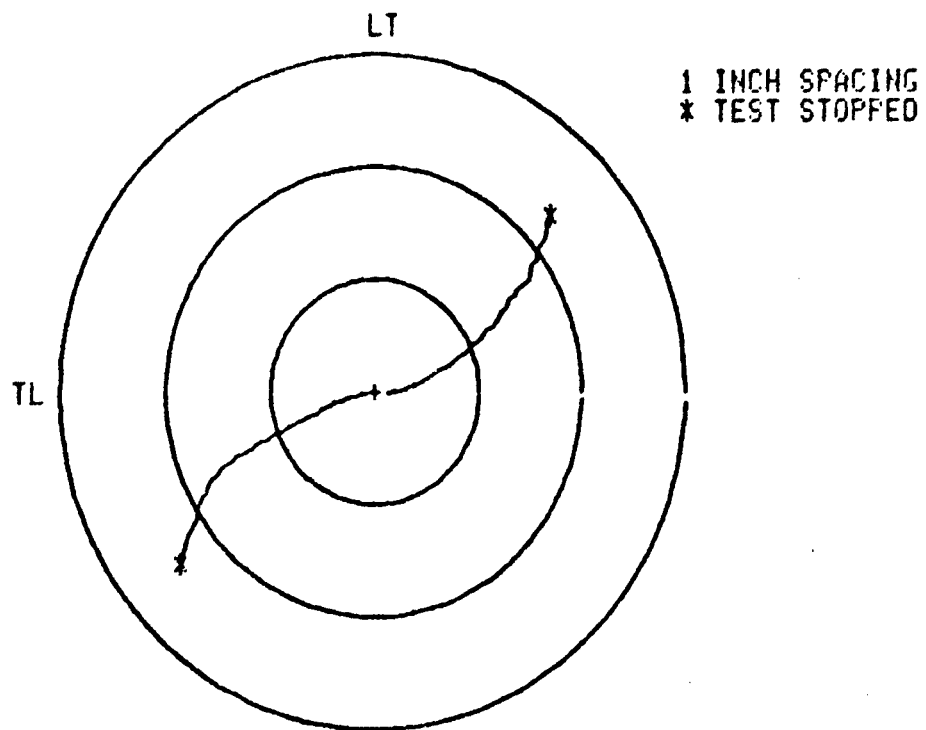


Figure 82. Crack Growth Profile of 7075-T7351
Cruciform Specimen No. 7-38
Test Case No. 141
 $\sigma_x = 15$ ksi, $\sigma_y = 12$ ksi, $R = 0.1$,
 $f = 5$ Hz

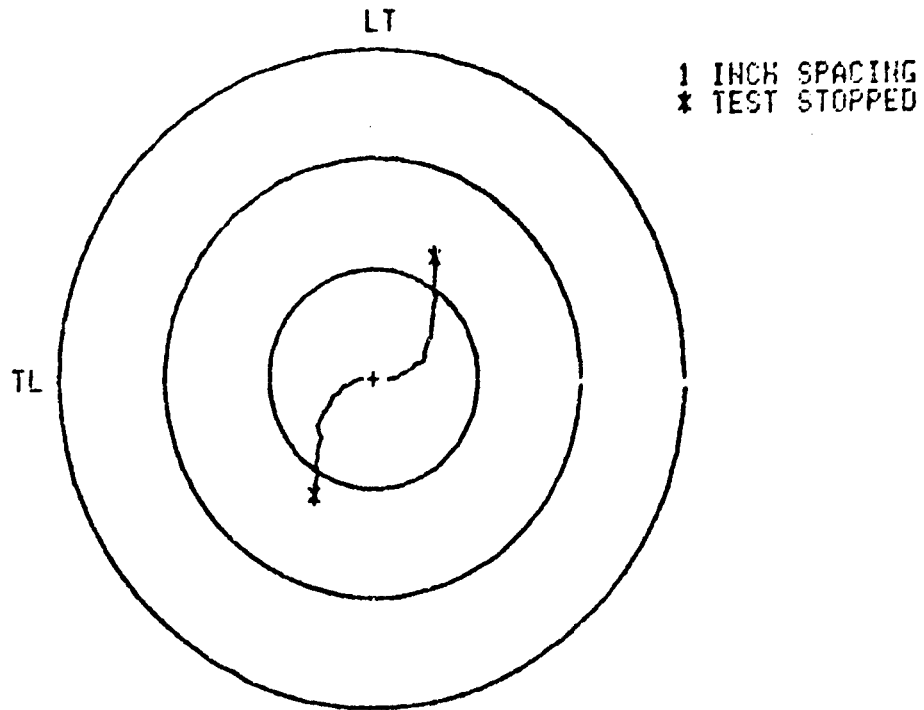


Figure 83. Crack Growth Profile of 7075-T7351
Cruciform Specimen No. 7-28
Test Case No. 68
 $\sigma_x = 18$ ksi, $\sigma_y = 12$ ksi, $R = 0.1$, $f = 5$ Hz

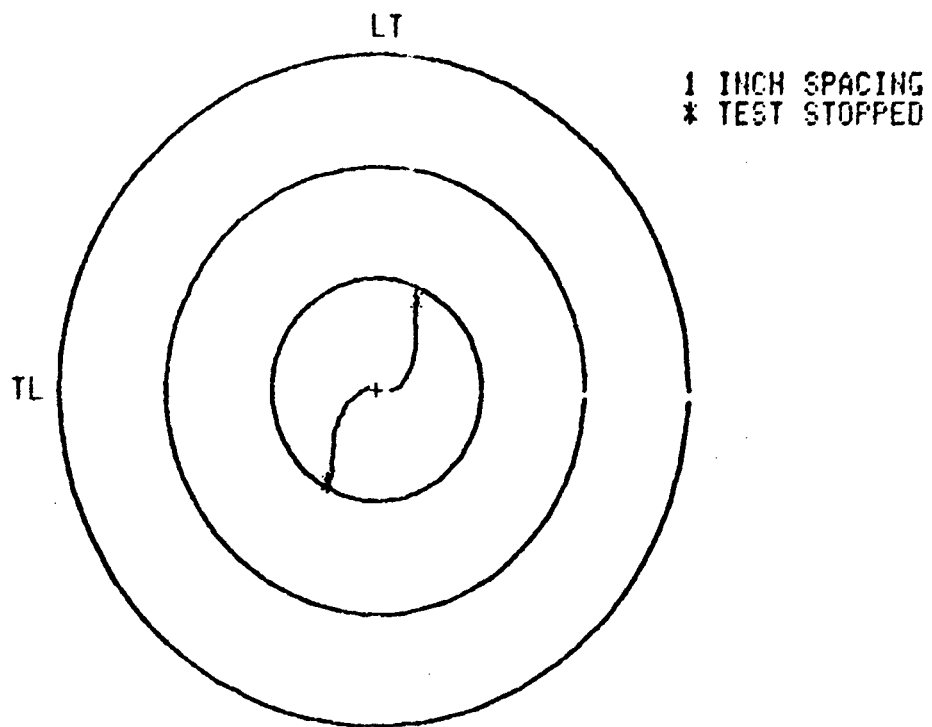


Figure 84. Crack Growth Profile of 7075-T7351
Cruciform Specimen No. 7-4
Test Case No. 142
 $\sigma_x = 21$ ksi, $\sigma_y = 12$ ksi, $R = 0.1$,
 $f = 5$ Hz

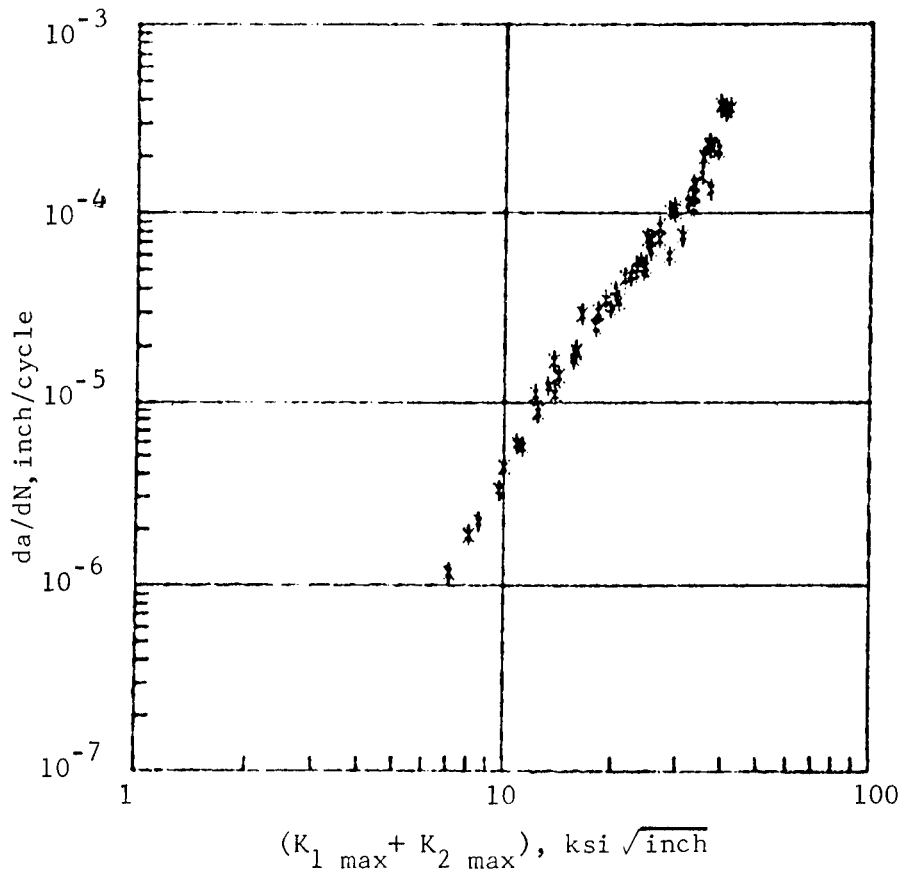


Figure 85. Crack Growth Rate Behavior of 7075-T7351
 Cruciform Specimen No. 7-38
 Test Case No. 141
 $\sigma_x = 15 \text{ ksi}$, $\sigma_y = 12 \text{ ksi}$, $R = 0.1$, $f = 5 \text{ Hz}$

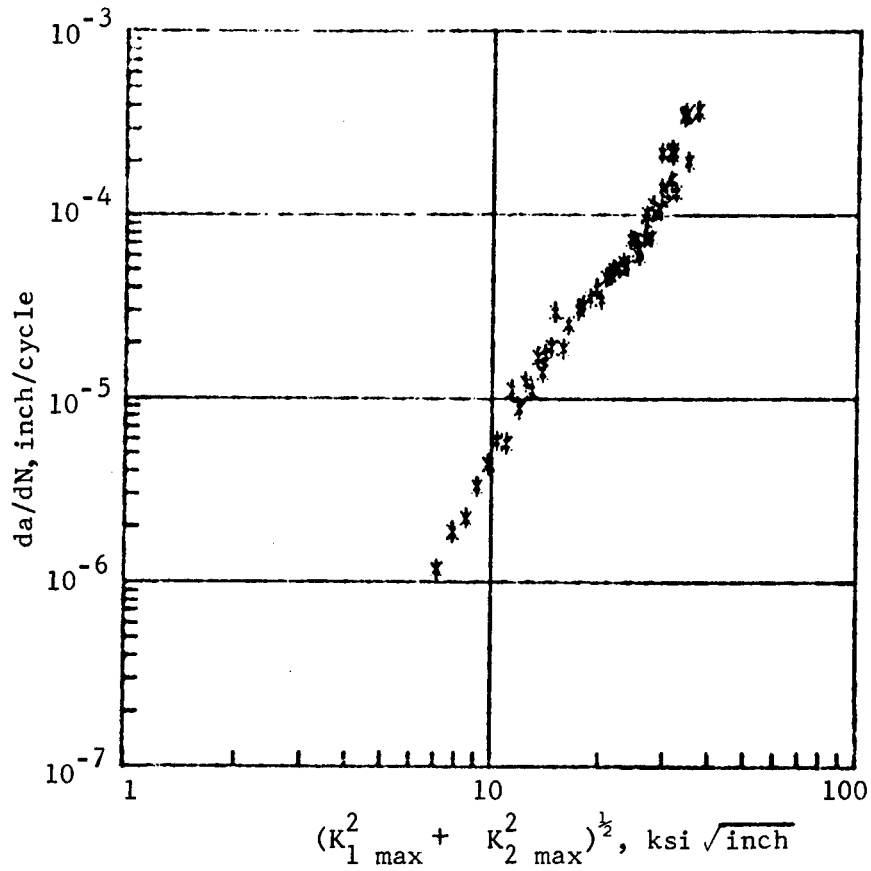


Figure 86. Crack Growth Rate Behavior of 7075-T7351
 Cruciform Specimen No. 7-38
 Test Case No. 141
 $\sigma_x = 15$ ksi, $\sigma_y = 12$ ksi, $R = 0.1$, $f = 5$ Hz

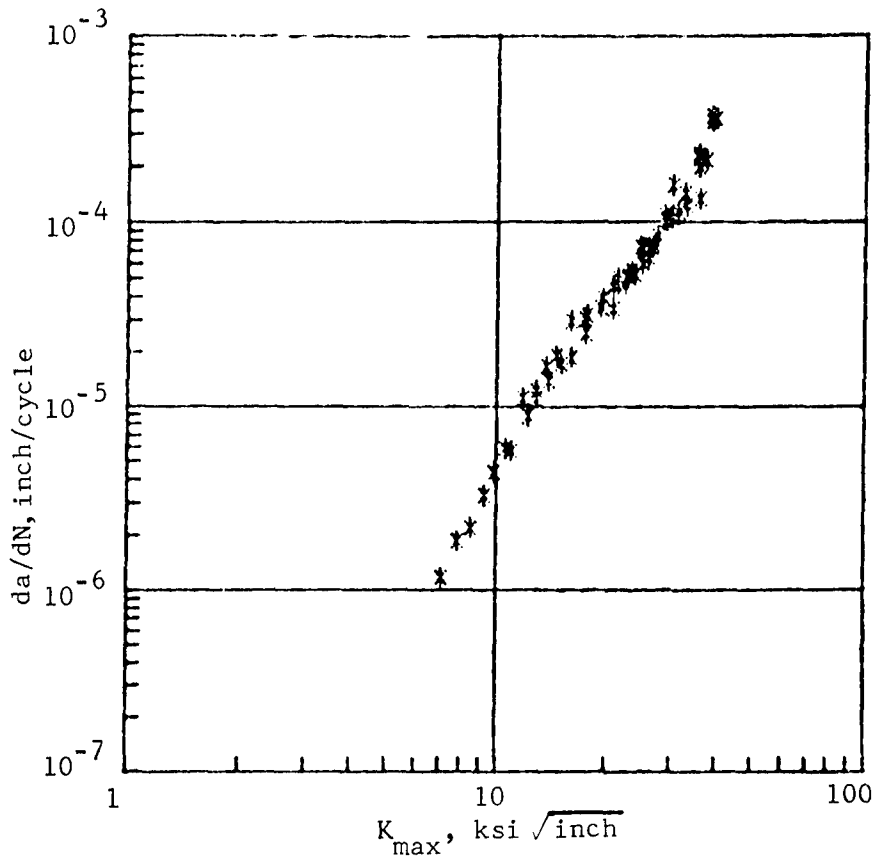


Figure 87. Crack Growth Rate Behavior of 7075-T7351
 Cruciform Specimen No. 7-38
 Test Case No. 141
 $\sigma_x = 15$ ksi, $\sigma_y = 12$ ksi, $R = 0.1$, $f = 5$ Hz

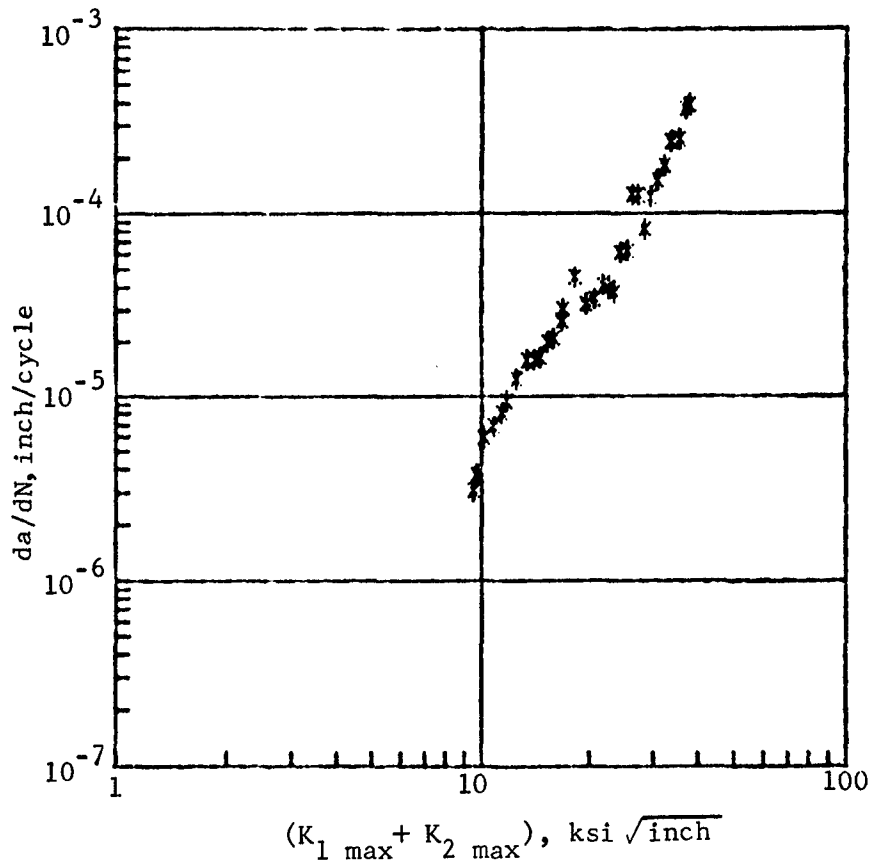


Figure 88. Crack Growth Rate Behavior of 7075-T7351
 Cruciform Specimen No. 7-28
 Test Case No. 68
 $\sigma_x = 18 \text{ ksi}$, $\sigma_y = 12 \text{ ksi}$, $R = 0.1$,
 $f = 5 \text{ Hz}$

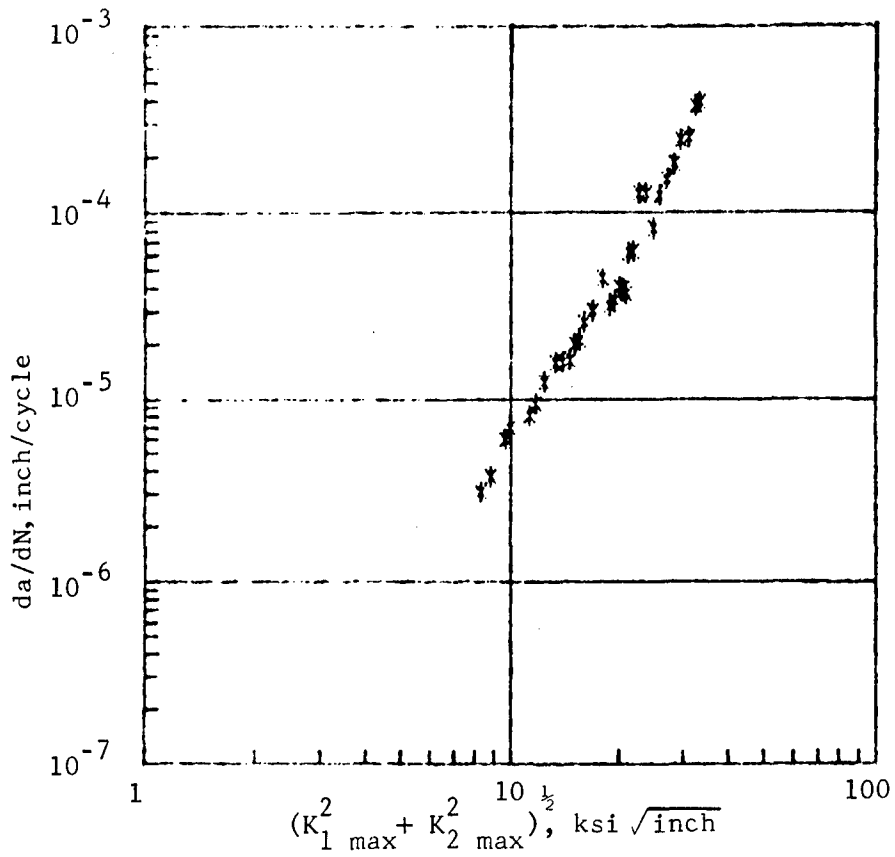


Figure 89. Crack Growth Rate Behavior of 7075-T7351
 Cruciform Specimen No. 7-28
 Test Case No. 68
 $\sigma_x = 18 \text{ ksi}, \sigma_y = 12 \text{ ksi}, R = 0.1, f = 5 \text{ Hz}$

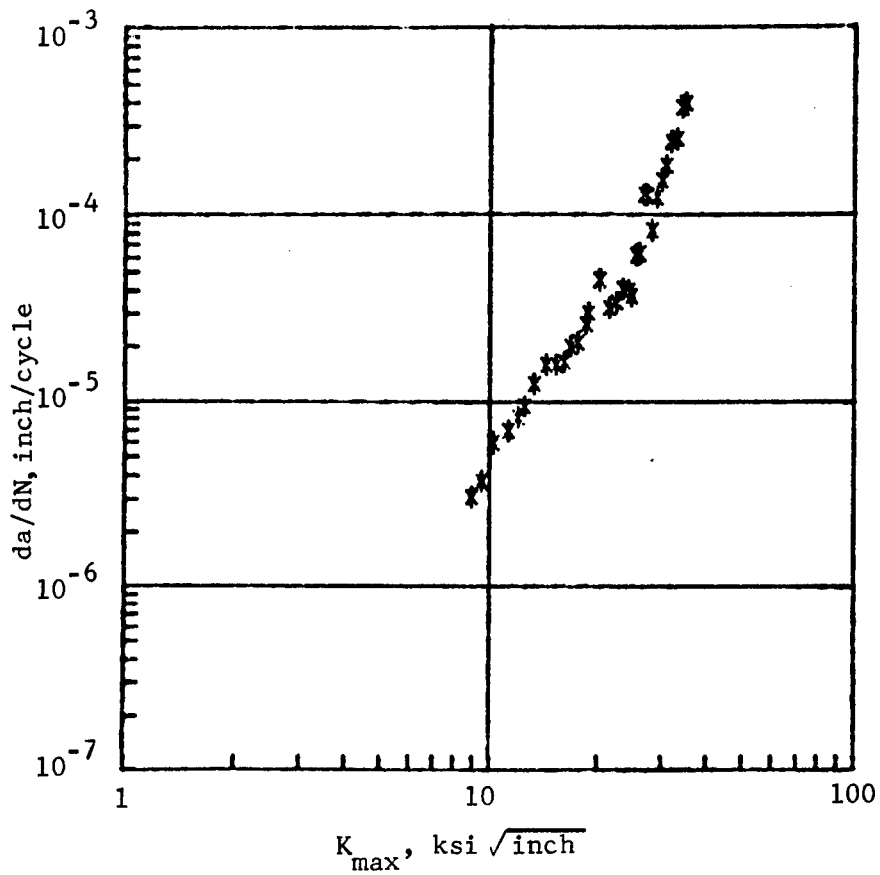


Figure 90. Crack Growth Rate Behavior of 7075-T7351
 Cruciform Specimen No. 7-28
 Test Case No. 68
 $\sigma_x = 18 \text{ ksi}, \sigma_y = 12 \text{ ksi}, R = 0.1, f = 5 \text{ Hz}$

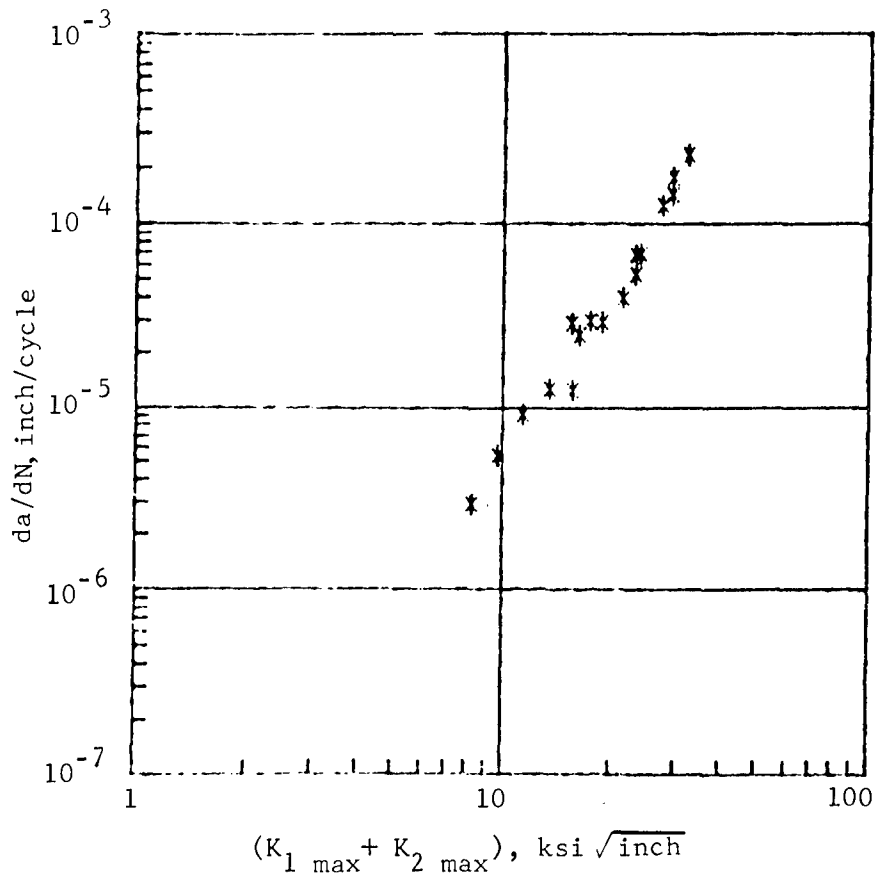


Figure 91. Crack Growth Rate Behavior of 7075-T7351
 Cruciform Specimen No. 7-4
 Test Case No. 142
 $\sigma_x = 21$ kis, $\sigma_y = 12$ ksi, $R = 0.1$, $f = 5$ Hz

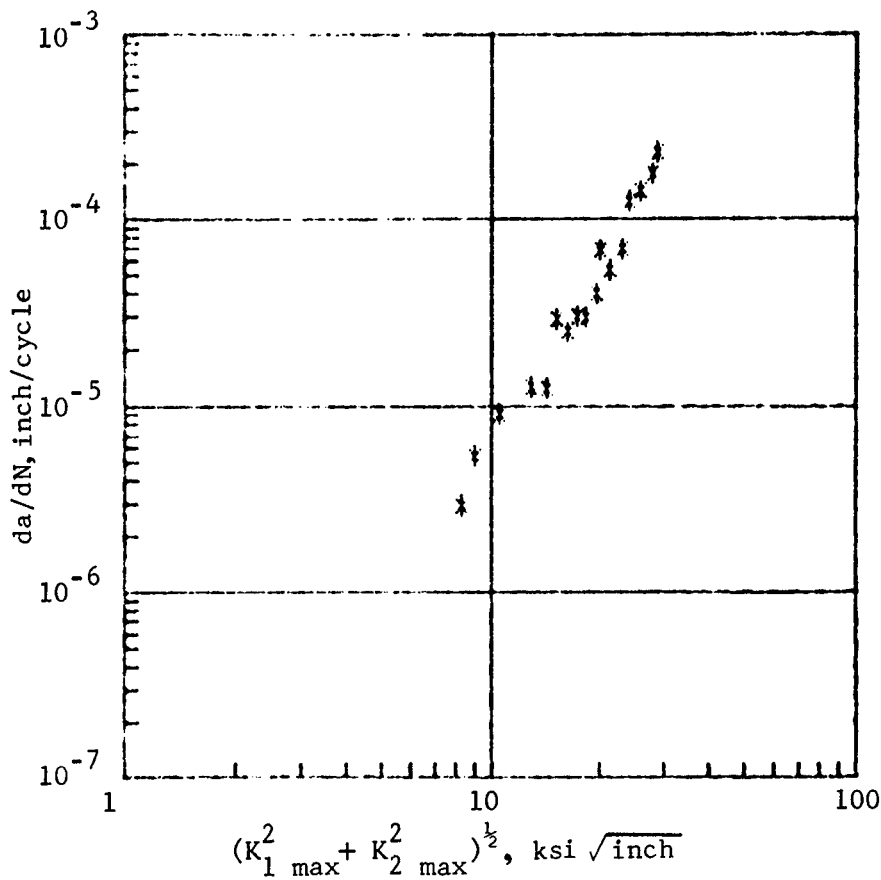


Figure 92. Crack Growth Rate Behavior of 7075-T7351
 Cruciform Specimen No. 7-4
 Test Case No. 142
 $\sigma_x = 21$ ksi, $\sigma_y = 12$ ksi, $R = 0.1$, $f = 5$ Hz

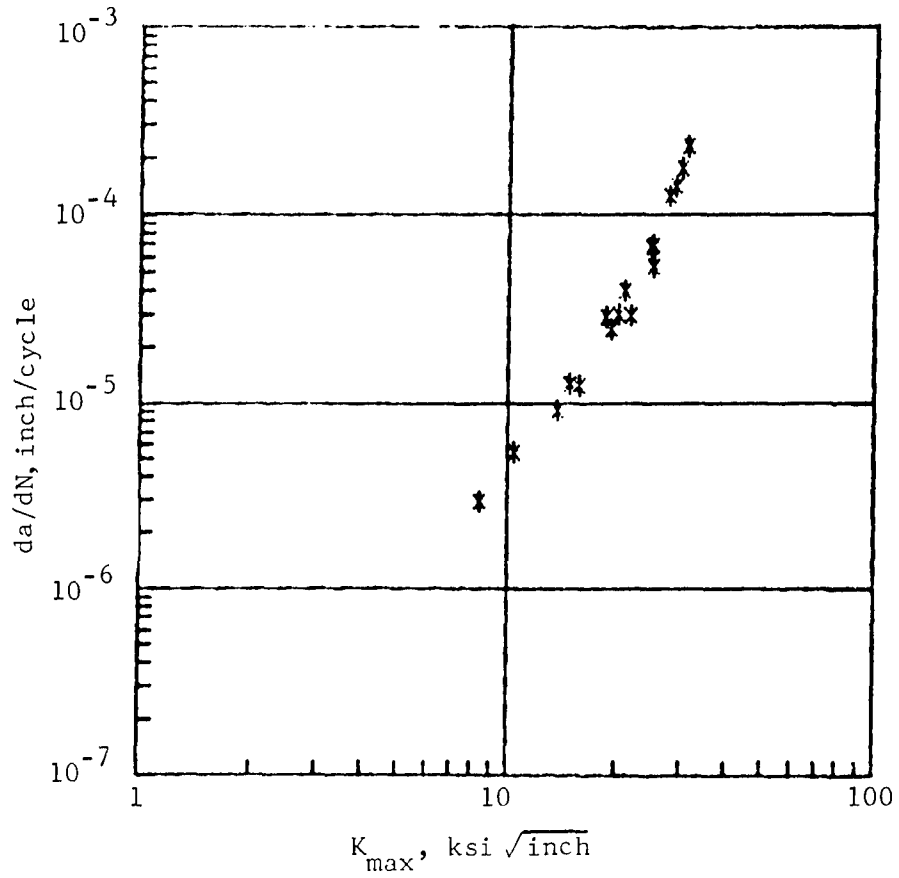


Figure 93. Crack Growth Rate Behavior of 7075-T7351
 Cruciform Specimen No. 7-4
 Test Case No. 142
 $\sigma_x = 21$ kis, $\sigma_y = 12$ ksi, $R = 0.1$, $f = 5$ Hz

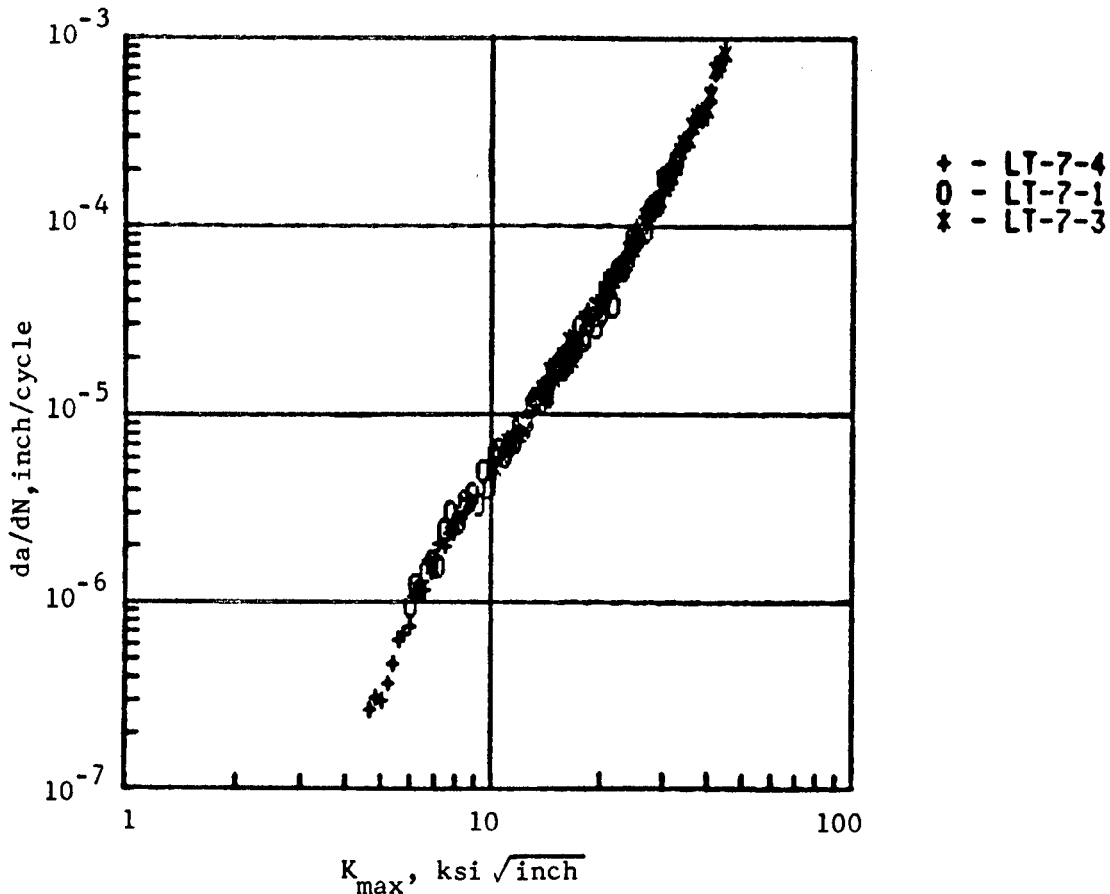


Figure 94. Baseline Crack Growth Rate Behavior for 7075-T7351, LT Direction (CCT Specimen, $R = 0.1$, $f = 5$ Hz)

each of these nine crack growth rate curves. The precision of the calculated K values was judged by comparing the K for the uniaxial case with a K calculated by a particular method, at a selected da/dN value. It is seen, from Table 5, that the total sum of K_1 and K_2 method seem to offer quite reasonable results. The vector sum of K_1 and K_2 method generally calculates a K value lower than expected. In contrast, the "equivalent a " method sometimes produces a K value slightly higher than expected. The perfect matches in the upper and lower da/dN regions where the crack was normal to σ_y and σ_x , respectively, obtained from the last method strongly suggested that stress intensity factor, crack growth rate and crack growth direction are controlled by the most dominating stress, not the principal stress, in a given stress field.

TABLE 5. COMPARISON BETWEEN ANALYSIS METHODS FOR A CURVED CRACK

METHOD	da/dN RANGE	BIAXIAL STRESS RATIO, σ_x/σ_y		
		1.25	1.5	1.75
$K = \sigma \sqrt{\pi a}$	Below 3×10^{-5}	Perfect	Perfect	Perfect
	Between 3×10^{-5} & 10^{-4}	Slightly Too High	Too High	Slightly Too High
	Above 10^{-4}	Too High	Perfect	Perfect
$K = \sqrt{K_1^2 + K_2^2}$	Below 3×10^{-5}	Perfect	Perfect	Perfect
	Between 3×10^{-5} & 10^{-4}	Too Low	Perfect	Too Low
	Above 10^{-4}	Perfect	Too Low	Too Low
$K = K_1 + K_2$	Below 3×10^{-5}	Perfect	Perfect	Perfect
	Between 3×10^{-5} & 10^{-4}	Too High	Perfect	Perfect
	Above 10^{-4}	Too High	Perfect	Perfect

A few words are given here to explain why the calculated K values were too high in the 1.25 biaxial ratio case. As it can be observed in Figures 82 to 84, the cracks in the other two higher biaxial ratio tests were relatively short and more importantly the entire crack path of these cracks were very close to the X and Y planes of the specimen. Therefore, the magnitude of the stress components, σ_x and σ_y , along the crack, were very much the same as those previously reported in Sections 4 and 5. Since the crack was long and far away from either the X and Y axis in the 1.25 biaxial ratio specimen, in the region where the crack was long, the magnitude of the stress components (or the biaxial ratio) might not be exactly the same, as could be expected.

After the best suited procedure for calculating K is selected, the second problem would be how to set up a mathematical procedure which can predict the entire crack propagation path of a crack starting from any initial length and angle. The computerized procedure discussed in Section 8.1 was applied to predict the crack growth history for Test Case No. 142 (B = 1.75). In this analysis, the Collipriest Equation, 42, was used to represent the baseline material crack growth rate behavior.

$$\frac{da}{dN} = C(K_{Cr} \cdot \Delta K_0)^{n/2} \cdot \text{EXP}[\gamma \cdot \ln(K_{Cr}/\Delta K_0)^{n/2}]$$

with

$$\gamma = \text{arctanh} \frac{\ln[\Delta K^2 / ((1 - R)K_{Cr} \cdot \Delta K_0)]}{\ln[(1 - R)K_{Cr}/\Delta K_0]} \quad (36)$$

The empirical constants K_{Cr} , ΔK_0 , C, and n, for the CCT specimen (in the LT direction) for both aluminum alloys were determined and are presented in Figures 95 and 96. Numerous computer runs were made using different combinations in empirical crack growth rate constants (i.e., different crack growth rate curves were fitted between the middle and the upper bounds of the CCT da/dN data). The best two of the computer runs are presented in

Tables 6 and 7. The results are compared to the actual test results shown in Table 8. In these two predictions, one of them exhibited good correlation on a_x (too fast on a_y) whereas the other one showed good correlation on a_y (too slow on a_x). The crack growth rate constants used in these two analyses were almost identical (only a small difference in C, 0.016 versus 0.0155, while the other three constants were the same in both analyses). Therefore, it is apparent that sensitivity is very high in this type of analysis. However, it is anticipated that improvements can be accomplished through obtaining an improved crack angle relationship, or using separate sets of da/dN constants for the da_x and the da_y components, etc. An important point to be made here is that the present crack growth concept, and approach, can be useful; a refined computational procedure can be developed following the aforementioned modifications.

9.3 The Effect of Cyclic Stress Ratio

Twelve cruciform specimens were tested at cyclic stress ratio of 0.7. The testing conditions for these specimens are listed in Table 9. A complete set of the crack growth rate curves and the tabulation of a versus N data are compiled in Volume II of this report. Typical crack growth rate curves (for $\sigma_x = 0$ and $\sigma_x = \pm \sigma_y$) are presented in Figures 97 to 100. Comparing these curves, it is seen that the biaxial stress effect is also negligible at $R = 0.7$. Furthermore, the cracks grew straight in all the tests (see Volume II).

9.4 Crack Coming Out From a Hole Tests

Ten specimens of the 7075-T7351 aluminum alloy containing either a 0.25 inch diameter hole or a 0.75 inch diameter hole were tested under three biaxial stress ratios ($\sigma_x = 0$, $\sigma_x = \pm \sigma_y$, see Table 10). The cyclic stress amplitude for all the ten tests was 0.1. Two of the ten tests were crack initiation tests. The remaining eight specimens contained very small saw cuts at both sides of the hole. Crack growth history for each test was recorded. A complete set of a versus N data and da/dN versus K_{\max} curves are compiled in Volume II of this report. The K values were calculated using the superposition technique (previously discussed in Section 6.3).

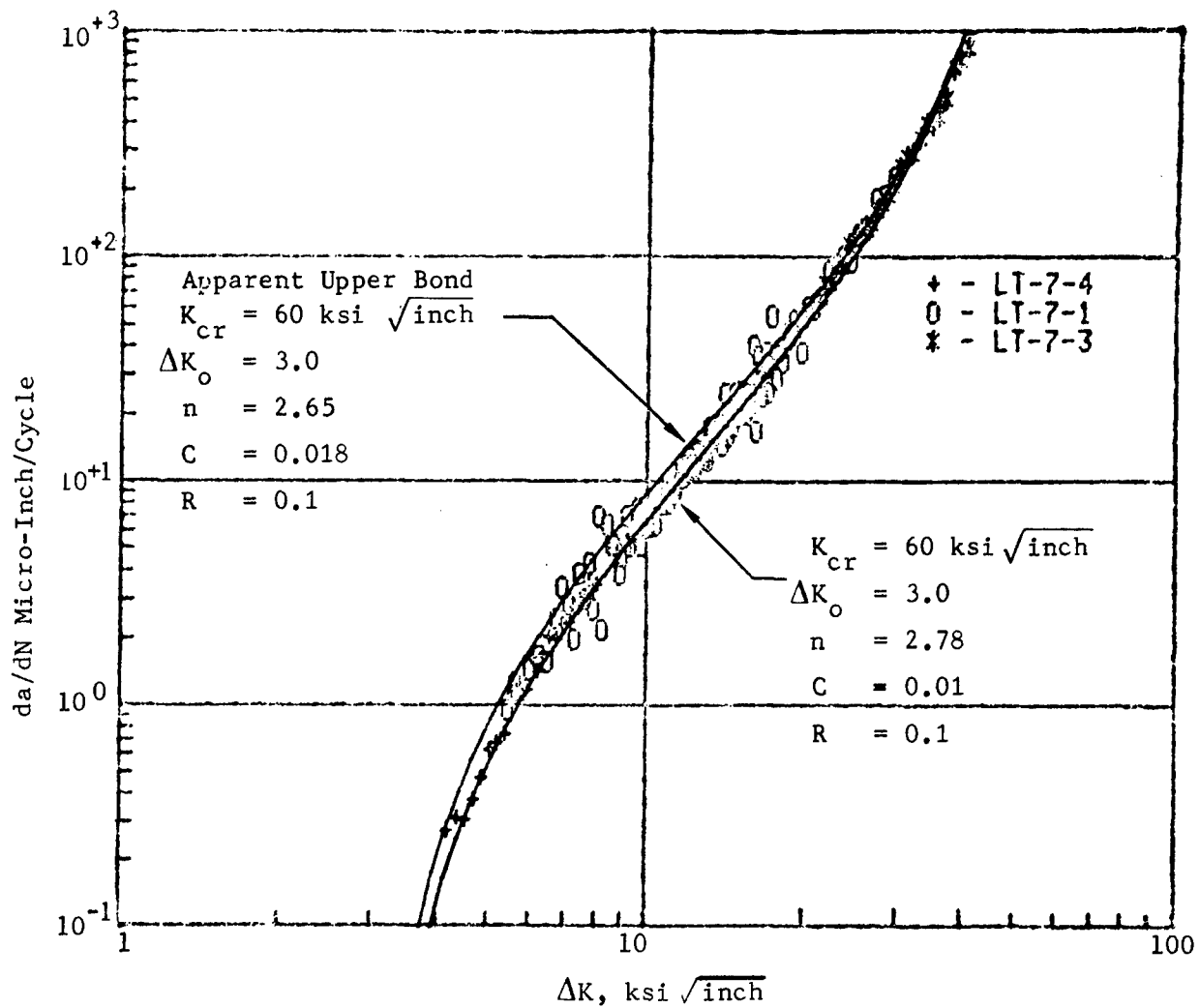


Figure 95. Baseline Crack Growth Rate Behavior
 for 7075-T7351, LT Direction
 (CCT Specimens, $R = 0.1$, $f = 5 \text{ Hz}$)

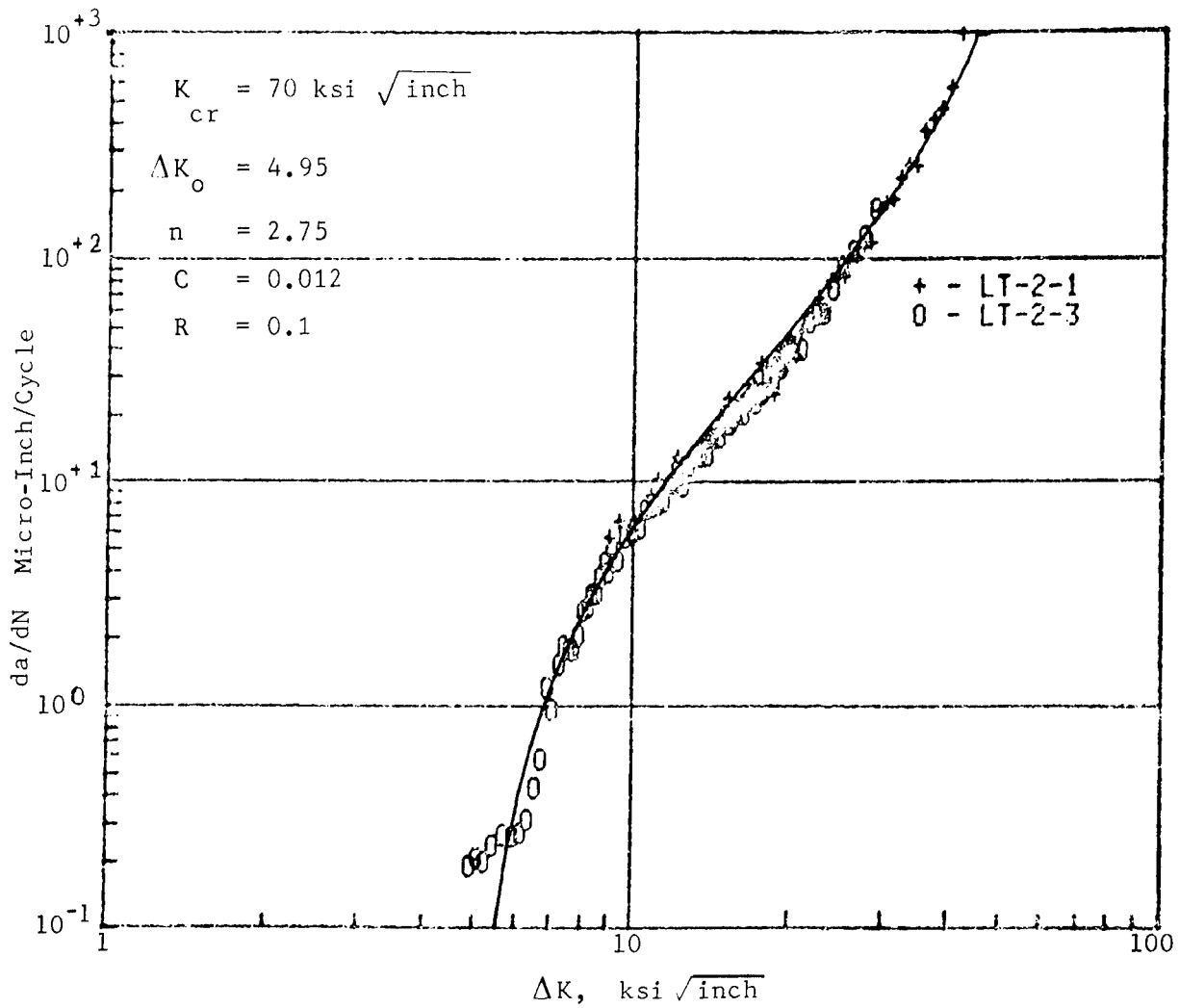


Figure 96. Baseline Crack Growth Rate Behavior for 2024-T351, LT Direction (CCT Specimens, $R = 0.1$, $f = 5\text{Hz}$)



TABLE 6. PREDICTED CRACK GROWTH HISTORY OF A 7075-T7351 SPECIMEN

STEP	(AX)	(AY)	KMAX	DADN	ACCUM. CYCLES
1	0.0027	0.1075	7.1274	0.2013D-05	0.0
2	0.0058	0.1373	8.1793	0.3199D-05	11790.0
3	0.0121	0.1744	9.4532	0.4998D-05	21200.0
4	0.0190	0.2022	10.4205	0.6645D-05	26170.0
5	0.0276	0.2284	11.3642	0.8501D-05	29850.0
6	0.0369	0.2516	12.2304	0.1044D-04	32500.0
7	0.0614	0.2980	14.1138	0.1549D-04	36640.0
8	0.0828	0.3294	15.5208	0.2011D-04	38800.0
9	0.0940	0.3437	16.2022	0.2265D-04	39650.0
10	0.1115	0.3640	17.2159	0.2682D-04	40740.0
11	0.1317	0.3852	18.3229	0.3196D-04	41740.0
12	0.1564	0.4083	19.6007	0.3877D-04	42700.0
13	0.1982	0.4427	21.6321	0.5185D-04	43910.0
14	0.2153	0.4554	22.4247	0.5783D-04	44300.0
15	0.2473	0.4774	23.8468	0.7000D-04	44910.0
16	0.3069	0.5137	26.3385	0.9678D-04	45760.0
17	0.3505	0.5373	28.0487	0.1203D-03	46220.0
18	0.4085	0.5657	30.1975	0.1576D-03	46690.0
19	0.4637	0.5902	32.1251	0.2008D-03	47030.0
20	0.5064	0.6077	33.5443	0.2404D-03	47240.0
21	0.5982	0.6419	36.4158	0.3486D-03	47580.0
22	0.6533	0.6606	38.0332	0.4328D-03	47730.0
23	0.7242	0.6829	40.0110	0.5697D-03	47880.0
24	0.7928	0.7030	41.8247	0.7427D-03	47990.0



Test Case No. 142, B = 1.75, R = 0.1

Collipriest's Crack Growth Rate Constants:

$$K_{cr} = 60.0 \text{ ksi} \sqrt{\text{inch}}$$

$$\Delta K_o = 3.0 \text{ ksi} \sqrt{\text{inch}}$$

$$C = 0.016$$

$$n = 2.65$$

TABLE 7. PREDICTED CRACK GROWTH HISTORY OF A 7075-T7351 SPECIMEN

STEP	(AX)	(AY)	KMAX	UADN	ACCUM. CYCLES
1	0.0027	0.1075	7.1274	0.1950D-05	0.0
2	0.0056	0.1361	8.1392	0.3050D-05	11790.0
3	0.0114	0.1712	9.3436	0.4676D-05	21200.0
4	0.0176	0.1971	10.2408	0.6123D-05	26170.0
5	0.0250	0.2212	11.1009	0.7709D-05	29850.0
6	0.0329	0.2422	11.8751	0.9314D-05	32500.0
7	0.0529	0.2836	13.5070	0.1330D-04	36640.0
8	0.0697	0.3110	14.6824	0.1672D-04	38800.0
9	0.0783	0.3233	15.2363	0.1852D-04	39650.0
10	0.0914	0.3405	16.0480	0.2137D-04	40740.0
11	0.1062	0.3581	16.9150	0.2473D-04	41740.0
12	0.1236	0.3769	17.8853	0.2892D-04	42700.0
13	0.1518	0.4042	19.3674	0.3628D-04	43910.0
14	0.1628	0.4139	19.9237	0.3939D-04	44300.0
15	0.1825	0.4305	20.8909	0.4527D-04	44910.0
16	0.2167	0.4565	22.4893	0.5652D-04	45760.0
17	0.2356	0.4723	23.5119	0.6486D-04	46220.0
18	0.2673	0.4902	24.7060	0.7593D-04	46690.0
19	0.2908	0.5045	25.6865	0.8623D-04	47030.0
20	0.3072	0.5139	26.3516	0.9392D-04	47240.0
21	0.3374	0.5305	27.5446	0.1093D-03	47580.0
22	0.3525	0.5384	28.1248	0.1176D-03	47730.0
23	0.3688	0.5467	28.7435	0.1272D-03	47880.0
24	0.3818	0.5530	29.2246	0.1351D-03	47990.0

Test Case No. 142, B = 1.75, R = 0.1

Collipriest's Crack Growth Rate Constants:

$$K_{cr} = 60.0 \text{ ksi } \sqrt{\text{inch}}$$

$$\Delta K_o = 3.0 \text{ ksi } \sqrt{\text{inch}}$$

$$C = 0.0155$$

$$n = 2.65$$



TABLE 8. ACTUAL CRACK GROWTH HISTORY OF A 7075-T7351 CRUCIFORM SPECIMEN

STEP	MAX. STRESS	AAX	AAV	ACCUM. CYCLES
1	12.0000	0.0027	0.1075	0.0
2	12.0000	0.0061	0.1374	11790.0
3	12.0000	0.0115	0.1646	21200.0
4	12.0000	0.0244	0.1884	26170.0
5	12.0000	0.0461	0.2099	29850.0
6	12.0000	0.0673	0.2277	32500.0
7	12.0000	0.1045	0.2651	36640.0
8	12.0000	0.1236	0.2843	38800.0
9	12.0000	0.1447	0.2965	39650.0
10	12.0000	0.1682	0.3098	40740.0
11	12.0000	0.1944	0.3235	41740.0
12	12.0000	0.2208	0.3335	42700.0
13	12.0000	0.2613	0.3599	43910.0
14	12.0000	0.2876	0.3620	44300.0
15	12.0000	0.3196	0.3680	44910.0
16	12.0000	0.3745	0.3896	45760.0
17	12.0000	0.4322	0.3900	46220.0
18	12.0000	0.4998	0.3911	46690.0
19	12.0000	0.5589	0.3993	47030.0
20	12.0000	0.6072	0.3954	47240.0
21	12.0000	0.6776	0.3998	47580.0
22	12.0000	0.7298	0.3889	47730.0
23	12.0000	0.7778	0.4056	47880.0
24	12.0000	0.8233	0.4205	47990.0



Test Case No. 142, B = 1.75, R = 0.1

TABLE 9. LOW AMPLITUDE TESTS

Material	Test Case	$\sigma_{y,max}$	$\sigma_{y,min}$	$\sigma_{x,max}$	$\sigma_{x,min}$	f	Notes
7075-T7351	47	12.0	8.4	12.0	8.4	5	
7075-T7351	48	12.0	8.4	-8.4	-12.0	5	
7075-T7351	49	12.0	8.4	6.0	4.2	10	
7075-T7351	50	12.0	8.4	-4.2	-8.4	8	
7075-T7351	11	12.0	8.4	0	0	15	1
7075-T7351	15	12.0	8.4	0	0	5	2
2024-T351	51	10.0	7.0	10.0	7.0	10	
2024-T351	52	10.0	7.0	-7.0	-10.0	10	
2024-T351	53	10.0	7.0	5.0	3.5	10	
2024-T351	54	10.0	7.0	-3.5	-5.0	10	
2024-T351	12	10.0	7.0	0	0	10	1
2024-T351	16	10.0	7.0	0	0	10	2

 Interferometry photographs
 TL direction

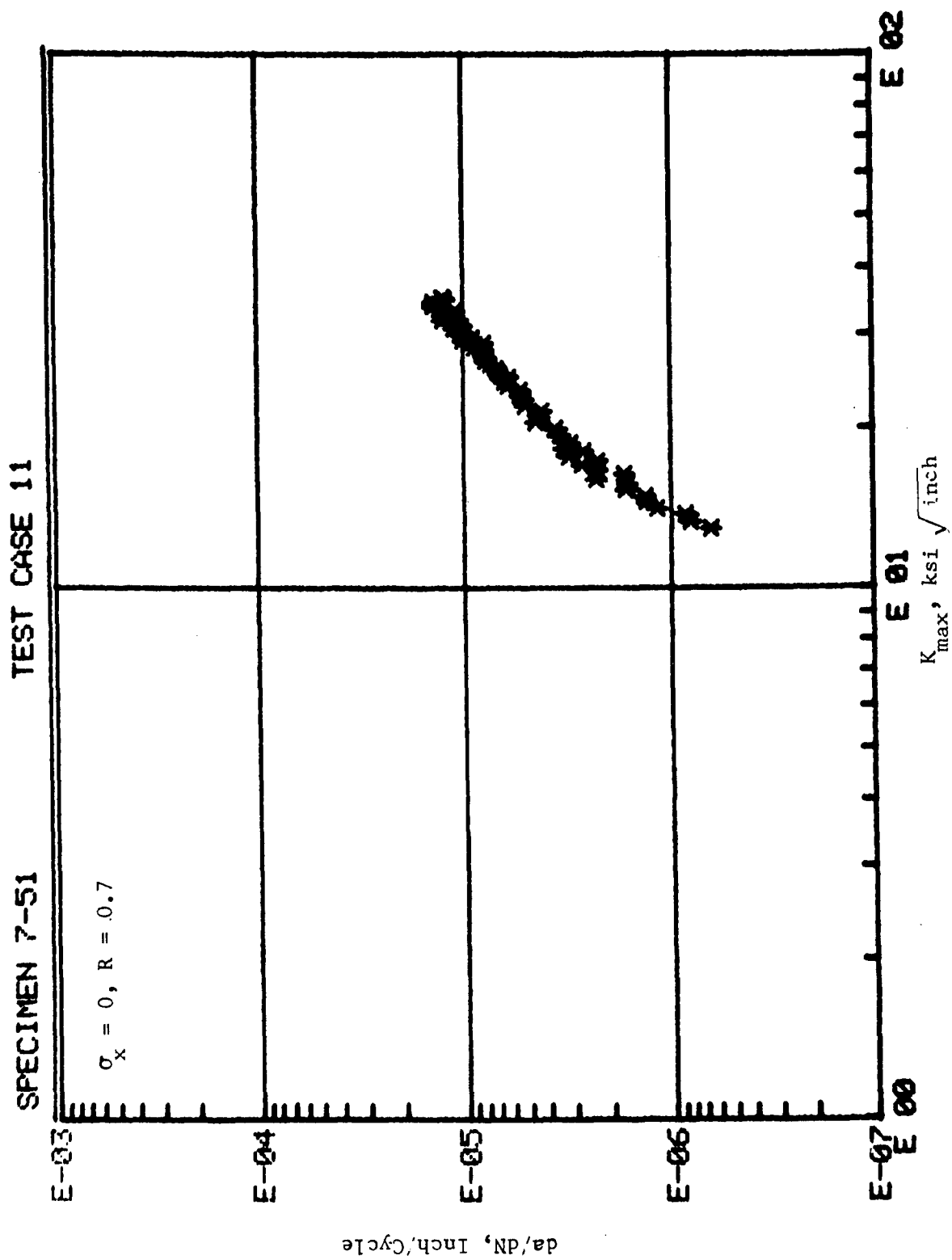


Figure 97. Cyclic Crack Growth Behavior of 7075-T7351 Cruciform Specimen

SPECIMEN 7-105 TEST CASE 48

$\sigma_x = -\sigma_y, R = 0.7$

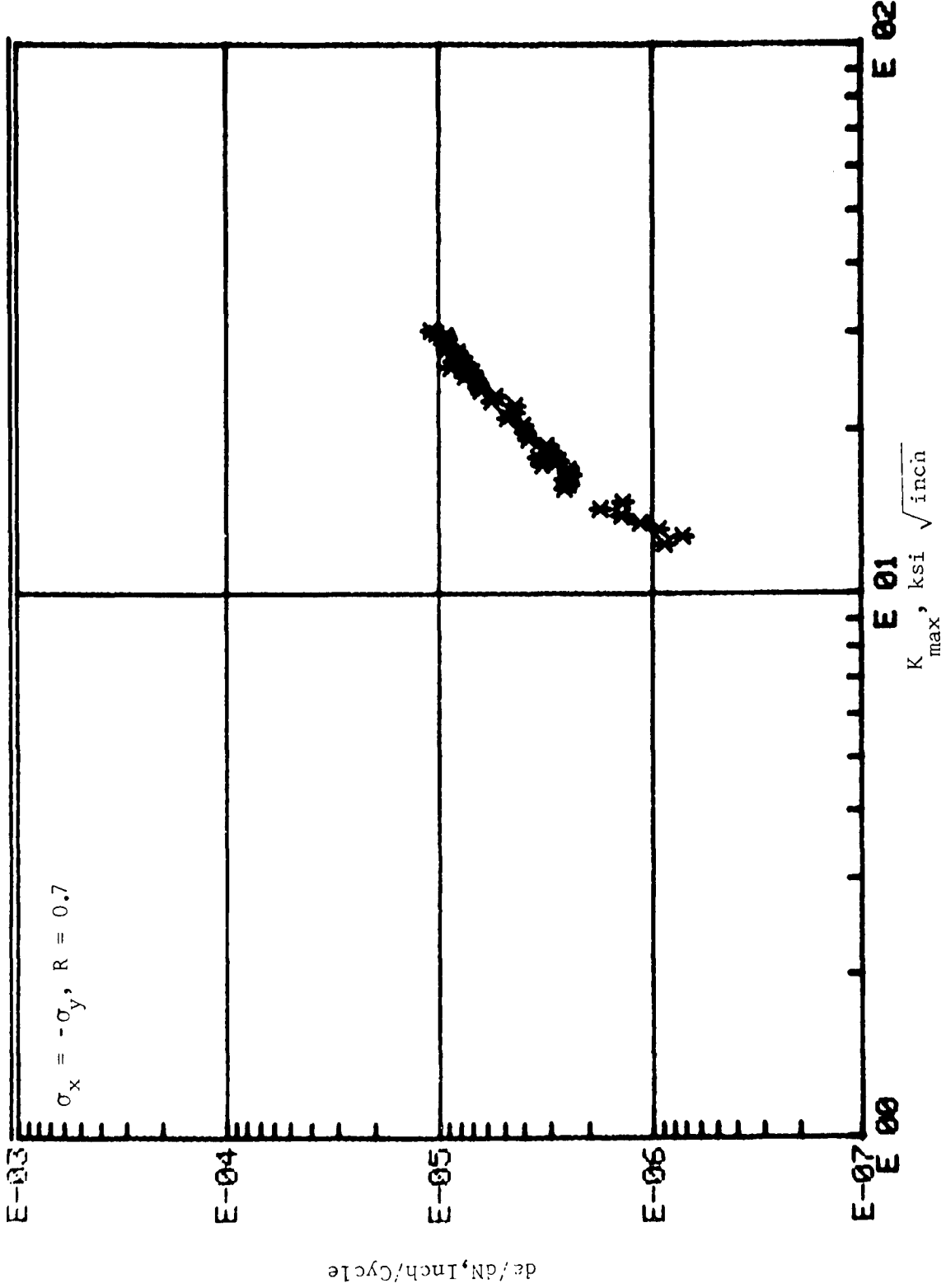


Figure 98. Cyclic Crack Growth Behavior of 7075-T7351 Cruciform Specimen

SPECIMEN 2-33 TEST CASE 12

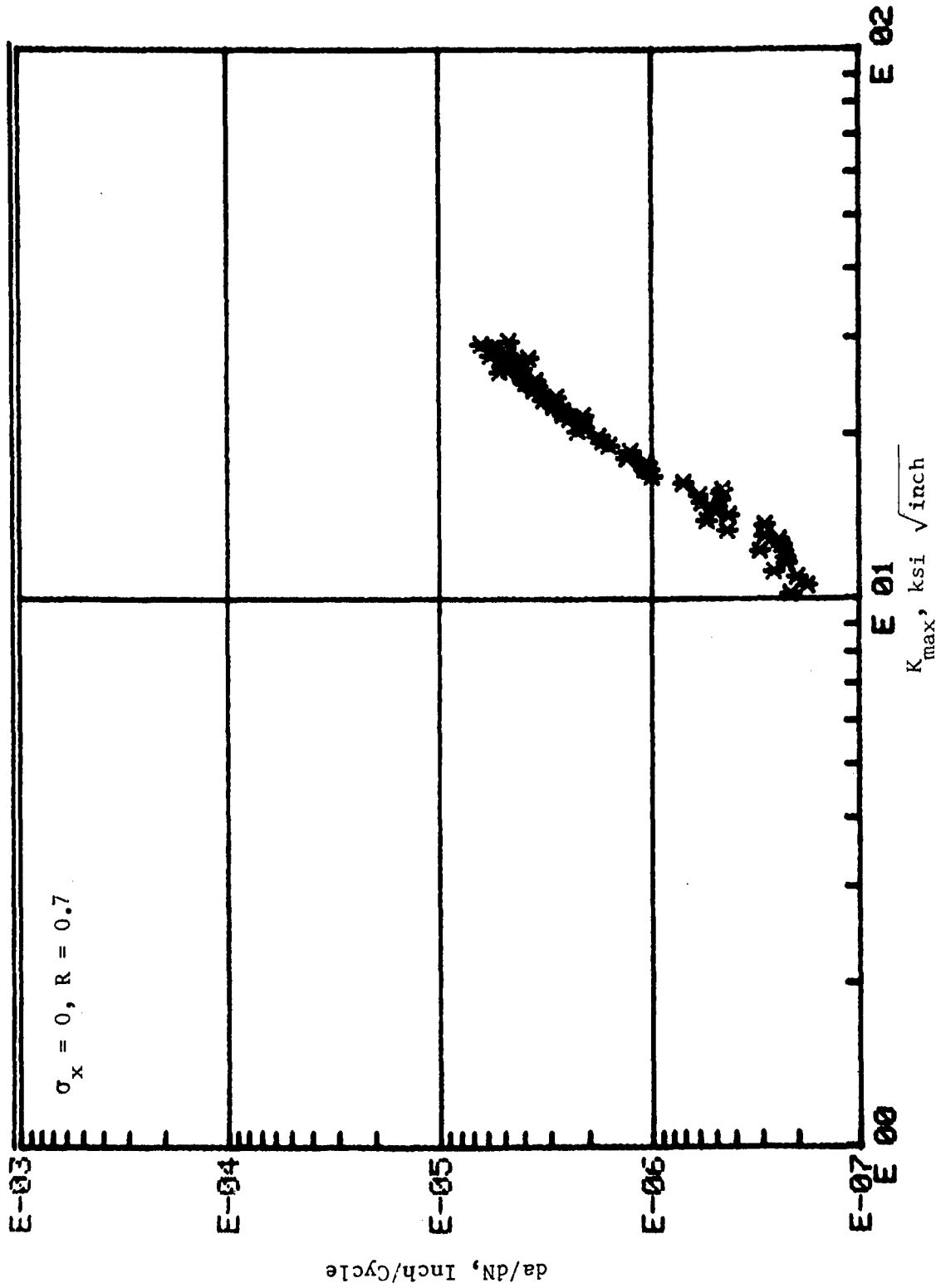


Figure 99. Cyclic Crack Growth Behavior of 2024-T351 Cruciform Specimen

SPECIMEN 2-19 TEST CASE 52

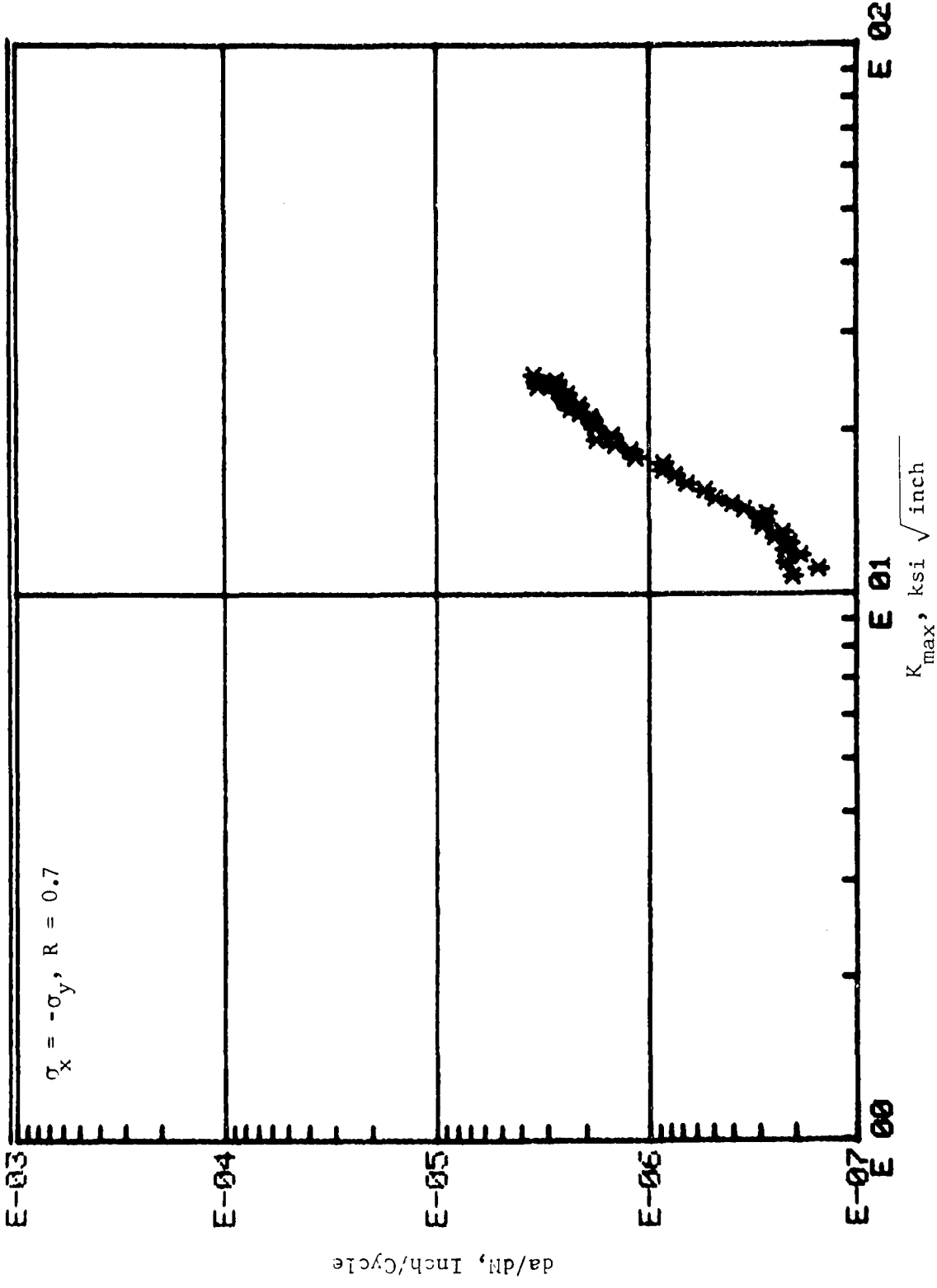


Figure 100. Cyclic Crack Growth Behavior of 2024-T351 Cruciform Specimen

TABLE 10. CRACKS AT A CIRCULAR HOLE TESTS

Material	Test Case	$\sigma_{y,max}$	$\sigma_{y,min}$	$\sigma_{x,max}$	$\sigma_{x,min}$	f	Notes
7075-T7351	86	12.0	1.2	0	0	5	1
7075-T7351	85	12.0	1.2	0	0	5	2
7075-T7351	17	18.0	1.8	0	0	-	2 3 4
7075-T7351	19	18.0	1.8	18.0	1.8	-	2 4
7075-T7351	87	12.0	1.2	12.0	1.2	5	1
7075-T7351	89	12.0	1.2	12.0	1.2	5	2
7075-T7351	90	12.0	1.2	12.0	1.2	5	2
7075-T7351	88	12.0	1.2	-1.2	-12.0	5	1
7075-T7351	91	12.0	1.2	-1.2	-12.0	5	2
7075-T7351	92	12.0	1.2	-1.2	-12.0	5	2

1 0.25 inch diameter hole

2 0.75 inch diameter hole

3 CCT specimen

4 Crack initiation test

Comparing the da/dN versus K_{max} curves for these cracks at a hole tests to da/dN versus K_{max} curves for specimens without a hole, it was observed that the crack growth rate behavior was the same in both cases. Again, the crack in all these specimens grew straight essentially parallel to the X-axis of the specimen.

9.5 Variable Amplitude Tests

Table 11 is a listing of the testing conditions for 13 specimens. Single overload was periodically applied to nine specimens. The remaining four specimens were subjected to spectrum loadings. Excepting Test Case No. 102, all the overloads had a magnitude twice that of the regular cyclic stress level (i.e., 20 ksi for the 2024-T351 specimens and 24 ksi for the 7075-T7351 specimens). In Specimen No. LT-2-5 (Test Case No. 102), the stress levels were 16.7 ksi for the first two overloads and 20 ksi for the subsequent overloads. The biaxial ratios for these specimens were either 0, +0.5 or -0.5. The spectrum load tests were conducted at four biaxial ratios (0, -.267, ±.5). Raw data for all these tests are compiled in Volume II of this report. The results are discussed in the following.

9.5.1 Single Overload Tests

Crack growth history and crack growth rate data for the periodically overloaded specimens are presented in Figures 101 to 118. In part (b) of Figures 110 to 118, the basic da/dN behavior associated with a particular test is revealed by excluding the retarded da/dN data points. Comparing these da/dN curves with the da/dN curves for tests without overload (i.e., those curves previously presented in Section 9.2), it is seen that the basic crack growth rate behavior in the overloaded specimen is the same as those in the regular (not overloaded) specimens.

TABLE 11. VARIABLE AMPLITUDE TESTS

Material	Test Case	$\sigma_{y,max}$	$\sigma_{y,min}$	$\sigma_{x,max}$	$\sigma_{x,min}$	f	Notes
7075-T7351	99	12.0	1.2	0	0	10	1 2
7075-T7351	103	12.0	1.2	6.0	0.6	10	1 2
7075-T7351	104	12.0	1.2	6.0	0.6	10	1
7075-T7351	105	12.0	1.2	-0.6	-6.0	10	1 2
7075-T7351	114	30.0	-	0	0		3
7075-T7351	115	30.0	-	-	-15.0		3
7075-T7351	116	30.0	-	15.0	-		3
7075-T7351	200	30.0	-	-	-8.0		3 4
2024-T351	101	10.0	1.0	0	0	10	1 2
2024-T351	102	10.0	1.0	0	0	10	4 5 6
2024-T351	108	10.0	1.0	5.0	0.5	10	1 2
2024-T351	109	10.0	1.0	5.0	0.5	10	1
2024-T351	110	10.0	1.0	-0.5	-5.0	10	1 2

- 1 Periodic single overload, overload ratio = 2.0 (in both X and Y directions when applicable)
- 2 Interferometry photographs
- 3 Spectrum load. Cyclic frequencies vary (15Hz for low loads and 2Hz for high loads)
- 4 Tested in uniaxial loading machine
- 5 Periodic single overload, overload ratio = 1.67, 2.0
- 6 CCT specimen

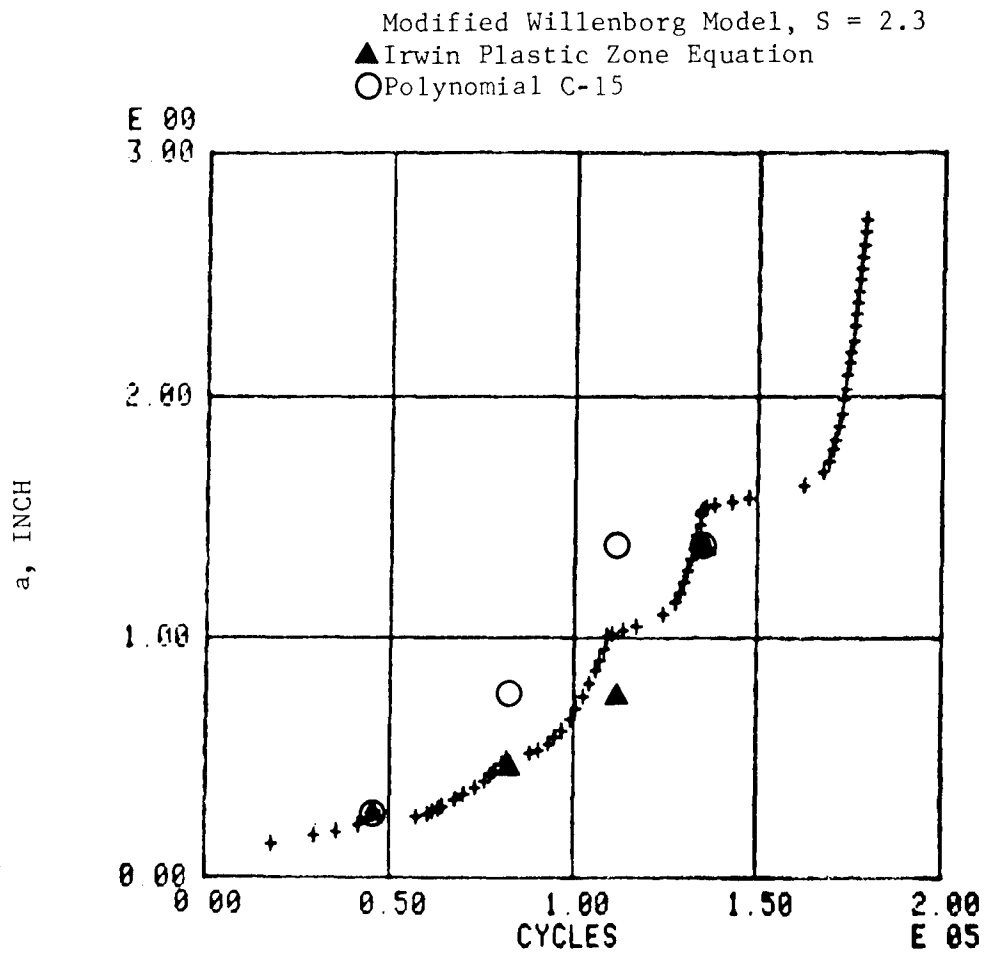


Figure 101. Crack Growth History of 7075-T7351
 Cruciform Specimen No. 7-114
 Test Case No. 99
 $\sigma_x = 0$, $\sigma_y = 12$ ksi, $R = 0.1$, $f = 10$ Hz
 Overload Ratio = 2.0

Modified Willenborg Model, S = 2.3
▲ Polynomial No. C-15

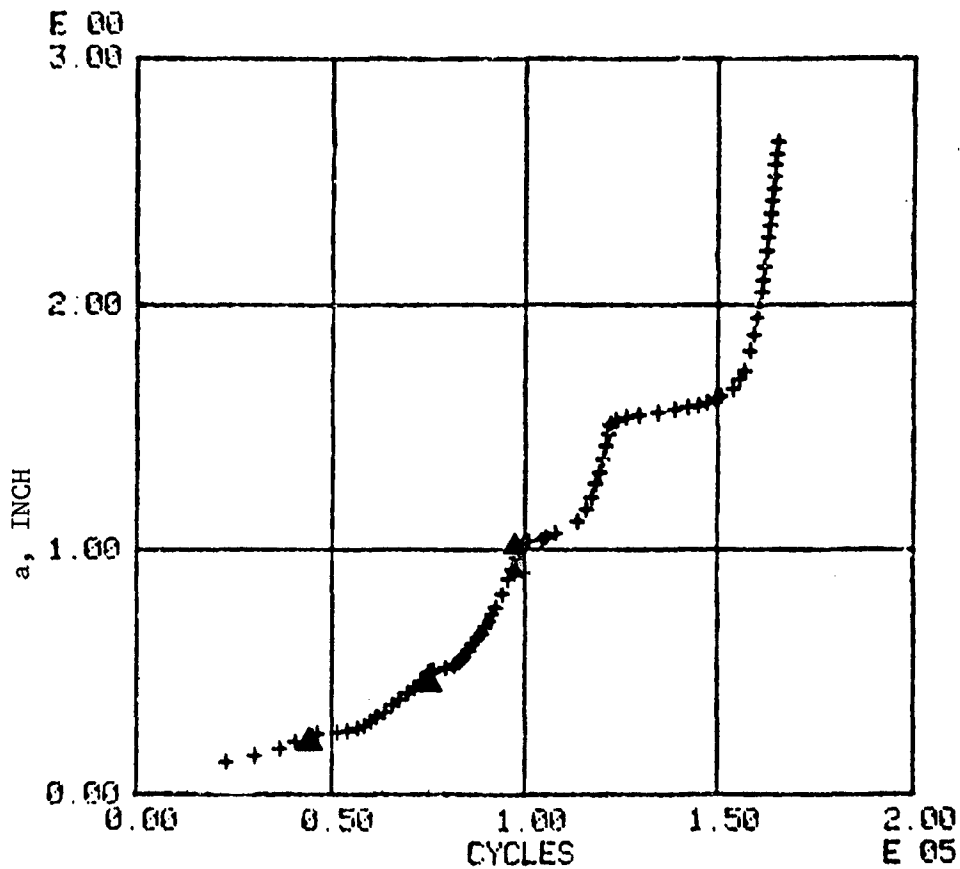


Figure 102. Crack Growth History of 7075-T7351
Cruciform Specimen No. 7-25
Test Case No. 103
 $\sigma_x = 6$ ksi, $\sigma_y = 12$ ksi, $R = 0.1$
 $f = 10$ Hz; Overload Ratio = 2.0

Modified Willenborg Model, S = 2.3

■ Polynomial No. C-15

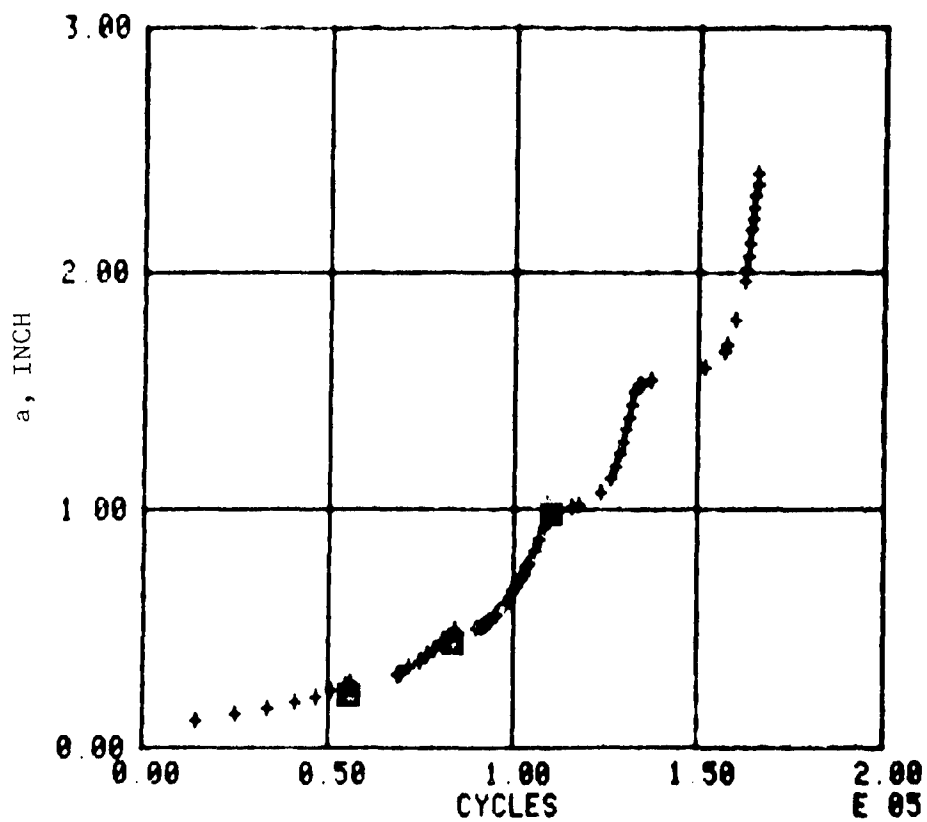


Figure 103. Crack Growth History of 7075-T7351
Cruciform Specimen No. 7-113
Test Case No. 104

$\sigma_x = 6$ ksi, $\sigma_y = 12$ ksi, $R = 0.1$, $f = 10$ Hz
Overload Ratio = 2.0

Modified Willenborg Model, $S = 2.3$

◇ Polynomial No. C-15

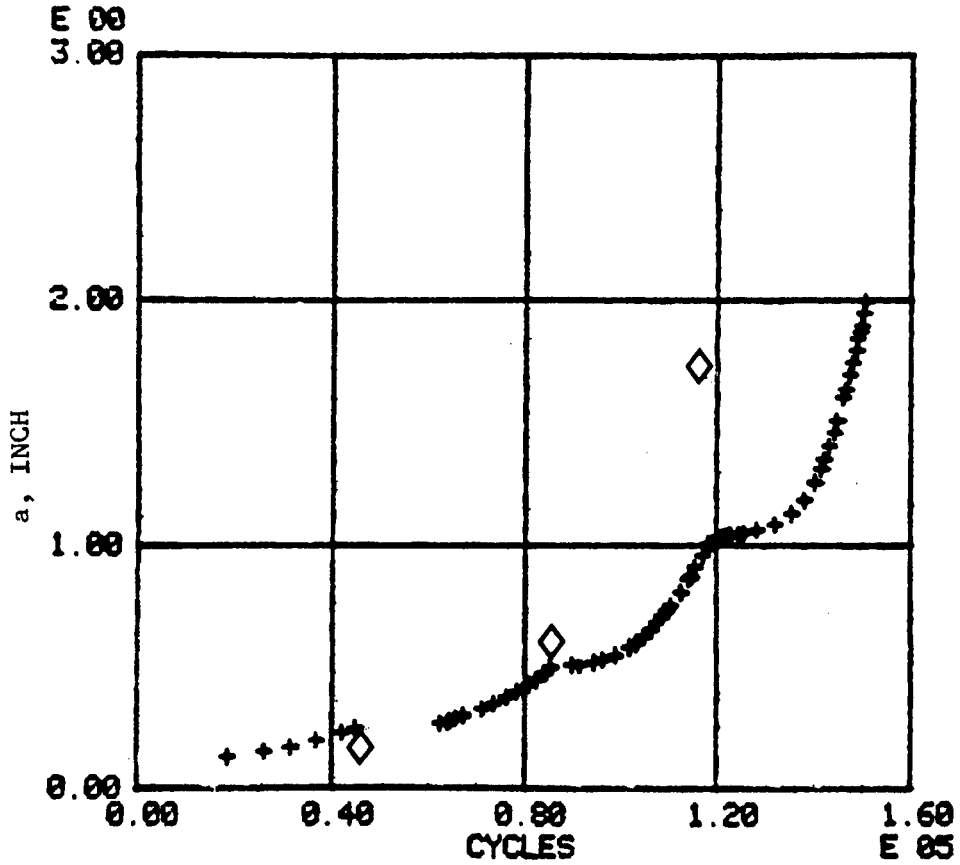


Figure 104. Crack Growth History of 7075-T7351
Cruciform Specimen No. 7-53
Test Case No. 105
 $\sigma_x = -6$ ksi, $\sigma_y = 12$ ksi, $R = 0.1$,
 $f = 10$ Hz; Overload Ratio = 2.0

Modified Willenborg Model, S = 2.3
○ Polynomial No. B-9

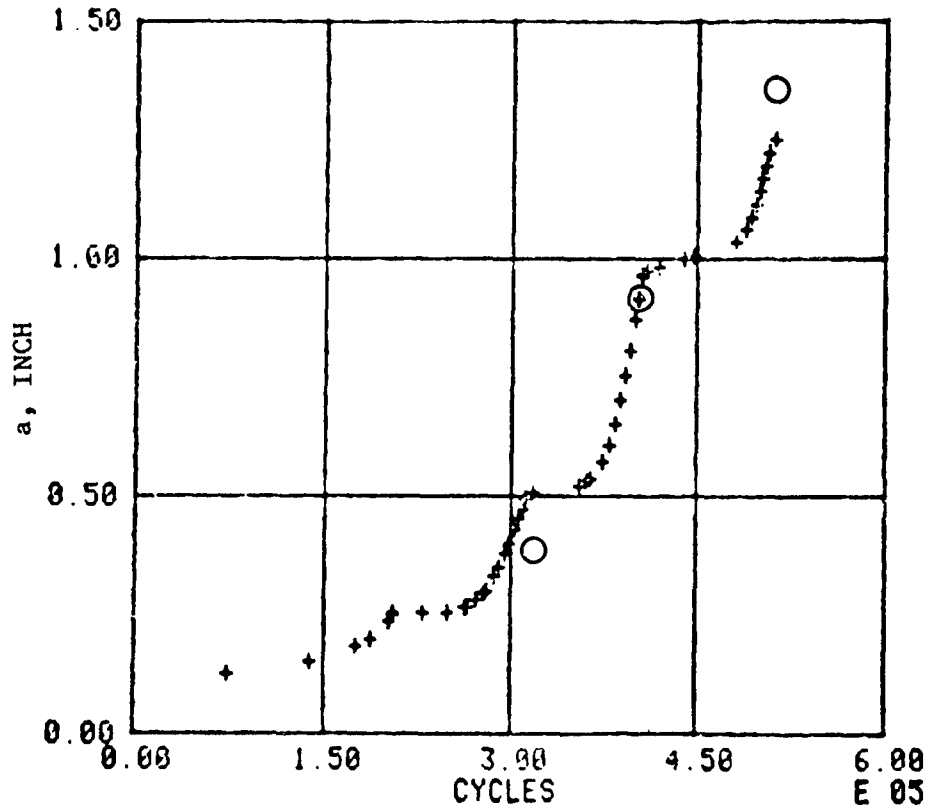


Figure 105. Crack Growth History of 2024-T351
Cruciform Specimen No. 2-24
Test Case No. 101

$\sigma_x=0, \sigma_y = 10$ ksi, $R = 0.1$, $f = 10$ Hz
Overload Ratio = 2.0

Modified Willenborg Model, $S = 2.3$
 Δ Polynomial No. B-9

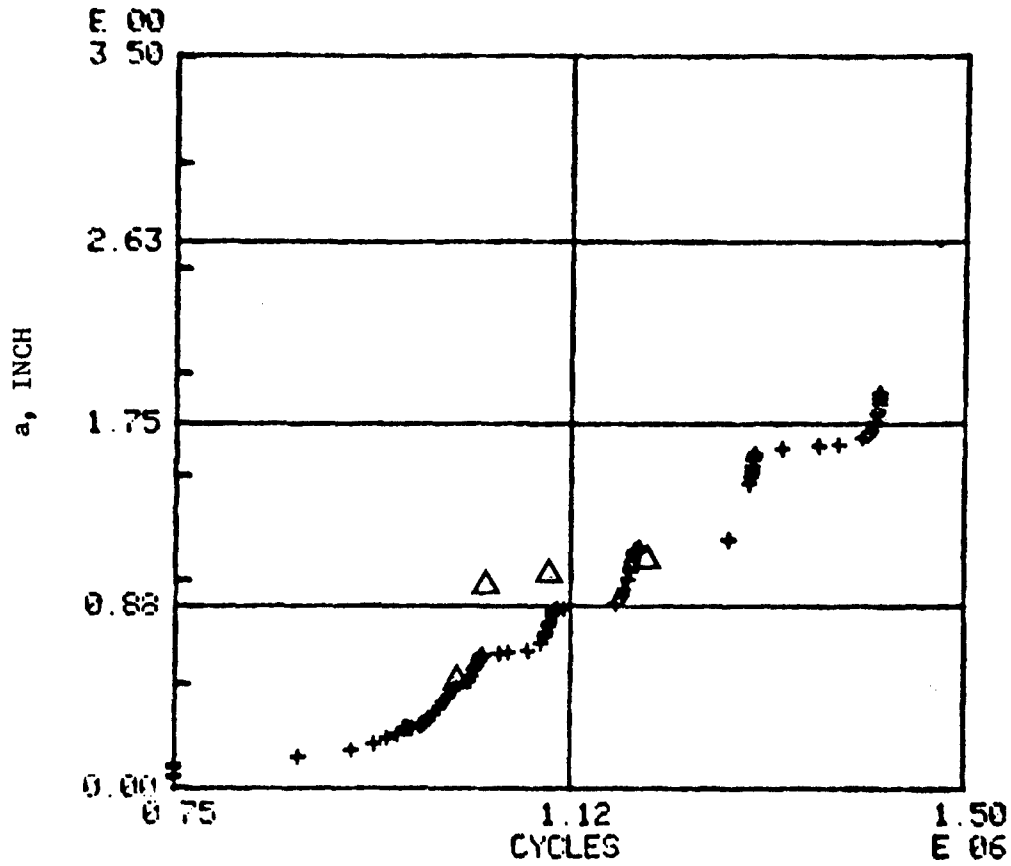


Figure 106. Crack Growth History of 2024-T351
Center-Cracked Panel
Specimen No. LT-2-5; Test Case No. 102
 $\sigma_x = 0$, $\sigma_y = 10$ ksi, $R = 0.1$
Overload Ratio = 1.67 and 2.0

Modified Willenborg Model, $S = 2.3$

○ Polynomial No. B-7

● Polynomial No. B-8

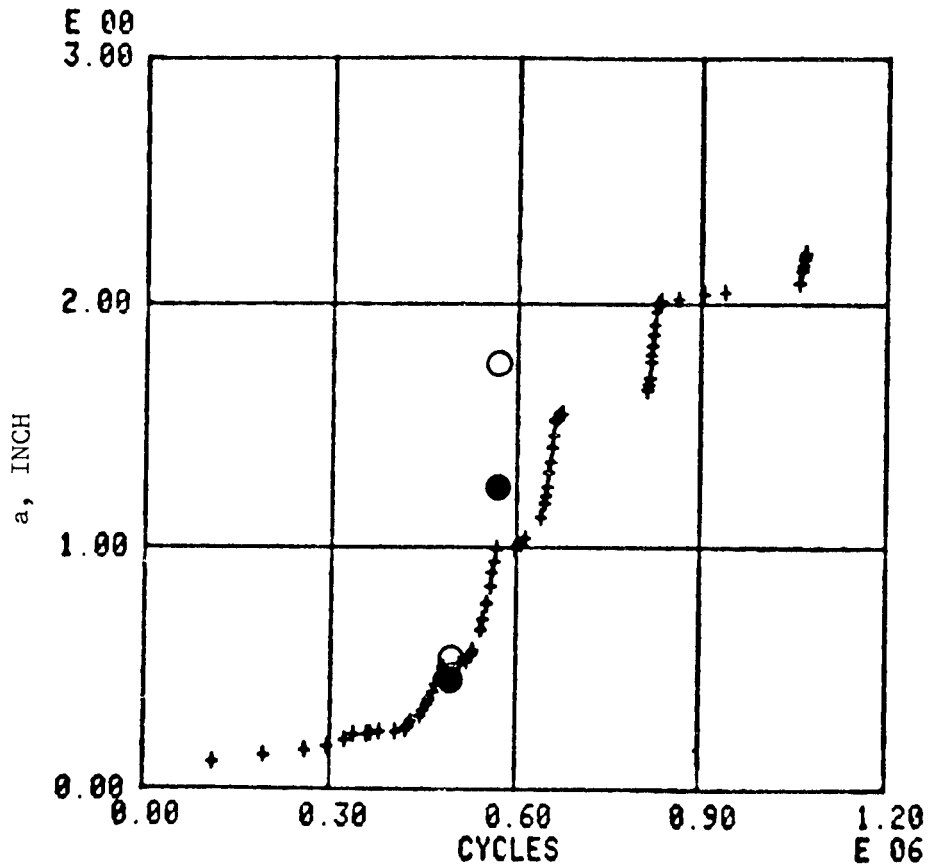


Figure 107. Crack Growth History of 2024-T351 Cruciform Specimen No. 2-38
Test Case No. 108
 $\sigma_x = 5$ ksi, $\sigma_y = 10$ ksi, $R = 0.1$,
 $f = 10$ Hz; Overload Ratio = 2.0

Modified Willenborg Model, $S = 2.3$

△ Polynomial No. B-7

▲ Polynomial No. B-8

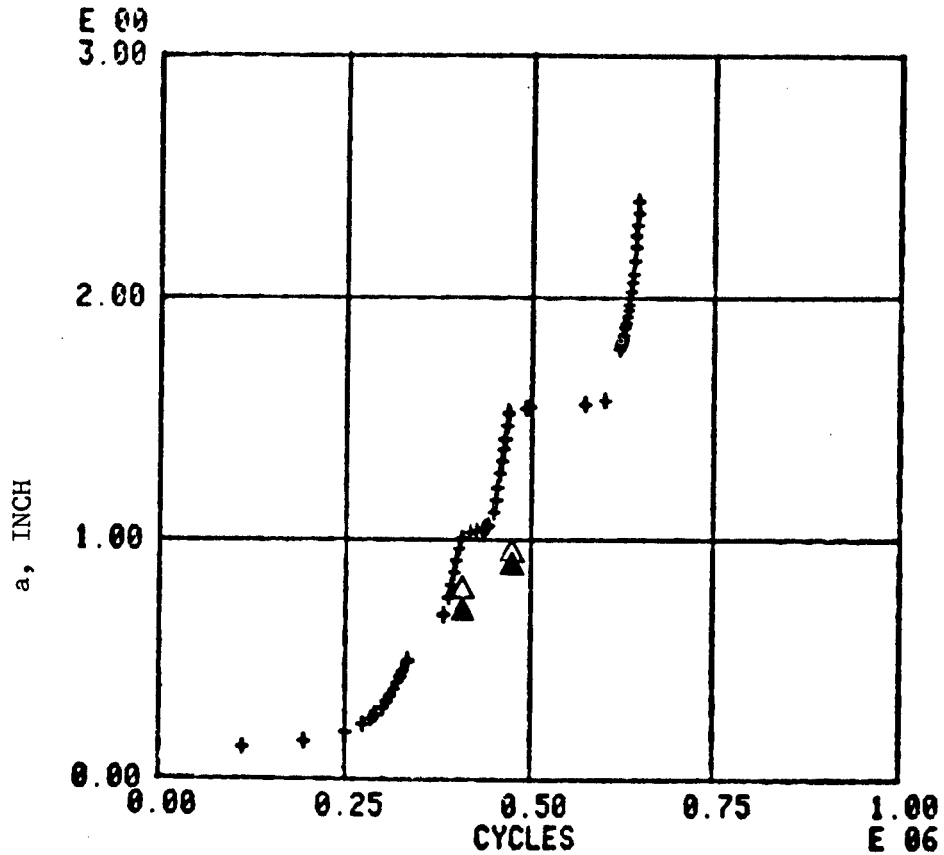


Figure 108. Crack Growth History of 2024-T351 Cruciform Specimen No. 2-34
Test Case No. 109
 $\sigma_x = 5$ ksi, $\sigma_y = 10$ ksi, $R = 0.1$,
 $f = 10$ Hz; Overload Ratio = 2.0

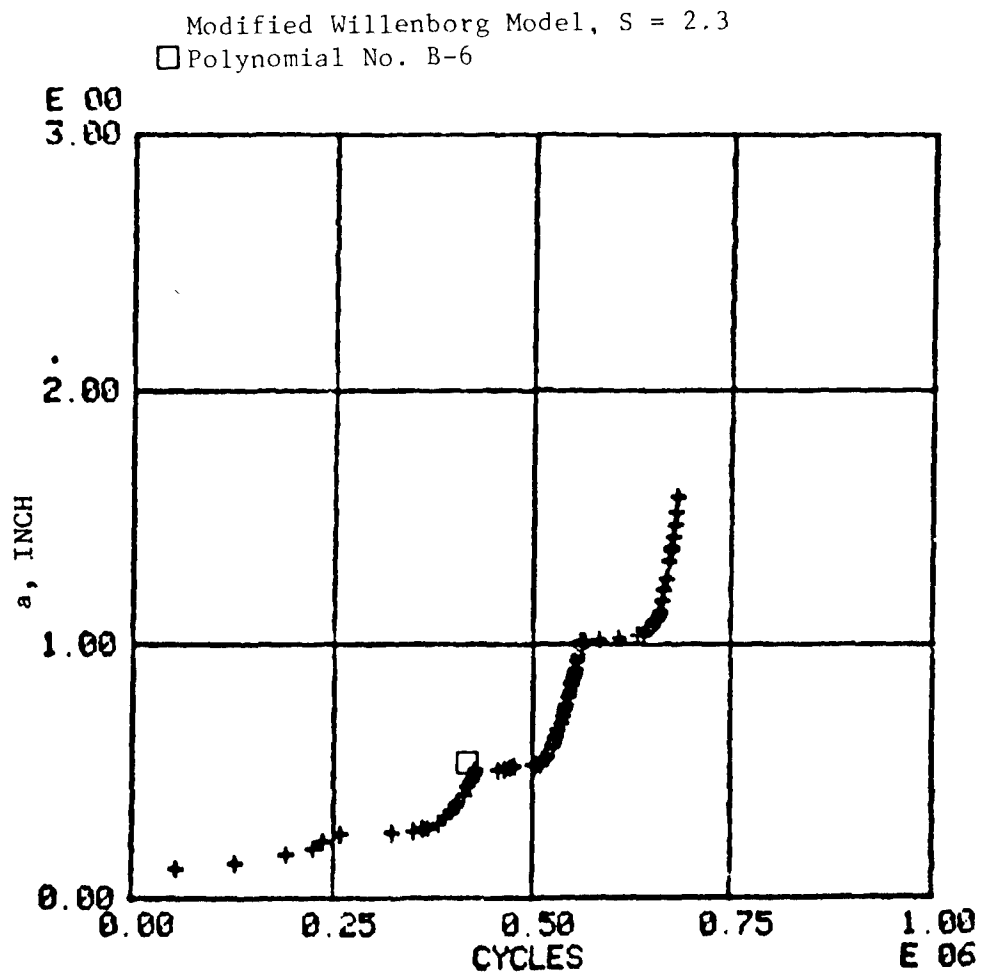


Figure 109. Crack Growth History of 2024-T351
 Cruciform Specimen No. 2-41
 Test Case No. 110
 $\sigma_x = -5$ ksi, $\sigma_y = 10$ ksi, $R = 0.1$, $f = 10$ Hz
 Overload Ratio = 2.0

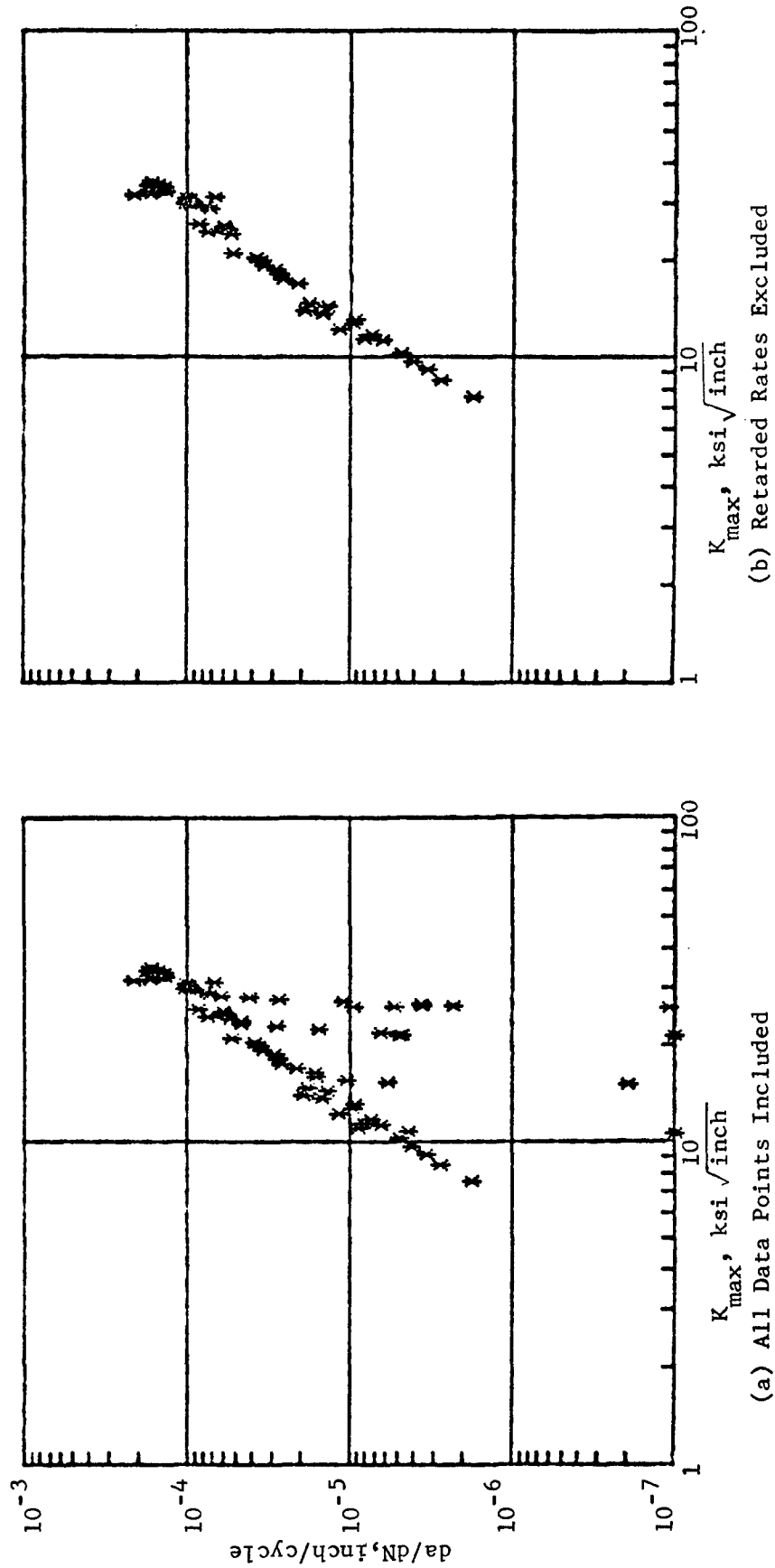
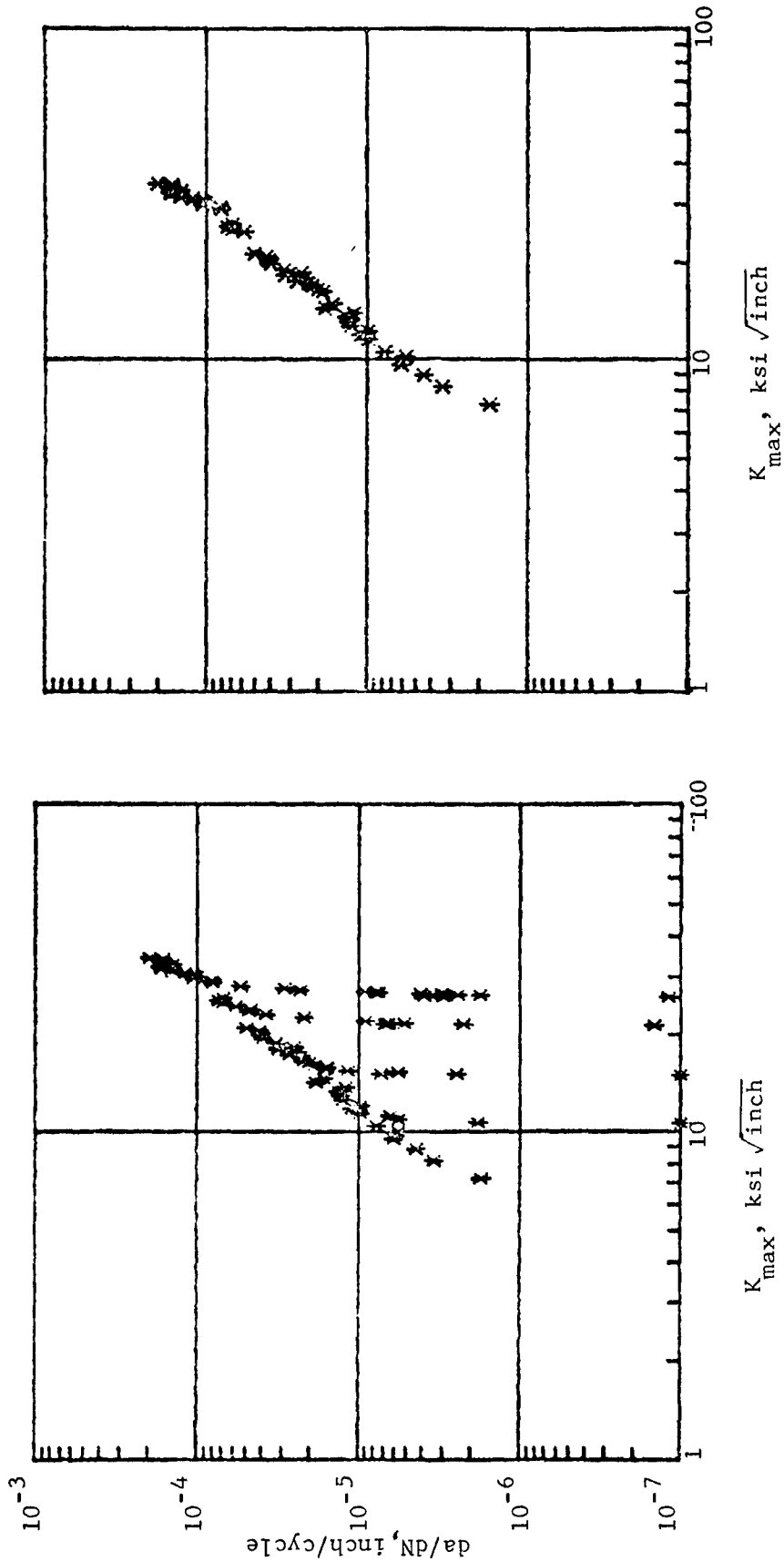


Figure 110. Crack Growth Rate Behavior of 7075-T7351, Cruciform Specimen No. 7-114, Test Case No. 99, $\sigma_x = 0$, $\sigma_y = 12$ ksi, $R = 0.1$, $f = 10$ Hz Overload Ratio = 2.0



(a) All Data Points Included

(b) Retarded Rates Excluded

Figure 111. Crack Growth Rate Behavior of 7075-T7351 Cruciform Specimen No. 7-25
 Test Case No. 103; $\sigma_x = 6$ ksi, $\sigma_y = 12$ ksi, $R = 0.1$, $f = 10$ Hz;
 Overload Ratio = 2.0

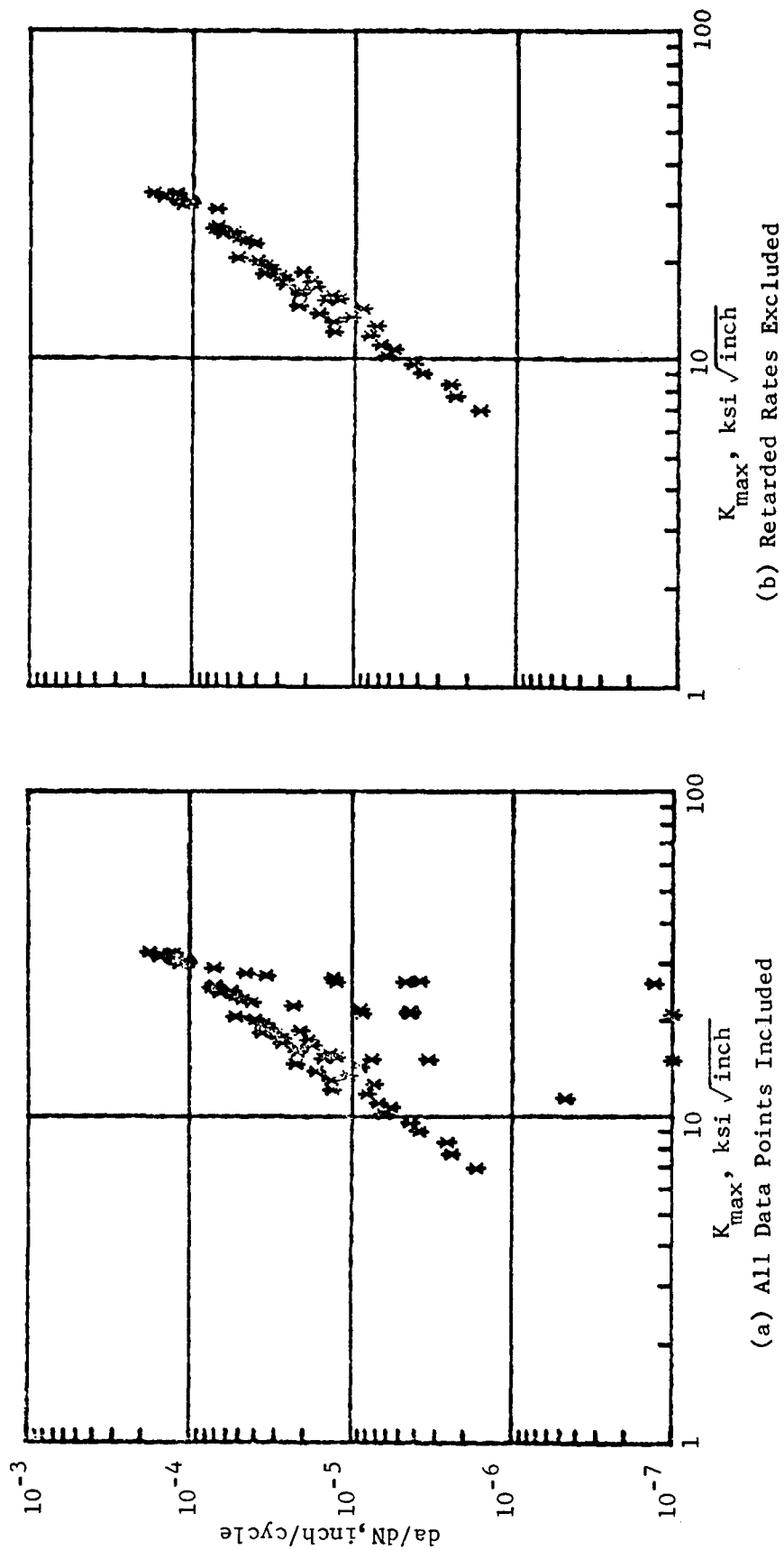


Figure 112. Crack Growth Rate Behavior of 7075-T7351 Cruciform Specimen No. 7-113, Test Case No. 104, $\sigma_x = 6$ ksi, $\sigma_y = 12$ ksi, $R = 0.1$, $f = 10$ Hz, Overload Ratio = 2.0

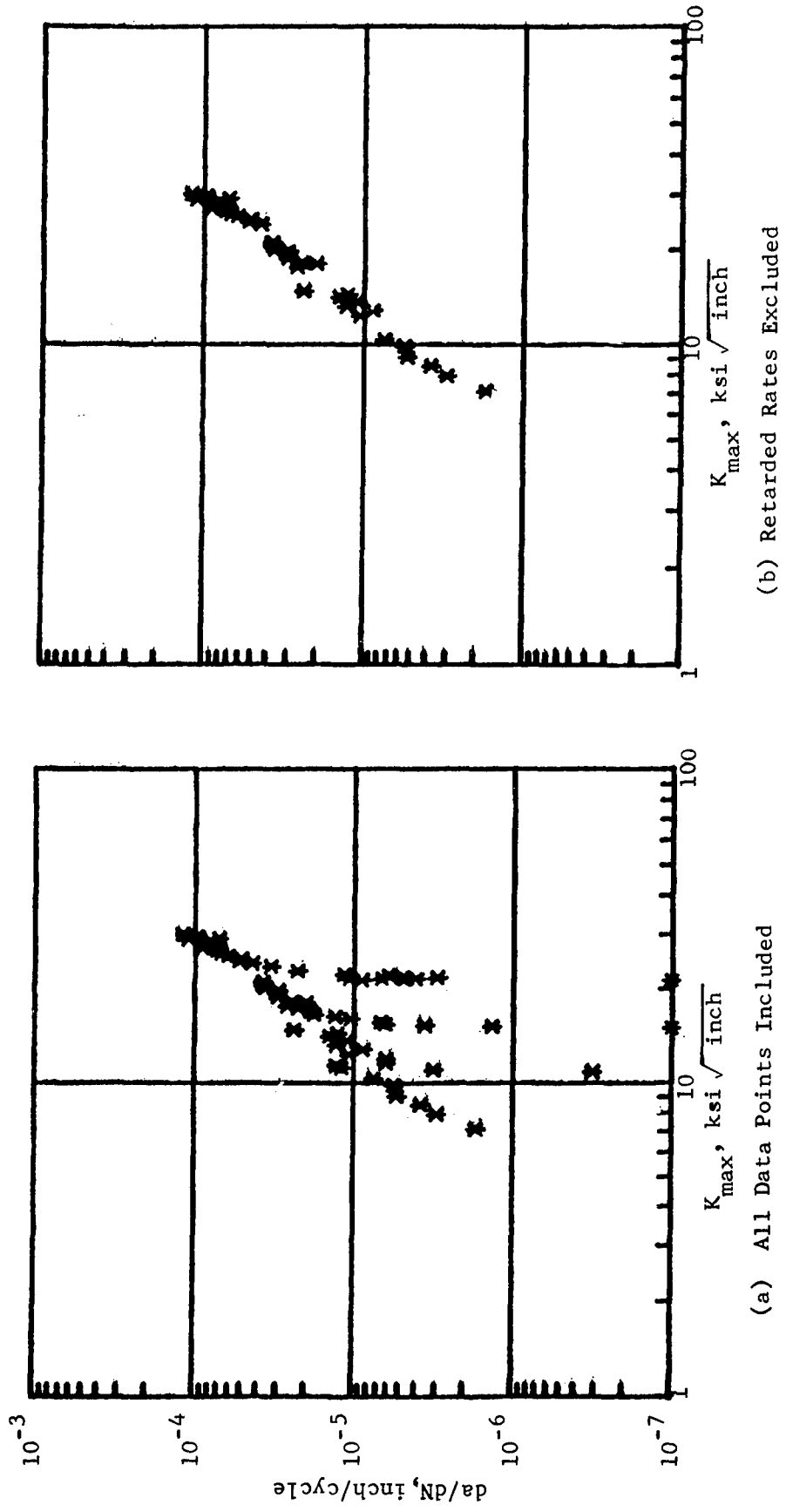


Figure 113. Crack Growth Behavior of 7075-T7351, Cruciform Specimen No. 7-53
 Test Case No. 105, $\sigma_x = -6 \text{ ksi}$, $\sigma_y = 12 \text{ ksi}$, $R = 0.1$, $f = 10 \text{ Hz}$, Overload Ratio = 2.0

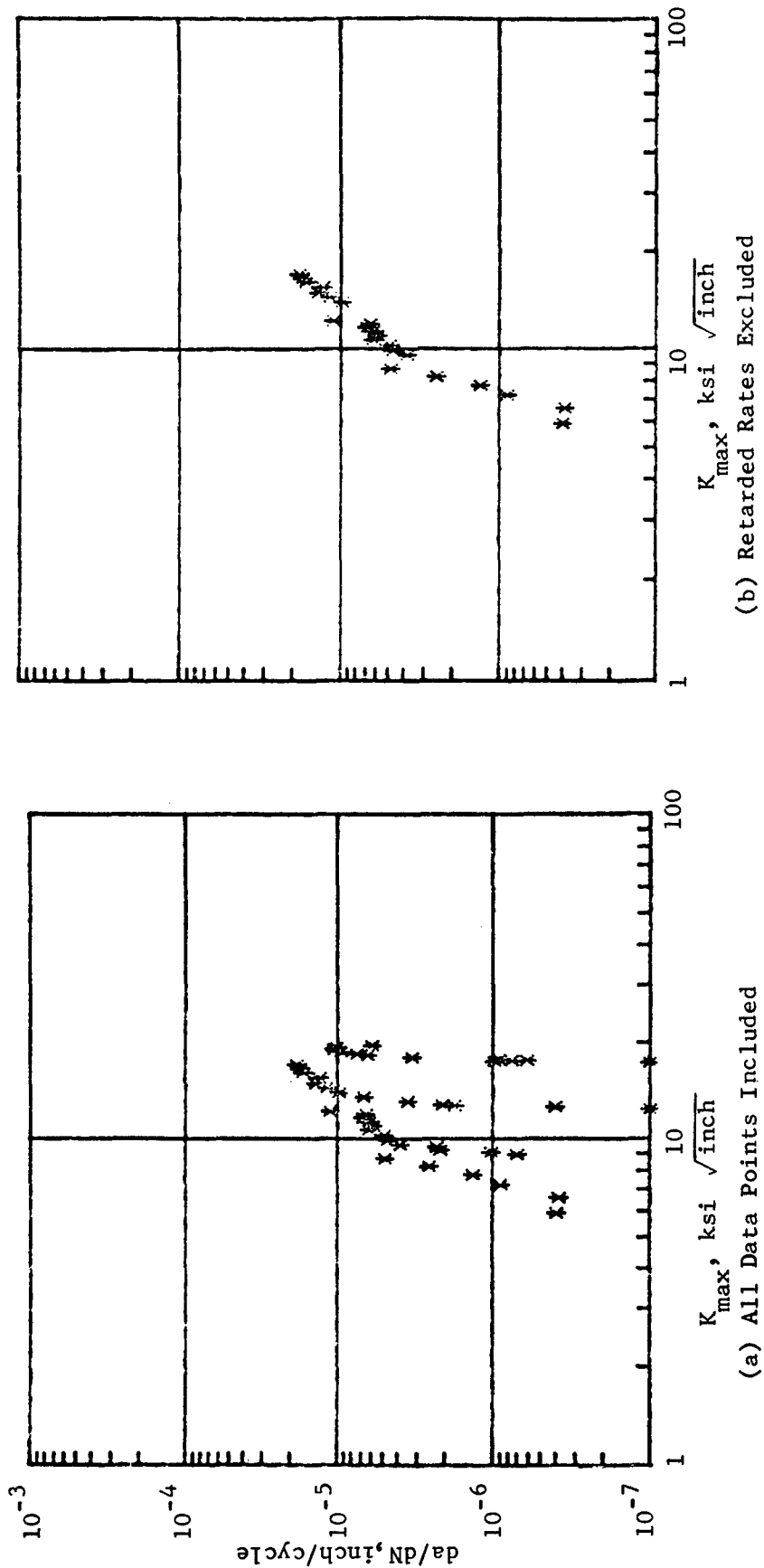
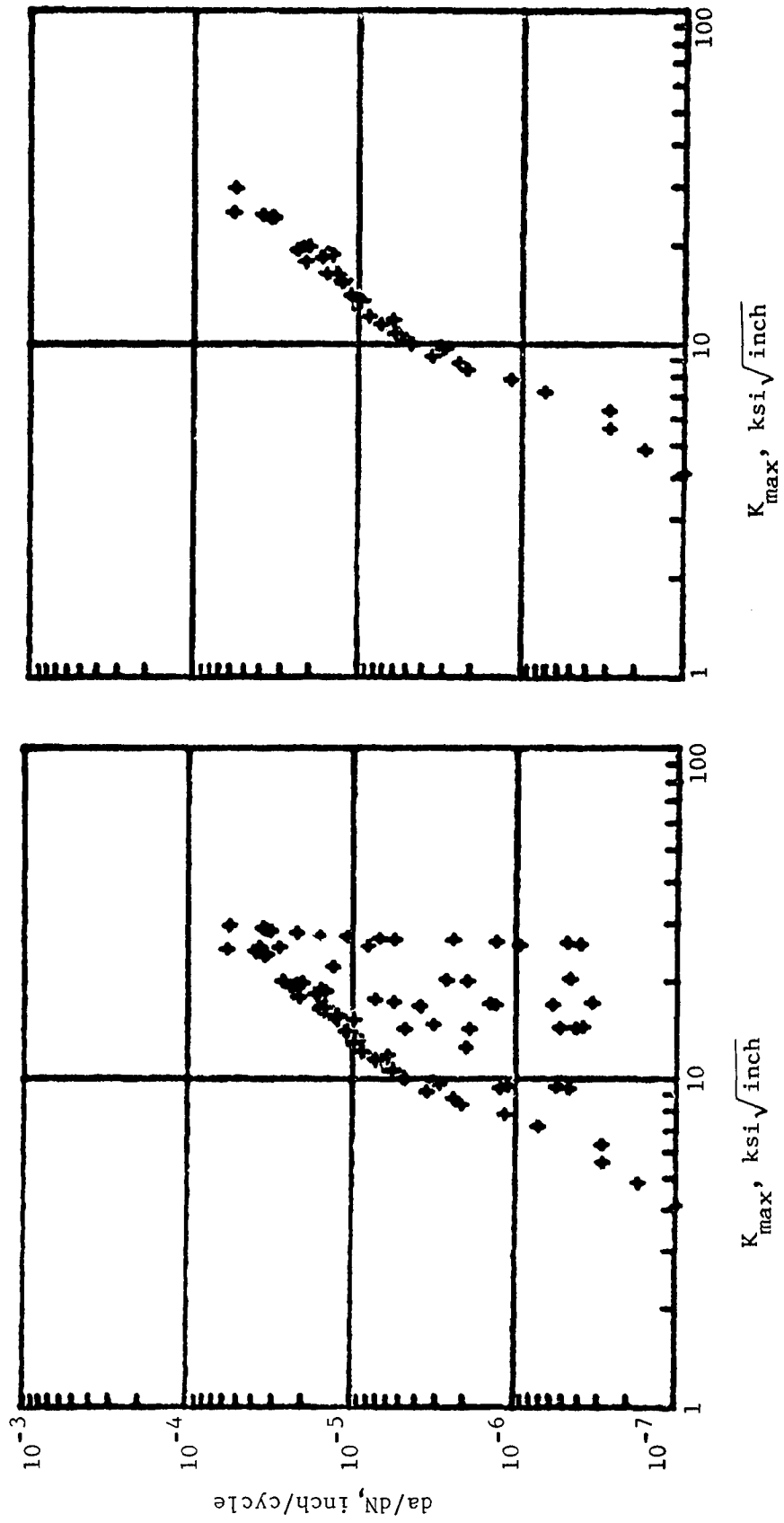


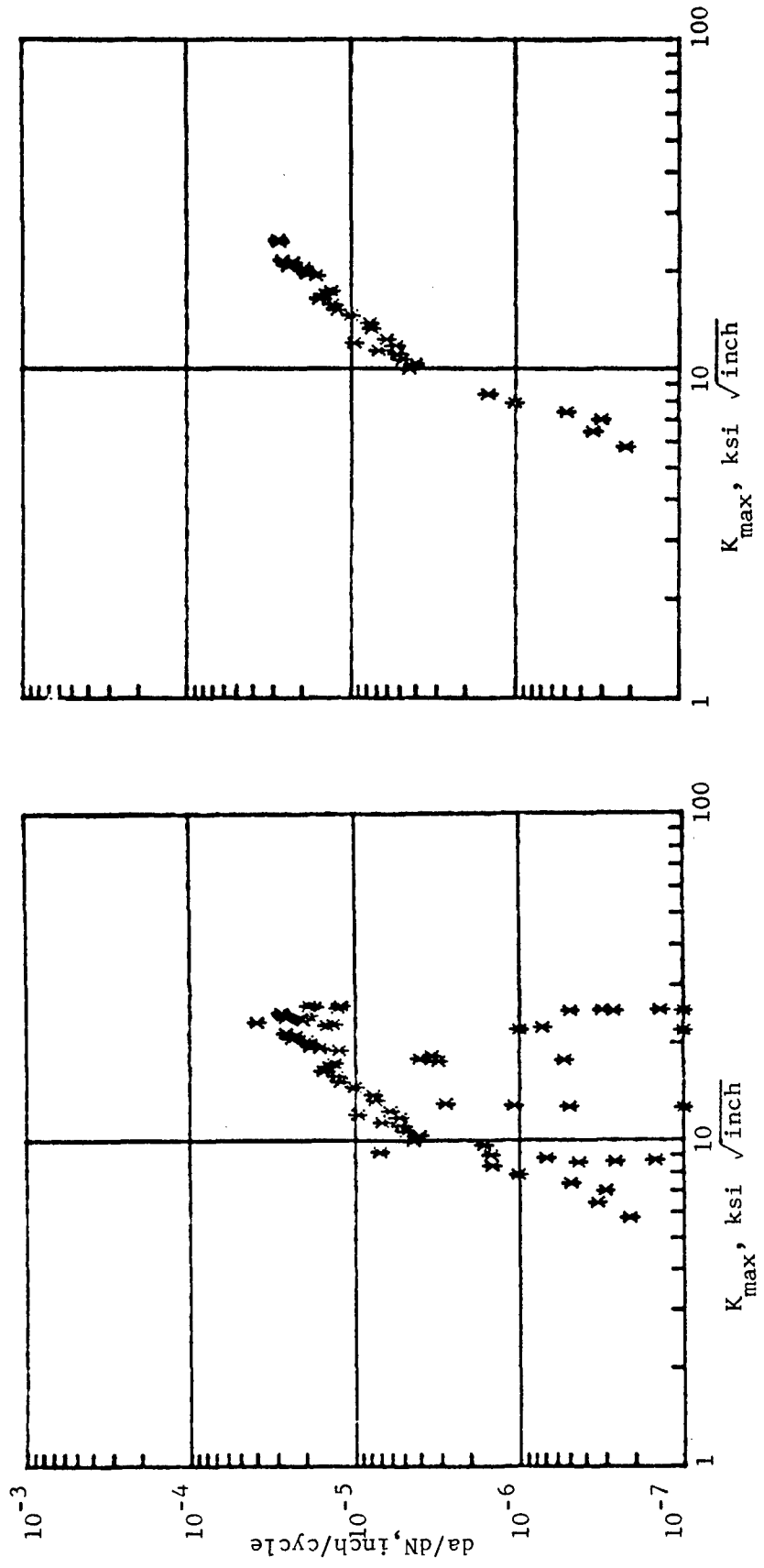
Figure 114. Crack Growth Rate Behavior of 2024-T351 Cruciform Specimen No. 2-24, Test Case No. 101, $\sigma_x = 0$, $\sigma_y = 10$ ksi, $R = 0.1$, $f = 10$ Hz, Overload Ratio = 2.0



(a) All Data Points Included

(b) Retarded Rates Excluded

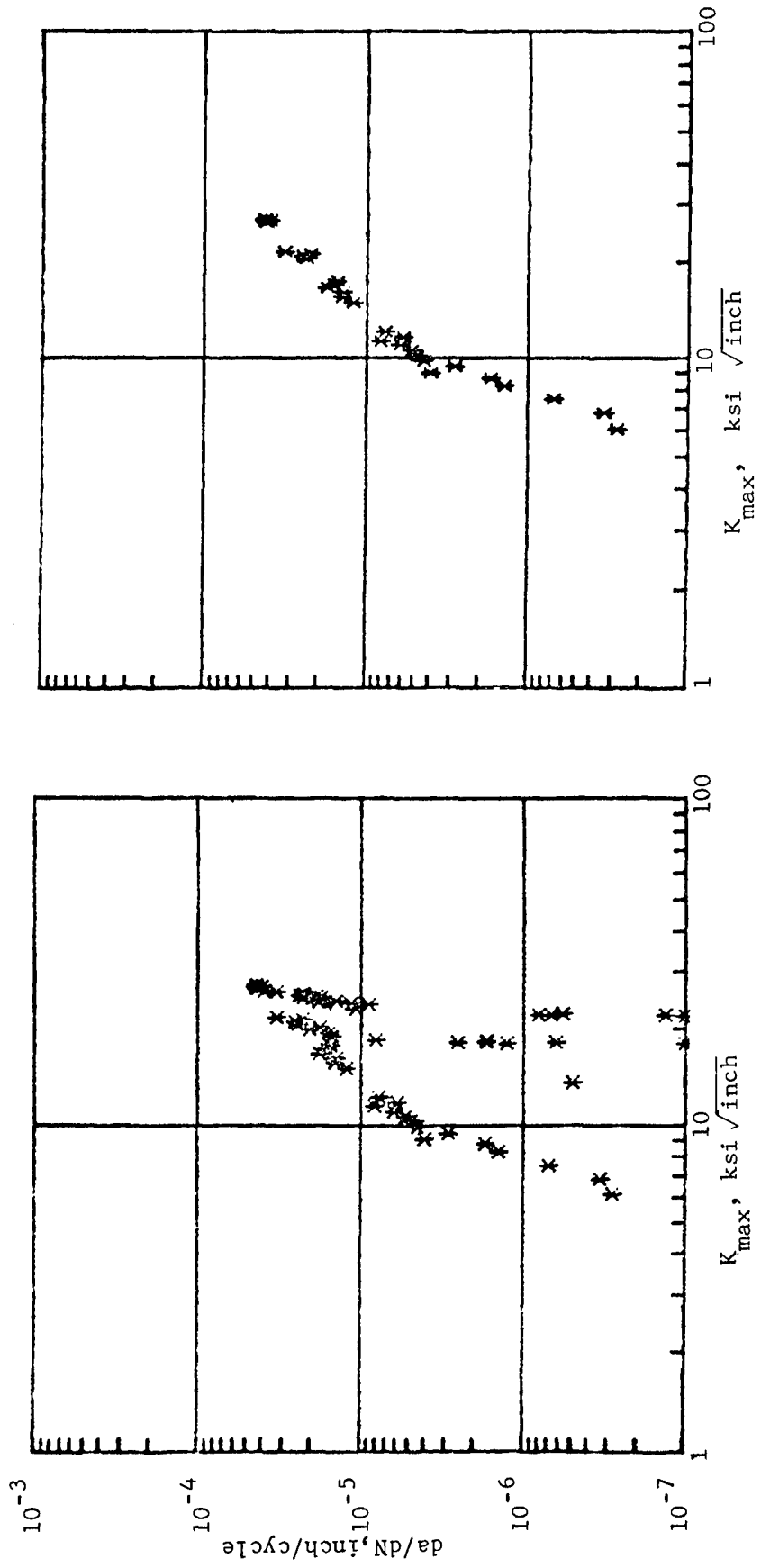
Figure 115. Crack Growth Rate Behavior of 2024-T351, CCT Specimen No. LT-2-5, Test Case No. 102, $\sigma_x = 0$, $\sigma_y = 10$ ksi, $R = 0.1$, $f = 10$ Hz, Overload Ratios = 1.67, 2.0.



(a) All Data Points Included

(b) Retarded Rates Excluded

Figure 116. Crack Growth Rate Behavior of 2024-T351, Cruciform Specimen No. 2-38
 Test Case No. 108, $\sigma_x = 5 \text{ ksi}$, $\sigma_y = 10 \text{ ksi}$, $R = 0.1$, $f = 10 \text{ Hz}$, Overload Ratio = 2.0



(a) All Data Points Included

(b) Retarded Rates Excluded

Figure 117. Crack Growth Behavior of 2024-T351, Cruciform Specimen No. 2-34
 Test Case No. 109, $\sigma_x = 5 \text{ ksi}$, $\sigma_y = 10 \text{ ksi}$, $R = 0.1$, $f = 10 \text{ Hz}$, Overload Ratio = 2.0

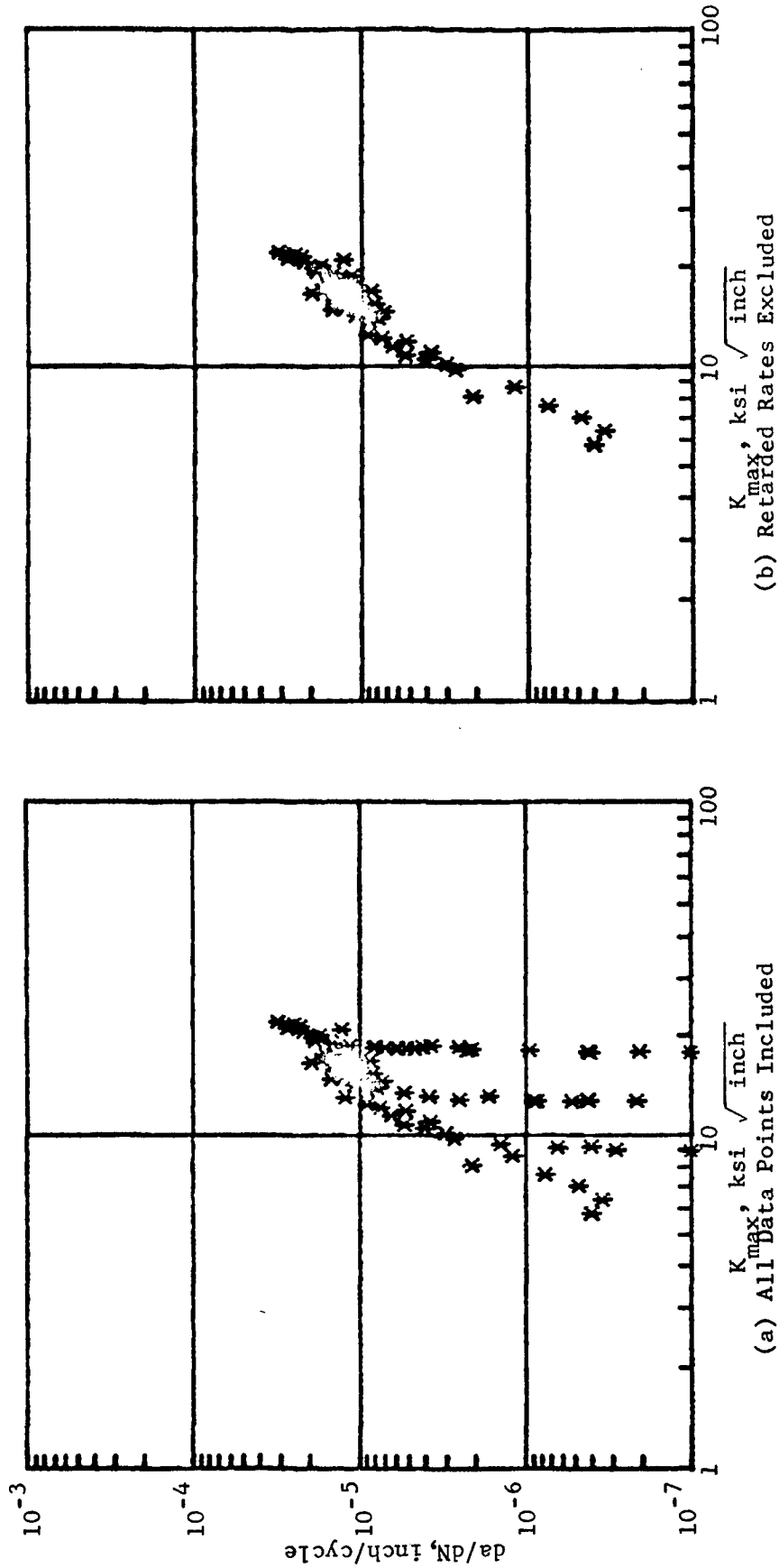


Figure 118. Crack Growth Behavior of 2024-T351, Cruciform Specimen No. 2-41
 Test Case No. 110, $\sigma_x = -5$ ksi, $\sigma_y = 10$ ksi, $R = 0.1$, $f = 10$ Hz, Overload Ratio = 2.0

Two approaches were taken to evaluate whether the crack growth rate behavior (after each overload) would have been affected by the variations of biaxial stress ratios. A straightforward approach was to take a delta cycle count (between each pair of overloads) in each specimen tested. Comparison of the delta cycles is presented in Table 12. The trend of the data seems to show that the negative biaxial stress field exhibits more retardation than the positive biaxial stress ratio of -0.5 than a zero biaxial ratio (uniaxial), and even more so when comparing the delta cycles between the -0.5 and +0.5 biaxial ratios. This phenomenon is more evident when the crack was short. For a > 1.0 inch (2 inches total crack length), the biaxial stress effect was not clear.

The current state-of-the-art fatigue crack growth concepts recognize the importance of crack tip plastic zone size on affecting the crack growth retardation behavior. Crack growth analysis models always build in a mathematical function for computing the crack tip plastic zone size at any point along the crack propagation path. As mentioned earlier, the residual plastic zone sizes, as well as the loaded plastic zone sizes, may depend on the combinations of σ_x and σ_y . Therefore, the general implication is that good correlation between a predicted crack growth history and a set of actual test data can be obtained by incorporating a properly determined crack tip plastic zone size relationship (as a function of stress level, crack length, material mechanical properties, state-of-stresses, i.e., plane stress or plane strain, and the biaxial stress ratio, etc) into a crack growth analysis model. The modified Willenborg model and the new retardation model were used to compute the crack growth histories for the periodic single overload specimens. The modified Willenborg model was applied to all nine tests but the new model was applied to the 2024-T351 specimens only. Due to the nonlinear behavior of the crack tip plastic zone sizes (see Section 7.3), estimated r_p values, as a nonlinear function of $(K_{max}/F_{ty})^2$, were used in the calculations. The estimates were based on the backtracked residual plastic zone sizes and expressed in a form of polynomials. Since the backtracked data were built-in with the actual testing conditions, the variables, $F(a)$, $\eta/2$, and γ in Equations 19 and 20 vanished. Thus, the complexities in determining these geometric terms were eliminated.

TABLE 12. PERIODIC SINGLE OVERLOAD TEST RESULTS

ALLOY	a (inch)	SPECIMEN AND TESTING CONDITION					
7075-T7351	0.25 } 0.50 } 1.00 } 1.50 }		T.C. 99 ($\sigma_x = 0$)	T.C. 103 ($\sigma_x = \sigma_y/2$)	T.C. 104	T.C. 105 ($\sigma_x = -\sigma_y/2$)	
		$\Delta N =$	34270	28740		40530	
		$\Delta N =$	27530	23420	25210	32660	
		$\Delta N =$	25540	23810	23650		
2024-T351	0.25 } 0.50 } 1.00 } 1.50 } 2.00 }		T.C. 102 (CCT)	T.C. 101 ($\sigma_x = 0$)	T.C. 108 ($\sigma_x = \sigma_y/2$)	T.C. 109	T.C. 110 ($\sigma_x = -\sigma_y/2$)
		$\Delta N =$		106370			169790
		$\Delta N =$		93900	85680 (Average = 78635)	71590	132130
		$\Delta N =$	113590 (Average = 110270)	106950	94600 (Average = 114715)	134830	122060
		$\Delta N =$			165300 (Average = 171555)	177810	

Since only a limited amount of backtracked plastic zone data was obtained from the present experiments, it would not be practical to determine a least square fit from each of the figures (in Section 7.3). Therefore, numerous hand-fitted curves were fed into the computer programs. The best suited polynomial(s) was found from comparison of the predicted and the actual crack growth histories. It should be noted that in all the following predictions, only one r_p function was applied to both the residual (after overload) and the current (at the subsequent lower cyclic loads) crack tip plastic zones.

In applying the modified Willenborg model, the geometric parameters γ and η in Equation 21 were fixed at 1.0 (for plane stress) and 2.0 (for full plastic zone), respectively. A best suited overload shut off ratio, S , was determined by comparing the results obtained from numerous computer runs. Different combinations of S and r_p - functions were inserted into each computer run. It was found that an S value of 2.3 would be best suited to both the 7075-T7351 and the 2024-T351 aluminum alloys.

Seventeen r_p functions for the 7075-T7351 material were fed into the computer program. After evaluation of all the results, it was determined that Polynomial No. C-15 was best suited to all five tests in three biaxial ratios (0, ± 0.5). The analytically determined data points are plotted in Figures 101 to 104 to compare with the actual crack growth history. In each test case, the analysis started from the initial crack length of that particular test; each data point plotted in the figure indicates the crack length corresponding to a load cycle just before the application of an overload. Notice that the first data point always correlated best with the test result. No overload in that period implies that the Collipriest constants for the material were properly determined and that the baseline da/dN curve was accurately reused. The case of analytic data points terminating in the middle of a crack growth history curve implies that no correlations were obtained beyond that point; either complete arrest or

rapid crack growth has occurred. It is interesting to note that Irwin's plastic zone equation also exhibited good correlation with the actual test results for Test Case No. 99, the uniaxial case (see Figure 101). The r_p curves for the Irwin equation and Polynomial No. C-15 are presented in Figure 119 for comparison.

Another seventeen r_p functions were used to evaluate the plastic zone size and biaxial loading effects (using the modified Willenborg model) on the 2024-T351 material. In these computer runs, the initial crack lengths were the experimental crack length at the first overload (i.e., the loading cycles prior to the first overload were deleted from the analysis). After examining all the analytical results, it was noticed that the analyses were extremely sensitive to changes in plastic zone functions. Good correlation was almost impossible to obtain. Four polynomials were selected from all the analyses. The analytic data points are plotted along with the experimental crack growth curves in Figures 105 to 109. Polynomial No. B-9 was considered to be the best for the uniaxial loading condition, whereas the polynomials No. B-7 and No. B-8 were selected for the 0.5 biaxial loading condition. As shown in Figure 109 the best selected polynomial (No. B-6), for $B = 0.5$, actually poorly correlated with the experimental data. Examination of the curves plotted in Figure 120 for these plastic zone functions rather surprisingly revealed that these four functions are almost identical especially between No. B-6 and No. B-7. The reason(s) for such sensitivities in using the modified Willenborg model on the 2024-T351 material cannot be detected at the present time. However, it is certain that considerable amount of modifications to this mathematical model will be required.

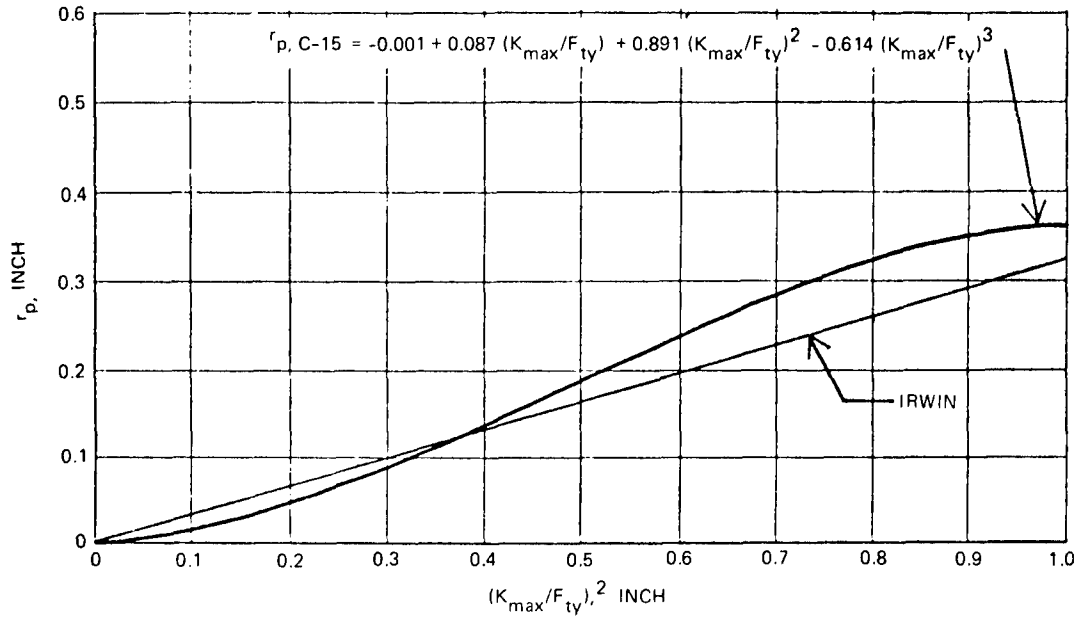


Figure 119. Crack Tip Plastic Zone Sizes in 7075-T7351 Cruciform Specimens

$$r_p, B-6 = 0.002 + 0.368 (K_{max}/F_{ty}) - 0.029 (K_{max}/F_{ty})^2 + 0.164 (K_{max}/F_{ty})^3$$

$$r_p, B-7 = 0.003 + 0.352 (K_{max}/F_{ty}) + 0.004 (K_{max}/F_{ty})^2 + 0.146 (K_{max}/F_{ty})^3$$

$$r_p, B-8 = 0.003 + 0.358 (K_{max}/F_{ty}) + 0.017 (K_{max}/F_{ty})^2 + 0.105 (K_{max}/F_{ty})^3$$

$$r_p, B-9 = 0.002 + 0.356 (K_{max}/F_{ty}) + 0.047 (K_{max}/F_{ty})^2 + 0.067 (K_{max}/F_{ty})^3$$

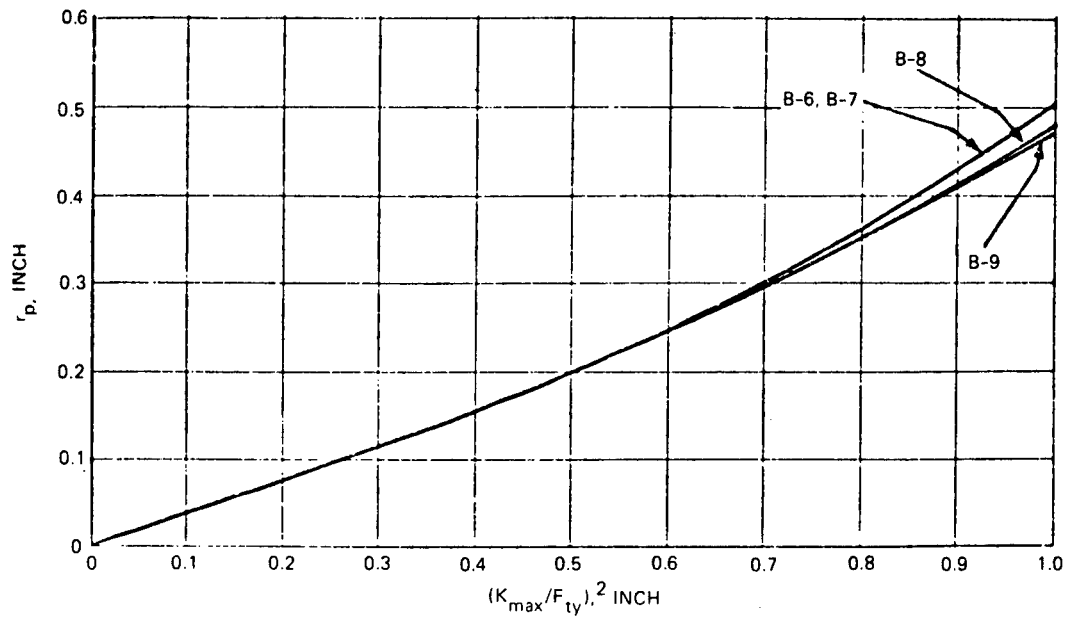


Figure 120. Crack Tip Plastic Zone Sizes in 2024-T351 Cruciform Specimens

The 2024-T351 specimens were reanalyzed by using the new retardation model. Again, various combinations of the Elber closure parameters (the values for C_1 and C_2) and r_p - polynomials were fed into the computer program. The best correlated r_p - polynomials are presented in Figure 121 and the comparisons between analytical and experimental data are presented in Figures 122 to 126. In these analyses, the following empirical constants were used.

$$\begin{aligned}
 \text{Paris } C &= 0.01 \text{ Micro-inch/cycle}/(\text{ksi } \sqrt{\text{inch}})^n \\
 \text{Paris } n &= 2.8265738 \\
 C_1 &= 0.5 \\
 C_2 &= 0.4 \\
 \eta &= 2.0 \\
 \gamma &= 1.0
 \end{aligned}$$

The initial crack length in each test case was again started from the crack length corresponding to the first overload. It can be seen in Figures 122 to 126 that the correlations are much better than those obtained from the modified Willenborg model. It is also shown in these figures that certain biaxial ratio goes with certain r_p - polynomial(s) thereby indicating the biaxial effect on crack growth retardation behavior.

In this program, the last overload in a test was often applied at $(K_{OL}/F_{ty})^2 \geq 0.75$. In the lower K_{OL} region, the correlations between test results and mathematical models were quite good; however, difficulties occurred at high K_{OL} levels. A literature survey was conducted of five Air Force reports [43 to 47] which contained a vast amount of experimental data on overload effects. The majority of the data covered a (K_{OL}/F_{ty}) range between 0.1 and 0.25, and never exceeded 0.3. Therefore, the difficulties encountered in the high K_{OL} region have never been experienced in the past.

$$r_{p, A-3} = -0.004 + 0.529 (K_{max} F_{ty}) - 1.822 (K_{max} F_{ty})^2 + 5.107 (K_{max} F_{ty})^3 - 2.665 (K_{max} F_{ty})^4$$

$$r_{p, A-7} = -0.004 + 0.465 (K_{max} F_{ty}) + 0.017 (K_{max} F_{ty})^2$$

$$r_{p, A-8} = -0.016 + 0.634 (K_{max} F_{ty}) + 0.994 (K_{max} F_{ty})^2$$

$$r_{p, RICE} = \pi (K_{max} F_{ty})^2 / 8.0$$

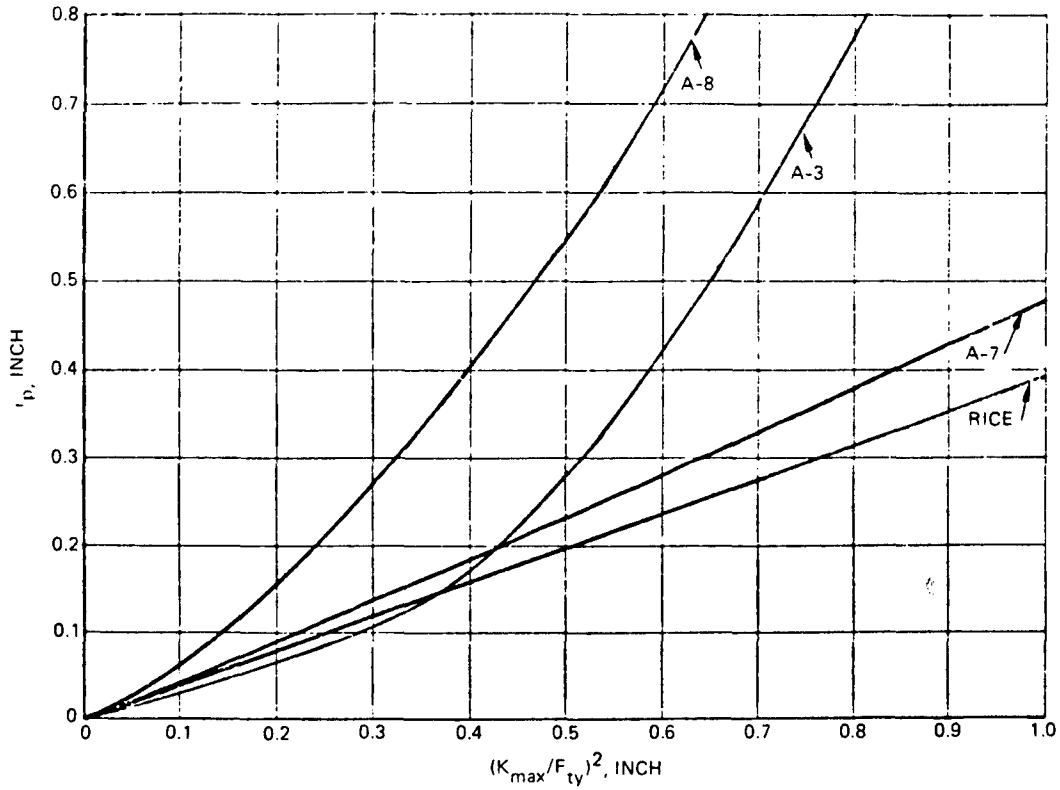


Figure 121. Crack Tip Plastic Zone Sizes in 2024-T351 Cruciform Specimens

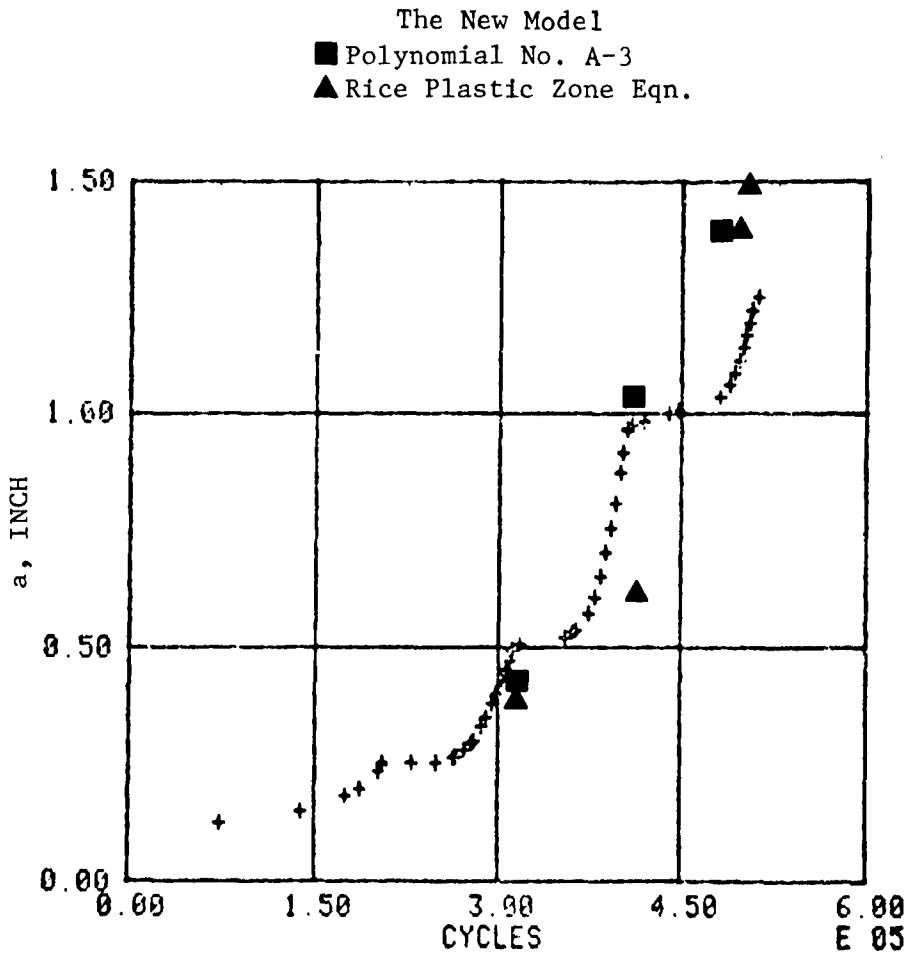


Figure 122. Crack Growth History of 2024-T351
 Cruciform Specimen No. 2-24
 Test Case No. 101
 $\sigma_x = 0, \sigma_y = 10$ ksi, $R = 0.1$, $f = 10$ Hz
 Overload Ratio = 2.0

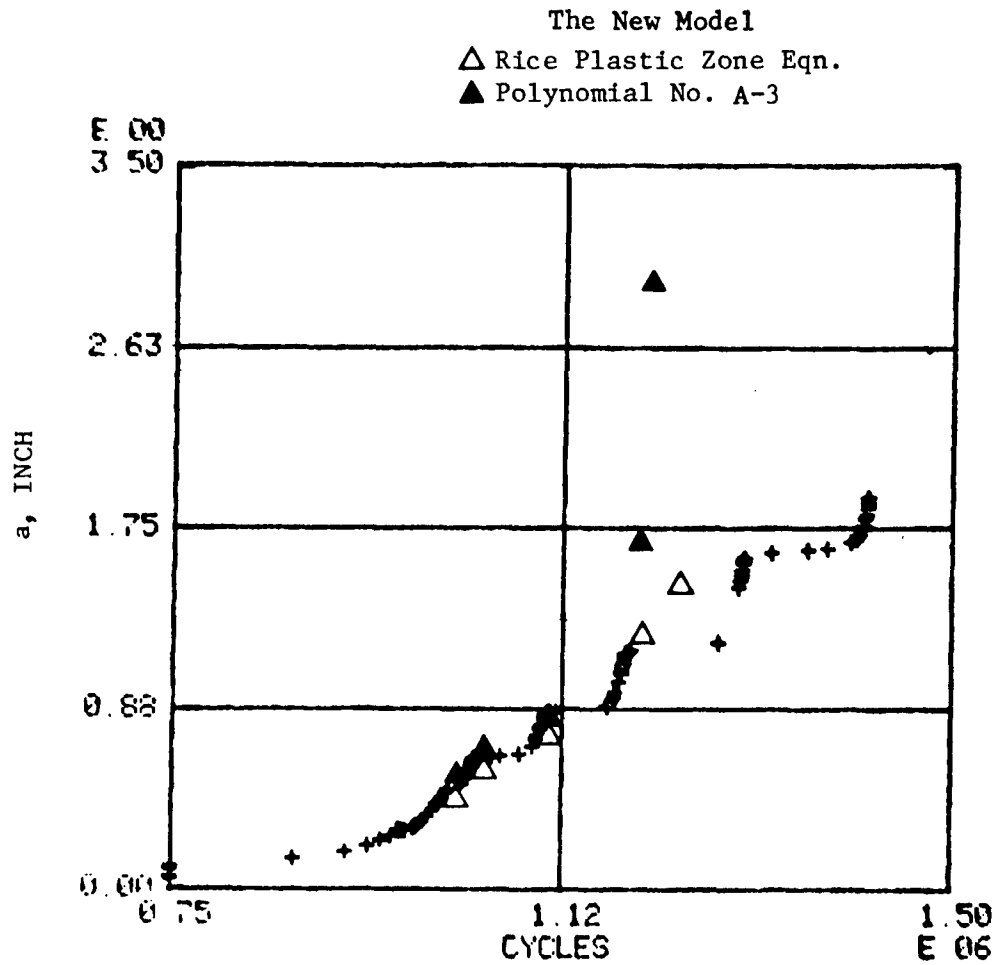


Figure 123. Crack Growth History of 2024-T351 Center-Cracked Panel; Specimen No. LT-2-5; Test Case No. 102; $\sigma_x = 0$, $\sigma_y = 10$ ksi, $R = 0.1$; Overload Ratio = 1.67 and 2.0

The New Model
 ◆ Polynomial No. A-7

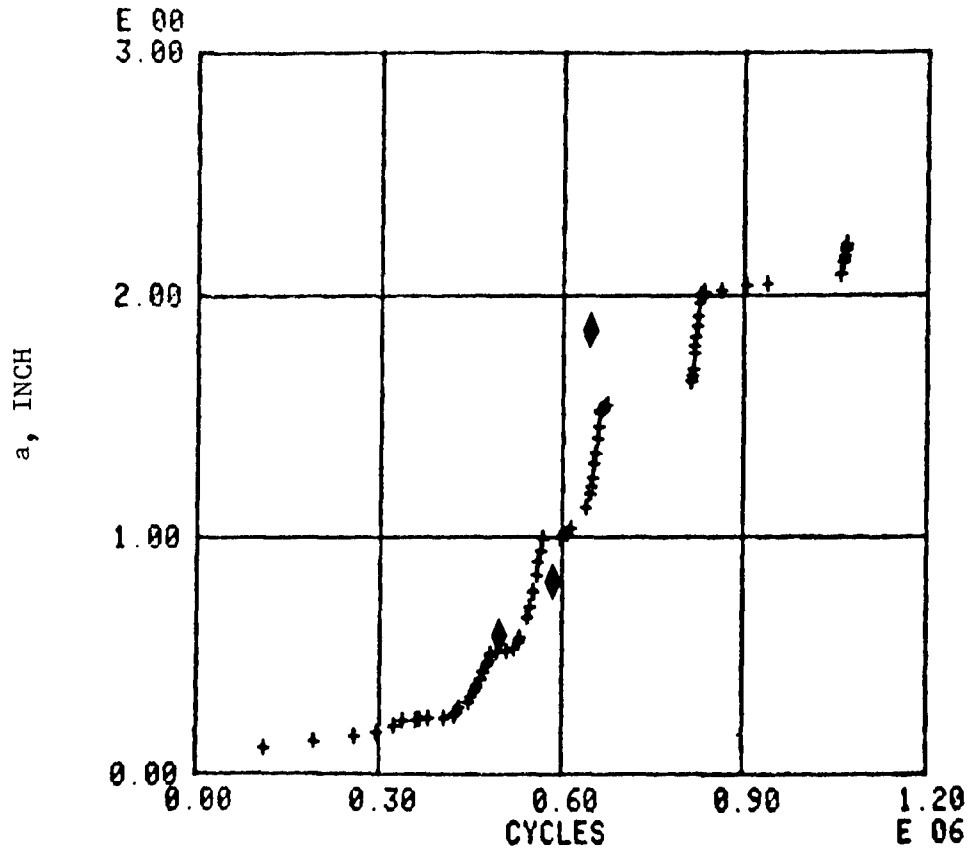


Figure 124. Crack Growth History of 2024-T351
 Cruciform Specimen No. 2-38
 Test Case No. 108
 $\sigma_x = 5$ ksi, $\sigma_y = 10$ ksi, $R = 0.1$,
 $f = 10$ Hz; Overload Ratio = 2.0

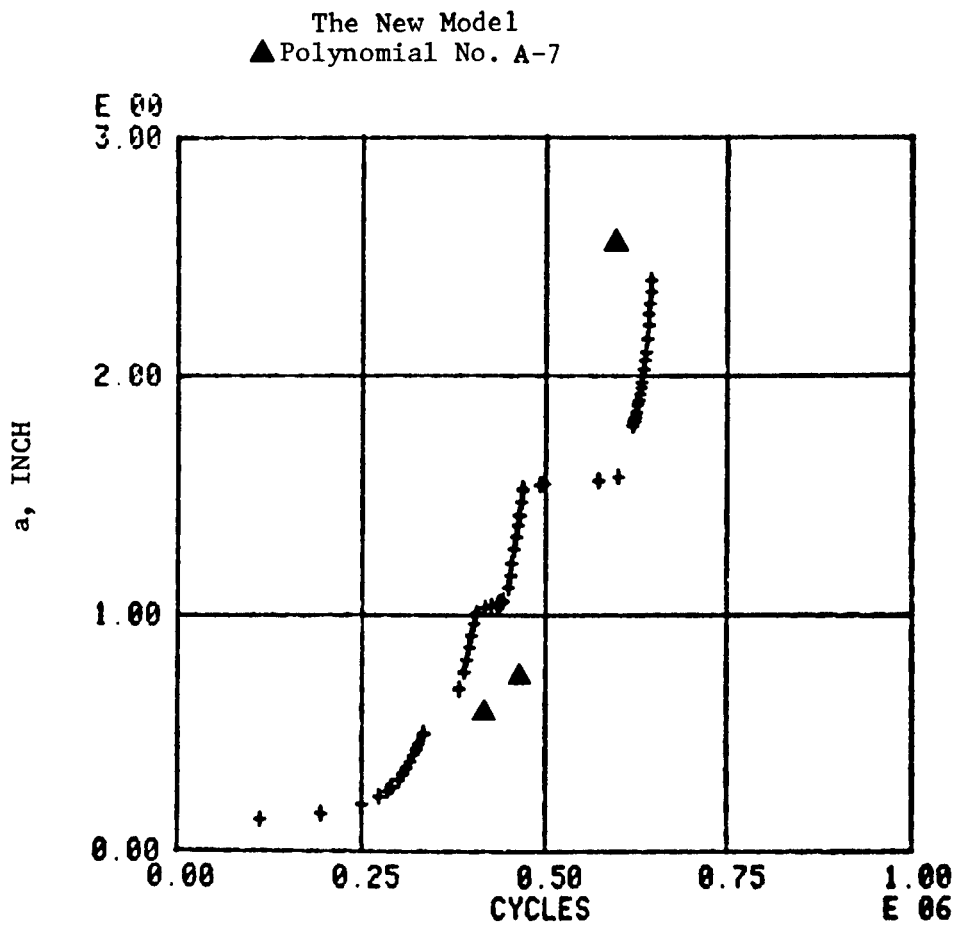


Figure 125. Crack Growth History of 2024-T351
 Cruciform Specimen No. 2-34
 Test Case No. 109
 $\sigma_x = 5$ ksi, $\sigma_y = 10$ ksi, $R = 0.1$,
 $f = 10$ Hz; Overload Ratio = 2.0

The New Model

● Polynomial No. A-8

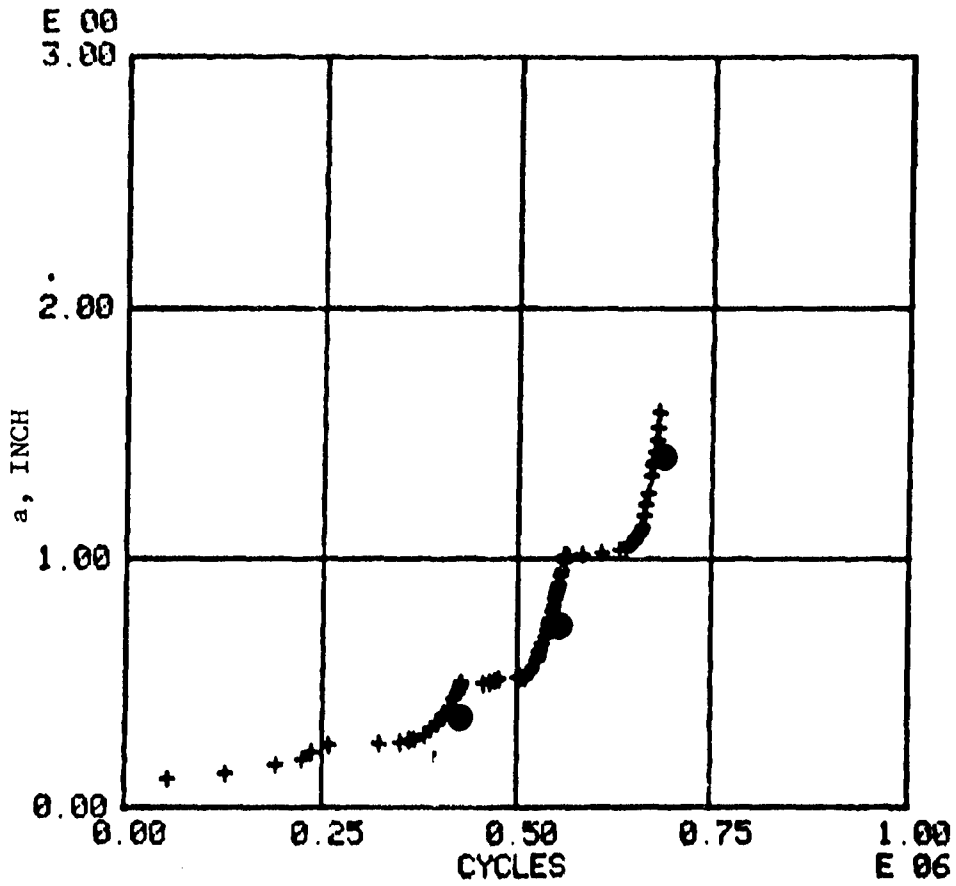


Figure 126. Crack Growth History of 2024-T351
Cruciform Specimen No. 2-41
Test Case No. 110
 $\sigma_x = -5$ ksi, $\sigma_y = 10$ ksi, $R = 0.1$,
 $f = 10$ Hz; Overload Ratio = 2.0

9.5.2 Spectrum Load Tests

Spectrum load tests were conducted on 7075-T7351 specimens at four biaxial ratios (0, -0.267, ± 0.5 , see Table 11). One specimen (B = -0.267) was first tested to obtain information on the effects of spectrum truncations. During the test duration, a full spectrum (see Table 13) and a truncated spectrum (by deleting some loading steps (see Table 14) were alternatively applied and crack growth rate at different test durations were compared. It was determined that loading steps containing stress levels below one-third of the peak stress level could be truncated without causing significant distortions in crack growth rate behavior. The truncated spectrum presented in Table 14 was then used for testing of the other three specimens. Crack growth histories ("a" versus number of blocks) for all four specimens are presented in Figure 127. Crack growth rate per block (da/dB) versus K_{\max} at the peak of each block and the crack growth profile for each test are presented in Figures 128 through 131. It is evident, from the crack growth histories or the da/dB curves, that the biaxial stress ratios affected the crack growth rate behavior. Comparing the biaxial stress ratios affected the crack growth rate behavior. Comparing the crack growth curves in Figure 127 with the delta cycle trend reported in Table 12, it is noticed that both single overload and spectrum load tests exhibited the same biaxial stress ratio trend on crack growth retardation; i.e., cracks grew faster at positive biaxial stress states but slower at negative biaxial loading conditions.

To analyze the spectrum load test results by using the modified Willenborg model, it would be logical to input the previously selected r_p - polynomial(s), from the single overload tests, into the computer program. As reported earlier, plastic zone function No. C-15 seemed to fit equally well to all the biaxial ratios between +0.5 and -0.5. Since σ_u was the same and the loading steps were the same in all the spectrum load specimens, there was only one analytical "crack length versus block" curve for all four biaxial loading conditions. Needless to say, it will be meaningless to compare one analytic curve against four experimental curves unless one could prove that the deviations in the test results were

TABLE 13. BLOCK SPECTRUM

Loading Step	P _{max} 	P _{min} 	Cycles
1	84.92	5.62	3
2	30.16	0	32
3	29.52	7.41	811
4	54.60	7.41	103
5	28.10	11.67	1234
6	77.78	7.41	6
7	44.60	11.67	372
8	91.75	5.62	1
9	24.60	7.41	778
10	68.25	7.41	20
11	38.89	11.67	811
12	58.25	0	203
13	33.33	11.67	1166
14	32.54	16.03	264
15	35.40	7.41	656
16	61.90	16.03	11
17	49.84	11.67	279
18	60.63	7.41	36
19	22.06	11.67	1834
20	20.00	7.41	914
21	47.78	0	2
22	79.68	16.03	1
23	41.43	7.41	421
24	100.00	5.62	1
25	12.92	0	111
26	60.79	11.67	97
27	23.49	0	412
28	47.46	16.03	61
29	54.12	11.67	139
30	37.46	0	8
31	74.29	11.67	7
32	19.21	0	1414
33	48.10	7.41	343

 Percent of peak stress in the spectrum
 (100 percent = 30 ksi)

TABLE 14. TRUNCATED SPECTRUM

Loading Step	P _{max} 	P _{min} 	Cycles
1	84.92	5.62	3
2	54.60	7.41	103
3	77.78	7.41	6
4	44.60	11.67	372
5	91.75	5.62	1
6	68.25	7.41	20
7	38.89	11.67	811
8	58.25	0	203
9	35.40	7.41	656
10	61.90	16.03	11
11	49.84	11.67	279
12	60.63	7.41	36
13	47.78	0	2
14	79.68	16.03	1
15	41.43	7.41	421
16	100.00	5.62	1
17	60.79	11.67	97
18	47.46	16.03	61
19	54.12	11.67	139
20	37.46	0	8
21	74.29	11.67	7
22	48.10	7.41	343

 Percent of peak stress in the spectrum

(100 percent = 30 ksi)

7075-T7351 Aluminum, $\sigma_{y, \max} = 30$ ksi

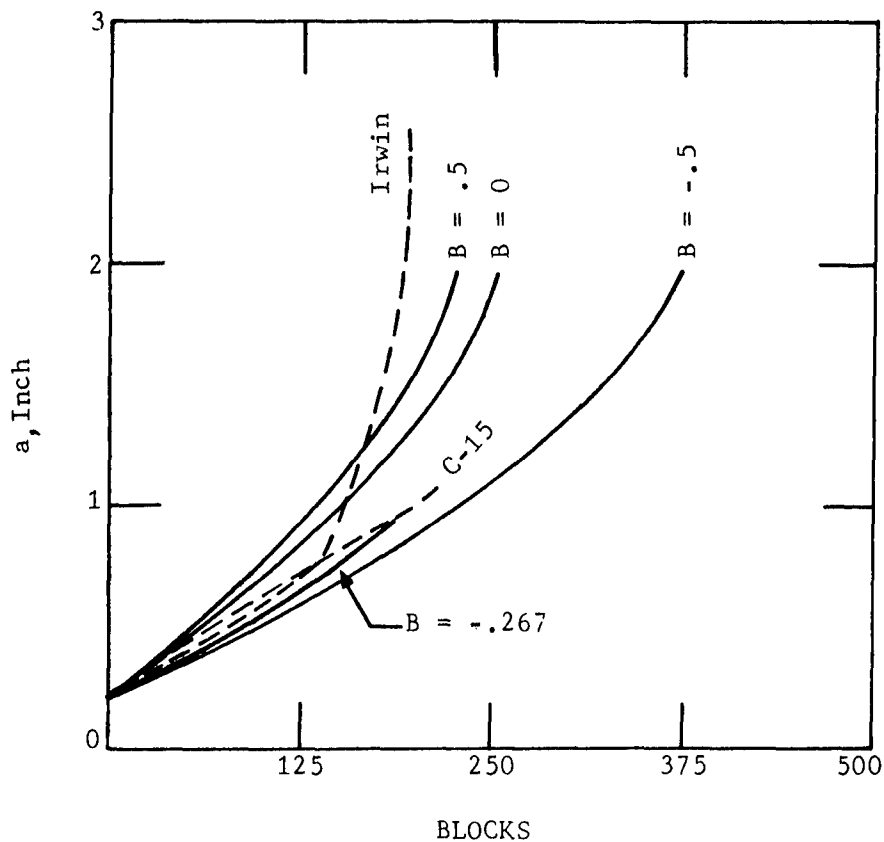
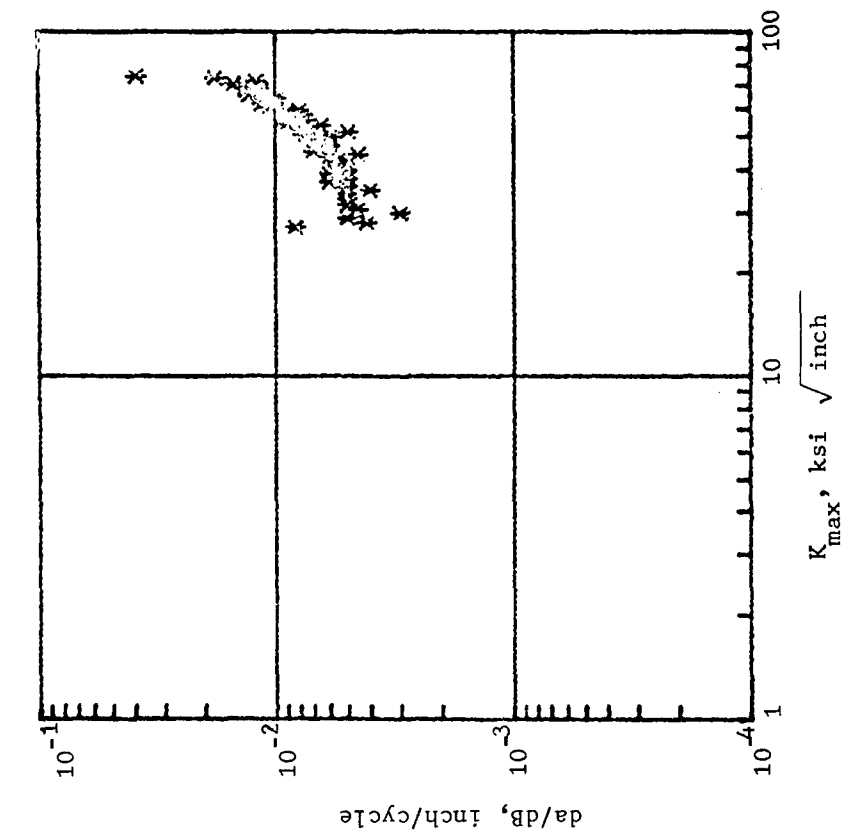
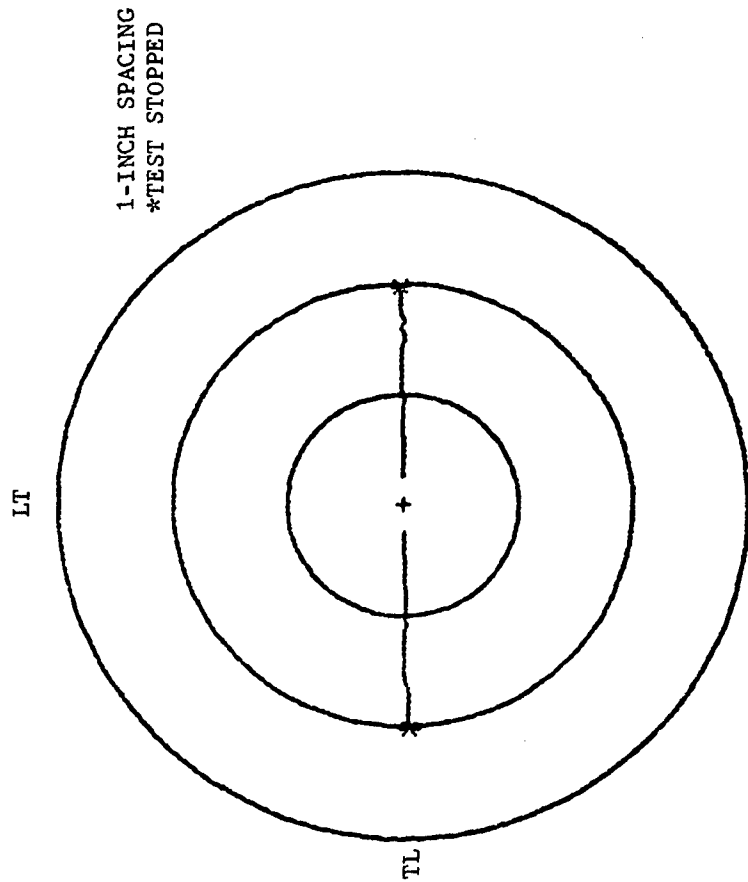


Figure 127. Crack Growth Histories of Cruciform Specimens under Biaxial-Spectrum Load Conditions

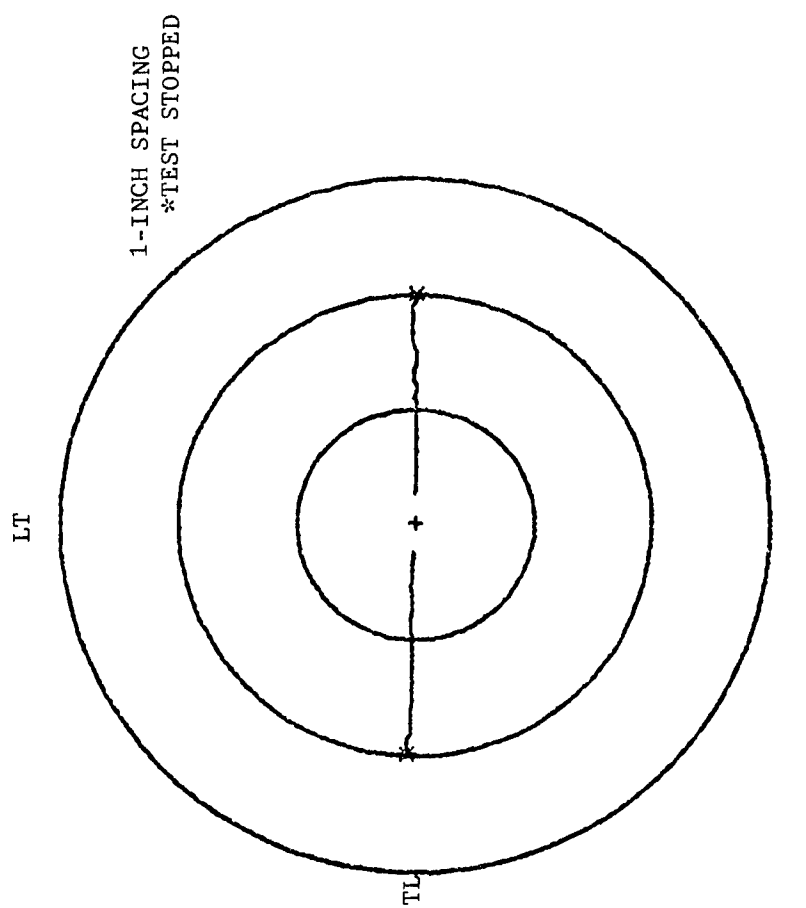


(a) Crack Growth Rate Behavior

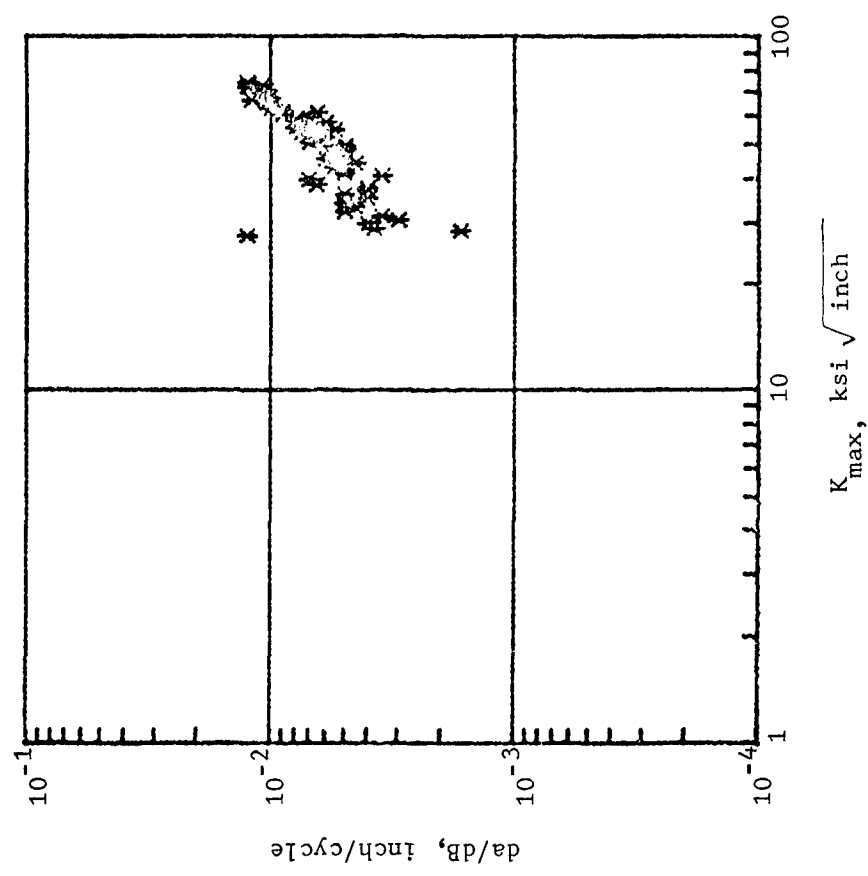


(b) Crack Growth Profile

Figure 128. Spectrum Crack Growth Test of 7075-T7351, Cruciform Specimen No. 7-8, Test Case No. 116, $\sigma_y, \text{max} = 30 \text{ ksi}$, $\sigma_x = \sigma_y/2$

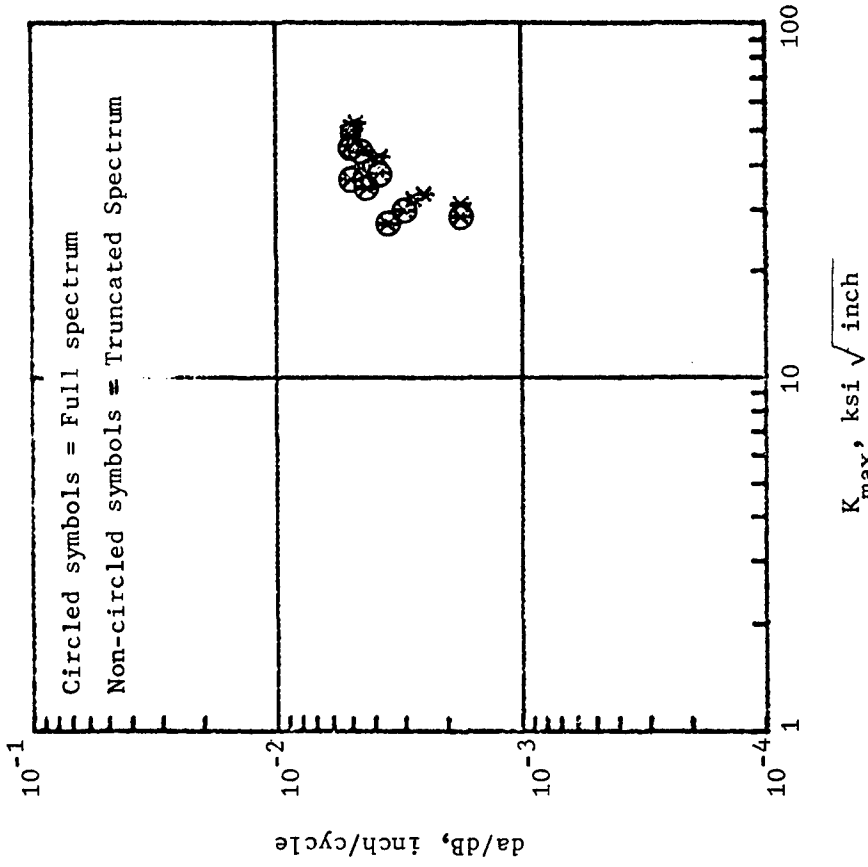


(b) Crack Growth Profile

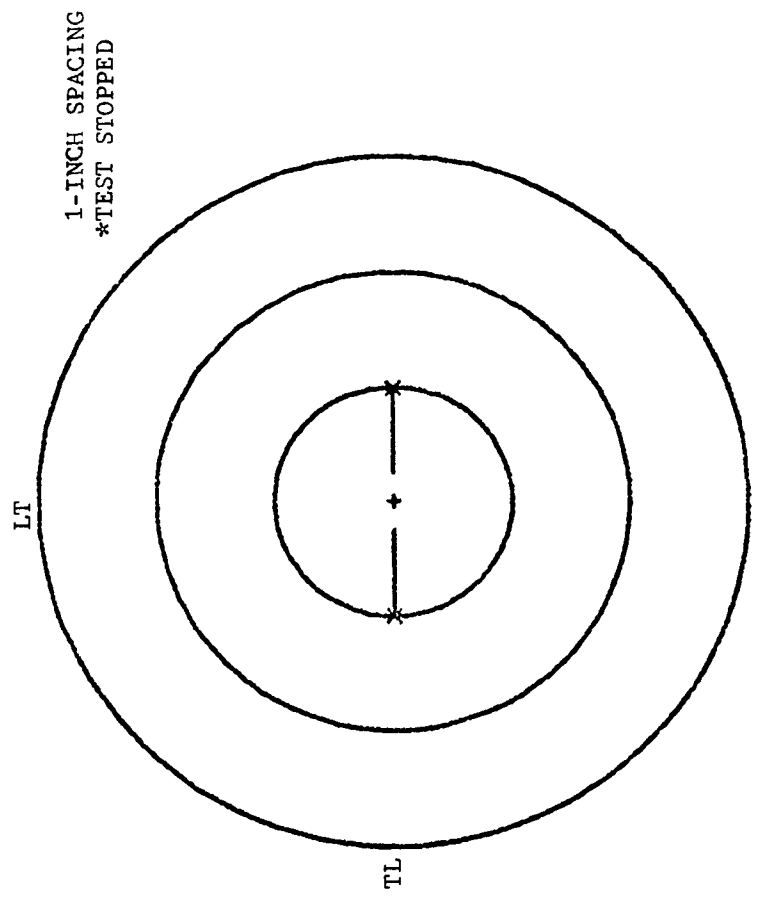


(a) Crack Growth Rate Behavior

Figure 129. Spectrum Crack Growth Test Of 7075-T7351, Cruciform Specimen No. 7-102, Test Case No. 114,
 σ_y , max = 30 ksi, $\sigma_x = 0$

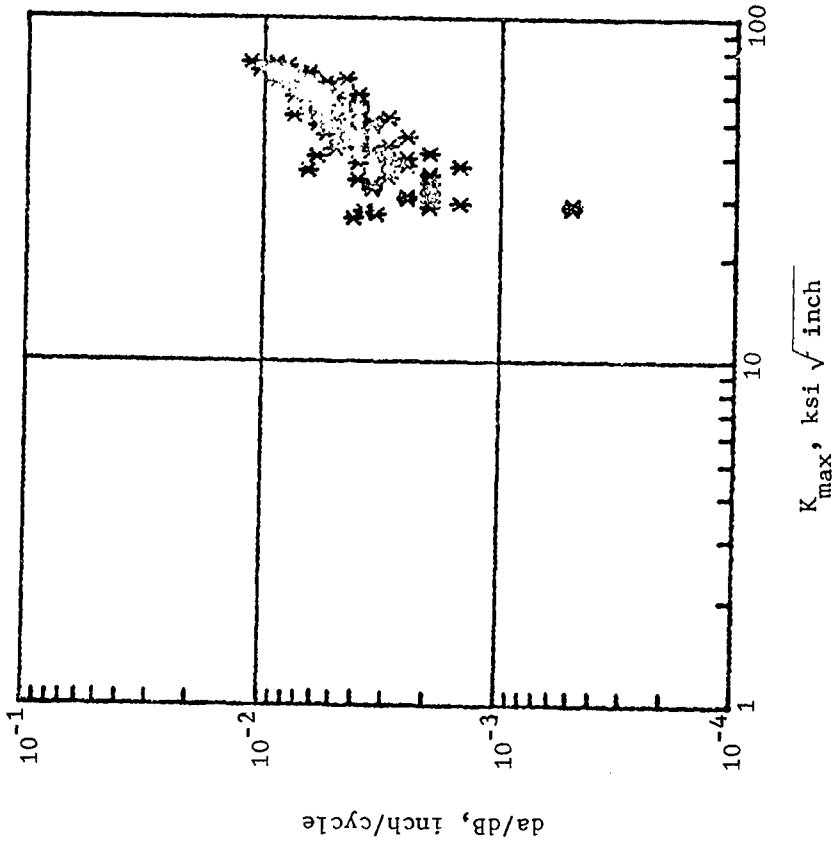


(a) Crack Growth Rate Behavior

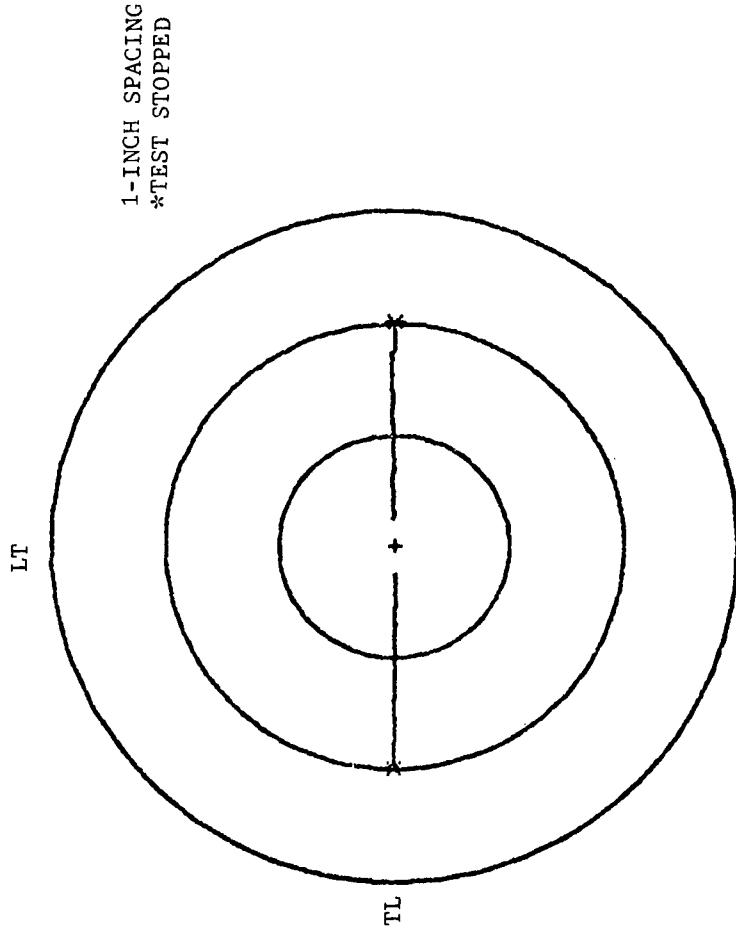


(b) Crack Growth Profile

Figure 130. Spectrum Crack Growth Test of 7075-T7351, Cruciform Specimen No. 7-63, Test Case No. 200, $\sigma_y, \text{max} = 30 \text{ ksi}$, $\sigma_x/\sigma_y = -0.267$



(a) Crack Growth Rate Behavior



(b) Crack Growth Profile

Figure 131. Spectrum Crack Growth Test of 7075-T7351, Cruciform Specimen No. 7-90, Test Case. No. 115, $\sigma_y, \max = 30 \text{ ksi}, \sigma_x = \sigma_y/2$

mainly experimental scatters, which was apparently not the case here. Just for the sake of comparison, a computer run was performed using the truncated spectrum and plastic zone polynomial No. C-15. The Irwin equation was also used for baseline comparison. The analytic crack growth histories are presented, along with the experimental data, in Figure 127.

At this point, it seems necessary to review the experimental data and find out why only r_p - function was obtained from the single overload data (for the 7075-T7351 material), whereas the spectrum load data indicated the need for four different plastic zone functions. The statistics on the variations of delta block counts between ± 0.5 biaxial ratios was extracted from the raw data of the spectrum load tests and are summarized in Table 15. Comparing the spectrum load test results (Table 15) and the single overload test results for the 7075-T7351 aluminum alloy (Table 12), it is seen that the variations in delta cycles between ± 0.5 biaxial ratios were 41 percent and 34 percent, respectively, for the first two pairs of overloads (for the crack in these specimens to grow from 0.5 inch to 1.0 inch and from 1.0 inch to 2.0 inches). However, the variations in delta blocks in the spectrum load tests were as high as 100 percent in the 0.5 to 1.0 inch crack length duration and an average of 61 percent in the remaining crack growth histories. Therefore, it is apparent that the biaxial ratio effects were magnified in the spectrum loading conditions. Since this experimental program only included a few tests in the variable amplitude loading conditions, more tests are required to generate sufficient information. Prior to that, development of a useful biaxial-crack-growth-retardation analysis procedure will be impossible. However, it is important to note that the test results generated from this program clearly indicated that there is a biaxial loading effect on crack growth retardation behavior.

TABLE 15. SPECTRUM LOAD TEST RESULTS*

2a (Inch)	Number Of Blocks		Variations In ΔB (%)
	B = 0.5	B = -0.5	
0.5	0	0	100
1.0	50	100	
2.0	135	225	47
3.0	190	315	64
4.0	225	376	74

*7075-T7351 cruciform specimens

9.6 Out-Of-Phase Loading Tests

Examination of Equations 1 and 2 revealed that the load-stress relationship characteristics in the current cruciform specimen design were not the same as those in an infinite sheet. In the out-of-phase cyclic loading conditions, the input loads for the cruciform specimen were adjusted in order to make the stresses in the cruciform specimen at any time during a cycle compatible with the stresses in an infinite sheet, particularly the instantaneous biaxial stresses ratios. A simple analytic procedure was formulated and described as follows.

1. In an ideal specimen, e.g., an infinite sheet, let σ_y be the reference stresses; i.e., let $\sigma_y^i = \sigma_y^o$ where the superscripts i and o denote in-phase and out-of-phase, respectively. Therefore, the sinusoidal waves for the biaxial stress components can be defined as

$$\sigma_y^o = \sigma_{y, \text{mean}} + (\sigma_{y, \text{mean}} - \sigma_{y, \text{min}}) \cdot \text{Sin } \omega t \quad (37)$$

$$\sigma_x^o = \sigma_{x, \text{mean}} + (\sigma_{x, \text{mean}} - \sigma_{x, \text{min}}) \cdot \text{Sin } (\omega t + \alpha) \quad (38)$$

where ωt is a time parameter, α is the phase angle and

$$\sigma_{y, \text{mean}} = \frac{1}{2} (\sigma_{y, \text{max}} + \sigma_{y, \text{min}}) \quad (39)$$

$$\sigma_{x, \text{mean}} = \frac{B}{2} (\sigma_{y, \text{max}} + \sigma_{y, \text{min}}) \quad (40)$$

with B being the biaxial stress ratio. The instantaneous biaxial stress ratio at any instant, ωt , will simply be the ratio of Equations 38 and 37, i.e.,

$$B_{\sigma}^{\omega t} = (\sigma_x^o / \sigma_y^o)_{\text{ideal}} \quad (41)$$

2. In a cruciform specimen, the stress and load relationship is given by

$$\sigma_y^c = \frac{P_y}{12} [6.55 - 1.73 B_p] \quad (42)$$

$$\sigma_x^c = \frac{P_x}{12} [6.57 B_p - 1.75] \quad (43)$$

where the superscript c stands for cruciform specimen, P_y is the load applied on the y axis of the cruciform specimen and B_p is the biaxial load ratio (P_x/P_y) in the cruciform specimen. In order to make both σ_x^c and σ_y^c and the instantaneous biaxial ratio in the cruciform specimen equal to those in an ideal specimen, set

$$\sigma_y^c = (\sigma_y^o)_{ideal} \quad (44)$$

and

$$\frac{\sigma_x^c}{\sigma_y^c} = \left(\frac{\sigma_x^o}{\sigma_y^o} \right)_{ideal} = B_\sigma^{\omega t} \quad (45)$$

therefore,

$$\frac{6.57 B_p^{\omega t} - 1.75}{6.55 - 1.73 B_p^{\omega t}} = B_\sigma^{\omega t} \quad (46)$$

and thus,
$$B_p^{\omega t} = \frac{6.55 B_\sigma^{\omega t} + 1.75}{6.57 + 1.73 B_\sigma^{\omega t}} \quad (47)$$

is the biaxial load ratio required for the cruciform specimen under out-of-phase condition at any instant, ωt .

3. Using Equations 42, 43 and 44 the loads, P_y and P_x corresponding to a given $B_p^{\omega\tau}$ would be

$$P_y^{\omega\tau} = 12\sigma_y^0 / (6.55 - 1.73 B_p^{\omega\tau}) \quad (48)$$

$$P_x^{\omega\tau} = B_p^{\omega\tau} \cdot P_y^{\omega\tau} \quad (49)$$

where σ_y is given in Equation 37. Therefore, the loads in the cruciform specimen, in any given time $\omega\tau$, corresponding to a given combination of $\sigma_{y, \max}$, $\sigma_{y, \min}$, B , and α , can be determined by using these equations.

The results of this analysis have indicated that the adjusted input loads ($P_y^{\omega\tau}$ or $P_x^{\omega\tau}$) for the loading conditions combining $R = 0.1$ and $B = -0.5$ (or -1.0), were actually oscillating between positive and negative loads. This loading condition required cyclically loading the test coupon from a negative load level (below zero) to a positive load level (above zero) and then dropping the load level back down to negative. This type of zero load crossing operation would have rapidly worn out the bearings in the biaxial test unit. Therefore, a test matrix consisting of a group of 7075-T7351 and 2024-T351 specimens was planned. The specimens were subjected to either (+) or (-) biaxial ratios at $R = 0.7$, or $R = 0.1$ with only the (+) biaxial ratios. Table 16 presents a listing of loads ($P_{y, \max}$, $P_{y, \min}$, $P_{x, \max}$ and $P_{x, \min}$) for $B = \pm 0.5$ and ± 1.0 , $\alpha = 180^\circ$ and $R = 0.1$ and 0.7 . Here, R was defined to be the ratio of $\sigma_{y, \min}$ and $\sigma_{y, \max}$ and $\sigma_{y, \max}$ was 12 ksi for the 7075-T7351 specimens and 10 ksi for the 2024-T351 specimens. Note that Test Cases No. 40 and 117 in Table 16 were not treated by load adjustments. The results of these tests demonstrated the magnitude of the problem (the effect of load adjusted versus load not adjusted). Test results are presented in Volume II of this report. Stress intensity factors for these tests were computed using the same procedure as

TABLE 16. LOADING CONDITIONS FOR 180° OUT-OF-PHASE CYCLIC STRESS TESTS ¹

Material	Test Case	B ²	P _{y,max}	P _{y,min}	P _{x,max}	P _{x,min}	R	B @ ωt=90°	B @ ωt=270°	Notes
7075-T7351	39	1.0	24.27	8.59	24.21	8.66	0.1	.10	10.000	3 5
7075-T7351	41	0.5	23.96	5.48	12.42	7.48	0.1	.05	5.000	3 5
2024-T351	43	1.0	20.23	7.16	20.17	7.21	0.1	.10	10.000	3 5
2024-T351	45	0.5	19.97	4.57	10.35	6.23	0.1	.05	5.000	3 5
7075-T7351	94	1.0	28.01	22.78	27.99	22.80	0.7	.70	1.429	5
7075-T7351	72	0.5	25.83	19.67	16.20	14.55	0.7	.35	0.714	3 5
7075-T7351	42	-0.5	21.47	13.44	-1.95	-7.38	0.7	-.35	-0.714	3 5
7075-T7351	118	-1.0	19.29	10.33	-10.20	-19.17	0.7	-.70	-1.429	6
2024-T351	112	1.0	23.34	18.98	23.32	19.00	0.7	.70	1.429	5
2024-T351	106	0.5	21.52	16.39	13.50	12.13	0.7	.35	0.714	3 5
2024-T351	46	-0.5	17.89	11.20	-1.63	-6.15	0.7	-.35	-0.714	3 5
2024-T351	44	-1.0	16.07	8.61	-8.50	-15.97	0.7	-.70	-1.429	3 5
7075-T7351	40	-1.0	17.40	1.70	-1.70	-17.40	0.1	-	-	4 5
7075-T7351	117	-1.0	17.40	12.20	-12.20	-17.40	0.7	-	-	4 5

¹ 10ksi at peak σ_y for 2024-T351 specimens, or 12ksi at peak σ_y for 7075-T7351 specimens

² Nominal σ_x/σ_y ratio, occurs at $\omega t=180^\circ$. FOR (+B): σ_y is max & σ_x is min at $\omega t=90^\circ$, σ_y is min & σ_x is max at $\omega t=270^\circ$. FOR (-B): Both σ_y & σ_x are max at $\omega t=90^\circ$, both σ_y & σ_x are min at $\omega t=270^\circ$.

³ Interferometry photographs

⁴ Load not adjusted

⁵ f = 10Hz

⁶ f = 15Hz

for the in-phase biaxial tests. It was noted that the crack growth rate versus K curve for the load adjusted cases were identical to those tested in the in-phase loading conditions. It was also clear that the crack growth rate curves for the test without load adjustments did not correlate with the test data previously obtained from the in-phase loading conditions.

Also indicated in Table 16, the biaxial ratio, in each test, was not constant throughout the test. It actually varied as each component of the sinusoidal waves oscillate across each other at different phase angles. For those tests conducted in the present program, the biaxial ratio could vary by a factor of 10 in each completed cycle. The crack was still growing straight and the crack growth rates were unchanged.

9.7 Miscellaneous Tests

In this section, experimental results for three particular types of tests are presented. These testing types were: sustained load tests, angle crack tests, and fracture tests. The test conditions are listed in Table 17.

9.7.1 Sustained Load Tests

In this type, σ_x was held constant at a predetermined level (matched with $\sigma_{y, \max}$ to form a desired biaxial ratio). Only σ_y was cyclically loaded to propagate the crack. Four specimens were tested at plus or minus 0.5 biaxial ratio with $R = 0.1$. The test results are compiled in Volume II of this report. Examining the da/dN versus K curves for these curves along with the baseline da/dN versus K curves presented in Section 9.2.1, it was revealed that the sustained lateral stress component did not cause any effect on crack growth rate behavior.

TABLE 17. MISCELLANEOUS TESTS

Material	Test Case	$\sigma_{y,max}$	$\sigma_{y,min}$	$\sigma_{x,max}$	$\sigma_{x,min}$	f	Notes
7075-T7351	95	12.0	1.2	6.0	6.0	5	1
7075-T7351	96	12.0	1.2	6.0	6.0	5	1
7075-T7351	97	12.0	1.2	-6.0	-6.0	5	1
7075-T7351	98	12.0	1.2	-6.0	-6.0	5	1
7075-T7351	79	12.0	1.2	0	0	5	2
7075-T7351	81	12.0	1.2	12.0	1.2	5	2
7075-T7351	83	12.0	1.2	-1.2	-12.0	5	2
7075-T7351	150	-	-	-	-	-	3
7075-T7351	123	-	-	-	-	-	3 4
7075-T7351	125	-	-	-	-	-	3 4 5
2024-T351	127	-	-	-	-	-	3 4
2024-T351	129	-	-	-	-	-	3 4 5

- 1 Sustained load test
- 2 Angle crack test, crack line oriented at 45° with respect to loading axes and sheet rolling direction.
- 3 Fracture test (monotonically loaded to failure), tested in uniaxial loading machine.
- 4 CCT specimen
- 5 TL direction

9.7.2 Angle Crack Tests

Three cruciform specimens consisting of a 45° slot were subjected to cyclic stresses at different biaxial stress ratios (0, ± 1.0). The specimens were precracked in the biaxial test frame at a biaxial ratio of 1.0, $P_{\max} = 25$ kips, and $R = 0.1$. This method produced a sharp fatigue crack from the elox slot and the crack was on the same plane as the elox slot, i.e., 45° in respect to the loading arms.

When the specimen was loaded to a -1.0 biaxial stress condition, the stress on the 45° plane was pure shear. Theoretically, the crack should have turned to a direction which is 70.5 degrees from the original cracked plane and then adjust itself to propagate in a direction normal to maximum K_1 . A sketch presented in Figure 132 shows that the crack did turn away from its original cracked plane. However, a pair of secondary cracks developed from the sharp corners of the elox slot. The test was terminated when the secondary cracks were discovered at approximately 80,000 cycles of testing time. Note that the original crack grew approximately 0.02 inch at each end and no "a versus N" record was collected.

The second specimen (Test Case No. 81) was tested under the one-to-one biaxial stress ratio condition. As discussed earlier, the stresses in all directions were identical and the crack tip stress intensities were pure Model 1. Therefore, the crack did grow straight and stayed on its original crack plane (see Figure 133). The da/dN versus K curve for this specimen (see Figure 134) was identical to the baseline crack growth rate curves presented in Section 9.2.1.

For the zero biaxial ratio condition, Test Case No. 79, the stress intensity at the tip of a 45° crack was one-half K_1 and one-half K_2 (see Figure 12). The initial turning angle at on-set of crack propagation should have been approximately 55° , clockwise from the original crack plane. Again, the final crack propagation path should have been normal to the maximum K_1 direction (i.e., normal to σ_y , see the actual crack growth profile presented in Figure 135). The K values for the test data points were calculated by using Figure 12 and Equation 15. Comparing the crack growth rate curves

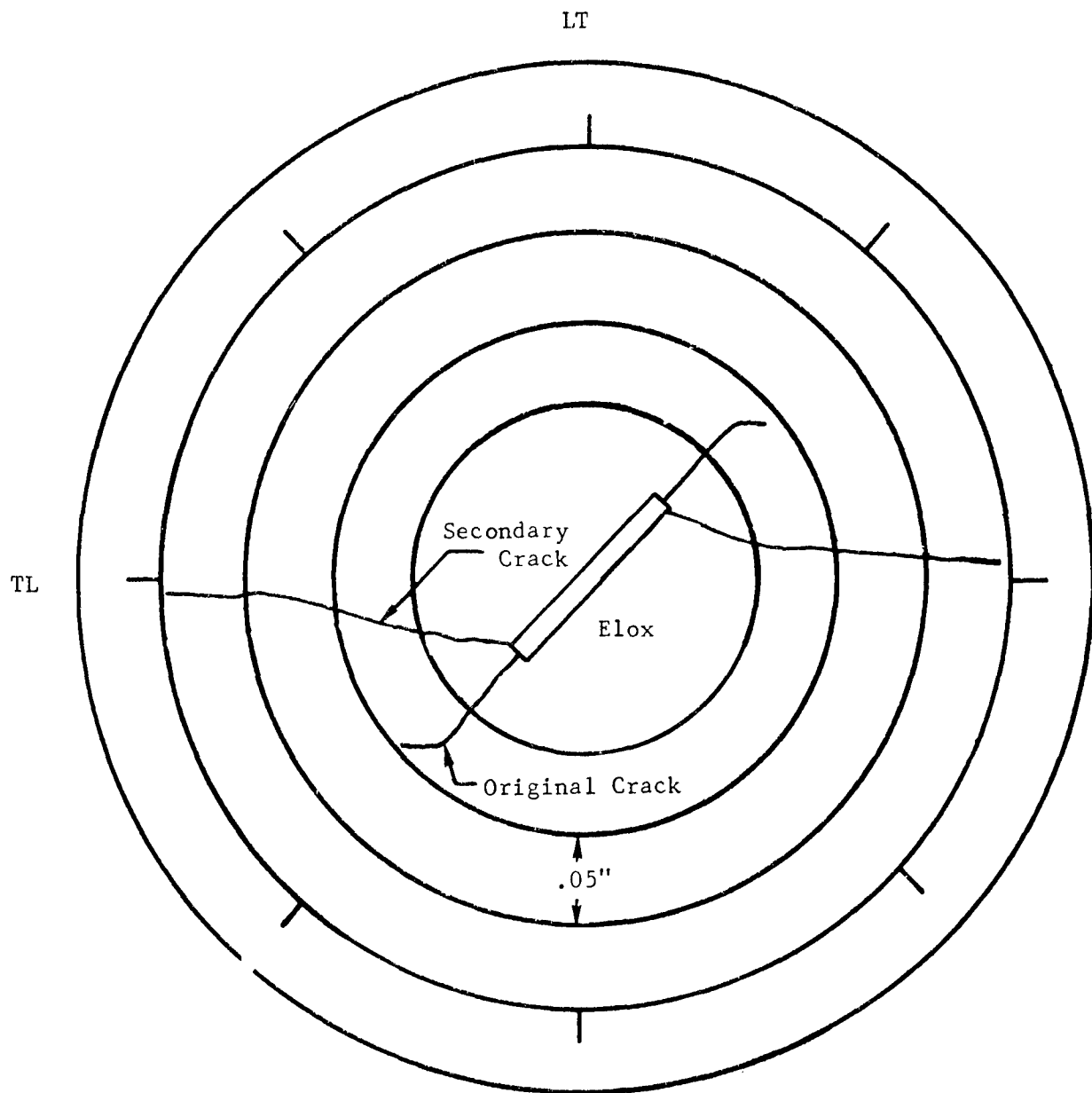


Figure 132. Sketch of a Crack Growth Profile of 7075-T7351
 Cruciform Specimen No. 7-5
 Test Case No. 83, Angle Crack
 $\sigma_x = -\sigma_y = -12$ ksi, $R = 0.1$,

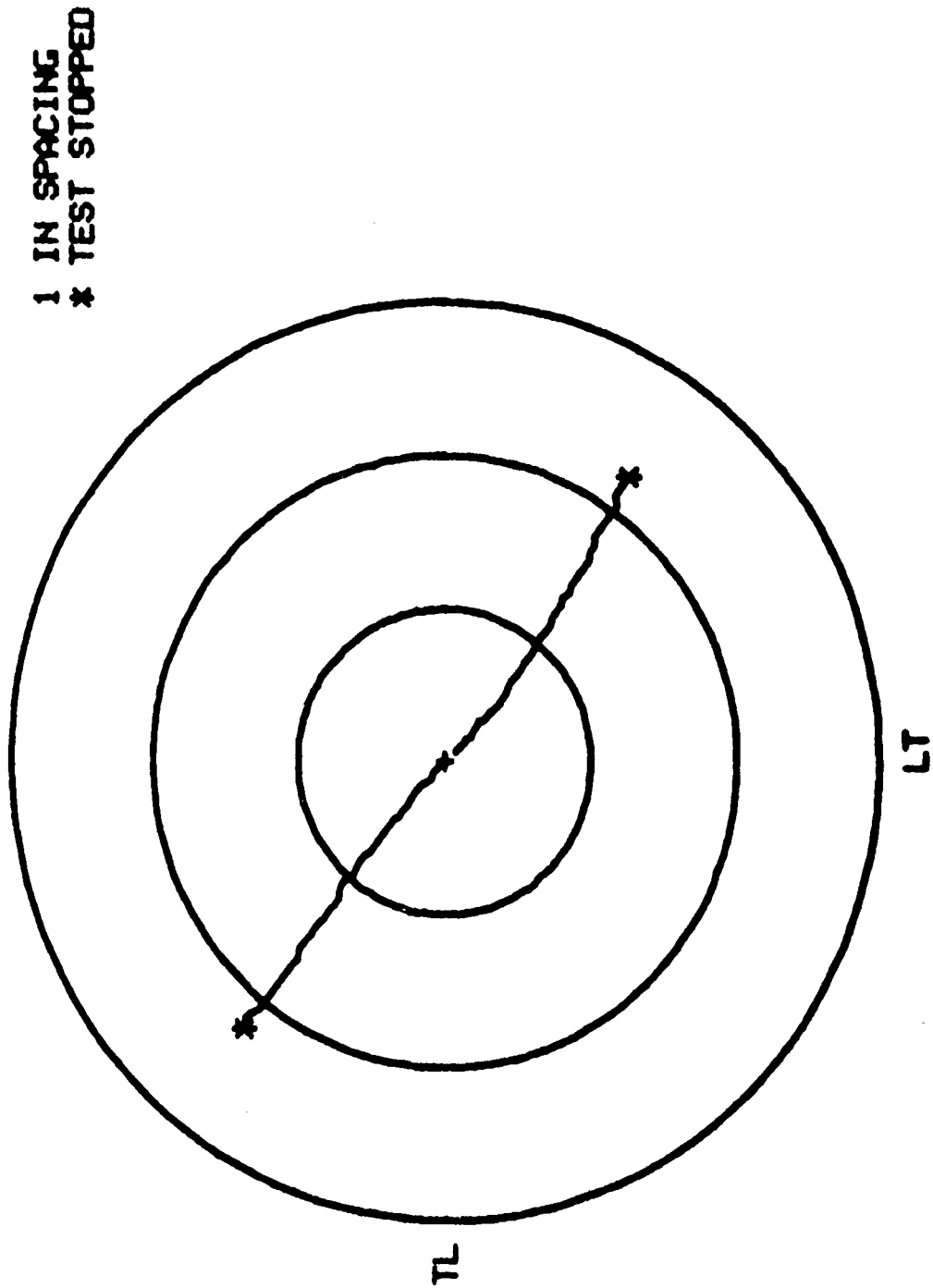


Figure 133. Crack Growth Profile of 7075-T7351 Cruciform Specimen No. 7-91,
Test Case No. 81, Angle Crack, $\sigma_x = +\sigma_y = 12 \text{ ksi}$, $R = 0.1$

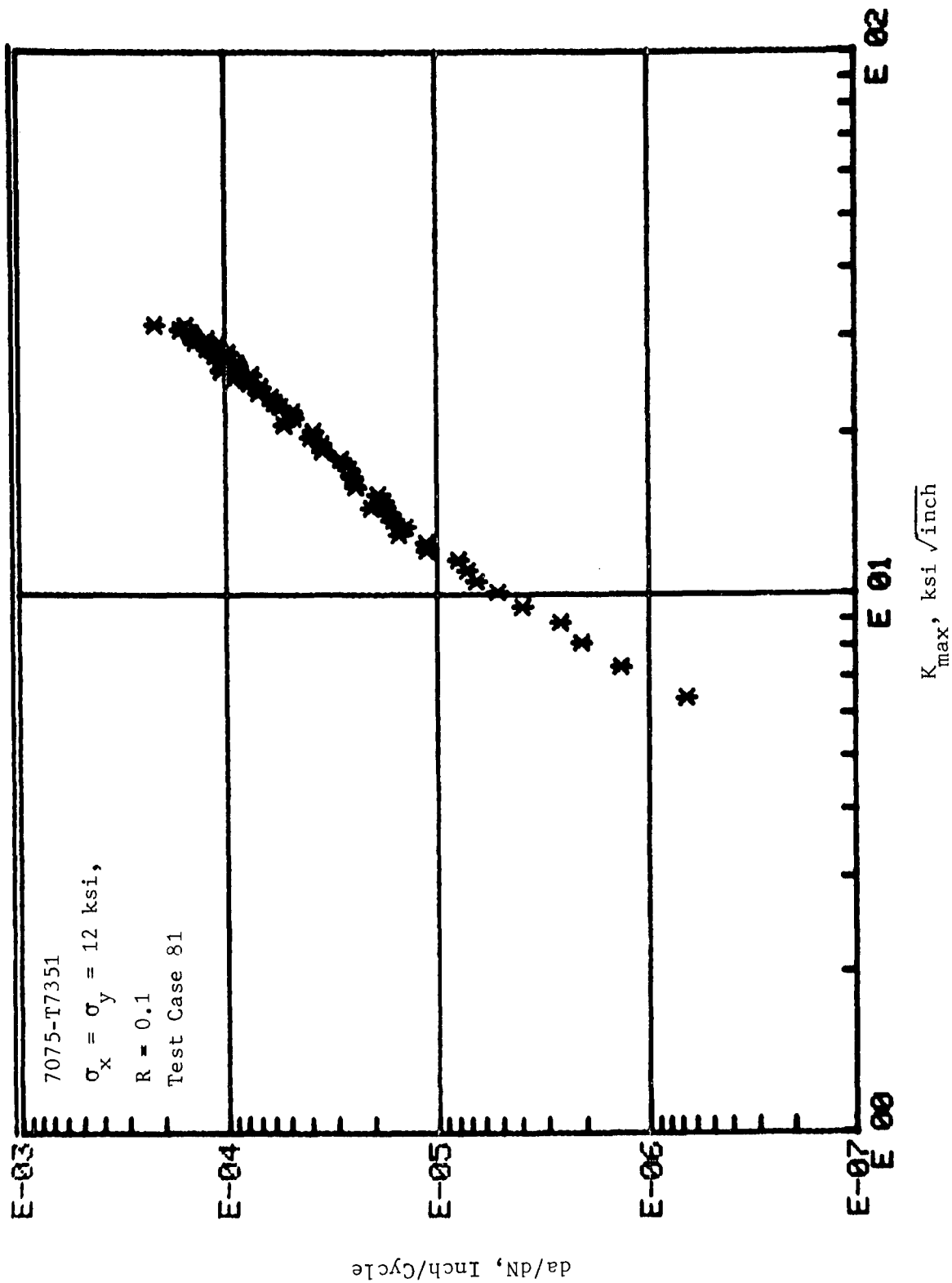


Figure 134. Cyclic Crack Growth Behavior of a 45° Angle Crack

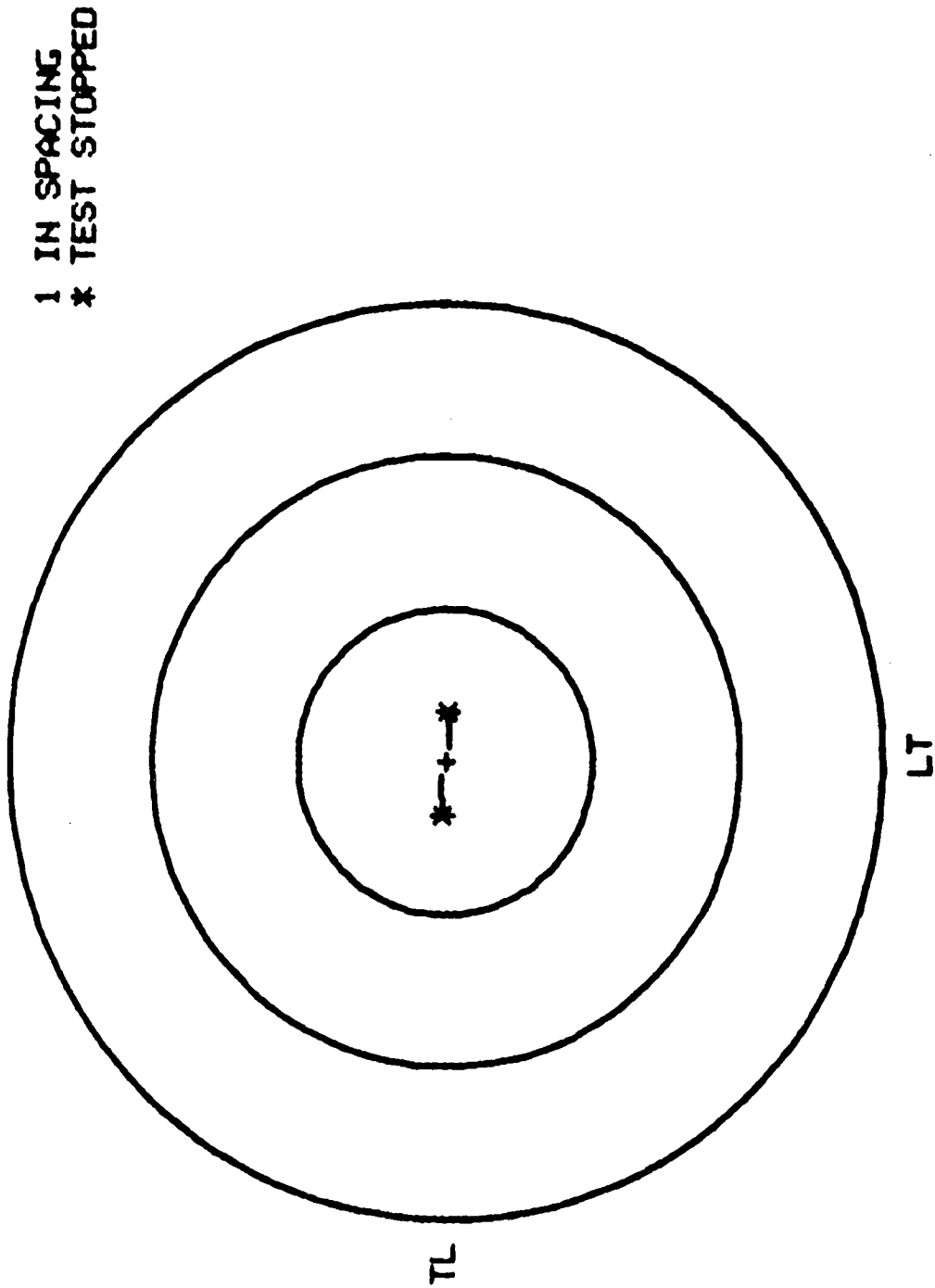


Figure 135. Crack Growth Profile of 7075-T7351 Cruciform Specimen No. 7-92,
Test Case No. 79, Angle Crack, $\sigma_x = 0$, $\sigma_y = 12$ ksi, $R = 0.1$

in Figures 134 and 136, the last several data points for this specimen fall right on the crack growth rate curve of the last specimen (Test Case No. 81). However, the first several data points at lower K levels (i.e., at shorter crack lengths) did not match the expected da/dN values. This was probably due to the fact that the crack was turning from a 45° position to a 0° position, the actual K values in the transition region were never determined.

9.7.3 Fracture Tests

Crack growth resistance curve (R-curve) tests were run for each material in both orientation (LT, TL). CCT specimens with a longer initial crack length ($a = 1.0$ inches) were used. ASTM ES61 was used as a guide to the test procedure. (Note: the specimen dimensions are not in the ASTM recommended range for this test type.)

Specimens were instrumented with back-to-back C.O.D. gauge calibrated to $\pm 1\%$ accuracy. Antibuckling guides were used to insure good alignment. The specimens were statically loaded; X-Y-Y recorders were used to monitor the two load versus compliance traces. As the compliance changed, periodic partial unloading of the specimen was required so that the compliance slopes could be computed. Prior to each unloading, visual crack length measurements on each of the two crack tips were recorded. Thus, at each data point, load, compliance, and optical crack length were recorded. Testing was continued to specimen failure.

Data analysis was performed using the following procedures.

1. The two crack tip measurements were averaged to determine the "a-optical."
2. a_{eff} (effective crack length) was solved for using Equation 10 of ASTM ES61.

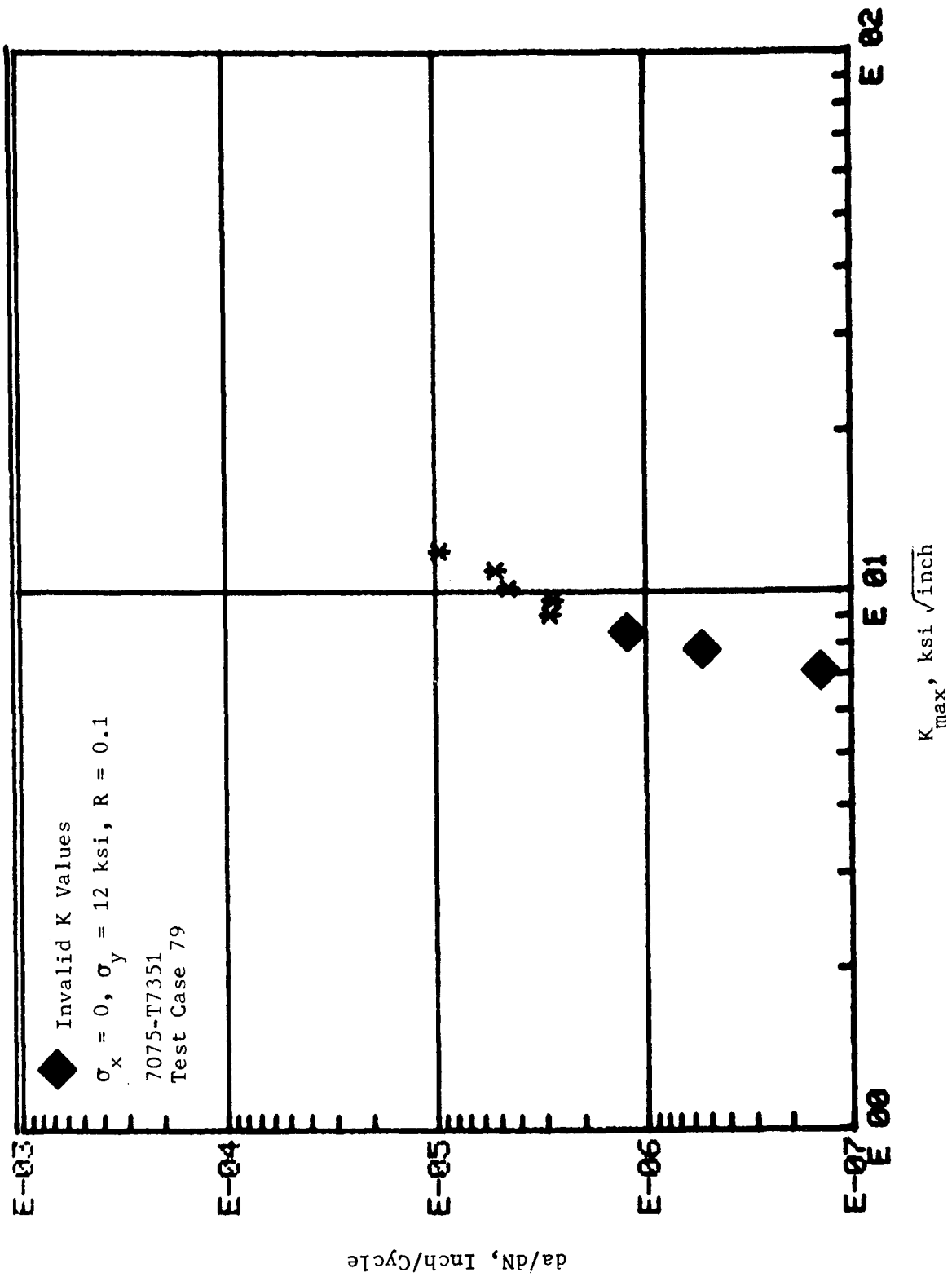
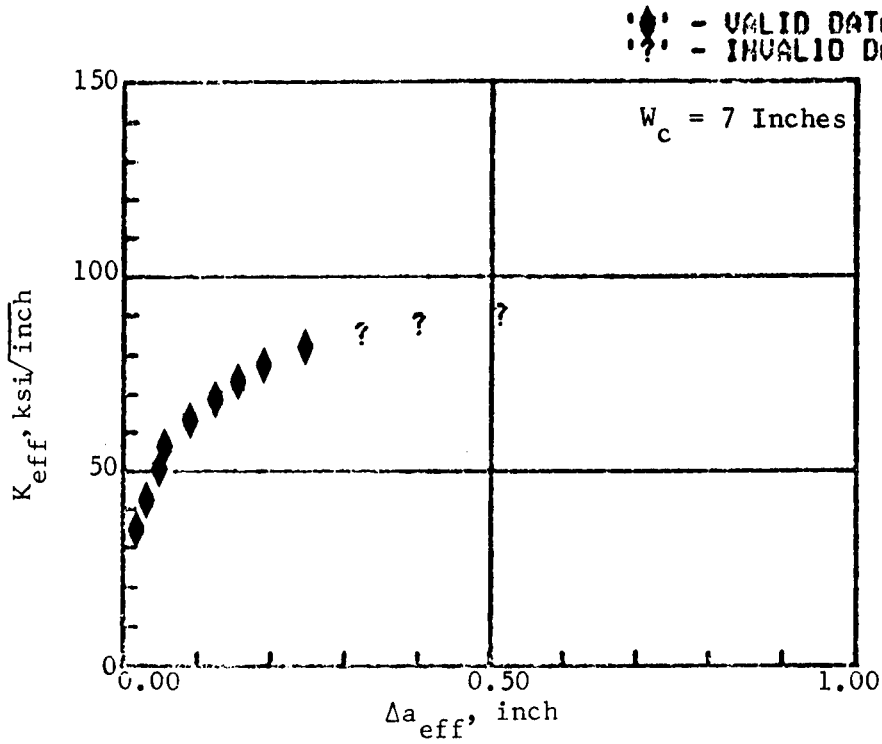


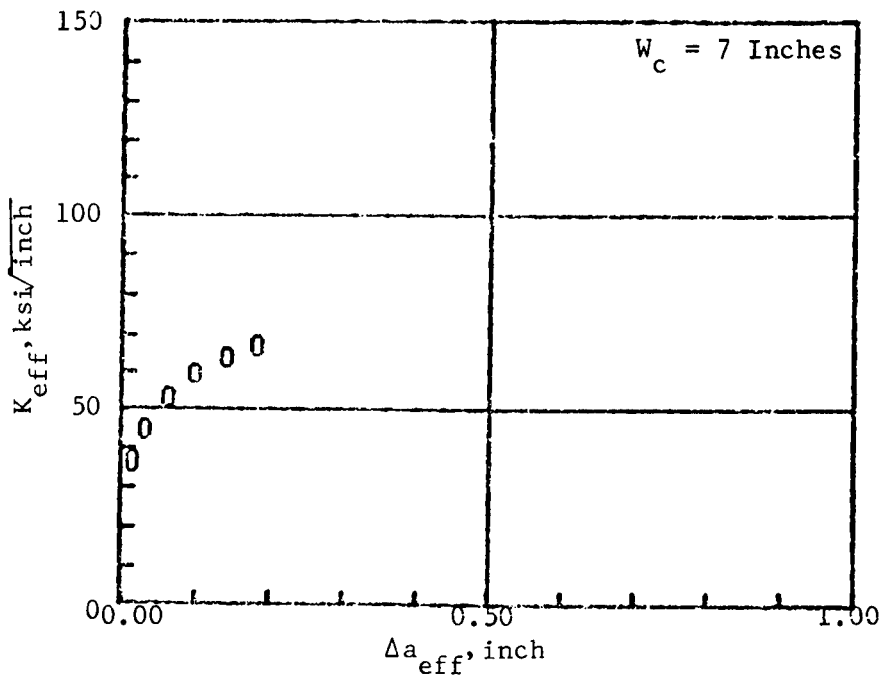
Figure 136. Cyclic Crack Growth Behavior of a 45° Angle Crack

3. K_{eff} (effective stress intensity) was calculated using a_{eff} above and the K solution for CCT specimens noted earlier.
4. The possibility of net section yielding was noted if the nominal stress exceeded 90% of the average 0.2% offset yield strength of corresponding tensile tests. ("?" on Figures 137 and 138)

A cruciform specimen (7075-T7351 alloy) was also loaded statically in an 84 kip uniaxial frame. The biaxial stress ratio in this specimen was -0.267. The specimen containing a 0.6 inch crack (total length) was initially loaded to 77 kip. No crack growth was noticed. The specimen crack was then cyclically grown to a total length of 4.2 inches. Monotonic load was reapplied and again reached the 77 kip level. Again, no crack growth record was obtained, and the test was terminated.



(a) Specimen No. LT-7-4, Test Case No. 123



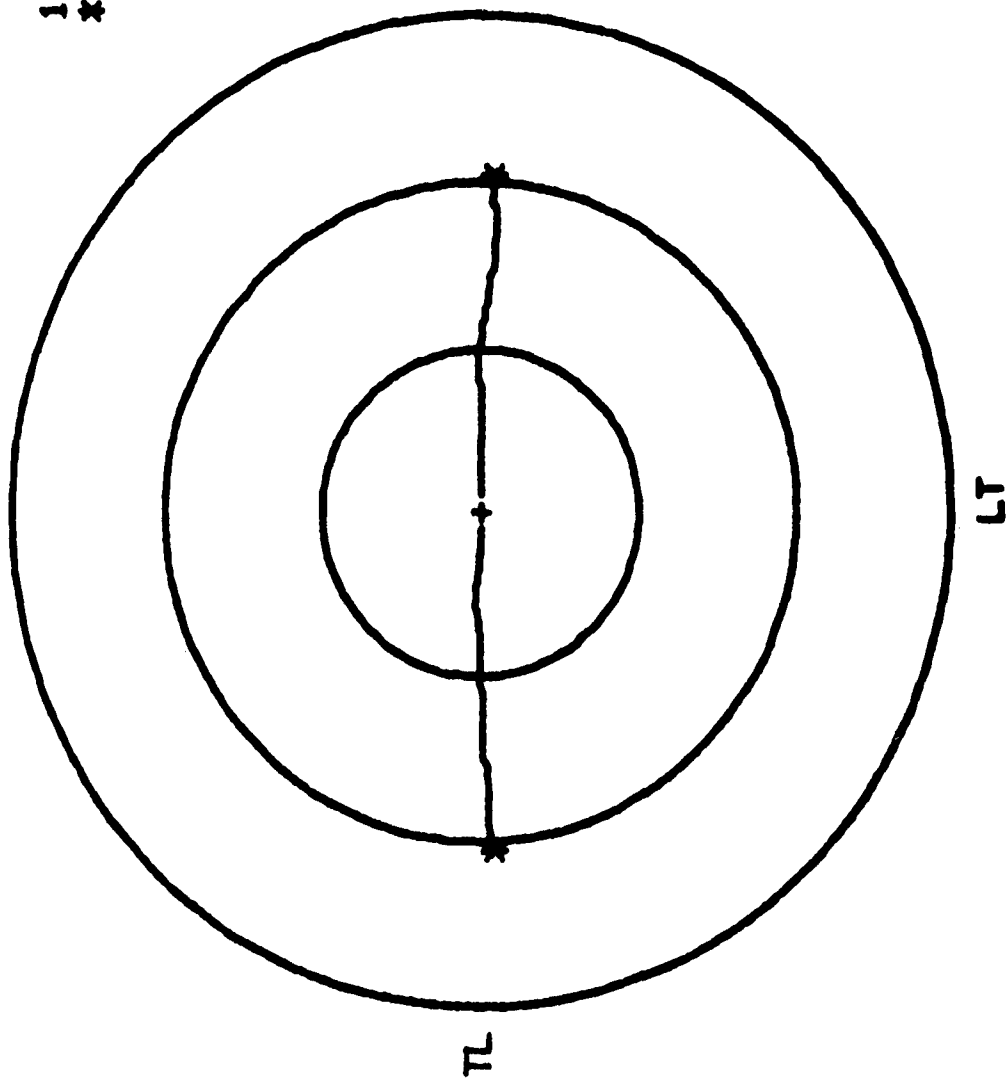
(b) Specimen No. TL-7-1, Test Case No. 125

Figure 137. Crack Growth Resistance Curve for 7075-T7351 CCT Specimen, $\sigma_x = 0$

SPECIMEN 2-23

TEST CASE 37

1 IN SPACING
* TEST STOPPED



SECTION X

GUIDELINES FOR FATIGUE CRACK GROWTH ANALYSIS

A general fatigue crack growth prediction analysis procedure consists of the following elements:

1. Geometry
2. Stress field
3. Stress intensity factor
4. Loads spectrum
5. Mathematical crack growth model

For a given structural configuration, if the geometric corrections to the crack tip stress intensities are known, e.g., the width correction factors for the CCT specimen, the first step would be to compute σ_x and σ_y , along an assumed crack plane, for an uncracked panel. Then, stress intensity factors will be those discussed in Section 6. For a biaxial stress ratio greater than unity, all the first three types of the cracks discussed in Section 6, i.e., center crack, angle crack, and crack at a hole, will become a curved crack. In this case, the methods discussed in Sections 6.4 and 8.1 apply.

In crack growth computations, existing mathematical models were found to be imperfect in accounting for retardation in a biaxial stress field. This investigation was restricted in scope to only evaluating existing models, although a limited amount of retardation model development was carried out. Pending the development of an improved mathematical model, the modified Willenborg model can be used for crack growth analysis under spectrum loading. The plastic zone polynomials used in this report (Section 9.5) are not recommended at the present time because it is uncertain whether the nonlinearity found to exist is inherent in the polynomials or is a function of the specimen geometry. For the time being, it is recommended that the Irwin and Rice plastic zone size equations be applied, respectively, to the 7075-T7351 and 2024-T351 materials.

SECTION XI

RECOMMENDATIONS FOR FUTURE RESEARCH

1. More periodic single overload tests should be conducted. The durations for applying the overloads and the magnitude of the overload should be carefully planned so that a full curve for r_p (as a function of K) can be developed. A large number of tests should be conducted to cover a wide range of biaxial ratios. Sufficient number of duplications should be included in each loading condition so that the r_p curves can be developed by statistical means. The backtracking technique for determining the plastic zone size is recommended.
2. Additional overload tests on CCT specimens of various width dimensions are needed to determine whether or not the crack tip plastic zone size nonlinearities observed in this study are attributable to specimen geometry effects.
3. Negative R cyclic crack growth data (both constant amplitude and spectrum containing tension-compression cycles) should be acquired.
4. An improved crack growth retardation analysis procedure should be developed.
5. More curved crack growth data should be acquired at various high biaxial ratios. Spectrum load tests, at the same biaxial ratio range, should also be conducted.
6. Improved analytic solution for the crack turning angle relationship for curved crack(s) should be developed. A generalized computer routine for growing a curved crack is needed.
7. More fracture data (at various biaxial ratios) should be acquired so that a failure criterion for crack(s) in a biaxial stress field can be developed.

REFERENCES

1. Paris, P.C. and Sih, G.C., in Fracture Toughness Testing and its Applications, ASTM STP 381, 1965, pp. 30-83.
2. Miller, K.J. and Kfoury, A.P., International Journal of Fracture, Volume 10, No. 3, September 1974, pp. 393-404.
3. Kfoury, A.P. and Miller, K.J., Fourth International Conference on Fracture, Waterloo, Canada, June 19-24, 1977, Paper No. MS294.
4. Hilton, P.D., International Journal of Fracture, Volume 9, No. 2, June 1973, pp. 149-156.
5. Smith, S.H., in Prospects of Fracture Mechanics, G.C. Sih, H.C. Van Elst, and D. Broek, Editors, Noordhoff International Publishing, Lyden, The Netherlands, 1974, pp. 367-388.
6. Adams, N.J.I., Engineering Fracture Mechanics, Volume 5, 1973, pp. 983-991.
7. Eftis, J., Subramonian, N. and Liebowitz, H., Engineering Fracture Mechanics, Volume 9, 1977, pp. 189-210.
8. Liebowitz, H., Lee, J.D., and Eftis, J., Engineering Fracture Mechanics, Volume 10, 1978, pp. 315-335.
9. Roberts, R. and Potheraj, S., Second International Conference on Structural Mechanics in Reactor Technology, Berlin, Germany, September 10-14, 1973, Paper No. L8/3.
10. Kibler, J.J. and Roberts, R., Journal of Engineering for Industry, Trans. ASME, Series B, November 1970, pp. 727-734.
11. Pook, L. and Holmes, P., International Conference on Fatigue Testing and Design, London, England, April 5-9, 1976.
12. Leever, P.S., Radon, J.C. and Culver, L.E., Journal of Mechanics and Physics of Solids, Volume 24, 1976, pp. 381-395.
13. Radon, J.C., Leever, P.S. and Culver, L.E., Fourth International Conference on Fracture, Waterloo, Canada, June 19-24, 1977, Paper No. MS47.
14. Radon, J.C., Leever, P.S. and Culver, L.E., Experimental Mechanics, Volume 17, 1977, pp. 228-232.
15. Hopper, C.D. and Miller, K.J., Journal of Strain Analysis, Volume 12, No. 1, 1977, pp. 23-28.

16. Liu, A.F., AIAA Journal, Volume 12, No. 2, February, 1974, pp. 180-185.
17. Beck, E.J., "Fatigue Flaw Growth Behavior in Stiffened and Unstiffened Panels Loaded in Biaxial Tension," NASA Report CR-128904, National Aeronautics and Space Administration, Washington, D.C., February 1973.
18. Zamrik, S.Y. and Shabara, M.A., Fourth Inter-American Conference on Materials Technology, Caracas, Venezuela, June 29 to July 4, 1975.
19. Joshi, S.R. and Shewchuk, J., Experimental Mechanics, Volume 10, No. 12, 1970, pp. 529-533.
20. Tada, H., Paris, P.C. and Irwin, G.R., The Stress Analysis of Cracks Handbook, Del Research Corporation, Hellertown, PA, 1973.
21. Tong, P., Pian, T.H.H. and Lasry, S., International Journal of Numerical Mathematics in Engineering, Volume 7, 1973, pp. 297-308.
22. Bowie, O.L., Journal of Mathematics and Physics, Volume 35, 1956, p. 60.
23. Newman, J.C., Jr., "An Improved Method of Collocation for the Stress Analysis of Cracked Plates with Various Shaped Boundaries," NASA Report TN D-6376, August 1971.
24. Howland, R.C.J., Trans, Royal Society (London), Series A, Volume 119, 1930, pp. 49-86.
25. Liu, A.F., Proceedings of the Second International Conference on Mechanical Behavior of Materials, American Society of Metals, 1976, pp. 601-605.
26. James, L.A. and Anderson, W.E., Engineering Fracture Mechanics, Volume 1, No. 3, 1969, p. 565.
27. Cotterell, B., International Journal of Fracture Mechanics, Volume 2, 1966, pp. 526-533.
28. Eftis, J. and Subramonian, N., Engineering Fracture Mechanics, Volume 10, 1978, pp. 43-67.
29. Irwin, G.R., in Treatise on Adhesives and Adhesion, R.L. Patrick, Editor, Marcel Dekker, New York, 1966, Chapter 7, pp. 233-267.
30. Erdogan, F. and Sih, G.C., Journal of Basic Engineering, Trans, ASME, Series, D, Volume 85, 1963, pp. 519-527.
31. Sih, G.F., in Mechanics of Fracture, Volume 1, Methods of Analysis and Solutions of Crack Problems, G.C. Sih, Editor, Noordhoff International Publishing, Leyden, The Netherlands, 1973, Introductory Chapter, pp. XXI-XLV.
32. Shah, R.C., in Fracture Analysis, ASTM STP 560, 1974, pp.29-52.

33. Rice, J.R., in Fatigue Crack Propagation, ASTM STP 415, 1967, p. 254 and p. 272.
34. Von Euw, E.F.J., "Effect of Overload Cycle(s) on Subsequent Fatigue Crack Propagation in 2024-T3 Aluminum Alloy," Ph.D Dissertation, Lehigh University, 1971.
35. Elber, W., in Damage Tolerance in Aircraft Structure, ASTM STP 486, 1971, pp. 230-242.
36. Iida, S. Kobayashi, A.S., Journal of Basic Engineering, Trans., ASME, Series D, Volume 91, 1969, pp. 764-769.
37. Chiu, S.T. and Liu, A.F. in Mechanics of Crack Growth, ASTM STP 590, 1976, pp. 263-280.
38. Sih, G.C., Paris, P.C. and Erdogan, F., Journal of Applied Mechanics, Trans, ASME, Series, E, Volume 29, 1962, pp. 306-312.
39. Willenborg, J., Eagle, R.M. and Wood, H.A., "Crack Growth Retardation Model Using an Effective Stress Concept," AFFDL TM-71-1-FBR, January 1971.
40. Gallagher, J.P. and Hughes, T.F., "Influence of Yield Strength on Overload Affected Fatigue Crack Growth Behavior in 4340 Steel," AFFDL TR-74-27, July 1974.
41. Paris, P.C., "The Growth of Cracks Due to Variations in Load," Ph.D Dissertation, Lehigh University, 1962.
42. Collipriest, J.E., Jr., in The Surface Crack: Physical Problems and Computational Solutions, J.L. Swedlow, Editor, ASME, 1972, pp. 43-62.
43. Bell, P.D. and Creager, M., "Crack Growth Analysis for Arbitrary Spectrum Loading," Volume I, Results and Discussion, AFFDL TR-74-129, October 1974.
44. Bell, P.D. and Feeney, W.J., "Fractographic Evaluation of Fracture Specimens," AFFDL-TR-75-152, March 1976.
45. Hall, L.R., Shah, R.C. and Engstrom, W.L., "Fracture and Fatigue Crack Growth Behavior of Surface Flaws and Flaws Originating at Fastener Holes," AFFDL TR-74-47 (2 Volumes), May, 1974.
46. Chanani, G.R., "Fundamental Investigation of Fatigue Crack Growth Retardation in Aluminum Alloys," AFFDL TR-76-156, September 1976.
47. McGee, W.M. and Hsu, T.M., "Effects of Underloads on Fatigue Crack Growth," AFFDL TR-77-2 (2 Volumes), March, 1977.